

Computational Study of Actinide- Noble Gas Systems

A thesis submitted to the University of Manchester for the degree

of

Doctor of Philosophy

in the Faculty of Science and Engineering

2023

Lin YANG

Department of Chemistry, School of Natural Sciences

-Blank page-

Content

Abstract	5
Declaration	7
Justification for Journal Format	9
Copyright Statement	11
Acknowledgments.....	13
Part I Introduction	
1 Literature Review on Actinide-noble Gas Systems.....	17
1.1 Actinide-noble gas systems in nuclear fuel	17
1.1.1 Advanced nuclear fuels	19
1.1.2 Fission gas release model.....	21
1.2 Molecular actinide-noble gas system	31
1.3 Summary, Aims, and Objectives.....	34
References	36
2 Theoretical Background	43
2.1 Hartree-Fock method (HF)	45
2.2 Post-Hartree-Fock methods	46
2.2.1 Møller-Plesset many-body perturbation theory (MPPT)	46
2.2.2 Coupled-cluster method	48
2.3 Density functional theory (DFT)	49
2.3.1 Hohenberg-Kohn theorems	49
2.3.2 Kohn-Sham equations	50
2.3.3 Exchange-correlation functionals.....	51
2.4 Basis set.....	55

2.4.1 Atom-centered basis set	55
2.4.2 Basis set superposition error	58
2.4.3 Plane waves.....	59
2.4.4 Pseudopotential	61
2.5 Ab initio molecular dynamics (AIMD)	65
2.6 Special quasi-random structure (SQS)	66
2.7 Diffusion coefficient from atomic jump process.....	68
2.8 Analytical techniques	74
2.8.1 Quantum theory of atom-in-molecule (QTAIM)	74
2.8.2 Interacting quantum atoms (IQA).....	77
2.9 Software Used	78
References.....	79

Part II Results

3 Incorporation of Kr and Xe in Uranium Mononitride.....	87
4 Diffusion of Krypton and Xenon in Uranium Mononitride	89
5 Incorporation and Migration of Xenon in Uranium-plutonium Mixed Nitride	91
6 High Coordination Number Actinide-Noble Gas Complexes.....	93

Part III Conclusions

7 Conclusions and Future Work	97
7.1 Conclusions.	97
7.2 Future work	99

Word count: 45,824

Abstract

This thesis reports studies of systems containing actinide (An) and noble gas (Ng) elements, in both the nuclear materials and coordination chemistry fields.

Among nuclear fuel fission products, noble gases (Ng, especially Kr and Xe) have low solubility and may release to the fuel-clad gap, which will lead to fuel swelling and thermal conductivity degradation. For the safe and efficient use of nuclear fuel, it is important to have a comprehensive understanding of fission gas release behaviours. However, the fission gas release model in actinide nitrides, promising candidates for use as a fuel in Generation IV reactors, is rudimentary. Chapter 3 studies the effect of non-stoichiometry of UN on point defect formation energy and Ng solution energy. The most stable defect types and the preferred trap sites of Ng under different stoichiometric conditions are reported. Chapter 4 investigates the diffusion of Ng in UN, and finds that the Ng diffusion is governed by the U vacancy-assisted mechanism. The calculated diffusion coefficients are in good agreement with the experiments. Chapter 5 extends the binary UN work to ternary (U, Pu)N. Actinide vacancy formation energy and Ng incorporation energy are found to be highly dependent on the chemical environment around the defects (*i.e.*, the number of U atoms in the first ($N_U(1NN)$) and second ($N_U(2NN)$) nearest-neighbour shell), which increase as $N_U(1NN)$ increases while decrease as $N_U(2NN)$ increases.

In coordination chemistry, An-Ng (especially He) complexes are candidate molecules for achieving high coordination numbers. Chapter 6 investigates the geometries, electronic structures, and bond properties of early An-Ng complexes, reporting 18-coordinate Th^{3+} -He and Th^{4+} -He systems for the first time. The covalency of the An-He bond in the group valent $AnHe_{17}^{q+}$ ($An = Ac - U$) species increases from $AcHe_{17}^{3+}$ to UHe_{17}^{6+} , while Ac-Ng bond covalency in $AcNg_{12}^{3+}$ increases as the Ng gets heavier.

-Blank page-

Declaration

No portion of the work referred to in the thesis has been submitted in support of an application for another degree or qualification of this or any other university or other institutes of learning.

-Blank page-

Justification for Journal Format

This thesis is in journal format, where chapters 3-6 are articles published in peer-reviewed journals. Submitting my thesis in journal format was to encourage publication throughout my study and to avoid unnecessary repetition of writing.

-Blank page-

Copyright Statement

- (i) The author of this thesis (including any appendices and/or schedules to this thesis) owns certain copyright or related rights in it (the “Copyright”) and they have given the University of Manchester certain rights to use such Copyright, including for administrative purposes.
- (ii) Copies of this thesis, either in full or in extracts and whether in hard or electronic copy, may be made only in accordance with the Copyright, Designs and Patents Act 1988 (as amended) and regulations issued under it or, where appropriate, in accordance with licensing agreements which the University has from time to time. This page must form part of any such copies made.
- (iii) The ownership of certain Copyright, patents, designs, trademarks and other intellectual property (the “Intellectual Property”) and any reproductions of copyright works in the thesis, for example graphs and tables (“Reproductions”), which may be described in this thesis, may not be owned by the author and may be owned by third parties. Such Intellectual Property and Reproductions cannot and must not be made available for use without the prior written permission of the owner(s) of the relevant Intellectual Property and/or Reproductions.
- (iv) Further information on the conditions under which disclosure, publication and commercialisation of this thesis, the Copyright and any Intellectual Property and/or Reproductions described in it may take place is available in the University IP Policy (see <http://documents.manchester.ac.uk/DocuInfo.aspx?DocID=24420>), in any relevant Thesis restriction declarations deposited in the University Library, the University Library’s regulations (see <http://www.library.manchester.ac.uk/about/regulations/>) and in the University’s policy on Presentation of Theses.

-Blank Page-

Acknowledgments

First, I would like to thank my supervisor Prof. Nikolas Kaltsoyannis for providing me with the opportunity to study in this group, and for his help throughout my PhD study. I am very grateful to him for allowing me to change my research direction from molecules to solids at the beginning of the second year, knowing that I am more interested in nuclear fuel. He is a model of what a supervisor should be. I would also like to thank all members of the Kaltsoyannis group (especially Jiali Chen and Xiaoyu Han) for their help and friendship. The great atmosphere and various activities, like baking rota and secret santa, make my office time enjoyable.

Thanks to the China Scholarship Council and The University of Manchester for a PhD studentship. I am also grateful to The University of Manchester for its Computational Shared Facility (CSF3, CSF4 and HPC pool) and associated support services, especially the Research IT team who helps me a lot in installing and running software.

Finally, I would like to thank my parent and my husband for their firm support. Although my parent knows nothing about my research, they always have confidence in me and are proud of me. Without my husband's encouragement, I would not have made up my mind to go abroad to study for the PhD alone.

-Blank page-

Part I

Introduction

-Blank page-

1 Literature Review on Actinide-noble Gas Systems

1.1 Actinide-noble gas systems in nuclear fuel

Since being commercially used in the 1950s, nuclear power has played an important role in global energy. As the second largest source of low-carbon power in the world, there are 411 nuclear reactors in operation with a maximum operating capacity of 369 GWe currently¹. The evolution of nuclear reactors can be divided into four generations^{2,3} (Figure 1-1). Generation I reactors were developed in the 1950s – 1960s, and use natural uranium and graphite as fuel and moderator, respectively¹. The last one, Wylfa 1 in the UK, was shut down at the end of 2015⁴. Generation II/III reactors typically use enriched uranium as fuel. They are usually cooled down and moderated by water, except for British gas-cooled reactors which use graphite moderators and CO₂ coolant⁵. Generation III/III+ reactors evolved from Generation II with enhanced safety. All commercial reactors currently in use or under construction are of these types.

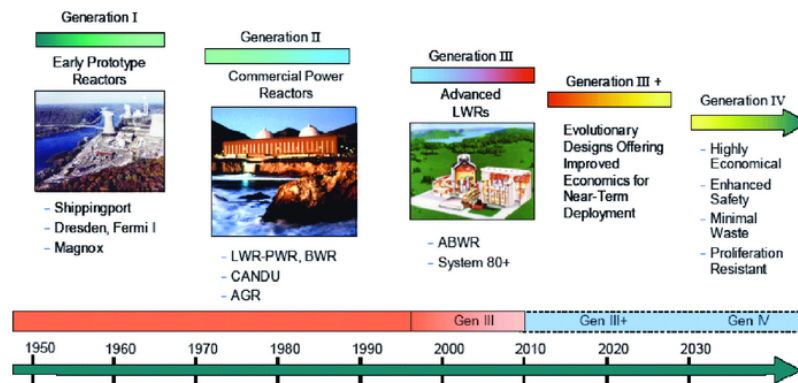


Figure 1-1. Evolution of nuclear power systems from Generation I to the future Generation IV systems. Reprinted from reference 3.

Designs of Generation IV reactors are considered revolutionary because of their discontinuity with Generation III. Compared with the Generation I-III reactors, Generation

IV reactors have the advantages of closed fuel cycles, higher operation temperature, longer core life, as well as larger capacity. The Generation IV international Forum (GIF), an international collective representing governments of 13 countries, has chosen six technologies that they believe are the future shape of nuclear energy (Figure 1-2)^{3, 6}: gas-cooled fast reactor (GFR), lead-cooled fast reactor (LFR), molten salt reactor (MSR), sodium-cooled fast reactor (SFR), supercritical water-cooled reactor (SCWR), and very high-temperature gas reactor (VHTR). The development of MSRs has two directions: one is molten salt fast neutron reactor (MSFR), which will take thorium into fuel cycles; and the other is fluoride salt-cooled high-temperature reactor (FHR), which has a similar fuel core structures as VHTR but uses molten salt as a coolant rather than helium⁷. Thus, there are seven reactor designs under development by the GIF. Among them, four designs are fast reactors (or fast-neutron reactors, FNR), and one can be built as a fast reactor (SCWR).

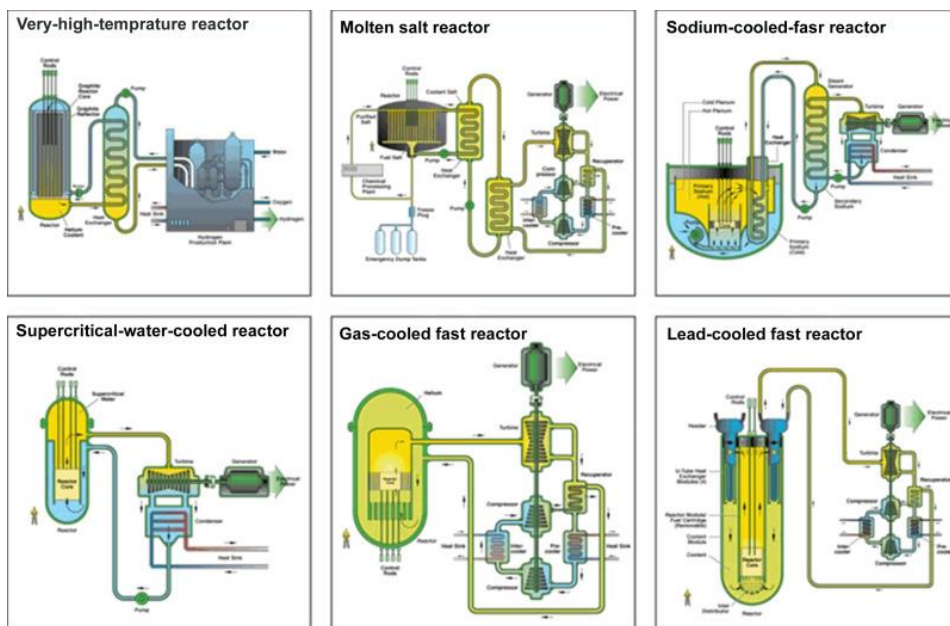


Figure 1-2. Six reactor technologies of Generation IV. Reprinted from reference 6 with permission from Elsevier.

1.1.1 Advanced nuclear fuels

Fuels for FNR are expected to have large actinide density, high thermal conductivity, good compatibility with fuel claddings and reactor coolant, and high melting points. Four advanced fuel types have been proposed and investigated for FNR: mixed-oxide fuel (MOX), metal alloy fuel, carbides, and nitrides⁸.

Mixed-oxide fuel (MOX). Oxide fuels are the preferred choice in all the main countries due to mature manufacturing and operation technologies established from the main commercial reactor – pressurized water reactor (PWR). They are being researched particularly in Europe and Russia, like the European gas-cooled fast reactor ALLEGRO⁹, the European lead-cooled fast reactor ALFRED¹⁰, and the Russian BN series¹¹. MOX fuels have higher melting temperatures than metal fuels and lower thermal expansion than carbides and nitrides, which contributes to their outstanding high-temperature performance¹². Compared with other fuel types, the thermal conductivity of MOX fuels is the lowest, which forms a temperature gradient with the centre region of fuel pellets being the hottest¹³. This prompts the fission gas release to the fuel-cladding gap, contributing to a low fuel swelling rate. On the other hand, the large temperature gradient leads to highly localized fuel microstructures, which makes it difficult to predict entire fuel behaviours by extrapolating from limited regions due to the unique contribution of each region¹³.

Metal fuel. Metal fuels are fabricated by adding alloying elements to uranium or uranium-plutonium fuels to enhance fuel properties, like melting temperature and irradiation resistance. For example, melting temperatures of U and U-40% Zr are 1400 K and 1795 K, respectively¹⁴. Many metal alloy fuels have been experimentally explored, like U-Cr and U-Mo in the UK Dounreay Fast Reactor¹⁵, U-Fs (Fs represents the mixture of Mo, Ru, Rh, Pd, Zr, and Nb) and U-Pu-Zr in US sodium-cooled breeder reactor EBR-II and the

following ARC-100¹⁶. Zr has been proven to be the best choice among various alloy elements because it efficiently enhances fuel-cladding compatibility by reducing interdiffusion between fuel and cladding¹⁷. Thus, more recent interests have focused on U-Pu-Zr. Compared with other fuel types, metal fuels have the highest actinide density and thermal conductivity. For example, U-10% Zr metallic fuel pins at 85% smear density provide 35 % more ²³⁸U than UO₂ pellets with a smear density of 93%¹⁸. However, metal fuels are not suitable for LFR due to solubility in coolant Pb and/or Bi, which may lead to fuel dissociation in cladding breaching accidents¹⁹.

Mixed carbides. There are several types of carbide fuels, like UC, UC₂, U₂C₃, and (U, Pu)C²⁰. Among them, monocarbide is the most favoured one for FNR with others being attractive for high-temperature gas-cooled reactors. Carbide fuels have a higher thermal conductivity than oxides, which results in a lower fuel temperature. Consequently, fission gas release rates are lower in carbide fuels, which may lead to greater fuel swelling. This is also a problem for nitride fuels. To overcome this, a larger fuel-cladding gap width is necessary to provide enough space for fuel swelling²⁰. Carbide fuels are mainly being researched in India, where a fast breeder test reactor (FBTR) with a fuel of 70% PuC + 30% UC has been running since 1985²¹.

Mixed nitrides. Thermal conductivity and actinide density of nitride fuels (UN+10-20%PuN) are about 7 and 1.3 times higher than the widely used oxide fuel UO₂²². Moreover, nitride fuels have longer fuel cycle times than oxide fuels. For example, by replacing a standard UO₂ fuel with UN at the same enrichment, in-core fuel residence time can be increased by 1.4 years, which will lead to fewer shut downs for reloading²³. An additional advantage of nitride fuels is their good compatibility with lead coolant, making them the preferred fuel type for LFR¹⁹. It is worth noting that enriched ¹⁵N should be used

in nitride fuels to avoid ^{14}C contamination by (n, p) reaction of ^{14}N ²⁴. Consequently, additional costs are required to enrich ^{15}N , which can be offset by lower U enrichment requirements in nitride fuels²⁵. Another issue of nitride fuels is possible dissociations at a temperature significantly lower than their congruent melting point (3123 K for UN) if nitrogen pressure is lower than a critical point (2.5×10^5 Pa for UN)²⁶. Nitride fuels are mainly being researched in USA, Russia, and Japan. (U, Pu)N fuel pins with Pu content of 18.6 wt% have been tested in Japan's JOYO experimental reactor²⁷. In Russia, nitride fuels have been tested in SFR BOR-60 with Pu content of 42 wt% and 57 wt%, and are planned to be loaded in future SFR BN-1200 and LFR BREST as a part of the "Breakthrough" project^{11, 28-29}. In the US, the secure transportable autonomous reactor (STAR) project is being designed and developed, which is an LFR using (U, TRU)N fuels (TRU represents transuranic elements)³⁰.

This thesis is focused on nitride fuels.

1.1.2 Fission gas release model

During the normal operation of nuclear reactors, fissions of actinides will generate amounts of fission products. Approximately 30% of the fission products are noble gases (Ng) xenon and krypton in UO_2 ³¹. Tests on the BOR-60 reactor with a fuel of $\text{U}_{0.55}\text{Pu}_{0.45}\text{N}$ found over 75% of the gas-phase components in the fuel-cladding gap are Xe and Kr²⁸. These Ng have very low solubility in the fuel matrix, which may migrate within fuel grains, form bubbles on grain boundaries, and/or release to fuel-cladding gaps. The presence of gases is detrimental to the thermomechanical properties of fuels in two aspects. On one hand, gas bubbles within the fuel matrix will lead to fuel swelling, which may induce pellet-cladding mechanical interaction³². Tanaka *et al.* experimentally and theoretically studied fission gas release (FGR) and swelling in (U, Pu)N fuel pins in the experimental fast reactor JOYO²⁷.

They found around 15% of fission gases were retained in bubbles with a corresponding swelling of about 7.4%, which leads to clad deformation. On the other hand, gas release to gap or precipitation in bubbles will degrade gap thermal conductance or fuel thermal conductivity, respectively. Pastore *et al.* reported an increased centreline temperature of UO_2 due to fission gas release, which positively feeds back to further FGR³³. Thus, to predict fuel performance and conduct risk assessments, it is necessary to have a comprehensive understanding of fission gas release behaviours in nuclear fuel.

Experimental fission gas release model

The release of fission gas can be divided into three stages (Figure 1-3)³¹: At the first stage, fission gases are generated and transported in bulk. The main fission gases Xe and Kr, generated by the beta decay of fissile materials (e.g., U^{235} and Pu^{239}), have very low solubility in the fuel matrix. They will be trapped by the thermal and irradiation induced defect clusters or sinks to form intragranular bubbles. Due to the impact of fission fragments, these bubbles may collapse, resulting in the release of gas atoms. Then the fission gas atoms will migrate within grains to form new intragranular bubbles, or migrate towards grain boundaries. The second stage is the formation of intergranular bubbles on grain boundaries (Figure 1-3(b)), and the growth of bubbles will link them to form paths for fission gas release to grain edges. At the third stage, grain edge tunnels will form, through which gases can be released to the fuel-clad gap (Figure 1-3(c)). In the whole process, bulk diffusion of single Ng atoms (in stage 1) is the slowest, which sets a timescale for FGR³⁴.

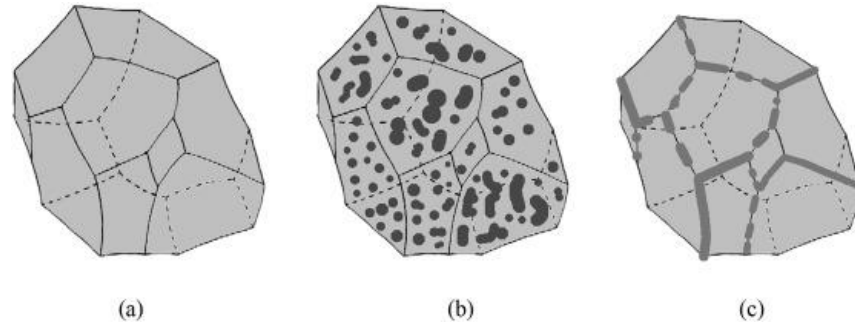


Figure 1-3. Illustration of fission gas release stages. (a) A grain of polycrystalline materials. The grain faces are the planes in grey, and the grain edges are the black lines between the two faces. (b) Grain boundary bubbles (black dots). (c) Grain edge gas tunnels. Reprinted from reference 31 with permission from Elsevier.

The bulk diffusion of a single Ng atom follows the Arrhenius law $D = D_0 \exp \left(-\frac{E_a}{k_B T} \right)$ with D_0 and E_a being the pre-exponential factor and activation energy, respectively. By measuring releases of Ng from single and polycrystalline UO_2 during irradiation, Turnbull *et al.* established a relation between Ng diffusion coefficient and temperature for bulk diffusion (Figure 1-4)³⁵⁻³⁷. At high-temperature ($T > 1653 \text{ K}$ with U enrichment of 20 %), motions of the Ng atoms are either independent or assisted by thermal vacancy concentration on the U sublattice, which is called intrinsic diffusion. Davies *et al.* reported an E_a and D_0 of 3.04 eV and $7.6 \times 10^{-10} \text{ m}^2/\text{s}$, respectively³⁸. In an intermediate temperature range, a lower activation energy was found, which leads to a higher diffusion coefficient. Turnbull *et al.* attributed this to a non-equilibrium vacancy concentration due to irradiation damage³⁵, which is called radiation-enhanced diffusion. In the low-temperature range, athermal contribution induced by irradiation dominates, although there are currently no widely accepted equations for athermal diffusion³⁵.

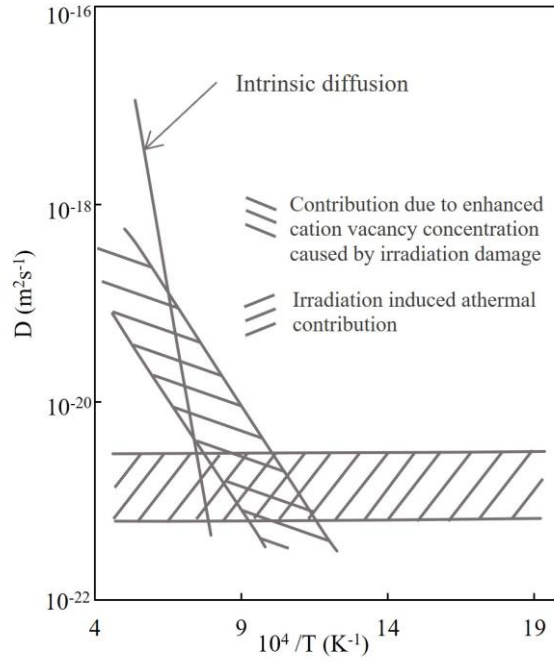


Figure 1-4. Possible components of the in-pile noble gas diffusion coefficient. Reprinted from reference 35 with permission from Elsevier.

Application of atomic simulation to fission gas release

Density functional theory (DFT) is the best tool to study single gas atom diffusion in the bulk (step 1) considering the small number of atoms required to describe a bulk system. As introduced in chapter 2.9, the diffusion rate of Ng in a bulk is determined by the Ng preferred trap sites and migration between different trap sites.

The preferred trap site of Ng in a fuel lattice is evaluated by the solution energy, which is the energy difference between a Ng-contained supercell and the corresponding perfect supercell. Alternatively, it can be calculated as the sum of the vacancy formation energy and Ng incorporation energy (the energy difference between a Ng-contained supercell and the corresponding defect supercell). Many studies found the most favourable trap site highly depends on fuel non-stoichiometry³⁹⁻⁴⁵. UO₂ has a wide range of non-stoichiometry, which can be expressed as UO_{2±x} with x being from a slightly negative value to 0.25⁴⁶.

Using the DFT method, Andersson *et al.* thoroughly studied point defects and Xe incorporation behaviour in UO_2 ^{39, 42, 47-49}. They found Xe solution energies, except for at Schottky defects, decrease from hypostoichiometric (UO_{2-x}) to hyperstoichiometric conditions (UO_{2+x})³⁹. The same trend is reported by Vathonne *et al.* for Kr⁴³. Moreover, as a semiconductor, the defect charge state, formed by bounding holes or electrons to the defects⁵⁰, also affects the solution energy of Ng in UO_2 . Vathonne *et al.* found that bound Schottky defect (BSD, $V_{\text{UO}_2}^0$), charged U-O vacancy cluster (V_{UO}^{2-}), and charged U vacancy (V_{U}^{4-}) are the most favourable trap sites for Kr in hypostoichiometric (UO_{2-x}), stoichiometric (UO_2), and hyperstoichiometric (UO_{2+x}) conditions, respectively⁴³. Differently, the most favourable site for Xe in UO_{2+x} is neutral U vacancy (V_{U}^0)³⁹. Bulk and point defect properties of mixed dioxides ((U, Pu) O_2 , (U, Th) O_2) have been investigated by several studies, which successfully established solid solution models for mixed oxides⁵¹⁻⁵⁴. The effect of chemical disorder on bound Schottky defect formation energies has been investigated by Bathellier *et al.* using empirical potentials, which provides a strategy to study point defect properties in mixed nuclear fuel⁵³.

Compared with UO_2 , the non-stoichiometry range of UN is narrow⁵⁵. And as metallic, the charge state is not necessary to be considered for nitrides. The incorporation of Ng in stoichiometric UN has been well studied, and close solution energies were reported by different work, which is thoroughly reviewed in chapter 3⁵⁶. By contrast, the work on nonstoichiometric UN is limited. Kocovski *et al.* discussed point defect formation energies under hyperstoichiometric (UN_{1+x}) and hypostoichiometric (UN_{1-x}) UN⁵⁷. They found U anti-site and N vacancy in UN_{1-x} are the most stable ones. The dependence of Ng incorporation on UN non-stoichiometry is first reported by our work in chapter 3⁵⁶. For mixed nitrides, simulations focused on their lattice properties⁵⁸⁻⁵⁹. Using the molecular

dynamics (MD) method, Kurosaki *et al.* studied the physicochemical properties of $\text{U}_{0.8}\text{Pu}_{0.2}\text{N}^{59}$. They found lattice parameter, thermal expansion coefficient, and compressibility of $\text{U}_{0.8}\text{Pu}_{0.2}\text{N}$ are between the values of UN and PuN. Geometric and electronic properties of $\text{A}_{0.5}\text{B}_{0.5}\text{N}$ (A, B = U, Np, Pu) are investigated by Zhang *et al.* using the DFT method⁵⁸. They found that the 5f states of all actinide atoms do not overlap with each other. The Ng incorporation in mixed nitrides has not been studied at the atomic level before due to the complicated solid solution model of mixed nitrides. Using the special quasi-random structure method, we have constructed (U, Pu)N solid solution model and investigated Xe incorporation behaviour⁶⁰.

The preferred trap sites in some other fuels have also been studied^{44-45, 61-63}. The same as nitrides, the charge state is not considered for carbides and silicides which are also metallic. Using the DFT method, Huang *et al.* calculated Xe incorporation energy in UC under different stoichiometric conditions⁴⁵. They found the most favourable sites are U vacancy and vacancy cluster containing a V_{U} and 3 V_{C} under C-rich and U-rich conditions, which is consistent with other works. For U_3Si_2 , U 2a vacancy is the most favourable one for all stoichiometric conditions, which is followed by interstitial site and Si vacancy⁴⁴.

In summary, in ceramic fuels, Ng prefers the trap sites containing actinide vacancy or actinide vacancy clusters.

For migration between different trap sites in UN, using the empirical potential, Kocovski *et al.* found Xe jump between interstitial sites by forming a Xe-U dumbbell has the lowest energy barrier⁶⁴. However, the solution energy of Xe at the interstitial site is much higher than that in a U vacancy site, leading to extra energy costs to move Xe from the most stable site to the interstitial one. By the *ab initio* molecular dynamics (AIMD) method, Zhang *et al.* found that an interstitial Xe atom spontaneously moves into the nearest-neighbouring

U vacancy site at low temperature without energy barrier⁶⁵. Then Xe diffusion happens by binding a second assisted U vacancy. The migration energy barriers for Kr and Xe in antiferromagnetic UN between different U vacancy types are reported to be 0.47 – 3.69 eV and 0.83 – 3.87 eV, respectively, by Claisse *et al.* using the climbing image nudged elastic band (CINEB) method (Figure 1-5)⁶⁶.

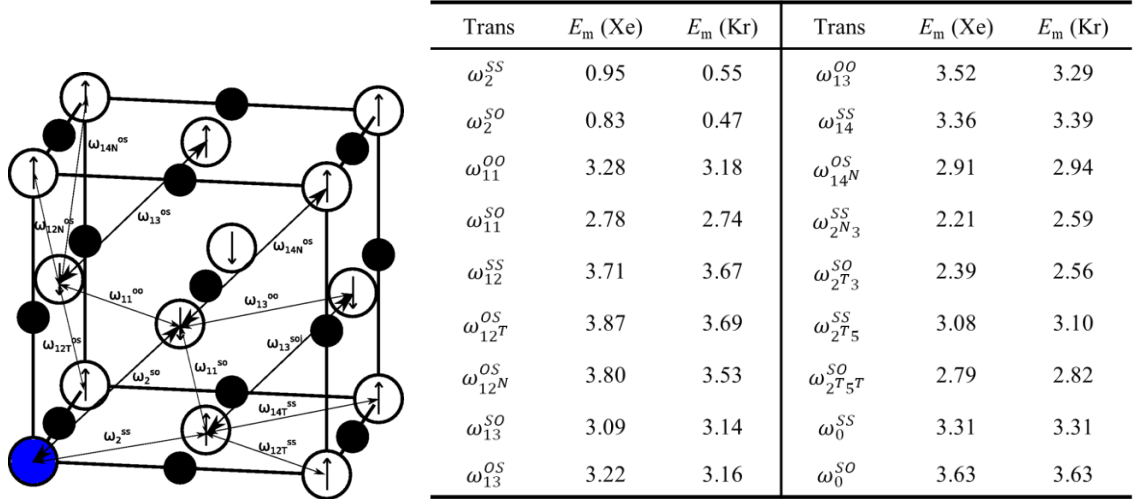


Figure 1-5. Left: solute atom (blue ball) migration in antiferromagnetic UN. White and black balls represent U and N, respectively. Right: migration energy (E_m /eV) of Xe and Kr in UN along the pathways as the left figure. Reprinted from reference 66 with permission from the American Physical Society (APS).

Compared with UN, migration studies in UO_2 are abundant^{31-32, 34}. The vacancy mechanism has been proved to be the dominant one for Ng diffusion in UO_2 , which involves two steps: Xe jumps from the initial trap site to the assisting vacancy, and the vacancy migrates to another nearest neighbouring site. The second step can occur through a direct mechanism or an indirect mechanism³⁴. In the former, a vacancy directly jumps to another nearest-neighbouring site (Figure 1-6)⁶⁷. In the latter, a vacancy jumps to a second nearest-neighbouring site, then returns to another nearest one⁶⁷. Using the CINEB method, Andersson *et al.* found migration of Xe between two V_U^{4-} has the lowest barrier, which is

about 0.44 eV lower than that between two neutral U vacancies⁴². Introducing extra O vacancies to the cluster increases the barrier by 1 – 2 eV. But their calculated Xe intrinsic diffusion rate using these atomic data is over one order of magnitude lower than the experiments (red circles in Figure 1-7). Perriot *et al.* attributed this underestimation to applying the LDA + U functional to calculate migration barriers⁴⁸. They found the GGA + U functional predicts migration barriers involving U vacancies around 1 eV lower than that using LDA + U , which well reproduces the experimental Xe diffusion coefficient (Figure 1-7).

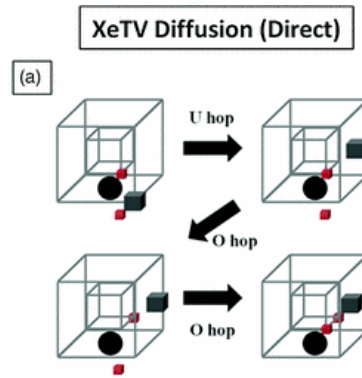


Figure 1-6. Xe-tetravacancy (XeTV, Xe is trapped at V_{UO_2} site) migration in UO₂ assisted by a V_U mechanism along the direct pathway. The black spheres, grey cubes, and small red cubes are Xe_U, V_U , and V_O , respectively. The large wireframe cube is a single unit cell of UO₂ and the inner wireframe cube corresponds to the oxygen atom positions. Reprinted from reference 67 with permission from the American Physical Society (APS).

For Ng migration in silicides, Andersson *et al.* used the CINEB method to study the migration of Xe in U₃Si₂⁴⁴. They found Xe migration is anisotropic and has the lowest barrier for jumping between two $V_{U_{4h}}$ sites in the *ab* plane. The energy barrier by the interstitial mechanism is larger than that by the vacancy mechanism. The same anisotropy has been reported by Hu *et al.*⁶⁸, but they found the lowest-barrier pathway is U_{4h} to U_{2a} vacancy along the *c* direction with the energy barrier being 1 eV larger than that obtained

by Andersson *et al.*. Moreover, the energy barriers for other pathways are also significantly different in these works.

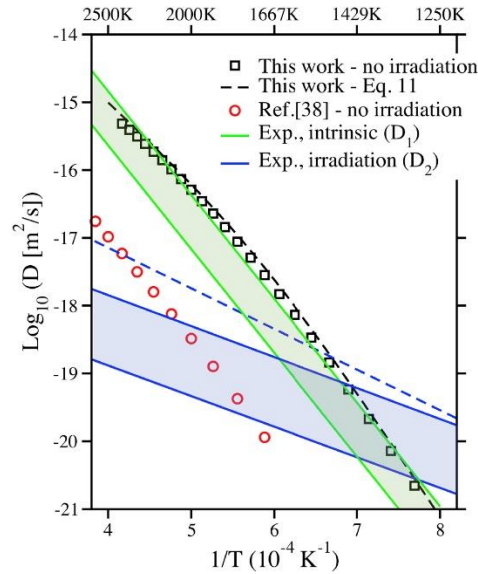


Figure 1-7. Total Xe diffusivity in UO_2 obtained by Perrit *et al.*. Reprinted from reference 48 with permission from Elsevier.

In addition to energy barriers, attempt frequency is another important factor to calculate the diffusion coefficient, which is determined by the vibrational frequency of initial and transition states. However, DFT calculations of attempt frequency have been deemed too costly and difficult to pursue. Two approximate methods can be used in direct DFT calculations. The one is to fix matrix atoms and study the motion of migrating atoms only⁶⁹⁻⁷¹, which has been used in our work in chapter 4⁷². The other is to approximate the original system by a smaller supercell, which contains migration atoms and their neighbouring matrix atoms only. This has been used by Andersson *et al.* to calculate Xe diffusivity in U_3Si_2 ⁴⁴.

Alternatively, many studies choose to use the molecular dynamics method based on empirical potentials for the costly attempt frequency calculation, although the accuracy of

MD simulations highly depends on the quality of the potential. Several different potentials have been used for the UN. By fitting the changes of lattice parameters to temperature and pressure, a Morse-type potential function added to a Busing-Ida type potential has been developed by Kurosaki *et al.*⁷³. Using this potential, the calculated heat capacity at constant volume agrees well with the experimental data. A parameter-free method based on lattice inversion was used by Chen *et al.* to derive another Morse-type potential for UN⁷⁴. The thermal expansion coefficient of the UN has been well reproduced by this potential. But the defect behaviour has not been taken into consideration by these two potentials. Then, a new one in the form of angular-dependent potential (ADF) has been developed by Kuksin *et al.* using a force-matching method to study the diffusion of point defects in UN⁷⁵. Although the calculated lattice parameter and elastic constant agree well with experiments, this potential fails to reproduce defect formation energies and migration energies obtained from DFT, as well as experimental formation energies of different U-N phases. Based on the same method, another ADF potential has been developed by Starikov *et al.* for a UN + Xe system⁷⁶. Compared with Kuksin *et al.*, they used a larger database by adding 10 new reference configurations. The calculated Xe diffusion coefficient agrees well with some experiments. Employing an empirical fitting procedure, a pairwise Buckingham potential with a many-body embedded atom method (EAM) has been developed by Kocevski *et al.* for Xe-incorporated UN⁵⁷. DFT defect formation energies and Xe incorporation energies are well predicted by this potential, but the negative Xe- V_U binding energy contrasts with the DFT value. They attributed this to the simplification of atomic interactions in the empirical potential. In the case of UO₂, the development of empirical potentials has been thoroughly reviewed in reference 32. An intrinsic issue for these empirical potentials is the inability to describe charge transfer, which restricts atoms to their formal charges. For example, only the formal +4, -2, and 0 charges were considered for U, O, and Kr in the

study of Kr diffusion in UO_2 using Buckingham-type potential⁴³. Thus, careful tests are necessary when using the MD method with empirical potentials, which is usually achieved by comparing with the information obtained from the DFT.

Using a combination of DFT and MD calculations, a full expression of Ng intrinsic diffusion coefficient in UO_2 has been well established in several studies. Perriot *et al.* found $\text{Xe}_{\text{U}_2\text{O}_y}$ clusters dominate Xe diffusion across the full temperature range with $\text{Xe}_{\text{U}_2\text{O}}$ having the highest rate⁴⁸. The obtained Xe total diffusivity is in good agreement with experiments above 1400 K. The diffusion coefficients of Kr in non-stoichiometric UO_2 have been reported by Vathonne *et al.*⁴³. Compared with that in UO_2 , the work on UN is still rudimentary. Only three works (including ours) have reported a full expression of Ng diffusion coefficient^{66, 72, 76}, which have been thoroughly compared in chapter 4⁷². While all these works focused on a single U vacancy-assisted mechanism, the effect of vacancy cluster size is still unclear. In U_3Si_2 , Xe diffusion coefficient is found to be anisotropic, and the diffusivity is faster than that in UO_2 under thermal conditions⁴⁴. These data have been utilized in an engineer-level code BISON to predict U_3Si_2 fuel performance in an advanced test reactor, which has successfully reduced uncertainties of BISON results⁷⁷.

1.2 Molecular actinide-noble gas system

Due to the periodic model and plane-wave basis used to predict Ng diffusion in nitride fuels, directly analysing the nature of actinide-Ng interaction becomes difficult. Molecular systems are particularly helpful for studying the nature of the An-Ng bond, which contributes to understanding Ng incorporation and migration in nuclear fuels. The direct U-Ng bond was first reported by Li *et al.* in 2002⁷⁸⁻⁷⁹. During the synthesis of CUO by laser ablation of U and CO in noble gas matrices, they found that the vibrational spectrum of CUO in an Ar matrix was different from that in a Ne matrix and that the spectral shift

from Ne to Ar was much larger than the normal “matrix shift”. Combined with density functional theory (DFT) calculations, they assigned the new spectrum in Ar to triplet CUO, but singlet CUO in Ne matrix. Such matrix-induced ground-state reversal suggests direct Ar-U bonding, and is also found in Kr and Xe matrices. One year later, more CUO-based An-Ng complexes were reported⁸⁰. These $\text{CUO}(\text{Ar})_{4-n}(\text{Ng})_n$ ($\text{Ng}=\text{Kr-Xe}$, $n=1-4$) complexes have the same triplet ground-state as CUO-Ar, which further proves the ground-state reversal induced by heavier noble gas matrices. Moreover, the U-Ng bond becomes stronger as the Ng moves down the noble gas group. This ground-state crossover is further proved by Tecmer *et al.* using the density matrix renormalization group (DMRG) algorithm⁸¹. They found a larger quantum entanglement of Ar_4 orbitals with CUO compared to that of Ne_4 . Andrews *et al.* attributed the U-Ng interaction mechanism to the donation of Ng lone pair electrons into vacant orbitals of U^{80} . Therefore, positively charged actinide compounds, like UO_2^{2+} , are expected to have stronger interaction with Ng elements. Later, the U-Ng complexes $[\text{UO}_2(\text{Ne})_6]^+$, $[\text{UO}_2(\text{Ng})_5]^+$ ($\text{Ng} = \text{Ar-Xe}$) and $\text{UO}_2(\text{Ng})_4$ ($\text{Ng} = \text{Ne, Ar}$) were reported in succession⁸²⁻⁸³. The larger average U-Ar binding energy in $[\text{UO}_2(\text{Ar})_5]^+$ ($5.64 \text{ kcal mol}^{-1}$) than that in $\text{CUO}(\text{Ar})_4$ (*e.g.* $3.85 \text{ kcal mol}^{-1}$) proved the prediction and indicated the influence of molecular charge on U-Ng interaction strength^{80, 83}, which is also found in AuXe_n^{q+} ⁸⁴. The IR spectrum of PuO_2 in Ar matrix is significantly lower than the calculated value of the isolated molecule by the SO-CASPT2 method, suggesting the different ground states of PuO_2 in Ar matrix and gas phase. Similar to UO_2 , this may be because of the interaction of Pu and Ar⁸⁵⁻⁸⁶.

Actinide-Ng (especially He) complexes are also potential molecules to achieve high coordination numbers. Coordination number (CN), originally defined as the total number of neighboring atoms directly bonded with the central atom in a molecule or ion, is a fundamental concept in coordination chemistry. The experimental and theoretical search

for compounds with high CN has a long history. Hermann *et al.* predicted the existence of PbHe_{15}^{2+} with CN of 15 by DFT calculation⁸⁷. Most importantly, they predicted that even higher CN was expected to exist in charged actinide-He interactions. Motivated by their work, Kaltsoyannis theoretically studied the structure of charged actinides coordinated by He atoms and reported 17-coordinated $\text{Ac}^{3+}\text{-He}$, $\text{Pa}^{4+}\text{-He}$, and $\text{Th}^{4+}\text{-He}$ complexes (Figure 1-8), a step forward as for several years previously the highest known CN was 16⁸⁸. However, a year later, the 18-coordinated $\text{Ac}^{3+}\text{-He}$ compound was reported by Ozama *et al.*, using the path integral molecular dynamics (PIMD) method⁸⁹. They found 18 He atoms were rigidly arranged in the first shell with a highly symmetrical D_{4d} structure. Besides, they reported the significant influence of basis set superposition error (BSSE) on CCSD(T) calculations with ECP basis sets. BSSE was neglected by Kaltsoyannis, as the employed basis sets were extensive, which could account for the different results. Ozama's work also indicated the possibility to get other stable charged actinide-He complexes with $\text{CN} \geq 18$ by appropriate methods. Our later simulation (chapter 6) proves the significant effect of BSSE⁹⁰, and found the same 18-coordinated $\text{Ac}^{3+}\text{-He}$ structure. Moreover, the coordination number of 18 is found for $\text{Th}^{3+}\text{-He}$ and $\text{Th}^{4+}\text{-He}$ systems.

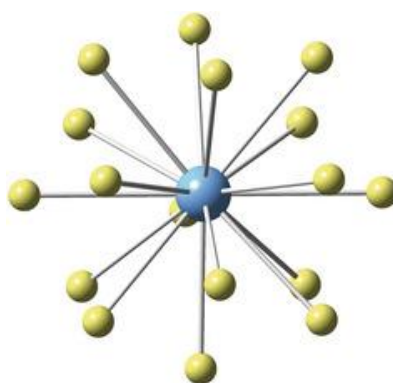


Figure 1-8. Optimized structure of AcHe_{17}^{3+} . Reprinted from reference 93 with permission from John Wiley and Sons.

Another field involving systems containing actinide and Ng is the Kr/Xe uptake and separation by metal-organic frameworks (MOF). Wang *et al.* successfully synthesized a new 3D Th-based organic framework (named SCU-11), in which Th^{4+} is 10-coordinate with a bicapped square prism coordination geometry⁹¹. This new MOF has high Xe capture capacity and Xe/Kr selectivity compared with previously reported materials. They attributed this to the similar window size to the Xe atomic radius and the higher affinity of Th^{4+} site to the more polarizable Xe over Kr due to the polarizability of Th^{4+} . Later, Mi *et al.* reported a new Th-based MOF (Th-BPYDC-I), which has a higher Kr/Xe separation rate due to the smaller window size⁹². Several other actinide-based MOFs were reported later, which usually use tetravalent actinides, although their Kr/Xe separation ability and interaction mechanism with Kr or Xe are not investigated⁹³.

1.3 Summary, Aims, and Objectives

In conclusion, although nitride fuels are promising candidates for the future fast reactors, the FGR model in them is still rudimentary. The central aim of this work is to develop a reliable method to model the FGR in nitride fuels. Specifically, the binary UN and ternary (U, Pu)N are studied. To achieve the overarching aim, following objectives are proposed:

- evaluate the performance of the DFT method for nitride systems;
- predict defect formation energies, Ng incorporation and migration energies in the considered nitrides;
- establish diffusion coefficient equations of Xe and Kr in UN;
- develop a comprehensive understanding of the nature of actinide-noble gas interactions.

This thesis is arranged as following:

Chapter 2 describes the theoretical background of methods that have been used in this thesis, as well as the used software.

Chapters 3-5 report calculations of Kr and Xe incorporation and diffusion in nitride fuels. The incorporation of Kr and Xe in uranium mononitride is reported in chapter 3, which was published in 2021 in the Journal of Physical Chemistry C (Lin Yang and Nikolas Kaltsoyannis, *J. Phys. Chem. C* 2021, 125, 26999-27008, <https://doi.org/10.1021/acs.jpcc.1c08523>). Chapter 4 reports the diffusion of Kr and Xe in uranium mononitride, in which diffusion coefficient equations are established. This work was published in 2022 in the Journal of Nuclear Materials (Lin Yang and Nikolas Kaltsoyannis, *J. Nucl. Mater.* 2022, 566, 153803, <https://doi.org/10.1016/j.jnucmat.2022.153803>). Chapter 5 extends the binary uranium mononitride work to uranium-plutonium mixed nitride. The effect of chemical environments on Xe and Kr incorporation and migration energy is reported. This work was published in the Journal of Nuclear Materials in 2023 (Lin Yang and Nikolas Kaltsoyannis, *J. Nucl. Mater.* 2023, 577, 154330, <https://doi.org/10.1016/j.jnucmat.2023.154330>).

Chapter 6 turns to molecular systems to study An-Ng interactions, which reveal the nature of the An-Ng interaction, and results consistent with chapter 3 and 5 have been found. Furthermore, highly-coordinated An-Ng complexes have been analysed to establish the covalency trend of the An-Ng bond across the An and Ng series. This work was published in 2021 in Physical Chemistry Chemical Physics (Lin Yang, Sophie Cooper and Nikolas Kaltsoyannis, *Phys. Chem. Chem. Phys.* 2021, 23, 4167, DOI: 10.1039/d0cp06175a).

Finally, general conclusions and expectations for future work are given.

References

- [1] A. Verbruggen, M. Schneider, J. Hazemann, M.V. Ramana, M. Sailer, T. Suzuki, A. Froggatt, C.v. Hirschhausen, A.J. Wimmers, N. Schneider, A. Stienne, F. Meinass, The World Nuclear Industry Status Report 2022, World Nuclear Industry, Paris, 2022.
- [2] G. Locatelli, M. Mancini, N. Todeschini, Generation IV Nuclear Reactors: Current Status and Future Prospects, *Energy Policy* 61 (2013) 1503-1520.
- [3] G.I.i. Forum, A Technology Roadmap for Generation IV Nuclear Energy Systems, U.S. DOE Nuclear Energy Research Advisory Committee and the Generation IV International Forum, 2002.
- [4] Wylfa Closes After Almost 45 years, 2015. <https://www.gov.uk/government/news/wylfa-closes-after-almost-45-years>. (Last accessed 06 March 2023 2023).
- [5] M. Margulis, E. Shwageraus, Advanced Gas-cooled Reactors Technology for Enabling Molten-salt Reactors Design-Estimation of Coolant Impact on Neutronic Performance, *Progress in Nuclear Energy* 125 (2020) 103382.
- [6] J.E. Kelly, Generation IV International Forum: A Decade of Progress Through International Cooperation, *Progress in Nuclear Energy* 77 (2014) 240-246.
- [7] Generation IV Nuclear Reactors, 2020. https://en.wikipedia.org/wiki/Advanced_Gas-cooled_Reactor. (Last accessed 06 March 2023 2023).
- [8] D. Petti, D. Crawford, N. Chauvin, Fuels for Advanced Nuclear Energy Systems, *MRS Bulletin* 34(1) (2009) 40-45.
- [9] B. Kvizda, G. Mayer, P. Vácha, J. Malesa, A. Siwec, A. Vasile, S. Bebjak, B. Hatala, ALLEGRO Gas-cooled Fast Reactor (GFR) Demonstrator Thermal Hydraulic Benchmark, *Nuclear Engineering and Design* 345 (2019) 47-61.
- [10] G. Grasso, C. Petrovich, D. Mattioli, C. Artioli, P. Sciora, D. Gugiu, G. Bandini, E. Bubelis, K. Mikityuk, The Core Design of ALFRED, a Demonstrator for the European Lead-cooled Reactors, *Nuclear Engineering and Design* 278 (2014) 287-301.
- [11] V. Rachkov, V. Poplavskii, A. Tsibulya, Y.E. Bagdasarov, B. Vasiliev, Y.L. Kamanin, S. Osipov, N. Kuzavkov, V. Ershov, M. Ashirmetov, Concept of an Advanced Power-generating Unit with a BN-1200 Sodium-cooled Fast Reactor, *Atomic Energy* 108 (2010) 254-259.
- [12] J.K. Watkins, A. Gonzales, A.R. Wagner, E.S. Sooby, B.J. Jaques, Challenges and Opportunities to Alloyed and Composite Fuel Architectures to Mitigate High Uranium Density Fuel Oxidation: Uranium Mononitride, *Journal of Nuclear Materials* 553 (2021) 153048.
- [13] R. Parrish, A. Aitkaliyeva, A Review of Microstructural Features in Fast Reactor Mixed Oxide Fuels, *Journal of Nuclear Materials* 510 (2018) 644-660.
- [14] D.E. Janney, C. Papesch, *Metallic Fuels Handbook, Part 1: Alloys Based on U-Zr, Pu-Zr, U-Pu, or U-Pu-Zr, Including Those with Minor Actinides (Np, Am, Cm), Rare-earth Elements (La, Ce, Pr, Nd, Gd), and Y; and Part 2: Elements and Alloys not Based on U-Zr, Pu-Zr, U-Pu, or U-Pu-Zr*, Idaho National Lab (INL), Idaho Falls, ID (United States), 2017.
- [15] M. Meyer, J. Gan, J. Jue, D. Keiser, E. Perez, A. Robinson, D. Wachs, N.

- Woolstenhulme, G. Hofman, Y. Kim, Irradiation Performance of U-Mo Monolithic Fuel, *Nuclear Engineering and Technology* 46(2) (2014) 169-182.
- [16] A.M. Yacout, K. Mo, A. Oaks, M. Billone, Y. Miao, J. Alicz, Qualification of Metallic Fuel Data for Advanced SFR Applications, *Nuclear Technology* (2022) 1-14.
- [17] G.L. Hofman, L.C. Walters, T. Bauer, Metallic Fast Reactor Fuels, *Progress in Nuclear Energy* 31(1-2) (1997) 83-110.
- [18] T. Sofu, A Review of Inherent Safety Characteristics of Metal Alloy Sodium-cooled Fast Reactor Fuel Against Postulated Accidents, *Nuclear Engineering and Technology* 47(3) (2015) 227-239.
- [19] T. Allen, D. Crawford, Lead-cooled Fast Reactor Systems and the Fuels and Materials Challenges, *Science and Technology of Nuclear Installations* 2007 (2007) 97486.
- [20] J. Kittel, B. Frost, J. Mustelier, K. Bagley, G. Crittenden, J. Van Dievoet, History of Fast Reactor Fuel Development, *Journal of Nuclear Materials* 204 (1993) 1-13.
- [21] B. Raj, H. Kamath, R. Natarajan, P.V. Rao, A Perspective on Fast Reactor Fuel Cycle in India, *Progress in Nuclear Energy* 47(1-4) (2005) 369-379.
- [22] A. Potapov, K. Karimov, M. Mazannikov, V. Shishkin, Y. Zaykov, Opening of Nitride Spent Nuclear Fuel, in IV Congress “Fundamental Research and Applied Developing of Recycling and Utilization Processes of Technogenic Formations” *KnE Materials Science*, 2020 438-445.
- [23] J. Zakova, J. Wallenius, Fuel Residence Time in BWRs with Nitride Fuels, *Annals of Nuclear Energy* 47 (2012) 182-191.
- [24] C. Ekberg, D. Ribeiro Costa, M. Hedberg, M. Jolkkonen, Nitride Fuel for Gen IV Nuclear Power Systems, *Journal of Radioanalytical and Nuclear Chemistry* 318 (2018) 1713-1725.
- [25] G.J. Youinou, R.S. Sen, Impact of Accident-tolerant Fuels and Claddings on the Overall Fuel Cycle: a Preliminary Systems Analysis, *Nuclear Technology* 188(2) (2014) 123-138.
- [26] E.V. Usov, V.I. Chukhno, I.G.e. Kudashov, T.y.V. Sycheva, Model for the Calculation of the Dissociation Rate of Nitride Fuel at High Temperatures, *High Temperature* 58 (2020) 222-226.
- [27] K. Tanaka, K. Maeda, K. Katsuyama, M. Inoue, T. Iwai, Y. Arai, Fission Gas Release and Swelling in Uranium-plutonium Mixed Nitride Fuels, *Journal of Nuclear Materials* 327(2-3) (2004) 77-87.
- [28] B. Rogozkin, N. Stepennova, Y.E. Fedorov, M. Shishkov, F. Kryukov, S. Kuzmin, O. Nikitin, A. Belyaeva, L. Zabudko, Results of $U_{0.55}Pu_{0.45}N$ and $U_{0.4}Pu_{0.6}N$ Mixed Mononitride Fuel Tests in a BOR-60 Reactor to Burnup 12% ha, *Atomic Energy* 110(6) (2011) 412.
- [29] A. Grachev, L. Zabud'ko, A. Glushenkov, Y.A. Ivanov, G. Kireev, M. Skupov, I. Gil'mutdinov, P. Grin, E. Zvir, F. Kryukov, Investigations of Mixed Uranium-plutonium Nitride fuel in Project Breakthrough, *Atomic Energy* 122(3) (2017) 185-199.
- [30] D. Wade, R. Doctor, K. Peddicord, STAR-H2: a Battery-type Lead-cooled Fast Reactor for Hydrogen Manufacture in a Sustainable Hierarchical Hub-spoke Energy Infrastructure, Japan (2003).

- [31] M. Tonks, D. Andersson, R. Devanathan, R. Dubourg, A. El-Azab, M. Freyss, F. Iglesias, K. Kulacsy, G. Pastore, S.R. Phillpot, M. Welland, Unit Mechanisms of Fission Gas Release: Current Understanding and Future Needs, *Journal of Nuclear Materials* 504 (2018) 300-317.
- [32] J. Rest, M.W.D. Cooper, J. Spino, J.A. Turnbull, P. Van Uffelen, C.T. Walker, Fission Gas Release From UO_2 Nuclear Fuel: A Review, *Journal of Nuclear Materials* 513 (2019) 310-345.
- [33] G. Pastore, L. Swiler, J.D. Hales, S.R. Novascone, D.M. Perez, B.W. Spencer, L. Luzzi, P. Van Uffelen, R.L. Williamson, Uncertainty and Sensitivity Analysis of Fission Gas Behavior in Engineering-scale Fuel Modeling, *Journal of Nuclear Materials* 456 (2015) 398-408.
- [34] D. Andersson, Density Functional Theory Calculations Applied to Nuclear Fuels, *Handbook of Materials Modeling* 2020, pp. 2121-2140.
- [35] J. Turnbull, C. Friskney, J. Findlay, F. Johnson, A. Walter, The Diffusion Coefficients of Gaseous and Volatile Species During the Irradiation of Uranium Dioxide, *Journal of Nuclear Materials* 107(2-3) (1982) 168-184.
- [36] J. Turnbull, The Effect of Grain Size on the Swelling and Gas Release Properties of UO_2 During Irradiation, *Journal of Nuclear Materials* 50(1) (1974) 62-68.
- [37] J. Turnbull, C. Friskney, The Relation Between Microstructure and the Release of Unstable Fission Products During High Temperature Irradiation of Uranium Dioxide, *Journal of Nuclear Materials* 71(2) (1978) 238-248.
- [38] D. Davies, G. Long, The Emission of Xenon-133 from Lightly Irradiated Uranium Dioxide Spheroids and Powders, United Kingdom Atomic Energy Authority, 1963.
- [39] D.A. Andersson, B.P. Uberuaga, P.V. Nerikar, C. Unal, C.R. Stanek, U and Xe Transport in UO_{2+x} : Density Functional Theory Calculations, *Physical Review B* 84(5) (2011) 054105.
- [40] X. Tian, T. Gao, G. Jiang, D. He, H. Xiao, The Incorporation and Solution of Krypton in Uranium Dioxide: Density Functional Theory Calculations, *Computational Material Science* 54 (2012) 188-194.
- [41] É. Bévilion, R. Ducher, M. Barrachin, R. Dubourg, First-principles Study of the Stability of Fission Products in Uranium Monocarbide, *Journal of Nuclear Materials* 426(1-3) (2012) 189-197.
- [42] D.A. Andersson, P. Garcia, X.Y. Liu, G. Pastore, M. Tonks, P. Millett, B. Dorado, D.R. Gaston, D. Andrs, R.L. Williamson, R.C. Martineau, B.P. Uberuaga, C.R. Stanek, Atomistic Modeling of Intrinsic and Radiation-enhanced Fission Gas (Xe) Diffusion in UO_2 : Implications for Nuclear Fuel Performance Modeling, *Journal of Nuclear Materials* 451(1-3) (2014) 225-242.
- [43] E. Vathonne, D.A. Andersson, M. Freyss, R. Perriot, M.W. Cooper, C.R. Stanek, M. Bertolus, Determination of Krypton Diffusion Coefficients in Uranium Dioxide Using Atomic Scale Calculations, *Inorganic Chemistry* 56(1) (2017) 125-137.
- [44] D.A. Andersson, X.Y. Liu, B. Beeler, S.C. Middleburgh, A. Claisse, C.R. Stanek, Density Functional Theory Calculations of Self- and Xe Diffusion in U_3Si_2 , *Journal of Nuclear Materials* 515 (2019) 312-325.

- [45] G.-Y. Huang, G. Pastore, B.D. Wirth, First-principles Study of Intrinsic Point Defects and Xe Impurities in Uranium Monocarbide, *Journal of Applied Physics* 128(14) (2020) 145102.
- [46] C. Guéneau, M. Baichi, D.a.a. Labroche, C. Chatillon, B. Sundman, Thermodynamic Assessment of the Uranium–oxygen System, *Journal of Nuclear Materials* 304(2-3) (2002) 161-175.
- [47] X.Y. Liu, B.P. Uberuaga, D.A. Andersson, C.R. Stanek, K.E. Sickafus, Mechanism for Transient Migration of Xenon in UO_2 , *Applied Physics Letters* 98(15) (2011) 151902.
- [48] R. Perriot, C. Matthews, M.W. Cooper, B.P. Uberuaga, C.R. Stanek, D.A. Andersson, Atomistic Modeling of Out-of-pile Xenon Diffusion by Vacancy Clusters in UO_2 , *Journal of Nuclear Materials* 520 (2019) 96-109.
- [49] C. Matthews, R. Perriot, M.W.D. Cooper, C.R. Stanek, D.A. Andersson, Cluster Dynamics Simulation of Xenon Diffusion During Irradiation in UO_2 , *Journal of Nuclear Materials* 540 (2020) 152326.
- [50] J.-P. Crocombette, Influence of Charge States on Energies of Point Defects and Clusters in Uranium Dioxide, *Physical Review B* 85(14) (2012) 144101.
- [51] P. Ghosh, A. Arya, Structural, Thermodynamic, Electronic and Elastic Properties of $\text{Th}_{1-x}\text{U}_x\text{O}_2$ and $\text{Th}_{1-x}\text{Pu}_x\text{O}_2$ Mixed Oxides, *Physical Chemistry Chemical Physics* 22(11) (2020) 6406-6417.
- [52] I.C. Njifon, M. Bertolus, R. Hayn, M. Freyss, Electronic Structure Investigation of the Bulk Properties of Uranium–plutonium Mixed Oxides (U, Pu) O_2 , *Inorganic Chemistry* 57(17) (2018) 10974-10983.
- [53] D. Bathellier, L. Messina, M. Freyss, M. Bertolus, T. Schuler, M. Nastar, P. Olsson, E. Bourasseau, Effect of Cationic Chemical Disorder on Defect Formation Energies in Uranium–Plutonium Mixed Oxides, *Journal of Applied Physics* 132(17) (2022) 175103.
- [54] M.S. Talla Noutack, G. Geneste, G. Jomard, M. Freyss, Investigation of the Bulk and Point Defect Properties in Uranium–plutonium Mixed Oxides (U, Pu) O_2 using DFT+ U : Effect of a Low Americium Content, *Journal of Applied Physics* 131(22) (2022) 225106.
- [55] T. Ogawa, Thermodynamic Properties of (U, Pu) N_{1-x} with a Sublattice Formalism—Equilibria Involving the Nonstoichiometric Nitrides, *Journal of Nuclear Materials* 201 (1993) 284-292.
- [56] L. Yang, N. Kaltsoyannis, Incorporation of Kr and Xe in Uranium Mononitride: A Density Functional Theory Study, *The Journal of Physical Chemistry C* 125(48) (2021) 26999-27008.
- [57] V. Kocovski, M.W. Cooper, A.J. Claisse, D.A. Andersson, Development and Application of a Uranium Mononitride (UN) potential: Thermomechanical Properties and Xe Diffusion, *Journal of Nuclear Materials* 562 (2022) 153553.
- [58] Y.-J. Zhang, Z.-J. Zhou, J.-H. Lan, T. Bo, C.-C. Ge, Z.-F. Chai, W.-Q. Shi, Theoretical Investigation on Electronic and Mechanical Properties of Ternary Actinide (U, Np, Pu) Nitrides, *Journal of Applied Physics* 122(11) (2017) 115109.
- [59] K. Kurosaki, K. Yano, K. Yamada, M. Uno, S. Yamanaka, A Molecular Dynamics Study on Uranium–plutonium Mixed Nitride, *Journal of Alloys Compounds* 319(1-2) (2001) 253-257.

- [60] L. Yang, N. Kaltsoyannis, Incorporation and Migration of Xenon in Uranium-plutonium Mixed Nitride; A Density Functional Theory Study, *Journal of Nuclear Materials* 577 (2023) 154330.
- [61] H. Gao, T. Lin, Y. Liu, X. Liu, M. Luo, A First-principles Study of Damage Induced by Gaseous Species He, Kr, and Xe on the Structure of Nuclear Fuel, U_3Si , *Journal of Applied Physics* 127(17) (2020) 175109.
- [62] M. Cooper, N. Kuganathan, P. Burr, M. Rushton, R. Grimes, C. Stanek, D. Andersson, Development of Xe and Kr Empirical Potentials for CeO_2 , ThO_2 , UO_2 and PuO_2 , Combining DFT with High Temperature MD, *Journal of Physics: Condensed Matter* 28(40) (2016) 405401.
- [63] É. Bévilion, R. Ducher, M. Barrachin, R. Dubourg, Investigation of the Diffusion of Atomic Fission Products in UC by Density Functional Calculations, *Journal of Nuclear Materials* 434(1-3) (2013) 240-247.
- [64] V. Kocevski, D.A. Rehn, M.W. Cooper, D.A. Andersson, First-principles Investigation of Uranium Mononitride (UN): Effect of Magnetic Ordering, Spin-orbit Interactions and Exchange Correlation Functional, *Journal of Nuclear Materials* 559 (2022) 153401.
- [65] Y.-J. Zhang, J.-H. Lan, C.-Z. Wang, Q.-Y. Wu, T. Bo, Z.-F. Chai, W.-Q. Shi, Theoretical Investigation on Incorporation and Diffusion Properties of Xe in Uranium Mononitride, *The Journal of Physical Chemistry C* 119(11) (2015) 5783-5789.
- [66] A. Claisse, T. Schuler, D.A. Lopes, P. Olsson, Transport Properties in Dilute UN(X) Solid Solutions (X=Xe,Kr), *Physical Review B* 94(17) (2016) 174302.
- [67] A.E. Thompson, C. Wolverton, Pathway and Energetics of Xenon Migration in Uranium Dioxide, *Physical Review B* 87(10) (2013) 104105.
- [68] J. Hu, M. Li, H. Gong, Q. Ren, Y. Liao, H. Xiao, X. Zu, First-principles Study of Fission Products Xe and Cs Behaviors in U_3Si_2 , *Journal of Physics: Condensed Matter* 34(16) (2022) 165702.
- [69] N. Zou, H.-J. Lu, X.-G. Lu, Impurity Diffusion Coefficients in BCC Nb from First-principles Calculations, *Journal of Alloys Compounds* 803 (2019) 684-688.
- [70] G. Ho, M.T. Ong, K.J. Caspersen, E.A. Carter, Energetics and Kinetics of Vacancy Diffusion and Aggregation in Shocked Aluminium via Orbital-free Density Functional Theory, *Physical Chemistry Chemical Physics* 9(36) (2007) 4951-4966.
- [71] X. Tang, R. Salehin, G.B. Thompson, C.R. Weinberger, Statistical Study of Vacancy Diffusion in TiC and TaC, *Physical Review Materials* 4(9) (2020) 093602.
- [72] L. Yang, N. Kaltsoyannis, Diffusion of Krypton and Xeon in Uranium Mononitride; a Density Functional Theory Study, *Journal of Nuclear Materials* 566 (2022) 153803.
- [73] K. Kurosaki, K. Yano, K. Yamada, M. Uno, S. Yamanaka, A Molecular Dynamics Study of the Heat Capacity of Uranium Mononitride, *Journal of Alloys Compounds* 297(1-2) (2000) 1-4.
- [74] P. Chen, X. Wang, X. Lai, G. Li, B. Ao, Y. Long, Ab initio Interionic Potentials for UN by Multiple Lattice Inversion, *Journal of Nuclear Materials* 404(1) (2010) 6-8.
- [75] A.Y. Kuksin, S. Starikov, D. Smirnova, V. Tseplyaev, The Diffusion of Point Defects in Uranium Mononitride: Combination of DFT and Atomistic Simulation with Novel Potential, *Journal of Alloys Compounds* 658 (2016) 385-394.

- [76] S. Starikov, A. Kuksin, D. Smirnova, A. Dolgodvorov, V. Ozrin, Multiscale Modeling of Uranium Mononitride: Point Defects Diffusion, Self-Diffusion, Phase Composition, Defect and Diffusion Forum 375 (2017) 101-113.
- [77] K. Gamble, G. Pastore, M. Cooper, D. Andersson, C. Matthews, B. Beeler, L. Aagesen, T. Barani, D. Pizzocri, Improvement of the BISON U_3Si_2 Modeling Capabilities Based on Multiscale Developments to Modeling Fission Gas Behavior, Journal of Nuclear Materials 555 (2021) 153097.
- [78] J. Li, B.E. Bursten, B. Liang, L. Andrews, Noble Gas-Actinide Compounds: Complexation of the CUO Molecule by Ar, Kr, and Xe Atoms in Noble Gas Matrices, Science 295(5563) (2002) 2242-2245.
- [79] B. Liang, L. Andrews, J. Li, B.E. Bursten, Noble Gas– Actinide Compounds: Evidence for the Formation of Distinct $CUO(Ar)_{4-n}(Xe)_n$ and $CUO(Ar)_{4-n}(Kr)_n$ ($n=1, 2, 3, 4$) Complexes, Journal of American Chemical Society 124(31) (2002) 9016-9017.
- [80] L. Andrews, B. Liang, J. Li, B.E. Bursten, Noble Gas– Actinide Complexes of the CUO Molecule with Multiple Ar, Kr, and Xe Atoms in Noble-Gas Matrices, Journal of American Chemical Society 125(10) (2003) 3126-3139.
- [81] P. Tecmer, K. Boguslawski, Ö. Legeza, M. Reiher, Unravelling the Quantum-Entanglement Effect of Noble Gas Coordination on the Spin Ground State of CUO, Physical Chemistry Chemical Physics 16(2) (2014) 719-727.
- [82] I. Infante, L. Andrews, X. Wang, L. Gagliardi, Noble Gas Matrices May Change the Electronic Structure of Trapped Molecules: the UO_2Ng_4 [$Ng=Ne, Ar$] case, Chemistry – A European Journal 16(43) (2010) 12804-7.
- [83] X. Wang, L. Andrews, J. Li, B.E. Bursten, Significant Interactions Between Uranium and Noble-gas Atoms: Coordination of the UO_2^+ Cation by Ne, Ar, Kr, and Xe Atoms, Angewandte Chemie International Edition 43(19) (2004) 2554-7.
- [84] S. Seidel, K. Seppelt, Xenon as a Complex Ligand: the Tetra Xenono Gold (II) Cation in $AuXe_4^{2+}(Sb_2F_{11}^-)_2$, Science 290(5489) (2000) 117-118.
- [85] A. Kovacs, R.J. Konings, J.K. Gibson, I. Infante, L. Gagliardi, Quantum Chemical Calculations and Experimental Investigations of Molecular Actinide Oxides, Chemical Review 115(4) (2015) 1725-1759.
- [86] A. Kovács, R.J. Konings, Computed Vibrational Frequencies of Actinide Oxides $AnO^{0/+2+}$ and $AnO_2^{0/+2+}$ ($An=Th, Pa, U, Np, Pu, Am, Cm$), The Journal of Physical Chemistry A 115(24) (2011) 6646-6656.
- [87] A. Hermann, M. Lein, P. Schwerdtfeger, The Search for the Species With the Highest Coordination Number, Angewandte Chemie International Edition 46(14) (2007) 2444-7.
- [88] N. Kaltsoyannis, Seventeen-Coordinate Actinide Helium Complexes, Angewandte Chemie International Edition 56(25) (2017) 7066-7069.
- [89] E. Ozama, S. Adachi, T. Takayanagi, M. Shiga, Quantum Simulation Verifies the Stability of an 18-Coordinated Actinium-Helium Complex, Chemistry 24(48) (2018) 12716-12721.
- [90] L. Yang, S. Cooper, N. Kaltsoyannis, High Coordination Number Actinide-noble Gas Complexes; a Computational Study, Physical Chemistry Chemical Physics 23(7) (2021) 4167-4177.

- [91] Y. Wang, W. Liu, Z. Bai, T. Zheng, M.A. Silver, Y. Li, Y. Wang, X. Wang, J. Diwu, Z. Chai, Employing an Unsaturated Th⁴⁺ Site in a Porous Thorium–organic Framework for Kr/Xe Uptake and Separation, *Angewandte Chemie International Edition* 57(20) (2018) 5783-5787.
- [92] P. Mi, L. Chen, X. Li, X. Wang, G. Li, L. Cheng, J. Lu, H. Zhang, Y. Wang, S. Wang, Enhanced Xe/Kr Separation via the Pore Size Confinement Effect of a Microporous Thorium-Based Metal–organic Framework, *Dalton Transactions* 51(40) (2022) 15233-15238.
- [93] K. Lv, C. Urbank, M. Patzschke, J. März, P. Kaden, S. Weiss, M. Schmidt, MOFs with 12-Coordinate 5f-Block Metal Centers, *The Journal of American Chemical Society* 144(7) (2022) 2879-2884.

2 Theoretical Background

Quantum mechanics is a powerful tool to study the microscopic world, in which the physical framework established by classical mechanics is no longer applicable. The motion of microscopic particles follows the Schrödinger equation, which can be written as¹:

$$\left(-\frac{\hbar^2}{2m}\nabla^2 + V\right)\Psi = i\hbar\frac{\partial\Psi}{\partial t} \quad (2.1)$$

in which \hbar is the reduced Planck constant, and m is the mass of the particle. V is the external potential where the particle exists. Ψ is a wave function at each point at each time t . The time-independent form can be written as:

$$H\Psi = E\Psi \quad (2.2)$$

in which H is the Hamiltonian operator. As a solution to the Schrödinger equation, the wavefunction Ψ contains all information of a system in a certain state, which provides a theoretical possibility to simulate any system. However, it is nearly impossible to explicitly solve the equation because of the large number of particles (nuclei and electrons) in a real many-body problem.

To overcome this difficulty, the Born-Oppenheimer approximation is usually adopted², assuming nuclear motions and electronic motions can be solved separately because electronic responses to the displacement of the nucleus are almost instantaneous due to their great mass differences. By the Born-Oppenheimer approximation, the overall wavefunction can be written as a product of nuclear wavefunction ($\Psi_N(\mathbf{R})$) and electronic wavefunction ($\Psi_e(\mathbf{r}, \mathbf{R})$):

$$\Psi(\mathbf{r}, \mathbf{R}) = \Psi_N(\mathbf{R})\Psi_e(\mathbf{r}, \mathbf{R}) \quad (2.3)$$

And the overall Schrödinger equation can be divided into the electronic equation (2.4) and nuclear equation (2.5):

$$H_0\Psi_e(\mathbf{r}, \mathbf{R}) = E_e(\mathbf{R})\Psi_e(\mathbf{r}, \mathbf{R}) \quad (2.4)$$

$$[T(\mathbf{R}) + E_e(\mathbf{R})]\Psi_N(\mathbf{R}) = E\Psi_N(\mathbf{R}) \quad (2.5)$$

in which $T(\mathbf{R})$ is nuclear kinetic energy, and $E_e(\mathbf{R})$ is electronic contributions to the total energy. Once the electronic Schrödinger equation is solved, the electronic energy ($E_e(\mathbf{R})$) can be used as the potential to solve the nuclear equation. In other words, the many-body problem is converted to the many-electron problem. In the following, we focus on how to solve the electronic Schrödinger equation.

However, even with the Born-Oppenheimer approximation, exact solutions of the Schrödinger equation can only be found in very few simple systems. The Hamiltonian for many-electron Schrödinger equation can be expanded as¹:

$$H_0 = -\sum_{i=1}^{N_e} \frac{\hbar^2}{2m_e} \nabla_i^2 - j_0 \sum_{i=1}^{N_e} \sum_{l=1}^{N_n} \frac{Z_l}{r_{li}} + \frac{1}{2} j_0 \sum_{i \neq j}^{N_e} \frac{1}{r_{ij}} \quad (2.6)$$

$$= \sum_{i=1}^{N_e} h_i + \frac{1}{2} j_0 \sum_{i \neq j}^{N_e} \frac{1}{r_{ij}} \quad (2.7)$$

in which $j_0 = e^2/4\pi\epsilon_0$. The first two terms of equation (2.6) are kinetic energy of electrons and potential energy between electrons and nuclei, which can be combined as the one-electron Hamiltonian (h_i). While the third term, electron-electron interaction, inhibits the use of the variation principle to analytically solve the equation. Thus, further

approximation methods, like Hartree-Fock (HF), post-HF, and density functional theory (DFT), are developed to make computations feasible.

2.1 Hartree-Fock method (HF)

Hartree-Fock method (HF)³ treats the electron-electron interaction in an “average” way, which assumes that each electron is moving in an electrostatic field of the nuclei and an average field of other $N_e - 1$ electrons. Then, the HF equation for an individual orbital wavefunction ($\varphi_m(i)$) is:

$$f_1 \varphi_m(1) = \varepsilon_m \varphi_m(1) \quad (2.8)$$

Where f_1 is the Fock operator, defined by the Coulomb operator (J_n) and exchange operator (K_n):

$$f_1 = h_1 + \sum_n \{2J_n(1) - K_n(1)\} \quad (2.9)$$

$$J_n(1) \varphi_m(1) = j_0 \int \varphi_n^*(2) \frac{1}{r_{12}} \varphi_m(1) \varphi_n(2) d\tau_2 \quad (2.10)$$

$$K_n(1) \varphi_m(1) = j_0 \int \varphi_n^*(2) \frac{1}{r_{12}} \varphi_n(1) \varphi_m(2) d\tau_2 \quad (2.11)$$

in which m and n refer to orbitals, and 1 and 2 refer to electrons. With a reasonable guess of an initial wavefunction, the Fock operator can be constructed. Then, equation (2.8) can be solved iteratively when the solutions converge to a pre-set threshold. And the overall many-electron wavefunction ($\Psi(\mathbf{r}, \mathbf{R})$) can be written as a Slater determinant¹:

$$\Psi(\mathbf{r}, \mathbf{R}) = \|\varphi_a(1) \varphi_b(2) \cdots \varphi_z(N)\| \quad (2.12)$$

2.2 Post-Hartree-Fock methods

As introduced above, the HF method does not fully consider the quantum mechanical effects on electron distribution because the effect of $N_e - 1$ electrons on the target one is treated in an average way. Moreover, the instantaneous interaction between electrons is also not included in the HF method. These deficiencies are summarized as the lack of electron correlation¹. To improve the description of electronic motions, some post-HF methods are proposed, like configuration interaction (CI)⁴, multi-configuration time-dependent Hartree (MCTDH)⁵, Møller-Plesset perturbation theory (MPPT)⁶, coupled cluster (CC)⁷, etc. We here focus on the MPPT and CC because they are used in this thesis.

2.2.1 Møller-Plesset many-body perturbation theory (MPPT)

Møller-Plesset many-body perturbation theory (MPPT)⁶ goes beyond the HF level by adding perturbation terms to an unperturbed zero-order Hamiltonian ($H_0^{(0)}$) to include the correlation energy:

$$H = H_0^{(0)} + \sum_k \lambda^k H^{(k)} \quad (2.13)$$

in which λ is an arbitrary value to control the size of perturbation terms. Similarly, the perturbed wavefunction and energy can be written as:

$$\Psi = \Psi_0^{(0)} + \sum_k \lambda^k \Psi^{(k)} \quad (2.14)$$

$$E = E_0^{(0)} + \sum_k \lambda^k E^{(k)} \quad (2.15)$$

Applying these perturbed terms to the time-independent Schrödinger equation (equation

(2.2)) yields a new electronic equation:

$$\begin{aligned} \left[H_0^{(0)} + \sum_k \lambda^k H^{(k)} \right] \left[\Psi_0^{(0)} + \sum_k \lambda^k \Psi^{(k)} \right] \\ = \left[E_0^{(0)} + \sum_k \lambda^k E^{(k)} \right] \left[\Psi_0^{(0)} + \sum_k \lambda^k \Psi^{(k)} \right] \end{aligned} \quad (2.16)$$

in which k represents the k^{th} -order perturbation term. In MPPT, the MPk indicates that up to k^{th} -order correction energies are included. $H_0^{(0)}$ is the HF Hamiltonian (H_{HF}), which is the sum of one-electron Fock operators:

$$H_{HF} = \sum_{i=1}^{N_e} f_i \quad (2.17)$$

The HF ground-state wavefunction ($\Psi_0^{(0)}$) is the eigenfunction of H_{HF} , and $E_0^{(0)}$ is the eigenvalue of H_{HF} . If we consider the first-order perturbation only, the first-order Hamiltonian ($H^{(1)}$) is:

$$H^{(1)}(i) = j_0 \sum_j \frac{1}{r_{ij}} - \sum_n \{2J_n(i) - K_n(i)\} \quad (2.18)$$

in which the sum of j omits the electron i , and n is all occupied orbitals. According to the perturbation theory, the first-order correction energy is the expectation value of $H^{(1)}$ over the ground-state HF wavefunction ($E^{(1)} = \langle \Psi_0^{(0)} | H^{(1)} | \Psi_0^{(0)} \rangle = 0$), which represents the E_{MP1} is identical to the HF energy. The second-order correction energy is:

$$E^{(2)} = \sum_{j \neq 0} \frac{\langle \Psi_j^{(0)} | H^{(1)} | \Psi_0^{(0)} \rangle \langle \Psi_0^{(0)} | H^{(1)} | \Psi_j^{(0)} \rangle}{E_0^{(0)} - E_j^{(0)}} \quad (2.19)$$

in which $\Psi_j^{(0)}$ is the wavefunction of the excited orbital, and also the eigenfunction of H_{HF} with the eigenvalue of $E_j^{(0)}$. The inclusion of the second-order correction is the commonly used MP2 method. And the higher-level MP3 and MP4 are also the standard methods for small molecules¹.

2.2.2 Coupled-cluster method

Coupled cluster (CC) theory⁷ is a highly accurate computational method going beyond the HF level by introducing the cluster operator C . Exact electronic wavefunctions can be obtained by correcting the HF wavefunction (Ψ_0) by an exponential operator (e^C):

$$\Psi = e^C \Psi_0 \quad (2.20)$$

with:

$$e^C = 1 + C + \frac{1}{2!} C^2 + \frac{1}{3!} C^3 + \dots \quad (2.21)$$

in which C is defined as the sum of all i -electron excitation operators C_i :

$$C = C_1 + C_2 + C_3 + \dots \quad (2.22)$$

with:

$$C_1 \Psi_0 = \sum_{a,p} t_a^p \Psi_a^p \quad C_2 \Psi_0 = \sum_{a,b,p,q} t_{ab}^{pq} \Psi_{ab}^{pq} \quad (2.23)$$

and so on. a, b are the occupied orbitals, and p, q are the virtual orbitals, *i.e.*, unoccupied

orbitals. t_a^p and t_{ab}^{pq} are termed as single- and double-excitation amplitudes, and so on. Note that the double-excitation determinant can be derived from both $C_2\Psi_0$ and $C_1C_1\Psi_0$ with the latter being one of the expansion terms of e^{C_1} . The difference between these two operators is significant: $C_2\Psi_0$ results from a connected double-excitation amplitude t_{ab}^{pq} , while the other is caused by two single-excitation amplitudes $t_a^p t_b^q$.

In the actual application of the CC method, CCD represents only the C_2 operator is used while CCSD uses $C = C_1 + C_2$. In CCSDT, C is expressed as $C_1 + C_2 + C_3$. However, it is demanding to explicitly calculate a triple-excitation, and hence perturbation theory is usually used to estimate the triple-excitation contribution, giving the CCSD(T) method.

2.3 Density functional theory (DFT)

Density functional theory (DFT) is one of the most dominant computational methods to study electronic structure. Different from the above wavefunction-based methods, the basic idea behind it is that the total energy of a many-electron system depends on its electron probability density ρ .

2.3.1 Hohenberg-Kohn theorems

The development of DFT is based on a set of assumptions, chief among them are two theorems proved by Kohn and Hohenberg and some equations proposed by Kohn and Sham^{1, 8-9}. The first theorem is the Hohenberg-Kohn existence theorem: *The ground-state energy and all other ground-state electronic structures of a system are uniquely determined by its electron density*. With this theorem, the ground-state energy (E) of a multi-electron system can be expressed as a functional of the electron density $\rho(\mathbf{r})$ at a point \mathbf{r} in space and written as $E[\rho]$. Although the existence theorem directly connects ground-state

properties to its electron density, how to construct the functional is still a question. The second theorem, which is called the Hohenberg-Kohn variational theorem, gives some clues: *The electron density that minimizes the energy functional is the true ground-state electron density.* In other words, if the functional form is known, the electron density can be iteratively solved.

2.3.2 Kohn-Sham equations

Although the general guidance is obtained according to the Hohenberg-Kohn variational theorem, a further step is needed to write down the actual form of the energy functional described by the Hohenberg-Kohn theorem. W. Kohn and L. J. Sham proposed that such a task can be solved by introducing a fictitious reference system that has the same electron density as a real system⁹. This fictitious system consists of N_e non-interacting electrons moving in a hypothetical external potential $v_{ref}(\mathbf{r})$, and has an electron density of $\rho(\mathbf{r})$. As the electrons are non-interacting, the ground-state wavefunction of the reference system can be described by a single Slater determinant composed from a set of one-electron Kohn-Sham spinorbital φ^{KS} :

$$\Psi_{ref} = \|\varphi_a^{KS}(1)\varphi_b^{KS}(2)\cdots\varphi_z^{KS}(N)\| \quad (2.24)$$

And the electron density can be constructed from the set of Kohn-Sham spinorbitals:

$$\rho(\mathbf{r}) = \sum_i^{N_e} |\varphi_m^{KS}(i)|^2 \quad (2.25)$$

Since an actual system has the same electron density as the reference one, the total energy of the actual system is:

$$E[\rho] = E_K[\rho] + E_J[\rho] + E_V[\rho] + E_{XC}[\rho] \quad (2.26)$$

where $E_K[\rho]$ is the kinetic energy, which is equal to that in the reference system. $E_J[\rho]$ is the electron-electron potential energy, which describes the Coulomb repulsion and can be expressed as:

$$E_J[\rho] = \frac{1}{2} \iint \frac{\rho(\mathbf{r}_1)\rho(\mathbf{r}_2)}{|\mathbf{r}_1 - \mathbf{r}_2|} d\mathbf{r}_1 d\mathbf{r}_2 \quad (2.27)$$

Self-interaction needs to be subtracted to eliminate the duplicate counts. $E_V[\rho]$ is the electron-nuclear interaction energy. Exchange-correlation energy $E_{XC}[\rho]$ can be divided into exchange part ($E_X[\rho]$) and correlation part ($E_C[\rho]$). The first three terms all have analytical forms, while the $E_{XC}[\rho]$ cannot be analytically expressed. Then the single-electron Kohn-Sham equation for an actual system can be written as:

$$\left(-\frac{\hbar^2}{2m} \nabla^2 + V(\mathbf{r}_i) + V_J(\mathbf{r}_i) + V_{XC}(\mathbf{r}_i) \right) \phi_m^{KS}(i) = \varepsilon_i \phi_m^{KS}(i) \quad (2.28)$$

in which $V(\mathbf{r}_i)$, $V_J(\mathbf{r}_i)$ and $V_{XC}(\mathbf{r}_i)$ are the external potential due to charged nuclei, electron-electron potential, and exchange-correlation potential, respectively. With a reasonable guess of initial Kohn-Sham spinorbitals, equation (2.28) can be solved iteratively to obtain the ground-state properties of an actual system.

2.3.3 Exchange-correlation functionals

As mentioned above, the exact form of $E_{XC}[\rho]$ (as well as V_{XC} , which is the derivative of $E_{XC}[\rho]$) is unknown, and scientists thus make great efforts to develop approximate forms. Perdew *et al.* proposed that current exchange-correlation functionals can be divided into five rungs with accuracy increasing from LDA to Generalized-RPA, which is the well-

known Jacob's ladder (Figure 2-1)¹⁰⁻¹¹.

Local density approximation (LDA) lies at the lowest level in Jacob's ladder, which is the simplest approach to approximate the exchange-correlation energy⁹. LDA is mainly derived from the homogeneous electron gas (HEG) model, in which an electron density is considered as uniform¹². V_{XC} at each point can be replaced by the known potential of the HEG with the same electron density as that position. Then the exchange-correlation energy is:

$$E_{XC}^{LDA}[\rho] = \int \rho(\mathbf{r}) \varepsilon_{XC}(\rho(\mathbf{r})) d\mathbf{r} \quad (2.29)$$

in which $\varepsilon_{XC}(\rho(\mathbf{r}))$ is the exchange-correlation energy of the HEG that have the electron density $\rho(\mathbf{r})$.

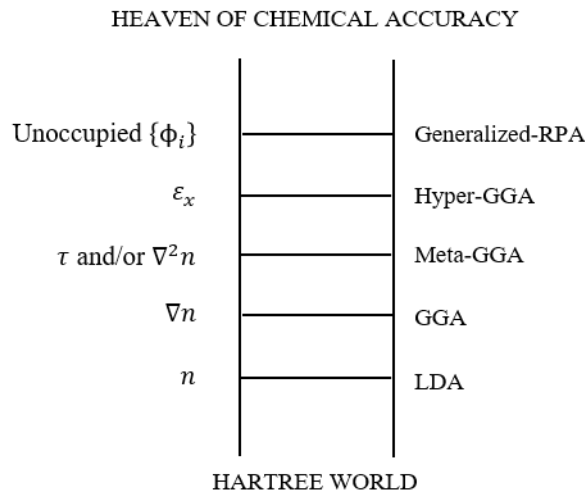


Figure 2-1. Jacob's ladder of density functional approximations¹⁰⁻¹¹.

LDA depends only on the local electron density at a point, while the density gradient is neglected. The generalized gradient approximation (GGA) method involves this factor¹³⁻

¹⁵, in which $E_{XC}[\rho]$ can be written as:

$$E_{XC}^{GGA}[\rho] = \int f(\rho(\mathbf{r}), \nabla\rho(\mathbf{r})) d\mathbf{r} \quad (2.30)$$

where $\nabla\rho(\mathbf{r})$ is the electron density gradient, and $f()$ is the chosen function and varies in different GGA functionals. The usually used PW91 and PBE belong to this family^{14, 16}. Although GGA functionals overcome the over-binding problem of the LDA method, it still has some drawbacks. The first one is that they failed to consider the van der Waals (vdW) interaction, which leads to inaccuracy in the reaction energy calculation¹⁷⁻¹⁸. Another one is related to self-interaction errors (SIE) resulting from the interaction of a single electron with its own density. Due to the SIE, wrong band gaps are sometimes predicted for systems with localized f electrons, like actinide and its oxide compounds¹⁹.

The development of meta-GGA, the third rung of Jacob's ladder, is based on two different lines. The first one makes use of the kinetic energy densities ($\tau(\mathbf{r})$) of the occupied Kohn-Sham orbitals ($\varphi_i(\mathbf{r})$)²⁰:

$$\tau(\mathbf{r}) = \sum_i^{occup} \frac{1}{2} |\nabla\varphi_i(\mathbf{r})|^2 \quad (2.31)$$

Then $E_{XC}[\rho]$ can be written as:

$$E_{XC}^{meta-GGA}[\rho] = \int f(\rho(\mathbf{r}), \nabla\rho(\mathbf{r}), \tau(\mathbf{r})) d\mathbf{r} \quad (2.32)$$

Due to the orbital dependency of the above approximation, the corresponding exchange-correlation potential $V_{XC}(\mathbf{r}_i) = \partial E_{XC}^{meta-GGA}[\rho] / \partial \rho$ cannot be directly calculated from the electron density. Thus, another line is to use the Laplacian of electron density ($\nabla^2\rho(\mathbf{r})$)²¹:

$$E_{XC}^{meta-GGA-L}[\rho] = \int f(\rho(\mathbf{r}), \nabla\rho(\mathbf{r}), \nabla^2\rho(\mathbf{r}))d\mathbf{r} \quad (2.33)$$

This is also called orbital-free meta-GGA functional.

The next rung is hybrid approaches, in which the exact exchange energy from HF theory is incorporated with that from the DFT level. For example, the commonly used PBE0 functional is composed of a 3:1 ratio of PBE and HF exchange energy and full PBE correlation energy²². In general, hybrid functionals predict a more accurate band gap compared with that of GGA, but the cost is more demanding.

However, the above local, semi-local, and hybrid functionals do not consider the long-range van der Waals (vdW) forces, which makes them less reliable on systems where vdW forces are important. To properly describe these systems in the DFT calculations, a correction dispersion term ($E_{C,disp}$) can be added to the conventional density functionals ($E_{XC}^{SL/hybrid}$)²³:

$$E_{XC} = E_{XC}^{SL/hybrid} + E_{C,disp} \quad (2.34)$$

There are several approaches that have been reported to construct the dispersion term. One is the atom-based pair type, which is a sum over the atom pairs²⁴:

$$E_{C,disp} = - \sum_{A < B} \sum_{n=6,8,10,\dots} f_n^{damp}(R_{AB}) \frac{C_n^{AB}}{R_{AB}^n} \quad (2.35)$$

in which C_n^{AB} , R_{AB} , and f_n^{damp} are the dispersion coefficients, distance between atom pair A-B, and damping function, respectively. The usually-used DFT-D3 belongs to this type.

Another one is vdW-DF functionals, originally proposed by Dion *et al.*²⁵:

$$E_{C,\text{disp}} = \frac{1}{2} \iint \rho(\mathbf{r}) \mu(\mathbf{r}, \mathbf{r}') \rho(\mathbf{r}') d^3r d^3r' \quad (2.36)$$

in which $\mu(\mathbf{r}, \mathbf{r}')$ is some generally defined function depending on $\mathbf{r} - \mathbf{r}'$. Due to the double spatial integration in this approach, it is therefore non-local and more expensive to calculate.

The first four rungs of Jacob's ladder consider only the occupied orbitals and fail to describe long-range interaction. Unoccupied orbitals are included in the fifth rung by random phase approximation (RPA)²⁶⁻²⁷. It provides a good description of long-range vdW interaction but has a huge error in short-range²⁸. These errors can be cancelled out in solids from the energy difference, like surface reaction energy and formation energy²⁹. But the error cancellation for molecules is still imperfect³⁰.

2.4 Basis set

In both HF-based and DFT methods, a set of basis functions must be used to construct wavefunction and charge density, which is the so-called basis set. For molecular calculations, atom-centred basis sets are commonly used. While for extended solid systems, plane-wave basis sets are used when the periodic boundary condition is implemented.

2.4.1 Atom-centered basis set

The molecular orbital is a linear combination of atomic basis functions. And two commonly used basis functions are Slater-type orbitals (STOs) and Gaussian-type orbitals (GTOs)^{1, 31}. STOs can be written as³²:

$$\psi_{nlm_l}(r, \theta, \varphi) = N r^{n_{\text{eff}}-1} e^{-\zeta r} Y_{lm_l}(\theta, \varphi) \quad (2.37)$$

where n , l and m_l are quantum numbers. The effective principal quantum number n_{eff}

is related to the true principal quantum number (n) as follows:

$$n \rightarrow n_{\text{eff}}: 1 \rightarrow 1 \quad 2 \rightarrow 2 \quad 3 \rightarrow 3 \quad 4 \rightarrow 3.7 \quad 5 \rightarrow 4.0 \quad 6 \rightarrow 4.2$$

N is a normalization constant, and $Y_{lm_l}(\theta, \varphi)$ is a spherical harmonic. Orbital exponent ζ describes the radial distribution. STOs have the same form as hydrogen-like orbitals, which are infinite at nuclei. A complete basis set consists of STOs with all permitted integral values of the quantum numbers and all positive values of ζ . However, the evaluation of many-center two-electron integrals is impractical.

GTOs³³, proposed by S.F. Boys in 1950, have the form of:

$$g_{ijk}(r, \theta, \varphi) = Nx^i y^j z^k e^{-\alpha r^2} Y_{lm_l}(\theta, \varphi) \quad (2.38)$$

in which the origin of the coordinates is the nucleus of an atom. N is a normalization constant, and α is a positive exponent, describing how diffuse the orbital is. i , j , and k are non-negative integers, taking values as follows:

Table 2-1. Possible i , j , and k values in Gaussian-type orbital

	Possible combination	Orbital Type
$i = j = k = 0$	(0, 0, 0)	s
$i + j + k = 1$	(1, 0, 0), (0, 1, 0), (0, 0, 1)	p
$i + j + k = 2$	(0, 1, 1), (1, 0, 1), (1, 1, 0), (2, 0, 0), (0, 2, 0), (0, 0, 2)	d

The most important advantage of GTOs is the product of two GTOs equals a GTO centred in the middle of two centres. As a result, a two-electron integral on many centres can be considered as an integral over two different centres, which is more computationally

feasible. However, GTOs give a poor description of orbitals at nuclei ($r \rightarrow 0$), which are not able to show the cusp (Figure 2-2)³¹. Moreover, GTOs decay too rapidly as r increases (Figure 2-2). To solve this limitation, several GTOs are usually linearly combined to form a contracted Gaussian function $\chi_0^{1,34}$:

$$\chi_0 = \sum d_{0i} g_i \quad (2.39)$$

where g_i is primitive GTOs, taking the form of equation (2.38), and d_{0i} is contraction coefficients.

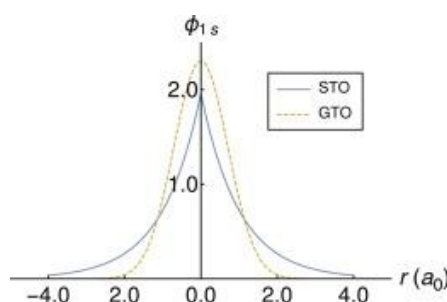


Figure 2-2. Unit exponent normalized STO versus GTO. Reprinted from reference 31 with permission from Elsevier.

In the simplest condition, each orbital from elementary valence theory is represented by one function, and the set of functions is called a minimal basis set. For example, a minimal basis set for Li to Ne (1s, 2s, and three 2p orbitals) consists of 5 basis functions. However, accurate calculations need a larger basis set because energies generated by a minimal basis set are not close to the HF limit. A commonly used method to extend a basis set is to double or triple the radial basis functions for each orbital, which is called double zeta (DZ) or triple zeta (TZ) basis set with the zeta representing the exponent of the STO basis functions. The increase of basis functions for all orbitals is computationally demanding. A compromise method between accuracy and efficiency is a split-valence basis set (SV basis

set), in which only the number of basis functions for valence orbital increases. Another method to improve accuracy is to include the polarization of orbitals. When atoms bond to form molecules, atomic orbitals are distorted by neighbouring atoms, which can be accounted for by including orbitals with l values higher than the maximum l in elementary valence theory. Another common additive is diffuse functions, in which basis functions are extended further from nuclei. This is important for anions because they have more diffusive orbitals than neutral or cationic atoms.

2.4.2 Basis set superposition error

The use of finite basis sets can lead to basis set superposition errors (BSSE), which usually occur in interaction energy calculation¹. Take the interaction energy (E_{int}) between two atoms as an example:

$$E_{\text{int}}(\text{AB}) = E(\text{AB}) - E(\text{A}) - E(\text{B}) \quad (2.40)$$

where $E(\text{AB})$, $E(\text{A})$, and $E(\text{B})$ are energies of compound AB, atom A, and atom B, respectively. If we use a finite basis set for atoms A and B, orbital for compound AB is the linear combination of the basis set for atom A and B in the calculation. In other words, the basis set for compound AB is larger than that for individual atoms, which can non-physically lower the $E(\text{AB})$ and incorrectly generate lower interaction energy.

A commonly used method to correct the BSSE is counterpoise correction³⁵, in which the total energy of atoms A and B are calculated from the basis set that is used for compound AB. To achieve this, a ghost atom is introduced in the single atom calculation with the distance (r_{AB}) being the same as that in the compound. The ghost atom has a basis set on it but no electrons to fill the orbitals.

2.4.3 Plane waves

Crystalline solids are constituted by periodically repeating unit cells, which include a regular array of atoms. In direct space, the primitive unit cell is the parallelepiped defined by Bravais lattice vectors \mathbf{a}_1 , \mathbf{a}_2 , and \mathbf{a}_3 with the volume (Ω) of:

$$\Omega = \mathbf{a}_1 \cdot (\mathbf{a}_2 \times \mathbf{a}_3) \quad (2.41)$$

And every lattice point can be described by these translation vectors:

$$\mathbf{R} = n_1 \mathbf{a}_1 + n_2 \mathbf{a}_2 + n_3 \mathbf{a}_3 \quad (2.42)$$

The periodicity of lattices (a) produces a periodic potential, in which electrons move. We can recall the wavefunction of an electron in one-dimensional periodic potentials, which takes the form of plane waves ($e^{ik \cdot x}$) with the wave vector k satisfying $k_1 = k_2 + m \cdot 2\pi/a$. We can see the wavefunction takes the periodicity of $2\pi/a$.

Reciprocal lattice vectors (\mathbf{b}_i) are defined as:

$$\mathbf{b}_i \cdot \mathbf{a}_j = 2\pi \delta_{ij} \quad (2.43)$$

where δ_{ij} is Kronecker delta. And every point in reciprocal space can be written as:

$$\mathbf{G} = m_1 \mathbf{b}_1 + m_2 \mathbf{b}_2 + m_3 \mathbf{b}_3 \quad (2.44)$$

Bloch proposed that the eigenstate of an electron in a periodic potential can be written as the product of a plane wave and a periodic function, which is the well-known Bloch's theorem³⁶:

$$\varphi_j(\mathbf{k}, \mathbf{r}) = e^{i\mathbf{k} \cdot \mathbf{r}} u_j(\mathbf{k}, \mathbf{r}) \quad (2.45)$$

in which the wave vector \mathbf{k} takes values from the first Brillouin zone. The index j runs over all states at the same \mathbf{k} . $u_j(\mathbf{k}, \mathbf{r})$ is a function that has the same periodicity as the lattices. By Fourier transformation, every periodic function can be expanded in a set of complete and orthonormal plane wave basis:

$$f_G^{PW} = \frac{1}{\sqrt{\Omega}} e^{i\mathbf{G}\cdot\mathbf{r}} \quad (2.46)$$

Therefore, the periodic function $u_j(\mathbf{k}, \mathbf{r})$ can be written as:

$$u_j(\mathbf{k}, \mathbf{r}) = u_j(\mathbf{k}, \mathbf{r} + \mathbf{R}) = \frac{1}{\sqrt{\Omega}} \sum_{\mathbf{G}} c_j(\mathbf{G}, \mathbf{k}) e^{i\mathbf{G}\cdot\mathbf{r}} \quad (2.47)$$

in which $c_j(\mathbf{G}, \mathbf{k})$ are expansion coefficients. And the full wavefunction can be written as:

$$\varphi_j(\mathbf{k}, \mathbf{r}) = \frac{1}{\sqrt{\Omega}} \sum_{\mathbf{G}} c_j(\mathbf{G}, \mathbf{k}) e^{i(\mathbf{G}+\mathbf{k})\cdot\mathbf{r}} \quad (2.48)$$

In real calculation, it is impractical to infinitely sum over all \mathbf{G} vectors, which can be approximated by a finite sum over a set of \mathbf{k} -points in the Brillouin zone. And there are a lot of schemes to sample the points, like the usually used Monkhorst-Pack and Γ -centered approaches³⁷. And cutoff energy (E_{cut}) is also used to truncate basis functions, which is defined as:

$$\frac{1}{2} |\mathbf{k} + \mathbf{G}|^2 \leq E_{cut} \quad (2.49)$$

which means at each \mathbf{k} -point, only \mathbf{G} vectors with kinetic energy lower than E_{cut} are included in the basis.

It is important to note that the biggest difference between plane waves and atom-centred

basis sets is that plane waves do not depend on the positions of nuclei, which implies that they are delocalized and good at dealing with delocalized electrons.

2.4.4 Pseudopotential

Most chemical interaction is governed by valence electrons, and core electrons are inert. To reduce computational costs, core electrons can be considered together with a nucleus as a rigid core with a cutoff radius of r_c by frozen-core approximation. Then the interaction between valence electrons and core is represented by a smooth effective potential, which is called pseudopotential in solid-state theory or effective core potential (ECP) in molecular quantum chemistry³⁶.

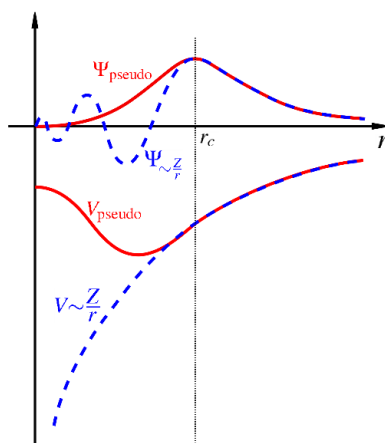


Figure 2-3. A sketch of pseudopotential. Blue dashed lines represent real nucleus potential and the wavefunction in it. Red solid lines are pseudopotential and the corresponding wavefunction. r_c is cutoff radius. Reprinted from reference 38.

As shown in Figure 2-3, real wavefunctions of valence electrons oscillate rapidly in the core region ($r < r_c$) to satisfy the orthogonality to the wavefunctions of core electrons. It is impractical to accurately reproduce them because the required basis set size will be extremely large. By pseudopotentials, the valence electrons in the core region can be described by a smooth pseudo wavefunction, which only requires a small basis set size.

And the pseudo wavefunctions outside the core region ($r > r_c$) are identical to their true wavefunctions. The basis set size can be reduced by increasing the core region or optimizing the smoothness of pseudopotentials.

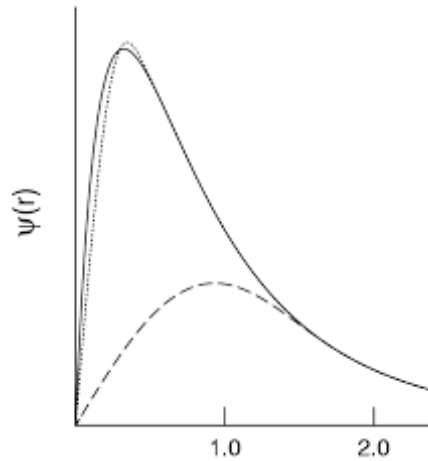


Figure 2-4. O 2p wavefunction (solid line), and corresponding pseudo wavefunctions generated from HSC (dotted line) and USPP (dashed line). Reprinted from reference 41 with permission from the American Physical Society (APS).

There are two commonly used pseudopotentials with plane waves: norm-conserving pseudopotentials and ultrasoft pseudopotentials³⁶. The norm-conserving pseudopotential, first proposed by Hamann, Schluter, and Chiang (HSC) in 1979 and further developed by others³⁹, keeps the normalization of pseudo wavefunction inside the core region to ensure that the pseudo wavefunction outside the core region is as close to the true wavefunctions as possible⁴⁰. In this method, the cutoff radius lies around the outermost maximum of all-electron wavefunctions to assure the norm-conservation condition. However, for systems containing highly localized valence orbitals (*e.g.*, O 2p orbitals), the resulting basis set size will be large. The ultrasoft pseudopotential (USPP), proposed by Vanderbilt, can solve this problem⁴¹. In USPP, the norm-conservation constraint is relaxed, and a charge difference term Q_{ij} between charges obtained from pseudo and all-electron wavefunctions is introduced into a nonlocal overlap operator. Then, the all-electron wavefunctions of each

state can be transferred to pseudo functions independently. And the r_c can be moved beyond the outermost maximum of all-electron wavefunctions (as O 2p orbital in Figure 2-4).

By generalization of the ideas of USPP and linear augmented-plane-wave methods, Blöchl proposed the projector augmented-wave (PAW) method⁴². In the PAW method, a whole space can be divided into interstitial region Ω_I and a collection of non-overlapping atomic regions Ω_a . The true wavefunction is derived from a pseudo wavefunction by linear transformation⁴³:

$$|\Psi\rangle = |\Psi_{\text{pseudo}}\rangle + \sum_i (|\phi_i\rangle - |\tilde{\phi}_i\rangle) \langle p_i | \Psi_{\text{pseudo}} \rangle \quad (2.50)$$

in which ϕ_i and $\tilde{\phi}_i$ are all-electron and pseudo partial waves, respectively. Pseudo partial waves are equivalent to all-electron partial waves at the Ω_I region, while at the Ω_a region, the pseudo wavefunction is only a computational tool and an approximation to the true wavefunction without the requirement of norm-conservation. p_i is the projector function, which satisfies $\langle p_i | \tilde{\phi}_i \rangle = \delta_{ij}$.

For the development of ECPs, there are two different approaches: shape-consistent and energy-consistent⁴⁴. The former is termed norm-conserving pseudopotentials in solid state theory, which is based on the same basic idea as above⁴⁵. The energy-consistent ECPs rely on total valence energies while making no use of wavefunction information⁴⁶⁻⁴⁷. Parameters for energy-consistent ECPs are adjusted to make the following expression become a minimum:

$$S = \sum_I w_I (E_I^{ECP} - E_I^{AE} + \Delta E_{\text{shift}})^2 := \min \quad (2.51)$$

in which E_I^{ECP} and E_I^{AE} represent the total valence energies for a state I at the ECP and all-electron (AE) levels, respectively. The weight w_I is used to increase the accuracy of the states of interest. ΔE_{shift} is the global shift from the all-electron (AE) reference state, which allows a systematic deviation of the E_I^{ECP} from the reference AE value. A large number of reference states is necessary to generate accurate parameters.

The use of ECPs also provides an efficient way to consider relativistic effects, which is important for actinide elements⁴⁸⁻⁴⁹. As shown in equation (2.52), the mass of an electron significantly increases because it moves at a large velocity:

$$m = m_0 [1 - (v/c)^2]^{-\frac{1}{2}} \quad (2.52)$$

in which m_0 is the rest mass. v and c are the velocity of the particle and light, respectively. Since orbital angular momentum is conserved, the electron mass increase leads to orbital contraction. For actinides, inner orbitals, *i.e.*, s-orbitals, contract more strongly due to the larger velocity of inner electrons. Consequently, the screening of the nucleus increases, which leads to radial expansions of d- and f-orbitals⁵⁰. Another complication induced by relativistic effects is spin-orbital coupling (SOC). It is a result of the interaction of spin and orbital magnetic moments of an electron. For AE calculations, additional computational efforts are required to account for relativistic operators. While in ECPs calculations, these operators for valence electrons can be replaced by their nonrelativistic analogs, and relativistic contributions are accounted for by a suitable parametrization of the ECPs to relativistic reference data. Thus, using relativistic ECPs (RECPs) can significantly save costs while ensuring accuracy. For actinides, the most

widely used RECP is the Stuttgart-Cologne energy-consistent small-core (60 core electrons) with the associated valence basis sets⁵¹⁻⁵³.

2.5 Ab initio molecular dynamics (AIMD)

The above HF, post-HF, and DFT methods focus on the ground state of a specific system and neglect the time dependence. But experimental measurement is an average over a huge number of states and finite time. Molecular dynamics (MD) simulation provides a theoretical framework to study this average behaviour by computing the time evolution of the system and averaging over a sufficiently long time. MD methods determine the motions of particles by numerically solving Newton's law³⁶:

$$F = ma \rightarrow -\nabla E = m\ddot{\mathbf{r}}(t) \quad (2.53)$$

In classical MD, predefined forces fields or potentials are required to describe the many-body interactions, which limits its application in systems where chemical bonding patterns change qualitatively during simulation time. Moreover, once only one species has been changed in a well-studied system, huge efforts are needed to build a new potential or forces field.

In *ab initio* MD (AIMD), the forces can be directly obtained from *ab initio* electronic structure calculation methods, *e.g.*, DFT. Two commonly used AIMD methods are Born-Oppenheimer molecular dynamics (BOMD) and Car-Parrinello molecular dynamics (CPMD)³⁶. In BOMD, electronic structures are calculated by solving the time-independent Schrödinger equation (equation (2.4)), and the position of nuclei follows classical mechanics:

$$M_I \ddot{\mathbf{R}}_I(t) = -\nabla_I \min\{\langle \Psi | H_0 | \Psi \rangle\}$$

$$E_0 \Psi = H_0 \Psi \quad (2.54)$$

in which M_I and \mathbf{R}_I are mass and position of the I th nucleus. This requires an SCF calculation of the electronic structure at each MD step. To prevent this costly self-consistent minimization at each step, Car and Parrinello introduce a fictitious dynamical variable, writing as an extended Lagrangian^{36, 54}:

$$\mathcal{L}_{CP} = \sum_I \frac{1}{2} M_I \dot{\mathbf{R}}_I^2 + \sum_i \mu \langle \dot{\phi}_i | \dot{\phi}_i \rangle - \langle \Psi | H_0 | \Psi \rangle + \sum_{ij} \Lambda_{ij} (\langle \phi_i | \phi_j \rangle - \delta_{ij}) \quad (2.55)$$

in which μ is the fictitious mass of electrons. Lagrange multipliers Λ_{ij} is used to ensure orthonormality. And the corresponding equations of motion are:

$$M_I \ddot{\mathbf{R}}_I(t) = -\nabla_I \langle \Psi | H_0 | \Psi \rangle$$

$$\mu \ddot{\phi}_i(t) = -H_0 \phi_i + \sum_j \Lambda_{ij} \phi_j \quad (2.56)$$

After an initial electronic minimization, the fictitious dynamical variable keeps them on the ground state corresponding to new nuclei configurations.

2.6 Special quasi-random structure (SQS)

Special quasi-random structure (SQS) approach is an efficient and popular tool to generate disordered crystalline alloys⁵⁵⁻⁵⁶. Optimization of SQS is based on a criterion that cluster correlations in SQS should be consistent with corresponding cluster correlations in fully disordered structures.

To understand the SQS, we should start with cluster correlation. For a crystalline

compound consisting of M_i species, the site occupation can be described by a variable σ_i , which takes values from 0 to $M_i - 1$. For a given structure, by constructing a point function $\gamma(\sigma_i)$ for each site, we then can quantify correlations between occupied multiple sites. A list of sites considered to calculate the correlation is defined as a cluster α . A cluster function ($\Gamma_\alpha(\sigma)$) is the product of all point functions:

$$\Gamma_\alpha(\sigma) = \prod_i \gamma_{\alpha_i, M_i}(\sigma_i) \quad (2.57)$$

α_i specifies the type of point functions for each site in the cluster, which takes the value from 0 to $M_i - 1$ with $\alpha_i = 0$ representing the site is not in the cluster. The point function should satisfy the orthogonality condition:

$$\frac{1}{M_i} \sum_{\sigma_i=0}^{M_i-1} \gamma_{\alpha_i, M_i}(\sigma_i) \gamma_{\beta_i, M_i}(\sigma_i) = \begin{cases} 1 & \text{if } \alpha_i = \beta_i \\ 0 & \text{otherwise} \end{cases} \quad (2.58)$$

It needs to be mentioned that the equation (2.57) is the product over all lattice sites. To reduce it to the cluster only, point functions also need to meet the condition of $\gamma_{0, M_i}(\sigma_i) = 1$. Then the cluster correlation is defined as:

$$\rho_\alpha(\sigma) \equiv \langle \Gamma_{\alpha'}(\sigma) \rangle_\alpha \quad (2.59)$$

in which the $\langle \dots \rangle_\alpha$ is an average of all clusters α' that is equivalent to cluster α by symmetry. In a fully disordered structure, atom distributions should be fully random and independent. Thus, the cluster correlation ($\rho_\alpha(\sigma^{rnd})$):

$$\rho_\alpha(\sigma^{rnd}) = \langle \prod_i \gamma_{\alpha'_i, M_i}(\sigma_i) \rangle_\alpha = \prod_i \langle \gamma_{\alpha'_i, M_i}(\sigma_i) \rangle_\alpha \quad (2.60)$$

in which $\langle \gamma'_{\alpha'_i, M_i}(\sigma_i) \rangle_\alpha$ is directly related to average compositions of site i , *i.e.*, the cluster correlation depends on compositions only.

Take a binary A_xB_{1-x} system as an example. In a binary compound, the commonly used point function is based on the language of the Ising model:

$$\begin{cases} \gamma_{1,2}(0) = -1 & \text{atom A at site } i \text{ in cluster} \\ \gamma_{1,2}(1) = +1 & \text{atom B at site } i \text{ in cluster} \\ \gamma_{0,2}(0) = +1 & \text{atom A at site } i \text{ outside cluster} \\ \gamma_{0,2}(1) = +1 & \text{atom B at site } i \text{ outside cluster} \end{cases} \quad (2.61)$$

Then the $\langle \gamma'_{\alpha'_i, M_i}(\sigma_i) \rangle_\alpha$ is equal to $x \times (-1) + (1 - x) \times 1 = 1 - 2x$. And pair cluster correlations for fully disordered $A_{0.5}B_{0.5}$ and $A_{0.25}B_{0.75}$ are $0 \times 0 = 0$ and $0.5 \times 0.5 = 0.25$, respectively.

SQS is generated by enumerating all possible structures of a given compound. The smaller the cluster correlation of the generated structure differs from a fully disordered state, the more random the structure is.

2.7 Diffusion coefficient from atomic jump process

Diffusion coefficient. If we consider macroscopic diffusion in solids from a microscopic view, it is actually continuous individual jumps of a particle between neighbouring lattice sites. And the total displacement is a sum of discrete jump lengths, which is in the order of lattice parameter in crystal. To establish diffusion coefficient equations, we can start with a simple model: interstitial diffusion in a cubic crystal. As in Figure 2-5, with driving forces, a net flux J from plane 1 to 2 is⁵⁷:

$$J = \Gamma n_1 - \Gamma n_2 \quad (2.62)$$

in which Γ is the jump rate from plane 1 to plane 2, *i.e.*, the number of jumps per unit time. n_1 and n_2 are the number of interstitial atoms per unit area in planes 1 and 2, respectively. And they can be related to a volume concentration C by:

$$n_i = C_i \times \lambda \quad (2.63)$$

in which λ is jump length. C changes slowly as a function of distance variable x :

$$C_1 - C_2 = -\lambda \frac{\partial C}{\partial x} \quad (2.64)$$

Inserting equations (2.63) and (2.64) to (2.62), the flux J is:

$$J = -\lambda^2 \Gamma \frac{\partial C}{\partial x} \quad (2.65)$$

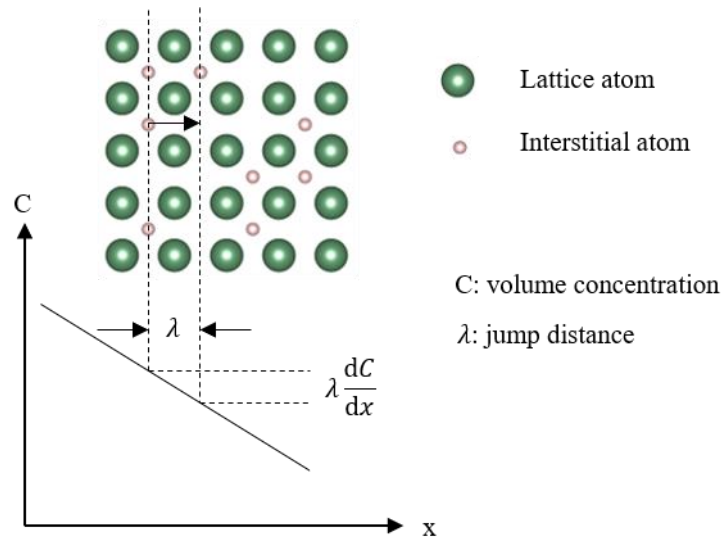


Figure 2-5. Schematic representation of interstitial diffusion of atoms in a lattice

By comparing equation (2.65) with Fick's first law $J = -D \nabla C$, we can see the diffusion coefficient $D = \Gamma \lambda^2$. Considering that particles can jump to 6 nearest-neighbouring interstices in a cubic lattice, the jump rate to a particular site is $\Gamma = \frac{1}{6} \Gamma_{tot}$. Thus, the

diffusion coefficient is:

$$D = \frac{1}{6} \Gamma_{tot} \lambda^2 \quad (2.66)$$

We can see that the diffusion coefficient is determined by jump rates and jump distance, the latter can be easily obtained from the lattice parameter. The question now turns to the calculation of jump rate Γ .

Jump rate. In a crystal, atoms oscillate around their equilibrium positions. To jump to a nearest-neighbouring vacancy or interstitial site, they need to squeeze through matrix atoms, which requires extra energy and high oscillated frequency. Using statistical thermodynamics, Vineyard proposed the individual jump rate ω (number of jumps per unit time to a particular neighbouring site) can be calculated by⁵⁸:

$$\omega = v_0 \exp \left(-\frac{G^m}{k_B T} \right) \quad (2.67)$$

in which v_0 is attempt frequency, *i.e.*, the vibrational frequency of the diffusing atom along the diffusion path. G^m is Gibbs free energy of migration.

In vacancy-assisted diffusion (Figure 2-6), the most important mechanism for self- and solute diffusion in crystalline solids, each atom moves through continuous exchanges with a neighbouring vacancy. The jump rate is thus also determined by the probability p to find a vacancy near the tracer or solute atom. For self-diffusion, the probability p is equal to site fraction of a vacancy, which can be calculated by equation (2.68) in thermal equilibrium⁵⁷:

$$p = C_V = \exp \left(-\frac{G_V^f}{k_B T} \right) = \exp \left(\frac{S_V^f}{k_B} \right) \exp \left(-\frac{H_V^f}{k_B T} \right) \quad (2.68)$$

in which G_V^f , H_V^f , and S_V^f are vacancy formation Gibbs free energy, enthalpy, and entropy, respectively. For solute diffusion, interactions between the solute atoms and neighbouring vacancies can affect the probability by:

$$p = C_V \exp \left(\frac{G^B}{k_B T} \right) \quad (2.69)$$

where G^B is Gibbs free energy of solute-vacancy binding. Thus, the jump rate of self- (Γ) and solute diffusion (Γ_2 , subscript 2 is used to distinguish it from self-diffusion) by the vacancy-assisted mechanism are:

$$\begin{aligned} \Gamma &= \omega C_V \\ \Gamma_2 &= \omega C_V \exp \left(\frac{G^B}{k_B T} \right) \end{aligned} \quad (2.70)$$

And the total jump rates are the product of Γ (or Γ_2) and coordination number Z in the lattice.

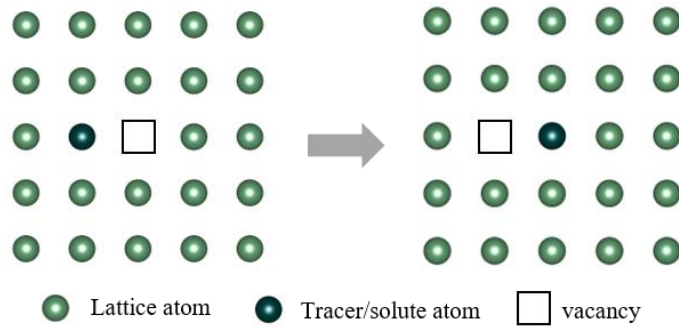


Figure 2-6. Monovacancy-assisted diffusion mechanism

Transition state search. As introduced in equation (2.67), the calculation of the jump rate involves the migration Gibbs free energy and attempt frequency, which requires the vibrational and energetic properties of the transition state (TS). According to harmonic transition state theory (hTST)⁵⁹⁻⁶⁰, the search for optimal transition states is the search for the highest-energy point along the minimum energy path (MEP). MEP is the most probable path connecting initial (IS) and final states (FS). And the maximum on MEP is the first-order saddle point on a potential energy surface (PES), *i.e.*, the maximum along one direction and the minimum along other directions.

Nudged elastic band (NEB) method is an efficient tool to find the MEP⁶¹. It inserts a set of images between IS and FS, and adds a spring interaction between the neighbouring images to mimic an elastic band. The total force (F_i) on each image is:

$$F_i = F_i^S|_{\parallel} - \nabla E(\mathbf{R}_i)|_{\perp} \quad (2.71)$$

where \mathbf{R}_i is a coordinate of an image i with \mathbf{R}_0 and \mathbf{R}_N being IS and FS which are fixed. $F_i^S|_{\parallel}$ is spring forces along the local tangent:

$$F_i^S|_{\parallel} = k(|\mathbf{R}_{i+1} - \mathbf{R}_i| - |\mathbf{R}_i - \mathbf{R}_{i-1}|)\hat{\mathbf{t}}_i \quad (2.72)$$

in which k is a spring constant and $\hat{\mathbf{t}}_i$ is a normalized vector along the local tangent.

$\nabla E(\mathbf{R}_i)|_{\perp}$ in equation (2.71) is a true force perpendicular to the local tangent:

$$\nabla E(\mathbf{R}_i)|_{\perp} = \nabla E(\mathbf{R}_i) - \nabla E(\mathbf{R}_i) \cdot \hat{\mathbf{t}}_i \quad (2.73)$$

where $E(\mathbf{R}_i)$ is the energy of the system. Then images are moved along the total force defined by equation (2.71) and converged on MEP when k is same for all images.

The climbing image NBE (CI-NEB) method includes a small modification to the NEB by

driving the highest-energy image to the saddle point⁶²⁻⁶³. The force on this image is modified to:

$$\begin{aligned} F_{i_{max}} &= -\nabla E(\mathbf{R}_{i_{max}}) + 2\nabla E(\mathbf{R}_{i_{max}})|_{\parallel} \\ &= -\nabla E(\mathbf{R}_{i_{max}}) + 2\nabla E(\mathbf{R}_{i_{max}}) \cdot \hat{\mathbf{t}}_{i_{max}} \hat{\mathbf{t}}_{i_{max}} \end{aligned} \quad (2.74)$$

By equation (2.74), the energy of the highest-energy image is not affected by the spring and can climb to the highest point on MEP.

Correlation factor. It needs to be noted that the above jump rate assumes all jumps are independent. This is true for interstitial diffusion considering each interstitial solute is likely to be surrounded by enough empty interstitial sites in a dilute interstitial solution. The probability of a solute atom jumping to each site is equal and independent of the previous step. But for vacancy-assisted diffusion, the motions of atoms are dependent on the previous jump, which can be accounted for by a correlation factor f .⁵⁷ Take self-diffusion as an example (Figure 2-6), after a first tracer-vacancy exchange, the probability of vacancy to one of its nearest neighbouring sites is uniform, which is equal to $\frac{1}{2}$. But the tracer atom has a higher probability of immediately jumping back, which leads to no net displacement. We then need the correlation factor to correct the total displacement induced by these immediate “jump backs”:

$$f = \lim_{n \rightarrow \infty} \frac{\langle \mathbf{R}^2 \rangle}{\langle \mathbf{R}_{\text{random}}^2 \rangle} \quad (2.75)$$

in which \mathbf{R} and $\mathbf{R}_{\text{random}}$ are real and uncorrelated total displacement of a particle by sequence atomic jumps, respectively. And $\langle \dots \rangle$ takes an average over an ensemble of particles.

Unfortunately, it is hardly possible to directly measure the f . Measurements of the isotope effect, which is close to the real correlation factor, have been made for self-diffusion. It is found the f highly depends on crystal structures and diffusion mechanisms, and the database has been well established for self-diffusion⁵⁷. For example, the f of self-diffusion by vacancy mechanism in body-centre cubic and face-centre cubic are 0.7272 and 0.7815, respectively⁶⁴⁻⁶⁵. Solute diffusion is more complex than self-diffusion, which also depends on solute species. The f of solute diffusion is usually described by the so-called “five-frequency model”, proposed by Lidiard *et al.*⁶⁶⁻⁶⁷.

2.8 Analytical techniques

2.8.1 Quantum theory of atoms-in-molecule (QTAIM)

Different from molecular orbital analysis, the quantum theory of atoms-in-molecules (QTAIM) is based on the topology of electron density⁶⁸⁻⁷⁰. For a molecule, electrons are distributed throughout real space, with electron density ($\rho(\mathbf{r})$) being measurable. Nuclei act as positive attractors in a negative electron cloud. Take the electron density of the phenolic region of a morphine molecule as an example (Figure 2-7), we can see $\rho(\mathbf{r})$ reaches a maximum at the positions of nuclei, at which the first derivative of electron density ($\nabla\rho(\mathbf{r})$) is zero.

There are also some local maximum or minimum points between nuclei, at which $\nabla\rho(\mathbf{r})$ are also zero. The points where $\nabla\rho(\mathbf{r}) = 0$ are called “critical points (CP)”. And an atom is defined as an area Ω surrounded by surfaces ($S(\Omega)$) on which flux of $\nabla\rho(\mathbf{r})$ is zero. And these zero-flux surfaces are defined as interatomic surfaces:

$$\nabla\rho(\mathbf{r}) \cdot \mathbf{n}(\mathbf{r}) = 0 \quad (2.76)$$

in which $n(\mathbf{r})$ is a unit vector normal to surface $S(\Omega)$. A bond path (BP) is a line connecting two atoms through the interatomic surface and having local maximum electron density.

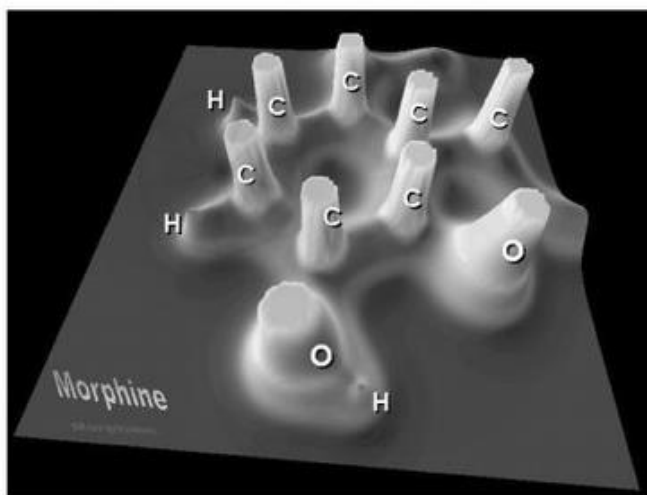


Figure 2-7. A relief map representing the electron density of the phenolic region of the morphine molecule. Reprinted from references 70 with permission from John Wiley and Sons.

To distinguish different CPs, we can introduce another important term, Laplacian of electron density $\nabla^2\rho(\mathbf{r})$, which represents curvatures of electron density:

$$\nabla^2\rho(\mathbf{r}) = \frac{\partial^2\rho(\mathbf{r})}{\partial x^2} + \frac{\partial^2\rho(\mathbf{r})}{\partial y^2} + \frac{\partial^2\rho(\mathbf{r})}{\partial z^2} \quad (2.77)$$

Along each direction, a positive (+1) or negative (−1) curvature represents a minimum or maximum of electron density along this direction at the CP; the sum of signs is termed as signature σ . We can then classify CPs according to the number of non-zero curvatures ω and signature σ , and denote them as (ω, σ) : (3, -3) nuclear critical point; (3, -1) bond critical point; (3, +1) ring critical point; (3, +3) cage critical point.

Bond critical point (BCP) properties, *e.g.*, electron and energy density, are useful

descriptors to evaluate the nature of chemical bonds. Electron density at BCP (ρ_{BCP}) reflects bond strength: $\rho_{\text{BCP}} > 0.2 \text{ au}$ and $< 0.1 \text{ au}$ generally represent covalent and closed-shell bonding, respectively. The sign of $\nabla^2\rho(\mathbf{r})$ at BCP ($\nabla^2\rho_{\text{BCP}}$) indicates if the electron density concentrates ($\nabla^2\rho(\mathbf{r}) < 0$) or depletes ($\nabla^2\rho(\mathbf{r}) > 0$) at BCP. As mentioned above, $\nabla^2\rho(\mathbf{r})$ is the sum of three curvatures, two of which are negative while the third one is positive at BCP. In closed-shell bonding (*e.g.*, ionic bonding), the positive one is dominant and $\nabla^2\rho_{\text{BCP}} > 0$. In contrast, $\nabla^2\rho_{\text{BCP}} < 0$ in covalent bonding⁷⁰. For energy density at BCP, a local form of the virial theorem can be written as:

$$\frac{\hbar^2}{4m}\nabla^2\rho(\mathbf{r}) = 2G(\mathbf{r}) + V(\mathbf{r}) \quad (2.78)$$

in which $G(\mathbf{r})$ is gradient kinetic energy density and is always positive. $V(\mathbf{r})$ is potential energy density, which is the average of virial forces exerted on the point and is always negative. Thus, bonding with $\nabla^2\rho_{\text{BCP}} < 0$ is dominated by a local reduction of $V(\mathbf{r})$. Conversely, it is governed by a local excess of kinetic energy.

QTAIM method also provides a tool to directly measure bond orders, *i.e.*, the number of electron pairs shared between two atoms by integrating exchange density over an atomic volume, which is termed as delocalization index (δ)⁷⁰⁻⁷¹. The delocalization index between two atoms ($\delta(A, B)$) is defined as:

$$\delta(A, B) = 2|F^\alpha(A, B)| + 2|F^\beta(A, B)| \quad (2.79)$$

in which $F^\sigma(A, B)$ is Fermi correlation:

$$F^\sigma(A, B) = -\sum_i \sum_j S_{ij}(A)S_{ji}(B) \quad (2.80)$$

where $S_{ij}(\Omega)$ is overlap integrals of two spin orbitals ($\sigma = \alpha$ or β) over a region Ω .

2.8.2 Interacting quantum atoms (IQA)

Based on QTAIM, Blanco *et al.* proposed an energy partitioning method – interacting quantum atoms (IQA)⁷². According to the IQA approach, the total energy of a molecule can be written as:

$$E = \sum_A E_{\text{net}}^A + \sum_A \sum_{B \neq A} E_{\text{int}}^{AB} \quad (2.81)$$

in which E_{net}^A and E_{int}^{AB} are atomic net energy and interatomic interaction energy, respectively:

$$\begin{aligned} E_{\text{net}}^A &= T^A + V_{en}^{AA} + V_{ee}^{AA} \\ E_{\text{int}}^{AB} &= V_{nn}^{AB} + V_{en}^{AB} + V_{ne}^{AB} + V_{ee}^{AB} \end{aligned} \quad (2.82)$$

where T^A is atomic kinetic energy. V_{ij}^{XY} ($X, Y = A, B$ and $i, j = e, n$) is the interaction energy between i of atom X and the j of atom Y .

E_{int}^{AB} is a good indicator of interactions between two atoms. The electron-electron term can be further partitioned into Coulomb (C), exchange (X), and correlation terms (corr):

$$V_{ee}^{AB} = V_C^{AB} + V_X^{AB} + V_{\text{corr}}^{AB} \quad (2.83)$$

Then E_{int}^{AB} can be rewritten as:

$$E_{\text{int}}^{AB} = V_{\text{cl}}^{AB} + V_{\text{xc}}^{AB} \quad (2.84)$$

where V_{cl}^{AB} and V_{xc}^{AB} are classical and exchange-correlation interaction energy, respectively:

$$V_{cl}^{AB} = V_{nn}^{AB} + V_{en}^{AB} + V_{ne}^{AB} + V_C^{AB}$$

$$V_{xc}^{AB} = V_X^{AB} + V_{corr}^{AB} \quad (2.85)$$

V_{xc}^{AB} contains all quantum terms and is a good descriptor of covalent contributions to the interatomic energy. The more negative the V_{xc}^{AB} is, the higher the degree of covalency.

2.9 Software Used

VASP. The Vienna Ab initio Simulation Package (VASP)⁷³⁻⁷⁶, developed by the Hafner Research Group at the University of Vienna, is used throughout chapters 3-5. It is a powerful tool for performing *ab initio* quantum mechanical calculations for periodic systems using plane wave basis sets and pseudopotentials. PAW method implemented in VASP is used in this thesis. The basic methodology for VASP is density functional theory (section 2.3), which is the main method used in this thesis. The code is compatible with many external tools or scripts, like the transition state searching tool VTST^{62-63, 77} and electronic structure plotting script vaspkit.

TURBOMOLE. TURBOMOLE⁷⁸ is a molecular *ab initio* computational chemistry program developed by the group of Professor Reinhart Ahlrichs at the University of Karlsruhe, which is used in chapter 6 with version 7.3. The code is capable of using many post-HF methods for quantum chemical simulations of molecules and clusters, like the MP2 used in this thesis.

AIMAll. All QTAIM and IQA calculations in chapter 6 were conducted in AIMAll⁷⁹ version 17.11.14, which is developed to perform quantitative and visual Atoms in Molecules analyses.

References

- [1] P.W. Atkins, R.S. Friedman, *Molecular Quantum Mechanics*, Oxford University Press, 2011.
- [2] M. Born, R. Oppenheimer, Zur Quantentheorie Der Molekeln, *Annalen der physik* 389 (1927) 457-484.
- [3] D.R. Hartree, The Wave Mechanics of an Atom with a Non-Coulomb Central Field. Part I. Theory and Methods, *Mathematical Proceedings of the Cambridge Philosophical Society*, Cambridge University press, 1928, pp. 89-110.
- [4] C.D. Sherrill, H.F. Schaefer III, The Configuration Interaction Method: Advances in Highly Correlated Approaches, *Advances in Quantum Chemistry*, Elsevier, 1999, pp. 143-269.
- [5] H.-D. Meyer, U. Manthe, L.S. Cederbaum, The Multi-configurational Time-dependent Hartree Approach, *Chemical Physics Letter* 165(1) (1990) 73-78.
- [6] C. Møller, M.S. Plesset, Note on An Approximation Treatment for Many-electron Systems, *Physical Review* 46(7) (1934) 618.
- [7] R.J. Bartlett, M. Musiał, Coupled-cluster Theory in Quantum Chemistry, *Reviews of Modern Physics* 79(1) (2007) 291.
- [8] P. Hohenberg, W. Kohn, Inhomogeneous Electron Gas, *Physical Review* 136(3B) (1964) B864.
- [9] W. Kohn, L.J. Sham, Self-consistent Equations Including Exchange and Correlation Effects, *Physical Review* 140(4A) (1965) A1133.
- [10] J.P. Perdew, K. Schmidt, Jacob's Ladder of Density Functional Approximations for the Exchange-correlation Energy, *AIP Conference Proceedings* 577 (2001) 1.
- [11] J.P. Perdew, Climbing the Ladder of Density Functional Approximations, *MRS Bulletin* 38(9) (2013) 743-750.
- [12] J.P. Perdew, A. Zunger, Self-interaction Correction to Density-functional Approximations for Many-electron Systems, *Physical Review B* 23(10) (1981) 5048.
- [13] J.P. Perdew, J.A. Chevary, S.H. Vosko, K.A. Jackson, M.R. Pederson, D.J. Singh, C. Fiolhais, Atoms, Molecules, Solids, and Surfaces: Applications of the Generalized Gradient Approximation for Exchange and Correlation, *Physical Review B* 46(11) (1992) 6671-6687.
- [14] J.P. Perdew, K. Burke, M. Ernzerhof, Generalized Gradient Approximation Made Simple, *Physical Review Letter* 77(18) (1996) 3865.
- [15] A.D. Becke, Density-functional Exchange-energy Approximation with Correct Asymptotic Behavior, *Physical Review A* 38(6) (1988) 3098-3100.
- [16] J.P. Perdew, Y. Wang, Accurate and Simple Analytic Representation of the Electron-gas Correlation Energy, *Physical Review B* 45(23) (1992) 13244.
- [17] G. Carchini, N. Almora-Barrios, G. Revilla-López, L. Bellarosa, R. Garcia-Muelas, M. Garcia-Melchor, S. Pogodin, P. Błoński, N. López, How Theoretical Simulations Can Address the Structure and Activity of Nanoparticles, *Topics in Catalysis* 56 (2013) 1262-1272.

- [18] J. Hafner, Ab-initio Simulations of Materials Using VASP: Density-functional Theory and Beyond, *Journal of Computational Chemistry* 29(13) (2008) 2044-2078.
- [19] S. Dudarev, D.N. Manh, A. Sutton, Effect of Mott-Hubbard Correlations on the Electronic Structure and Structural Stability of Uranium Dioxide, *Philosophical Magazine B* 75(5) (1997) 613-628.
- [20] J.P. Perdew, S. Kurth, A. Zupan, P. Blaha, Accurate Density Functional with Correct Formal Properties: A step Beyond the Generalized Gradient Approximation, *Physical Review Letter* 82(12) (1999) 2544.
- [21] J.P. Perdew, L.A. Constantin, Laplacian-level Density Functionals for the Kinetic Energy Density and Exchange-correlation Energy, *Physical Review B* 75(15) (2007) 155109.
- [22] C. Adamo, V. Barone, Toward Reliable Density Functional Methods Without Adjustable Parameters: The PBE0 Model, *The Journal of Chemical Physics* 110(13) (1999) 6158-6170.
- [23] VASP. https://www.vasp.at/wiki/index.php/Category:Van_der_Waals_functionals (Last accessed 01 June 2023).
- [24] S. Grimme, J. Antony, S. Ehrlich, H. Krieg, A Consistent and Accurate *ab initio* Parametrization of Density Functional Dispersion Correction (DFT-D) for the 94 Elements H-Pu. *The Journal of Chemical Physics* 132 (2010) 154104.
- [25] M. Dion, H. Rydberg, E. Schröder, D. C. Langreth, B. I. Lundqvist, Van Der Waals Density Functional for General Geometries. *Physical Review Letter* 92 (2004) 246401.
- [26] J. Harl, L. Schimka, G. Kresse, Assessing the Quality of the Random Phase Approximation for Lattice Constants and Atomization Energies of Solids, *Physical Review B* 81(11) (2010) 115126.
- [27] F. Furche, Molecular Tests of the Random Phase Approximation to the Exchange-correlation Energy Functional, *Physical Review B* 64(19) (2001) 195120.
- [28] Z. Yan, J.P. Perdew, S. Kurth, Density Functional for Short-range Correlation: Accuracy of the Random-phase Approximation for Isoelectronic Energy Changes, *Physical Review B* 61(24) (2000) 16430.
- [29] B. Xiao, J. Sun, A. Ruzsinszky, J. Feng, J.P. Perdew, Structural Phase Transitions in Si and SiO₂ Crystals via the Random Phase Approximation, *Physical Review B* 86(9) (2012) 094109.
- [30] P. Mori-Sánchez, A.J. Cohen, W. Yang, Failure of the Random-phase-approximation Correlation Energy, *Physical Review A* 85(4) (2012) 042507.
- [31] I.S. Ulusoy, A.K. Wilson, Slater and Gaussian Basis Functions and Computation of Molecular Integrals, *Mathematical Physics in Theoretical Chemistry*, Elsevier, 2019, pp. 31-61.
- [32] J.C. Slater, Atomic Shielding Constants, *Physical Review* 36(1) (1930) 57.
- [33] S.F. Boys, Electronic Wave Functions II. A Calculation for the Ground State of the Beryllium Atom, *Proceedings of the Royal Society of London. Series A. Mathematical and Physical Sciences* 201(1064) (1950) 125-137.
- [34] J.G. Hill, Gaussian Basis Sets for Molecular Applications, *International Journal of Quantum Chemistry* 113(1) (2013) 21-34.

- [35] S.F. Boys, F. Bernardi, The Calculation of Small Molecular Interactions by the Differences of Separate Total Energies. Some Procedures with Reduced Errors, *Molecular Physics* 19(4) (1970) 553-566.
- [36] D. Marx, J. Hutter, *Ab initio Molecular Dynamics: Basic Theory and Advanced Methods*, Cambridge University Press, 2009.
- [37] H.J. Monkhorst, J.D. Pack, Special Points for Brillouin-zone Integrations, *Physical Review B* 13(12) (1976) 5188.
- [38] Wikipedia, Pseudopotential. <https://en.wikipedia.org/wiki/Pseudopotential>. (Last accessed 08 March 2023).
- [39] G.B. Bachelet, D.R. Hamann, M. Schlüter, Pseudopotentials That Work: From H to Pu, *Physical Review B* 26(8) (1982) 4199.
- [40] D. Hamann, M. Schlüter, C. Chiang, Norm-conserving Pseudopotentials, *Physical Review Letter* 43(20) (1979) 1494.
- [41] D. Vanderbilt, Soft Self-consistent Pseudopotentials in a Generalized Eigenvalue Formalism, *Physical Review B* 41(11) (1990) 7892.
- [42] P. E. Blöchl, Projector Augmented-Wave Method, *Physical Review B* 50 (1994) 17953.
- [43] G. Kresse, D. Joubert, From Ultrasoft Pseudopotentials to the Projector Augmented-Wave Method, *Physical Review B* 59(1999) 1758.
- [44] M. Dolg, Effective Core Potentials, *Modern Methods and Algorithms of Quantum Chemistry* 3 (2000) 507-540.
- [45] N.S. Mosyagin, A. Zaitsevskii, A.V. Titov, Shape-consistent Relativistic Effective Potentials of Small Atomic Cores, *International Review of Atomic and Molecular Physics* 1(1) (2010) 63-72.
- [46] M. Dolg, H. Stoll, H. Preuss, R.M. Pitzer, Relativistic and Correlation Effects for Element 105 (hahnium, Ha): a Comparative Study of M and MO (M= Nb, Ta, Ha) Using Energy-adjusted ab initio Pseudopotentials, *The Journal of Physical Chemistry* 97(22) (1993) 5852-5859.
- [47] M. Dolg, Efficient Quantum Chemical Valence-only Treatments of Lanthanide and Actinide Systems, *AIP Conference Proceedings*, American Institute of Physics, 2012, pp. 80-91.
- [48] K.S. Pitzer, Relativistic Effects on Chemical Properties, *Accounts of Chemical Research* 12(8) (1979) 271-276.
- [49] M. Dolg, X. Cao, Relativistic Pseudopotentials: Their Development and Scope of Applications, *Chemical Review* 112(1) (2012) 403-480.
- [50] M. Seth, M. Dolg, P. Fulde, P. Schwerdtfeger, Lanthanide and Actinide Contractions: Relativistic and Shell Structure Effects, *Journal of the American Chemical Society* 117(24) (1995) 6597-6598.
- [51] W. Küchle, M. Dolg, H. Stoll, H. Preuss, Energy-adjusted Pseudopotentials for the Actinides. Parameter Sets and Test Calculations for Thorium and Thorium Monoxide, *The Journal of Chemical Physics* 100(10) (1994) 7535-7542.
- [52] X. Cao, M. Dolg, H. Stoll, Valence Basis Sets for Relativistic Energy-consistent Small-core Actinide Pseudopotentials, *The Journal of Chemical Physics* 118(2) (2003)

487-496.

[53] X. Cao, M. Dolg, Segmented Contraction Scheme for Small-core Actinide Pseudopotential Basis Sets, *Journal of Molecular Structure: THEOCHEM* 673(1-3) (2004) 203-209.

[54] R. Car, M. Parrinello, Unified Approach for Molecular Dynamics and Density-functional Theory, *Physical Review Letter* 55(22) (1985) 2471.

[55] A. Zunger, S.-H. Wei, L. Ferreira, J.E. Bernard, Special Quasirandom Structures, *Physical Review Letter* 65(3) (1990) 353.

[56] A. Van de Walle, P. Tiwary, M. De Jong, D. Olmsted, M. Asta, A. Dick, D. Shin, Y. Wang, L.-Q. Chen, Z.-K. Liu, Efficient Stochastic Generation of Special Quasirandom Structures, *CALPHAD* 42 (2013) 13-18.

[57] H. Mehrer, *Diffusion in Solids: Fundamentals, Methods, Materials, Diffusion-controlled Processes*, Springer Science & Business Media, 2007.

[58] G.H. Vineyard, Frequency Factors and Isotope Effects in Solid State Rate Processes, *Journal of Physics and Chemistry of Solids* 3(1-2) (1957) 121-127.

[59] H. Eyring, The Activated Complex in Chemical Reactions, *The Journal of Chemical Physics* 3(2) (1935) 107-115.

[60] D.G. Truhlar, B.C. Garrett, S.J. Klippenstein, Current Status of Transition-state Theory, *The Journal of Physical Chemistry* 100(31) (1996) 12771-12800.

[61] H. Jónsson, G. Mills, K.W. Jacobsen, Nudged Elastic Band Method for Finding Minimum Energy Paths of Transitions, *Classical and Quantum Dynamics in Condensed Phase Simulations*, World Scientific 1998, pp. 385-404.

[62] G. Henkelman, B.P. Uberuaga, H. Jónsson, A Climbing Image Nudged Elastic Band Method for Finding Saddle Points and Minimum Energy Paths, *The Journal of Chemical Physics* 113(22) (2000) 9901-9904.

[63] G. Henkelman, H. Jónsson, Improved Tangent Estimate in the Nudged Elastic Band Method for Finding Minimum Energy Paths and Saddle Points, *The Journal of Chemical Physics* 113(22) (2000) 9978-9985.

[64] G. Montet, Integral Methods in the Calculation of Correlation Factors in Diffusion, *Physical Review B* 7(2) (1973) 650.

[65] K. Compaan, Y. Haven, Correlation Factors for Diffusion in Solids, *Transactions of the Faraday Society* 52 (1956) 786-801.

[66] A. Lidiard, CXXXIII. Impurity Diffusion in Crystals (Mainly Ionic Crystals with the Sodium Chloride Structure), *The London, Edinburgh, and Dublin Philosophical Magazine and Journal of Science* 46(382) (1955) 1218-1237.

[67] A. Lidiard, The Influence of Solutes on Self-diffusion in Metals, *Philosophical Magazine* 5(59) (1960) 1171-1180.

[68] R.F. Bader, T. Nguyen-Dang, *Quantum theory of Atoms in Molecules–Dalton Revisited*, *Advances in Quantum Chemistry*. Academic Press, Elsevier, 1981, pp. 63-124.

[69] R.F.W. Bader, *Theory of Atoms in Molecules*, 1995. https://www.chemistry.mcmaster.ca/aim/aim_0.html. (Last accessed 08 March 2023).

[70] C.F. Matta, R.J. Boyd, *An Introduction to the Quantum Theory of Atoms in Molecules*,

The Quantum Theory of Atoms in Molecules: From Solid State to DNA and Drug Design (2007).

[71] X. Fradera, M.A. Austen, R.F. Bader, The Lewis Model and Beyond, *The Journal of Physical Chemistry A* 103(2) (1999) 304-314.

[72] M.A. Blanco, A. Martin Pendás, E. Francisco, Interacting Quantum Atoms: A Correlated Energy Decomposition Scheme Based on the Quantum Theory of Atoms in Molecules, *Journal of Chemical Theory and Computation* 1(6) (2005) 1096-109.

[73] G. Kresse, J. Hafner, Ab initio Molecular Dynamics for Liquid Metals, *Physical Review B* 47(1) (1993) 558.

[74] G. Kresse, J. Furthmüller, Efficiency of ab-initio Total Energy Calculations for Metals and Semiconductors Using a Plane-wave Basis Set, *Computational Materials Science* 6(1) (1996) 15-50.

[75] G. Kresse, J. Furthmüller, Efficient Iterative Schemes for ab initio Total-energy Calculations Using a Plane-wave Basis Set, *Physical Review B* 54(16) (1996) 11169.

[76] VASP. <https://www.vasp.at/>. (Last accessed 08 March 2023).

[77] VTST Tools. <https://theory.cm.utexas.edu/vtsttools/>. (Last accessed 08 March 2023).

[78] S.G. Balasubramani, G.P. Chen, S. Coriani, M. Diedenhofen, M.S. Frank, Y.J. Franzke, F. Furche, R. Grotjahn, M.E. Harding, C. Hättig, TURBOMOLE: Modular Program Suite for ab initio Quantum-chemical and Condensed-matter Simulations, *The Journal of Chemical Physics* 152(18) (2020) 184107.

[79] T.A. Keith, AIMAll, TK Gristmill Software, Overland Park KS, USA, 2019.

-Blank page-

Part II

Results

-Blank page-

3 Incorporation of Kr and Xe in Uranium Mononitride

This chapter is the author published article (adapted with permission Lin Yang and Nikolas Kaltsoyannis, Incorporation of Kr and Xe in Uranium Mononitride: A Density Function Theory Study, *J. Phys. Chem. C* 2021, 125, 26999-27008. <https://doi.org/10.1021/acs.jpcc.1c08523>. Copyright 2021 American Chemical Society), which has 16 pages in total. All work in this chapter was completed by myself under the supervision of Prof. Nikolas Kaltsoyannis.

Incorporation of Kr and Xe in Uranium Mononitride: A Density Functional Theory Study

Lin Yang and Nikolas Kaltsoyannis*



Cite This: *J. Phys. Chem. C* 2021, 125, 26999–27008



Read Online

ACCESS |



Metrics & More

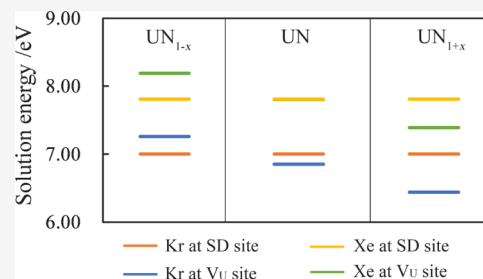


Article Recommendations



Supporting Information

ABSTRACT: Uranium nitride is a material of considerable fundamental interest and is a promising candidate for an advanced nuclear fuel. We here study intrinsic point defects and incorporation of the fission gas atoms Kr and Xe in UN by density functional theory, including the first report of the effects of non-stoichiometry. The defect formation energies of U and N vacancies are found to be highly dependent on stoichiometry. The most stable defect types are N vacancies under U-rich and near-stoichiometric conditions but U vacancies under N-rich conditions. The existence of a defect significantly affects the magnetic moment of UN, especially defects involving U vacancies. The incorporation of Kr and Xe in UN induces relaxation of the atomic positions of U and N atoms adjacent to Kr or Xe, with the displacement induced by Xe being more significant than that by Kr due to the larger atomic radius of the former. The calculated solution energy of Kr and Xe in a perfect UN supercell shows that the most energetically favorable sites are Schottky defects and U vacancies under U-rich and N-rich conditions, respectively. Under near-stoichiometric conditions, Kr and Xe behave differently, with the former preferring a U vacancy and the latter preferring the Schottky defect. Bader charge analysis indicates larger charge transfer to noble gases on Kr incorporation than on Xe incorporation, consistent with the higher electronegativity of Kr.



INTRODUCTION

Uranium nitride (UN) is a metallic solid with a face-centered cubic crystal structure. It is interesting both fundamentally and also because it is a promising candidate for use as a nuclear fuel in so-called Generation IV nuclear reactors due to its high metal density and melting temperature and excellent thermal conductivity.^{1,2} Given the difficulty of experimentally studying radioactive materials such as UN, computational simulation is particularly valuable, although the use of density functional theory (DFT) to study the electronic structure of actinide materials is not straightforward due to the combined challenges of relativistic effects and the strong correlation of 5f electrons. Indeed, standard DFT functionals can yield erroneous predictions for actinide materials, most notably the failure of GGA functionals to reproduce the experimentally determined insulating behavior of the actinide dioxides; the over-delocalization of the 5f electrons by the GGA approach incorrectly predicts these oxides to be metallic.³ This is typically corrected by the application of the Hubbard *U* term, which reduces the 5f delocalization.^{4–8}

Over time, the radioactive fission of the actinide atoms in nuclear fuel generates a large number of products, including the noble gases (Ng) Kr and Xe, which have a low solubility in the fuel. These gas atoms may migrate in the fuel matrix, form bubbles inside and on the boundary of the grains, or escape to the fuel-clad gap, with the former leading to fuel swelling and the latter degrading the thermal conductivity of fuel rods.⁹ Fission gas behavior in UO₂ nuclear fuel has been extensively studied,^{10–15} including by computational approaches; Ander-

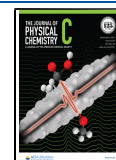
sson et al. developed diffusion coefficient models of Xe and Kr in UO₂ by combining DFT with empirical potentials, which qualitatively agrees with the available experimental data.^{13,14} They also reported significant influence of non-stoichiometry on Ng behavior in UO₂.

For the safe and efficient use of nitride fuels, it is therefore important to have a comprehensive understanding of their properties, including the generation and migration of fission products in the fuel matrix, especially as post-reactor studies using (U, Pu)N mixed fuel found relative yields of 19 and 19.3% of Kr and Xe, respectively, in the fuel-clad gap.¹⁶ However, compared with UO₂, gas release models for UN are rudimentary. There are several theoretical works on the behavior of Kr and Xe in UN,^{17–20} but they are based on different methods and the results are not consistent. Klipfel et al. studied the incorporation of Kr and Xe in UN using the DFT/GGA(PBE) approach;¹⁷ although spin-polarization was included, it is not clear whether an antiferromagnetic (AFM) or ferromagnetic (FM) order was used. They found that the preferred trap site for Ng is the Schottky defect (SD), and a weak charge transfer to Ng was reported. Zhang et al.

Received: September 28, 2021

Revised: November 8, 2021

Published: November 22, 2021



investigated the incorporation and migration of Xe in AFM by the DFT + *U* method;²⁰ although their Xe incorporation energies are close to the values reported by others,^{17,19} the UN defect formation energies are quite different from other works that used standard GGA functionals.^{21,22}

The discrepancy might originate from the different descriptions of the UN electronic structure by the DFT and DFT + *U* approaches. According to angle-resolved photoelectron spectroscopy (ARPES),²³ the U 5f electrons are fully itinerant in UN. A theoretical study by the self-interaction-corrected local spin density (SIC-LSD) approach also showed the itinerant electronic structure of UN²⁴ and reported that standard LSDA approaches which treat all the U 5f electrons as itinerant successfully reproduced the experimental UN band structure.²³ However, including the Hubbard *U* correction overestimated the U 5f localization with the states near the Fermi level being underestimated,^{18,25} which is contrary to the strong and narrow U 5f peak near the Fermi level in the photoemission spectrum.²⁶ Although conventional DFT gives a good description of the UN electronic structure, the FM state is predicted to be the ground state by the PBE functional,²⁵ and FM ordering is always used in UN research work when the standard DFT approach is employed.^{17,22,27} Therefore, comparison between the defect and Ng incorporation behavior in AFM and FM UN is needed to support the use of the FM state.

Based on the above-mentioned considerations, in this work, we systematically study the incorporation behavior of Kr and Xe in AFM and FM UN. Bulk properties are predicted by the PW91, PW91 + *U*, PBE, SCAN, and HSE06 functionals to compare their performance in describing the UN fuel matrix. Then, the formation energies of UN intrinsic point defects (vacancy, Frenkel pair, and SD) are calculated, and the effect of non-stoichiometry is investigated. Finally, the incorporation of Kr and Xe in perfect and defective UN is simulated. We believe that our work is interesting both fundamentally and that it may contribute to fission gas release models in UN.

METHODS

DFT Calculations. The DFT calculations reported in this work are conducted using the Vienna Ab initio Simulation Package (VASP) version 6.1.2.^{28–30} The cutoff energy for the plane waves is set to 520 eV. Up to 640 eV was tested with the total energy being listed in Table S1, which shows that the total energy change in the UN bulk is less than 0.01% above 520 eV. The orbital partial occupancy is described by the Methfessel–Paxton method with a smearing width of 0.2 eV. The tetrahedron method with Blöchl corrections was used to accurately describe the electronic density of states. The Monkhorst–Pack sampling method with $10 \times 10 \times 10$ *k*-point meshes was applied for bulk ground-state studies.

The crystal structure of UN is face-centered cubic (NaCl). Experimental work shows that UN is a conductor with an AFM ordering under 53 K.³¹ To predict the ground state of the UN bulk, we assessed the performance of four DFT approaches: the generalized gradient approximation (GGA) with the PW91³² and PBE³³ functionals, the *meta*-GGA SCAN functional,³⁴ the hybrid HSE06³⁵ functional, and the Hubbard-corrected PW91 + *U* method. For the latter, the rotationally invariant method introduced by Dudarev et al.³⁶ was used, with an effective Hubbard parameter (U_{eff}) of 1.85 eV, which has been shown to perform well for UN.²¹

The defect formation energy and Ng incorporation behavior are studied in a $2 \times 2 \times 2$ supercell (64 atoms) using a $3 \times 3 \times 3$ *k*-point mesh. Meshes up to $5 \times 5 \times 5$ were tested with the results being listed in Table S2, which shows that the total energy is well-converged at $3 \times 3 \times 3$. During geometry optimization, the volume and shape of the supercell were fixed with only the atomic positions being allowed to relax, thus avoiding volume changes induced by the interaction between the defect and its periodic images.³⁷ All the structures were optimized with a force convergence limit of 0.01 eV/Å.

Defect Formation Energies and Ng Incorporation Energies. The incorporation of impurities in UN is facilitated by point defects. In this work, the U vacancy (V_{U}), N vacancy (V_{N}), U Frenkel pair (FP_{U}), N Frenkel pair (FP_{N}), and UN SD are considered. Because UN is metallic, the defect charge state is not taken into consideration. The defect formation energies (E_{f}) are calculated from

$$E_{\text{f}} = E_{\text{defect}} - E_{\text{perfect}} \pm \sum n_{\text{A}} \mu_{\text{A}} + E_{\text{el}} \quad (1)$$

where E_{defect} and E_{perfect} are the total energies of the defective and perfect UN supercell, respectively, and n_{A} and μ_{A} are the number and chemical potential of all atoms added or removed to create the defect, respectively. Considering that the stoichiometry of the supercell containing SDs does not change, the formation energy of the SD can be simplified as

$$E_{\text{f}}(\text{SD}) = E_{\text{defect}} - \frac{n-1}{n} E_{\text{perfect}} \quad (2)$$

in which n is the number of formula units in the perfect UN supercell. Then, the formation energy of the SD is independent of the chemical potential. E_{el} is the energy correction term due to the elastic field induced by point defects. The inclusion of defects or solute atoms in the crystal matrix is expected to induce a long-range elastic field. Due to the supercell approach, in which the periodic model is implemented, the defect or solute atom can interact with its periodic images. When the supercell size is sufficiently large, the elastic field will vanish within the supercell and have a negligible effect on the defect formation energy. However, $2 \times 2 \times 2$ is insufficient to neglect such interactions,³⁸ especially for large defects (e.g. SD). Thus, the elastic field correction term is necessary. The method introduced by Varvenne et al.³⁹ and the ANETO script developed by them are used to estimate this term.

Similar to the defect formation energy, the Ng solution energy [$E_{\text{s}}(\text{Ng})$] is the energy needed to incorporate the Ng atom in the perfect UN supercell, which can be calculated from

$$E_{\text{s}}(\text{Ng}) = E_{\text{Ng} \in \text{defect}} - E_{\text{perfect}} \pm \sum n_{\text{A}} \mu_{\text{A}} + E_{\text{el}} \quad (3)$$

where $E_{\text{Ng} \in \text{defect}}$ is the UN supercell containing the Ng atom at the defect site. To evaluate the ability of UN to trap the Ng solute atom into the pre-existing defect, the Ng incorporation energy [$E_{\text{i}}(\text{Ng})$] is calculated from

$$E_{\text{i}}(\text{Ng}) = E_{\text{Ng} \in \text{defect}} - E_{\text{defect}} - \mu_{\text{Ng}} + E_{\text{el}} \quad (4)$$

RESULTS AND DISCUSSION

Properties of the UN Bulk. As stated in the Introduction, previous calculations of Ng behavior in UN have employed the DFT + *U* method,^{19,20} which fails to correctly describe the electronic structures of itinerant actinide compounds (e.g., UC, PuC, and PuN^{25,40–42}). Application of conventional DFT

predicts FM UN as the ground state.^{25,43} To compare the performance of different functionals, we studied both the FM and AFM UN bulk properties with the GGA (PBE and PW91), PW91 + *U*, SCAN, and HSE06 approaches. The calculated relative energy ($\Delta E/\text{eV}$), lattice parameter ($a/\text{\AA}$), and magnetic moment (μ/μ_B) are listed in Table 1. The relative energy is the energy difference between AFM and FM states.

Table 1. Relative Energy (ΔE), Lattice Parameter (a), and Magnetic Moment (μ) of AFM and FM Bulk UN Obtained from Various Density Functionals and from Experiments

method	$\Delta E/\text{eV}$		$a/\text{\AA}$		μ/μ_B	
	AFM	FM	AFM	FM	AFM	FM
PW91	0.128	0	4.856	4.870	0.97	1.17
PBE	0.158	0	4.865	4.868	1.05	1.25
PW91 + <i>U</i>	0	0.074	4.927	4.916	1.59	1.71
SCAN	0	0.235	4.856	4.837	1.65	1.37
HSE06	0	0.448	4.927	4.912	1.92	1.58
expt ³¹			4.886		0.75	

The GGA functionals perform significantly differently from the hybrid and *meta*-GGA functional and the DFT + *U* scheme, with the later three behaving similarly. PW91 and PBE predict FM to be the ground state, with the total energy of the AFM states being 0.13 and 0.16 eV higher, respectively. By contrast, the AFM state is predicted to be the ground state by PW91 + *U*, SCAN, and HSE06, and the energy difference between the two magnetic states obtained from HSE06 is the largest. The calculated lattice parameters are all reasonably close to the experimental data; while PW91 + *U* and HSE06 slightly overestimate the value, the standard GGA functionals and SCAN are opposite. Turning to the magnetic moment, UN is experimentally observed to be AFM below 53 K with a magnetic moment of $0.75 \mu_B$.³¹ The calculated values vary significantly, and the conventional DFT functionals reproduce experiments better, with the value obtained from PW91 being

the closest to experimental data. PW91 + *U*, SCAN, and HSE06 significantly overestimate the magnetic moment. The UN magnetic order originates from the itinerant U 5f electrons,²³ but DFT + *U* and the hybrid functional overestimate the localization of the 5f electrons. To the best of our knowledge, there are no studies of the SCAN functional's performance in describing the electronic structure of 5f compounds, but it overestimates the magnetic moment of transition metals due to over-localization of the 3d electrons.⁴⁴ The magnetic moment of FM UN is slightly larger than that of the AFM state for PW91, PBE, and PW91 + *U*, while it is opposite for SCAN and HSE06.

To further study the electronic structure of UN, the density of states (DOS) is calculated and is plotted in Figure 1a–d. A non-self-consistent calculation is not currently supported for *meta*-GGA functionals in VASP, so the SCAN data are not included. It can be seen from Figure 1a–d that all the functionals correctly predict UN as metallic, but the states near the Fermi level are quite different. Figure 1d shows that the HSE06 U 5f DOS at the Fermi level is low, and Figure 1c indicates that this is also the case at the GGA + *U* level, as observed in other studies.^{18,25} This is in disagreement with photoemission and ARPES experiments, which see a strong U 5f peak near the Fermi level (0–2 eV).^{23,26} The DOS obtained from PW91 and PBE better reproduce experiment. The underestimation of states near the Fermi level by DFT + *U* and HSE06 is because the localization of U 5f electrons is overestimated, and states that should be near the Fermi level are over-stabilized to lower energy (Figure S1). This is clearly related to the high magnetic moment obtained from PW91 + *U* and HSE06, as discussed above.

Overall, the standard GGA functionals predict very similar values for the lattice parameter and magnetic moments of the FM and AFM states and indicate that the FM arrangement is the ground state by a small energy, by contrast to PW91 + *U*, SCAN, and HSE06, which predict an AFM ground state. However, the electronic structure of UN is better reproduced at the GGA level, and we therefore favor this approach for our

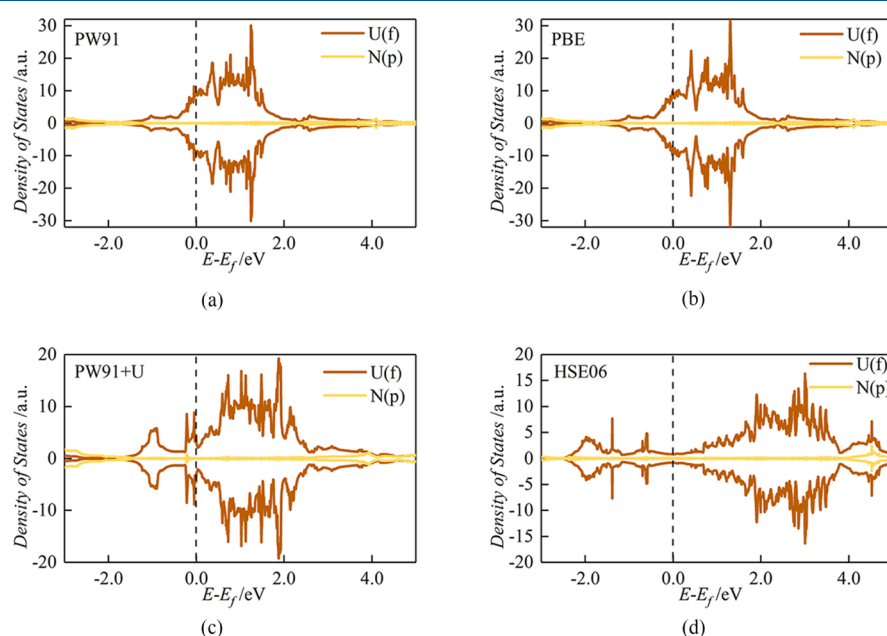


Figure 1. Density of states of the AFM UN bulk at (a) PW91, (b) PBE, (c) PW91 + *U*, and (d) HSE06 levels.

calculations. As PW91 performs better than PBE for the magnetic moment calculation, it is used in the following defect and Ng incorporation studies.

Intrinsic Point Defects. As discussed above, the PW91 functional reasonably describes the electronic structure of UN but predicts the FM order as the ground state. In this section, we study the effect of the magnetic order (AFM and FM) on the defect structure and formation energy. Based on the optimized UN unit cell, the $2 \times 2 \times 2$ supercell is established to study the intrinsic point defects in UN. V_U , V_N , FP_N , FP_U , and UN SD are considered. For AFM UN, a U atom with a positive magnetic moment was removed to create the V_U and SD.

As stated in eq 1, the chemical potentials of U and N are needed for the vacancy formation energy calculation. Many previous studies have taken a N_2 molecule and α -bulk U as reference states to calculate the chemical potential of N and U, respectively.^{17,22} However, the chemical potential should be a range and is highly related to stoichiometric conditions. According to the phase diagram of UN,⁴⁵ near-stoichiometric UN should be bound by U-rich conditions (in equilibrium with bulk U) and N-rich conditions (in equilibrium with U_2N_3). Using the total energy of bulk α -U and U_2N_3 , the calculated μ_U and μ_N are as follows: $-11.98 \text{ eV} < \mu_U < -11.15 \text{ eV}$ and $-10.99 \text{ eV} < \mu_N < -10.17 \text{ eV}$ (details are given in the Supporting Information). Hence, the range of the U chemical potential in UN is 0.83 eV, larger than the 0.24 eV for UC^{46} though smaller than the 7.59 eV for UO_2 .¹⁴ We, therefore, consider the following conditions in our work

- (i) U-rich conditions (UN_{1-x}) with $\mu_U = -11.15 \text{ eV}$ and $\mu_N = -10.99 \text{ eV}$;
- (ii) N-rich conditions (UN_{1+x}) with $\mu_U = -11.98 \text{ eV}$ and $\mu_N = -10.17 \text{ eV}$;
- (iii) Near-stoichiometric conditions (UN) with $\mu_U = -11.56 \text{ eV}$ and $\mu_N = -10.58 \text{ eV}$ (midpoint of the range).

The calculated defect formation energies (E_f) of AFM and FM UN under the three conditions are listed in Tables 2 and S5, and the energies without the elastic field correction are summarized in Tables S3 and S4. To the best of our knowledge, there is no previous work discussing the effect of

Table 2. Defect Formation Energy Considering Non-stoichiometry (E_f) and Calculated From Bulk U and the N_2 Molecule [$E_f^{(1)}$] and the Total Magnetic Moment (μ) of AFM and FM UN^a

magnetic order	defect type	E_f/eV			$E_f^{(1)}/\text{eV}$	μ/μ_B
		UN_{1-x}	UN	UN_{1+x}		
AFM	V_U	3.17	2.75	2.34	3.17	-7.48
	V_N	1.76	2.18	2.59	4.42	1.06
	FP_N	4.90	4.90	4.90	4.90	-1.00
	SD bound	4.17	4.17	4.17	4.17	-10.43
	SD unbound	4.96	4.96	4.96	4.96	-8.1
FM	V_U	3.43	3.01	2.60	3.43	
	V_N	1.90	2.31	2.72	4.56	
	FP_U	9.46	9.46	9.46	9.46	
	FP_N	5.04	5.04	5.04	5.04	
	SD bound	4.17	4.17	4.17	4.17	
	SD unbound	5.15	5.15	5.15	5.15	

^aThe V_U defect and SD are created by removing a U atom with a positive magnetic moment.

non-stoichiometry on the UN defect formation energies. The defect formation energies [$E_f^{(1)}$] calculated versus bulk U and the N_2 molecule are also provided.

The formation energies of single U and N vacancies calculated from the N_2 molecule and bulk α -U are close for the AFM and FM states, 3.17 and 4.42 eV for the former and 3.43 and 4.56 eV for the latter. The lower formation energy of the U vacancy shows that it is energetically more favorable than the N vacancy. N and U vacancy formation energies obtained in other works are summarized in Table S5. This reveals a large range of reported values, especially when the total energies of isolated N and U atoms are used as their chemical potential. Our calculated results are close to the values of 3.74 and 4.24 eV reported by Klipfel et al.,¹⁷ and 3.22 and 4.42 eV reported by Bocharov et al.,²² using the PBE and PW91 functionals for FM UN, respectively.

Considering the non-stoichiometry, the defect formation energies of V_U and V_N vary under the three regimes, with the AFM and FM states showing the same trend. The formation energy of V_U decreases from U-rich to N-rich conditions, while that of V_N is opposite, that is, the stability of V_U increases from UN_{1-x} to UN_{1+x} but that of V_N reduces. Under U-rich conditions (UN_{1-x}), the N vacancy is more favorable than V_U with a V_N formation energy of 1.76 and 1.90 eV for the AFM and FM states, respectively. This is also true in near-stoichiometric UN, while V_U is more energetically favorable for N-rich conditions (UN_{1+x}). The trend that the most stable defect is different under various conditions has also been reported for UO_2 , for which V_U^{4+} has the lowest formation energy under O-rich conditions, while V_O^{2+} is the most stable in U-rich and near-stoichiometric cases.⁷ For U_2Si_3 , although V_U is the most stable site under all three conditions, the formation energy of the Si vacancy increases from U-rich to Si-rich cases.⁴⁷

We find that the defects influence the magnetic moment of the U atoms in AFM UN to different extents, while the effect on FM UN is very small. The total magnetic moments μ of the AFM UN supercell containing different defect types are listed in Table 2. It can be seen that the total magnetic moment of the supercell containing V_N is $1.06 \mu_B$, while the value for the V_U defect system is $-7.38 \mu_B$. The total magnetic moment of the UN supercell containing a U vacancy is expected to be $-0.97 \mu_B$ because a U atom with a positive magnetic moment is removed to create the vacancy. To explain the significant deviation for the V_U defect system, the magnetic moments of the nearest-neighbor and next-nearest-neighbor U atoms around the vacancy are shown in Figure 2a,b. The positive and negative magnetization directions of the nearest-neighbor U atoms are due to the AFM order of UN. For the N vacancy, only the adjacent U atoms are affected with the μ values slightly increasing. Bader analysis shows that the charge of these U atoms increases by about 0.28 e. However, the U vacancy affects the magnetic moments of both the nearest-neighbor and the next-nearest-neighbor U atoms. The next-nearest-neighbor U atoms are the U atoms with an N atom between the U and the defect. It can be seen from Figure 2b that the μ value of the nearest-neighbor U atoms with the positive magnetic moment decreases, while the value of the U atoms with the negative moment rises slightly. In addition, the μ direction of the next-nearest-neighbor U atoms is reversed, and its value reduces by about $0.41 \mu_B$. Thus, both the nearest- and next-nearest-neighbor U atoms contribute to the significant deviation of the total magnetic moment. Lan et

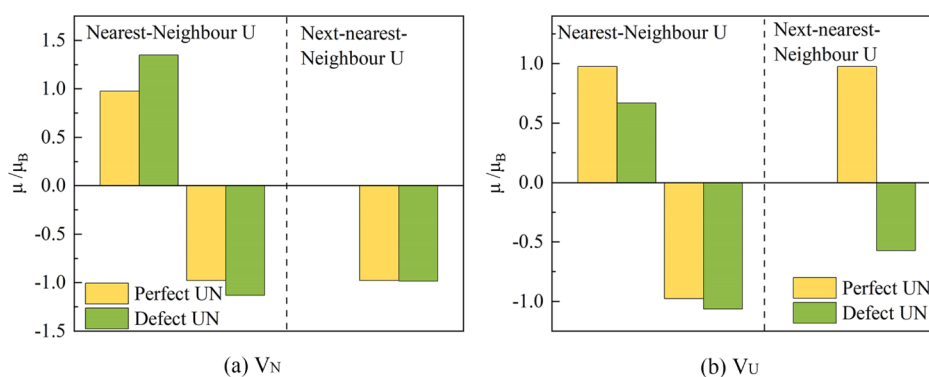


Figure 2. Magnetic moment of the nearest-neighbor U atoms and next-nearest-neighbor U atoms around the (a) N vacancy and (b) U vacancy in AFM UN. For comparison, the values of the corresponding U atoms in the perfect UN supercell are also plotted.

al.²¹ also reported a change in the total magnetic moments of defective AFM UN, in which the change induced by the U vacancy is larger than that by the N vacancy, but they did not analyze the magnetic moment change of the individual U atoms. Bader charge analysis shows that the negative charge of the adjacent N atoms around the U vacancy is reduced by 0.18 e, while the charge change in the nearby U atoms is negligible.

The Frenkel pair defect is a point defect formed by an atom leaving its place to create a vacancy and becoming an interstitial atom. A stable U Frenkel pair structure is not obtained for the AFM UN supercell because, during the optimization, atom U28 (Figure S2) moves to the U vacancy site followed by the U interstitial atom migrating to the U28 original site, leading to the perfect UN supercell. The FP_U defect is located for FM UN (Figure 3a) with a formation energy of 9.46 eV. The stable N Frenkel pair structure (Figure

3b) is obtained for both AFM and FM UN with similar formation energies (4.90 and 5.04 eV, respectively). The much lower formation energy of FP_N than that of FP_U is as expected, considering the large size of U. The total magnetic moment of the FP_N defective supercell is $-1.0 \mu_B$, indicating that the N Frenkel pair defect has a slight influence on the AFM UN magnetization.

The SD refers to a type of point defect consisting of vacancy sites in the same stoichiometric ratio as the original crystal. Bound and isolated SDs are considered in this work, and the optimized structures are shown in Figure 3c,d. Table 2 shows that the formation energy of the bound SD is slightly lower than that of the isolated SD for both AFM and FM UN. This indicates that the bound SD is more energetically favorable, in agreement with the literature.⁴⁸ Moreover, the elastic field effect for all defects is negligible compared with the defect formation energy, and the value for the bound SD is the largest (Tables S3 and S4). This is not unexpected, considering the larger size of bound SDs. The total magnetic moments of the supercell containing the bound SD and unbound SD are $-10.43 \mu_B$ and $-8.10 \mu_B$, respectively. As with V_U , which also involves the removal of a positive magnetic U atom, the significant deviation is due to the effect of the U vacancy on magnetic moments of the nearby U atoms.

Overall, the structures and formation energies of the defects are similar in AFM and FM UN, indicating the limited effect of the magnetic order on the UN defect behavior. We find that the single-point defects (V_U and V_N) are more favorable than double-point defects (FP and SD). Considering the stoichiometric conditions, the N vacancy has the lowest formation energy for U-rich and near-stoichiometric cases, while the U vacancy is the most stable in N-rich conditions. Moreover, defects involving the U vacancy have a greater impact on the supercell magnetic moment.

Incorporation of Kr and Xe. As suggested in the previous section, the bound SD is more favorable than the isolated one, and the formation energies of FP_U and FP_N are larger than those of other defect types. Thus, only the N vacancy, U vacancy, bound SD, and the interstitial site are considered as we study the incorporation of Kr and Xe in UN. The relaxed structures of Ng in FM and AFM UN are shown in Figures 4a–h and S3, respectively.

As with the defect structures, the relaxed Ng incorporation structures in AFM and FM UN are similar, indicating the limited effect of the magnetic order. It is worth noting that for the SD, the Ng atom is located between V_U and V_N , closer to V_U , rather than being situated at the U vacancy site. Moreover,

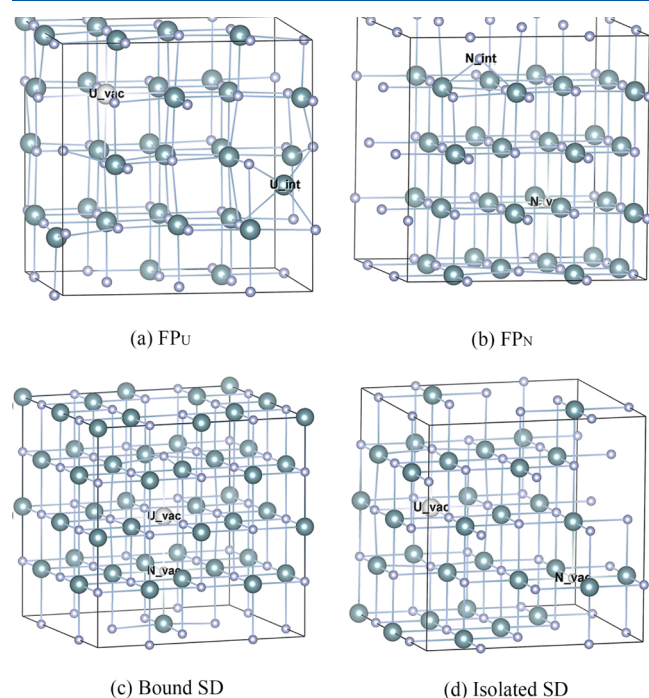


Figure 3. Relaxed FM UN supercell containing the (a) U Frenkel pair, (b) N Frenkel pair defect, (c) bound SD, and (d) unbound SD. The teal, gray, and white balls represent uranium, nitrogen, and vacancy sites, respectively. AFM shares the same defect structures as FM UN.

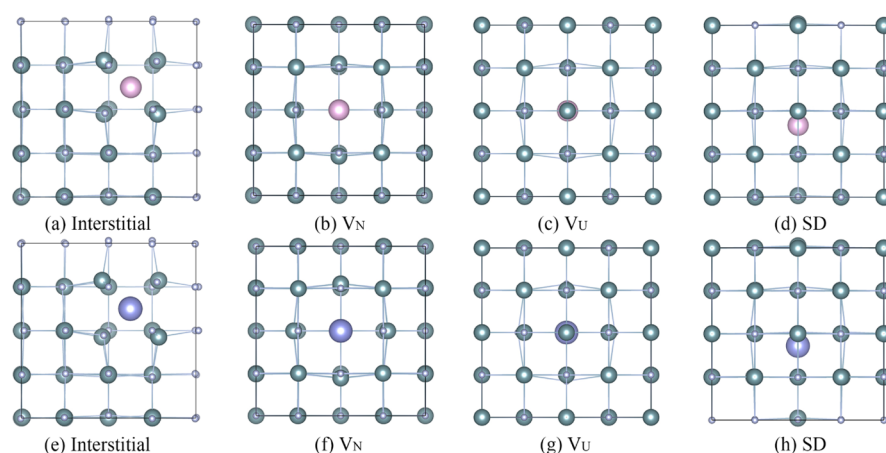


Figure 4. Relaxed structures of (a–d) Kr and (e–h) Xe in the FM UN supercell at different sites. The teal, gray, pink, and purple balls represent uranium, nitrogen, krypton, and xenon, respectively.

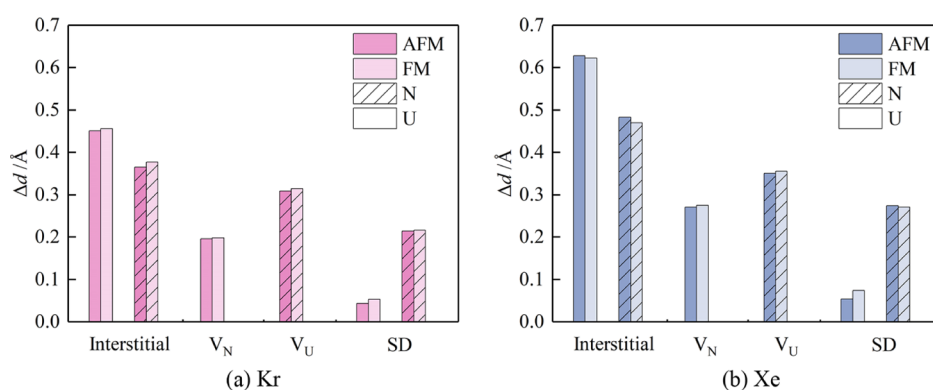


Figure 5. Coordinate change (Δd) of the U (plain) or N (patterned) atoms around (a) Kr and (b) Xe in the AFM and FM UN supercells containing the Ng impurity at different sites. Δd is the displacement of matrix atoms from their original position, and positive values mean that they move away from Kr or Xe.

the incorporation of Ng at all considered trap sites induces the displacement of U and N atoms to different extents. To compare the displacements, the coordinate changes of U and N atoms around the Ng are plotted in Figure 5. As for the incorporation structures, the displacements of U or N atoms in AFM and FM UN are similar. The coordinate change induced by Xe is significantly larger than that by Kr, which is not unexpected considering the larger atomic radius of Xe. It can also be seen from Figure 5a,b that the UN matrix atoms have the largest displacement when the Ng atom is incorporated at the interstitial site, which is due to the small size of the interstitial trap site. For the SD site, the displacement of nearby N atoms is more obvious than that of U, consistent with a relaxed structure in which the Ng atom is closer to V_U .

The calculated solution energy (E_s) and incorporation energy (E_i) of Kr and Xe in UN are listed in Tables 3 and 4, respectively. As stated in the Methods section, the solution and incorporation energies represent the energetic cost of trapping the Ng atom in perfect or defective UN supercells, respectively. It can be seen from Table 3 that the solution energies of Kr in perfect AFM and FM UN are very close to each other. Together with the similar relaxed structures, these highlight the similar solution behavior of Kr in AFM and FM UN. The solution energies at the interstitial site are notably higher than those at other sites due to the small steric space, which indicates that the interstitial site is the least favorable one for Kr incorporation. This is consistent with the largest displace-

Table 3. Kr Solution Energies (E_s) and Incorporation Energies (E_i) in AFM and FM UN Supercells and the Bader Charge of Ng (q_{Ng})

magnetic order	defect type	E_s /eV			E_i /eV	q_{Ng}/e
		UN _{1-x}	UN	UN _{1+x}		
AFM	interstitial	12.52	12.52	12.52	12.52	-0.16
	V_N	8.09	8.50	8.91	6.32	-0.77
	V_U	6.96	6.54	6.13	3.79	-0.10
	SD	6.73	6.73	6.73	2.56	-0.16
FM	interstitial	12.56	12.56	12.56	12.56	-0.18
	V_N	7.95	8.36	8.78	6.05	-0.89
	V_U	7.26	6.85	6.44	3.84	-0.13
	SD	7.00	7.00	7.00	2.53	-0.16

ment of the nearby UN matrix atoms. For monovacancy trap sites (V_N and V_U), the solution energy depends highly on stoichiometric conditions. The solution energy of Kr trapped at an N vacancy increases from UN_{1-x} to UN_{1+x}, while that of Kr at V_U behaves in the opposite way. The values at V_U are generally lower than those at V_N , which is as expected considering the larger steric space of the former. The most energetically favorable site for Kr is different under the three conditions. Under U-rich conditions (UN_{1+x}), Kr at an SD trap site has the lowest solution energy—6.73 and 7.00 eV for AFM and FM states, respectively. However, for near-

Table 4. Xe Solution Energies (E_s) and Incorporation Energies (E_i) in AFM and FM UN Supercells and the Bader Charge of Ng (q_{Ng})

magnetic order	defect type	E_s /eV			E_i /eV	q_{Ng}/e
		UN _{1-x}	UN	UN _{1+x}		
AFM	interstitial	15.53	15.53	15.53	15.53	-0.06
	V _N	10.90	11.32	11.73	9.14	-0.39
	V _U	7.86	7.45	7.04	4.70	0.10
	SD	7.29	7.29	7.29	3.12	-0.11
FM	interstitial	15.58	15.58	15.58	15.58	0.01
	V _N	10.65	11.06	11.48	8.75	-0.34
	V _U	8.19	7.81	7.39	4.79	0.15
	SD	7.81	7.81	7.81	3.31	-0.13

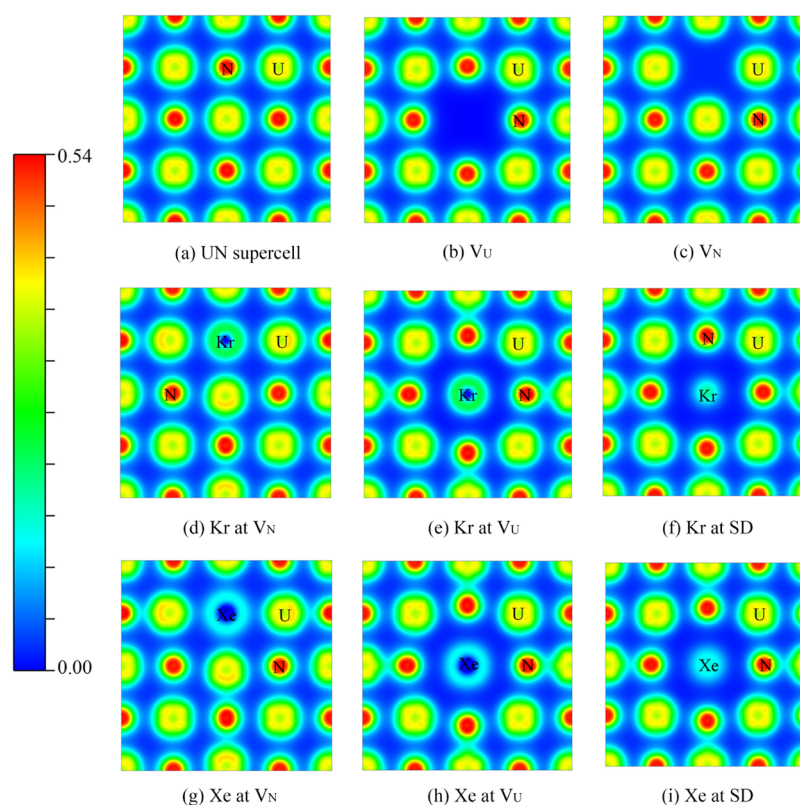
stoichiometric and N-rich conditions, the solution energy at V_U is lower, with the energy difference between the V_U and SD trap sites increasing from UN to UN_{1+x}. This is similar to the reported Kr incorporation behavior in UO₂, where the most favorable trap site is the SD and U monovacancy under U-rich and O-rich conditions, respectively.¹⁴

For the incorporation of Kr in the UN supercell containing pre-existing vacancy defects, the incorporation energies are lower than the solution energy of Kr in the perfect supercell due to the positive defect formation energies discussed above. The incorporation of Kr at the SD site is the most favorable with E_i of 2.56 and 2.53 eV in AFM and FM UN, respectively.

The behavior of Xe in UN (Table 4) has similar trends to that of Kr. The solution and incorporation energies in AFM and FM UN are close, and they are all slightly larger than those of Kr, due to the larger atomic radius of Xe, and consistent

with the trend of the displacements of the UN matrix atoms. However, the most stable trap site of Xe in perfect UN is slightly different from that of Kr. Under U-rich and N-rich conditions, the most energetically favorable site for Xe is the SD and V_U, respectively, which is the same as that for Kr. However, under near-stoichiometric conditions, the solution energy of Xe at the SD site in AFM UN is lowest, and the SD and V_U have the same solution energy in FM UN. This is different from the case for Kr, for which V_U is the most stable site under near-stoichiometric conditions. For the incorporation of Xe in the UN supercell containing pre-existing vacancy defects, the SD site is the most favorable, with an E_i of 3.12 and 3.31 eV in AFM and FM UN, respectively. Our results thus extend the current literature, which reports the SD as the most stable site.^{19,20}

To study the effect of Ng incorporation on the electronic structures of the UN supercell, the Bader charges of Ng have been calculated (Tables 3 and 4). Electron transfer from the adjacent U or N atoms to the trapped Kr atom can be seen from the negative Bader charge of Kr at the four sites, with the charge being slightly more negative in FM UN. Due to the filled electronic structure of Kr, the charge transfer is moderate. For Xe, the charge transfer is smaller than that for Kr, which is expected, considering the lower electronegativity of Xe. This is supported by the lower Xe(p) peak in the DOS at the corresponding vacancy site, versus the situation for Kr(p) (Figure S4). As with Kr, the charges of Xe in the AFM and FM UN systems are similar. Moreover, q_{Ng} is the most negative when the Ng atom is trapped at the V_N site while least negative at the V_U site, with the latter even being positive for Xe, which agrees with the higher Kr(p) [or Xe(p)] peak at the V_N site

**Figure 6.** Charge density distribution (a.u.) of the (001) surface for the (a) UN perfect supercell, (b) V_U and (c) V_N defect supercell, (d–f) Kr, and (g–i) Xe incorporated in FM UN at different vacancy sites.

(Figure S4). This is because when the Ng atom is trapped at V_N and V_U , the nearest matrix atoms are U and N, respectively, which tend to lose or obtain electrons to reach their formal charge as in the perfect supercell.

Figures 6a–i and S5 summarize the (001) plane charge density distributions of Ng incorporated in the FM and AFM UN supercells. Similar charge distributions are found between the incorporation of Ng in AFM UN and the corresponding FM UN, indicating that the magnetic order of UN has a quite limited effect on the electronic structure of UN with incorporated Ng. The more considerable charge density distribution around Kr than that around Xe is consistent with the larger absolute Kr Bader charge. Compared with the charge density distribution of the perfect (Figure 6a) and V_N defect (Figure 6c) UN supercells, the incorporation of Kr and Xe at the N vacancy site leads to clear charge accumulation on adjacent U atoms toward nearby N atoms which are opposite to the Ng (Figure 6d,g), and a moderate interaction between the U atom and the nearby N atom can be observed. For Ng in V_U and SD sites, a significant increase in the charge density between N atoms and the neighboring U atoms can be seen. The change induced by Xe incorporation is more noticeable than that by Kr, because of the shorter N–U distance induced by the larger displacement of the nearby N atoms in the Xe incorporated systems (Figure 5).

CONCLUSIONS

In this contribution, we have studied the incorporation behavior of fission gas atoms, that is, Kr and Xe, in UN and studied the effect of the UN magnetic order on this behavior. We began by identifying the most appropriate form of DFT to study UN, which has fully itinerant 5f electrons, concluding that conventional GGA functionals perform better than hybrid and meta-GGA functionals and the GGA + *U* approach.

Using the PW91 functional, we simulated intrinsic point defects and explored the effect of non-stoichiometry. We found that the defect structures and formation energies are similar in AFM and FM UN, indicating a limited effect of the magnetic ordering. The calculated chemical potential range of U in UN is 0.83 eV, and the defect formation energy of U and N vacancies is dependent upon the non-stoichiometry. We found that the monovacancy formation is more energetically favorable than vacancy pairs, and a bound SD is more stable than an isolated one. Under U-rich and near-stoichiometric conditions, the N vacancy has the lowest formation energy, while the energy of U vacancies is the lowest under the N-rich condition. We also found that the defect can affect the UN magnetic moment in the AFM state, especially defects involving the U vacancy. This is because the U vacancy not only influences the magnetic moment of the nearest-neighbor U atoms but also the next-nearest atoms.

We studied the incorporation of Kr and Xe in the UN interstitial site, U vacancy, N vacancy, and the bound SD sites. Similar incorporation geometries, solution energies, and electronic structures are found for Ng in AFM and FM UN, further indicating the small influence of the UN magnetic order. Kr and Xe cause relaxation of the atomic positions of the nearby UN matrix atoms, and the displacement induced by Xe is more significant than that by Kr due to the larger atomic radius of the former. Because the steric space of the interstitial trap site is the smallest, the deviation of the U and N atoms adjacent to the interstitial Ng atom is the largest. The calculated energy results show that the solution energies of Kr

and Xe in a perfect UN supercell are larger than the incorporation energies of Kr and Xe in UN supercells containing the pre-existing defects due to the positive defect formation energies (except at the interstitial site). The lower energy of Kr in UN indicates that the incorporation of a Kr atom is more stable than that of Xe. The most stable site of Ng in a perfect UN supercell depends on non-stoichiometry. Under U-rich and N-rich conditions, Kr and Xe prefer the SD and U vacancy, respectively, but Kr and Xe behave differently under near-stoichiometric conditions, where the former prefers the U vacancy, while the latter prefers the SD site. The charge density distribution suggests the increasing interaction between U and N atoms near the Ng.

We believe that our work justifies the use of the GGA approach and FM ordering in the study of Ng incorporation in UN. We are currently studying Kr and Xe diffusion, to further improve the fission gas release model in UN.

ASSOCIATED CONTENT

Supporting Information

The Supporting Information is available free of charge at <https://pubs.acs.org/doi/10.1021/acs.jpcc.1c08523>.

Computational methods for the U and N chemical potential in UN; cutoff energy and supercell size convergence test; uncorrected defect formation energies and the elastic field correction term for AFM and FM UN; N and U vacancy formation energies calculated versus the N_2 molecule and U bulk and isolated N and U atoms; partial density of states of U *f* orbitals in AFM UN bulk; unrelaxed UN supercell containing the U Frenkel pair defect; relaxed structures and the charge density distribution of Kr and Xe in the AFM UN supercell at different sites; and density of states of the Kr- and Xe-incorporated UN supercell (PDF)

AUTHOR INFORMATION

Corresponding Author

Nikolas Kaltsoyannis – Department of Chemistry, School of Natural Sciences, The University of Manchester, Manchester M13 9PL, U.K.; orcid.org/0000-0003-0293-5742; Email: nikolas.kaltsoyannis@manchester.ac.uk

Author

Lin Yang – Department of Chemistry, School of Natural Sciences, The University of Manchester, Manchester M13 9PL, U.K.

Complete contact information is available at: <https://pubs.acs.org/doi/10.1021/acs.jpcc.1c08523>

Notes

The authors declare no competing financial interest.

ACKNOWLEDGMENTS

We are grateful to the China Scholarship Council and The University of Manchester for a PhD studentship for L.Y. We are also grateful to The University of Manchester for its Computational Shared Facility and associated support services.

REFERENCES

- (1) Petti, D.; Crawford, D.; Chauvin, N. Fuels for Advanced Nuclear Energy Systems. *MRS Bull.* **2009**, 34, 40–45.

- (2) Allen, T. R.; Crawford, D. C. Lead-Cooled Fast Reactor Systems and the Fuels and Materials Challenges. *Sci. Technol. Nucl. Install.* **2007**, *2007*, 1–11.
- (3) Dudarev, S. L.; Manh, D. N.; Sutton, A. P. Effect of Mott-Hubbard Correlations on the Electronic Structure and Structural Stability of Uranium Dioxide. *Philos. Mag. B* **1997**, *75*, 613–628.
- (4) Chen, J.-L.; Kaltsoyannis, N. Computational Study of Plutonium-Amercium Mixed Oxides ($\text{Pu}_{0.92}\text{Am}_{0.08}\text{O}_{2-x}$); Water Adsorption on {111}, {110}, and {100} Surfaces. *J. Phys. Chem. C* **2020**, *124*, 6646–6658.
- (5) Collard, J.; Steele, H.; Kaltsoyannis, N. Computational study of HCl adsorption on stoichiometric and oxygen vacancy PuO_2 {111}, {110} and {100} surfaces. *J. Nucl. Mater.* **2020**, *530*, 151951.
- (6) Chen, J.-L.; Kaltsoyannis, N. DFT + U study of $\text{U}_{1-y}\text{An}_y\text{O}_{2-x}$ (An = Np, Pu, Am and Cm) {1 1 1}, {1 1 0} and {1 0 0} surfaces. *Appl. Surf. Sci.* **2021**, *537*, 147972.
- (7) Vathonne, E.; Wiktor, J.; Freyss, M.; Jomard, G.; Bertolus, M. DFT + U investigation of charged point defects and clusters in UO_2 . *J. Phys.: Condens. Matter* **2014**, *26*, 325501.
- (8) Pegg, J. T.; Aparicio-Anglès, X.; Storr, M.; de Leeuw, N. H. DFT + U Study of the Structures and Properties of the Actinide Dioxides. *J. Nucl. Mater.* **2017**, *492*, 269–278.
- (9) Tonks, M.; Andersson, D.; Devanathan, R.; Dubourg, R.; El-Azab, A.; Freyss, M.; Iglesias, F.; Kulacsy, K.; Pastore, G.; Phillpot, S. R.; Welland, M. Unit Mechanisms of Fission Gas Release: Current Understanding and Future Needs. *J. Nucl. Mater.* **2018**, *504*, 300–317.
- (10) Liu, X.-Y.; Uberuaga, B. P.; Andersson, D. A.; Stanek, C. R.; Sickafus, K. E. Mechanism for transient migration of xenon in UO_2 . *Appl. Phys. Lett.* **2011**, *98*, 151902.
- (11) Thompson, A. E.; Wolverton, C. First-principles study of noble gas impurities and defects in UO_2 . *Phys. Rev. B* **2011**, *84*, 134111.
- (12) Thompson, A. E.; Wolverton, C. Pathway and Energetics of Xenon Migration in Uranium Dioxide. *Phys. Rev. B* **2013**, *87*, 104105.
- (13) Andersson, D. A.; Garcia, P.; Liu, X.-Y.; Pastore, G.; Tonks, M.; Millett, P.; Dorado, B.; Gaston, D. R.; Andrs, D.; Williamson, R. L.; et al. Atomistic modeling of intrinsic and radiation-enhanced fission gas (Xe) diffusion in UO_{2+x} : Implications for nuclear fuel performance modeling. *J. Nucl. Mater.* **2014**, *451*, 225–242.
- (14) Vathonne, E.; Andersson, D. A.; Freyss, M.; Perriot, R.; Cooper, M. W. D.; Stanek, C. R.; Bertolus, M. Determination of Krypton Diffusion Coefficients in Uranium Dioxide Using Atomic Scale Calculations. *Inorg. Chem.* **2017**, *56*, 125–137.
- (15) Perriot, R.; Matthews, C.; Cooper, M. W. D.; Uberuaga, B. P.; Stanek, C. R.; Andersson, D. A. Atomistic modeling of out-of-pile xenon diffusion by vacancy clusters in UO_2 . *J. Nucl. Mater.* **2019**, *520*, 96–109.
- (16) Rogozkin, B. D.; Stepennova, N. M.; Fedorov, Y. E.; Shishkov, M. G.; Kryukov, F. N.; Kuzmin, S. V.; Nikitin, O. N.; Belyaeva, A. V.; Zabudko, L. M. Results of $\text{U}_{0.55}\text{Pu}_{0.45}\text{N}$ and $\text{U}_{0.4}\text{Pu}_{0.6}\text{N}$ Mixed Mononitride Fuel Tests in a BOR-60 Reactor to Burnup 12% H.A. *At. Energy* **2011**, *110*, 412–429.
- (17) Klipfel, M.; Van Uffelen, P. Ab Initio Modelling of Volatile Fission Products in Uranium Mononitride. *J. Nucl. Mater.* **2012**, *422*, 137–142.
- (18) Claisse, A.; Klipfel, M.; Lindbom, N.; Freyss, M.; Olsson, P. GGA+U Study of Uranium Mononitride: A Comparison of the U-ramping and Occupation Matrix Schemes and Incorporation Energies of Fission Products. *J. Nucl. Mater.* **2016**, *478*, 119–124.
- (19) Claisse, A.; Schuler, T.; Lopes, D. A.; Olsson, P. Transport Properties in Dilute UN(X) Solid Solutions (X=Xe,Kr). *Phys. Rev. B* **2016**, *94*, 174302.
- (20) Zhang, Y.-J.; Lan, J.-H.; Wang, C.-Z.; Wu, Q.-Y.; Bo, T.; Chai, Z.-F.; Shi, W.-Q. Theoretical Investigation on Incorporation and Diffusion Properties of Xe in Uranium Mononitride. *J. Phys. Chem. C* **2015**, *119*, 5783–5789.
- (21) Lan, J.-H.; Zhao, Z.-C.; Wu, Q.; Zhao, Y.-L.; Chai, Z.-F.; Shi, W.-Q. First-principles DFT+U modeling of defect behaviors in anti-ferromagnetic uranium mononitride. *J. Appl. Phys.* **2013**, *114*, 223516.
- (22) Bocharov, D.; Gryaznov, D.; Zhukovskii, Y. F.; Kotomin, E. A. DFT Calculations of Point Defects on UN(001) Surface. *Surf. Sci.* **2011**, *605*, 396–400.
- (23) Fujimori, S.-i.; Ohkochi, T.; Okane, T.; Saitoh, Y.; Fujimori, A.; Yamagami, H.; Haga, Y.; Yamamoto, E.; Onuki, Y. Itinerant nature of U 5f states in uranium mononitride revealed by angle-resolved photoelectron spectroscopy. *Phys. Rev. B* **2012**, *86*, 235108.
- (24) Petit, L.; Svane, A.; Szotek, Z.; Temmerman, W. M.; Stocks, G. M. Ground-State Electronic Structure of Actinide Monocarbides and Mononitrides. *Phys. Rev. B* **2009**, *80*, 045124.
- (25) Wen, X.-D.; Martin, R. L.; Scuseria, G. E.; Rudin, S. P.; Batista, E. R. A Screened Hybrid DFT Study of Actinide Oxides, Nitrides, and Carbides. *J. Phys. Chem. C* **2013**, *117*, 13122–13128.
- (26) Norton, P. R.; Tapping, R. L.; Creber, D. K.; Buyers, W. J. L. Nature of the 5f electrons in uranium nitride: A photoelectron spectroscopic study of UN, U, UO_2 , ThN, and Th. *Phys. Rev. B* **1980**, *21*, 2572–2577.
- (27) Pukari, M.; Runevall, O.; Sandberg, N.; Wallenius, J. Vacancy formation and solid solubility in the U-Zr-N system. *J. Nucl. Mater.* **2010**, *406*, 351–355.
- (28) Kresse, G.; Hafner, J. Ab initio molecular dynamics for liquid metals. *Phys. Rev. B* **1993**, *47*, 558.
- (29) Kresse, G.; Furthmüller, J. Efficiency of Ab-Initio Total Energy Calculations for Metals and Semiconductors Using a Plane-wave Basis Set. *Comput. Mater. Sci.* **1996**, *6*, 15–50.
- (30) Kresse, G.; Furthmüller, J. Efficient iterative schemes for ab initio total-energy calculations using a plane-wave basis set. *Phys. Rev. B* **1996**, *54*, 11169.
- (31) Curry, N. A. An Investigation of the Magnetic Structure of Uranium Nitride by Neutron Diffraction. *Proc. Phys. Soc.* **1965**, *86*, 1193.
- (32) Perdew, J. P.; Wang, Y. Accurate and Simple Analytic Representation of the Electron-Gas Correlation Energy. *Phys. Rev. B* **1992**, *45*, 13244.
- (33) Perdew, J. P.; Burke, K.; Ernzerhof, M. Generalized Gradient Approximation Made Simple. *Phys. Rev. Lett.* **1996**, *77*, 3865.
- (34) Sun, J.; Ruzsinszky, A.; Perdew, J. P. Strongly Constrained and Appropriately Normed Semilocal Density Functional. *Phys. Rev. Lett.* **2015**, *115*, 036402.
- (35) Krukau, A. V.; Vydrov, O. A.; Izmaylov, A. F.; Scuseria, G. E. Influence of the Exchange Screening Parameter on the Performance of Screened Hybrid Functionals. *J. Chem. Phys.* **2006**, *125*, 224106.
- (36) Dudarev, S. L.; Botton, G. A.; Savrasov, S. Y.; Humphreys, C. J.; Sutton, A. P. Electron-Energy-Loss Spectra and the Structural Stability of Nickel Oxide: An LSDA+U Study. *Phys. Rev. B* **1998**, *57*, 1505.
- (37) Huang, G.-Y.; Juslin, N.; Wirth, B. D. First-Principles Study of Vacancy, Interstitial, Noble Gas Atom Interstitial and Vacancy Clusters in BCC-W. *Comput. Mater. Sci.* **2016**, *123*, 121–130.
- (38) Burr, P. A.; Cooper, M. W. D. Importance of Elastic Finite-Size Effects: Neutral Defects in Ionic Compounds. *Phys. Rev. B* **2017**, *96*, 094107.
- (39) Varvenne, C.; Bruneval, F.; Marinica, M.-C.; Clouet, E. Point defect modeling in materials: Coupling ab initio and elasticity approaches. *Phys. Rev. B* **2013**, *88*, 134102.
- (40) Havela, L.; Wastin, F.; Rebizant, J.; Gouder, T. Photoelectron Spectroscopy Study of PuN. *Phys. Rev. B* **2003**, *68*, 085101.
- (41) Shorikov, A. O.; Lukoyanov, A. V.; Korotin, M. A.; Anisimov, V. I. Magnetic State and Electronic Structure of the δ and α Phases of Metallic Pu and Its Compounds. *Phys. Rev. B* **2005**, *72*, 024458.
- (42) Gouder, T.; Havela, L.; Shick, A. B.; Huber, F.; Wastin, F.; Rebizant, J. Variability of 5f States in Plutonium Carbides. *J. Phys.: Condens. Matter* **2007**, *19*, 476201.
- (43) Atta-Fynn, R.; Ray, A. K. Density Functional Study of the Actinide Nitrides. *Phys. Rev. B* **2007**, *76*, 115101.
- (44) Ekholm, M.; Gambino, D.; Jönsson, H. J. M.; Tasnádi, F.; Alling, B.; Abrikosov, I. A. Assessing the SCAN Functional for Itinerant Electron Ferromagnets. *Phys. Rev. B* **2018**, *98*, 094413.
- (45) Okamoto, H. N-U (Nitrogen-Uranium). *J. Phase Equilib.* **1997**, *18*, 107.

- (46) Huang, G.-Y.; Pastore, G.; Wirth, B. D. First-Principles Study of Intrinsic Point Defects and Xe Impurities in Uranium Monocarbide. *J. Appl. Phys.* **2020**, *128*, 145102.
- (47) Andersson, D. A.; Liu, X.-Y.; Beeler, B.; Middleburgh, S. C.; Claisse, A.; Stanek, C. R. Density functional theory calculations of self- and Xe diffusion in U_3Si_2 . *J. Nucl. Mater.* **2019**, *515*, 312–325.
- (48) Kuksin, A. Y.; Starikov, S. V.; Smirnova, D. E.; Tseplyaev, V. I. The Diffusion of Point Defects in Uranium Mononitride: Combination of DFT and Atomistic Simulation with Novel Potential. *J. Alloys Compd.* **2016**, *658*, 385–394.

Incorporation of Kr and Xe in Uranium Mononitride; a Density Functional Theory Study

Lin Yang and Nikolas Kaltsoyannis*

Department of Chemistry, School of Natural Sciences, The University of Manchester, Oxford Road, Manchester M13 9PL

Supporting Information

Method for determining the chemical potential of U and N in UN. According to the phase diagram of UN, near-stoichiometric UN should be bound by U rich condition (in equilibrium with bulk U) and N rich condition (in equilibrium with U_2N_3). Then the chemical potential of U (μ_{U}) and N (μ_{N}) should follow the following equation:

$$E(\text{U}_x\text{N}_y) = x\mu_{\text{U}} + y\mu_{\text{N}}$$

in which $E(\text{U}_x\text{N}_y)$ is the total energy of U_xN_y phase. From the PW91 functional, the total energies of bulk α -U (U_4), UN (U_4N_4), and U_2N_3 are -44.60 eV, -88.58 eV, and -54.46 eV, respectively. Applying these values to the above equation, the calculated μ_{U} and μ_{N} are: $-11.98 \text{ eV} < \mu_{\text{U}} < -11.15 \text{ eV}$ and $-10.99 \text{ eV} < \mu_{\text{N}} < -10.17 \text{ eV}$.

Table S1. Cutoff energy convergence test.

Cutoff energy /eV	Total energy /eV
520	-88.5805
550	-88.5814
580	-88.5834
610	-88.5855
640	-88.5878

Table S2. Supercell size convergence test.

Cutoff energy /eV	Total energy /eV
$3 \times 3 \times 3$	-709.1991674
$4 \times 4 \times 4$	-709.2048496
$5 \times 5 \times 5$	-709.2142592

Table S3. Uncorrected defect formation energies (E_f) and the elastic field correction term (E_{el}) for AFM UN.

	E_f/eV			E_{el}/eV
	UN_{1-x}	UN	UN_{1+x}	
V_U	3.17	2.75	2.34	0.00
V_N	1.76	2.18	2.59	0.00
FP_N	4.92	4.92	4.92	0.04
SD bound	4.26	4.26	4.26	0.20
SD unbound	4.96	4.96	4.96	0.00

Table S4. Uncorrected defect formation energies (E_f) and the elastic field correction term (E_{el}) for FM UN.

	E_f/eV			E_{el}/eV
	UN_{1-x}	UN	UN_{1+x}	
V_U	3.43	3.01	2.60	0.00
V_N	1.90	2.31	2.72	0.00
FP_U	9.46	9.46	9.46	0.01
FP_N	5.04	5.04	5.04	0.00
SD bound	4.47	4.47	4.47	0.60
SD unbound	5.15	5.15	5.15	0.00

Table S5. N and U vacancy formation energies calculated vs N_2 molecule and U bulk ($E_f^{(1)}$), and isolated N and U atoms ($E_f^{(2)}$).

	$E_f^{(1)}/\text{eV}$			$E_f^{(2)}/\text{eV}$		
	VN	VU	Magnetic order	VN	VU	Magnetic order
Present work	4.42	3.17	AFM			
	4.56	3.43	FM			
Ref [1]	4.24	3.74	Spin-polarization	9.43	10.55	Spin-polarization
Ref [2]	4.42	3.22	FM	9.56	10.39	FM
Ref [3]				7.81	6.89	AFM
Ref [4]				9.4	9.1	Neglect spin-polarization

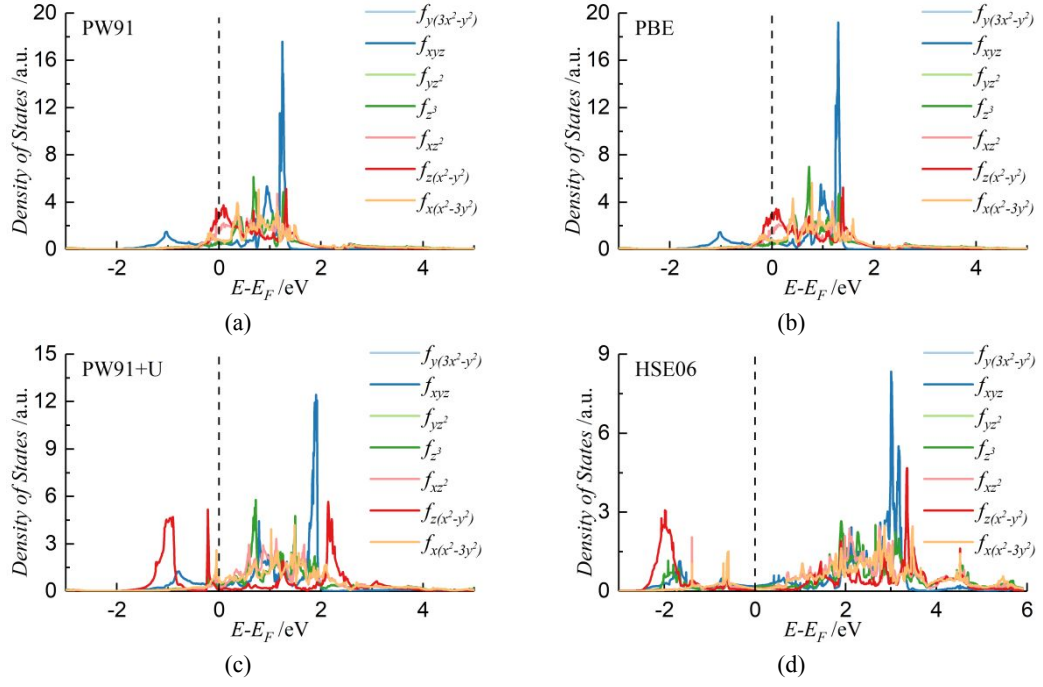


Figure S1. The partial density of states of the U f orbitals in AFM UN bulk obtained from PW91, PW91+U, PBE, and HSE06. Only the spin up states are shown as representation.

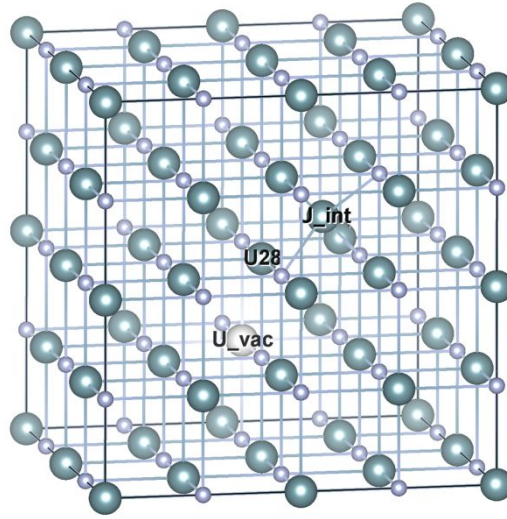


Figure S2. Unrelaxed UN supercell containing U Frenkel pair defect.

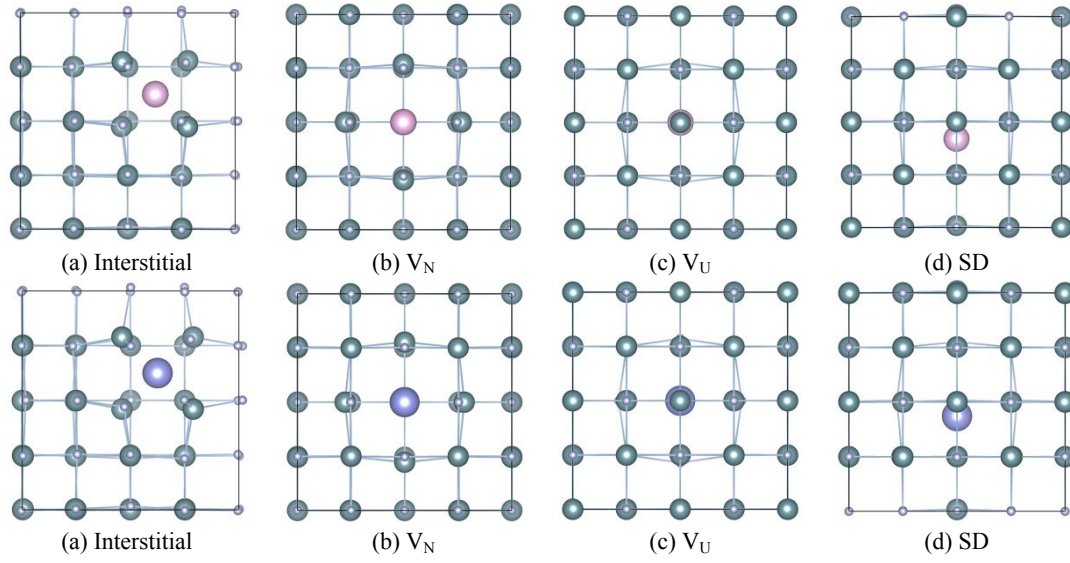


Figure S3. Relaxed structures of (a)-(d) Kr and (e)-(h) Xe in AFM UN supercell at different sites. The teal, grey, pink, and purple balls represent uranium, nitrogen, krypton, and xenon elements, respectively.

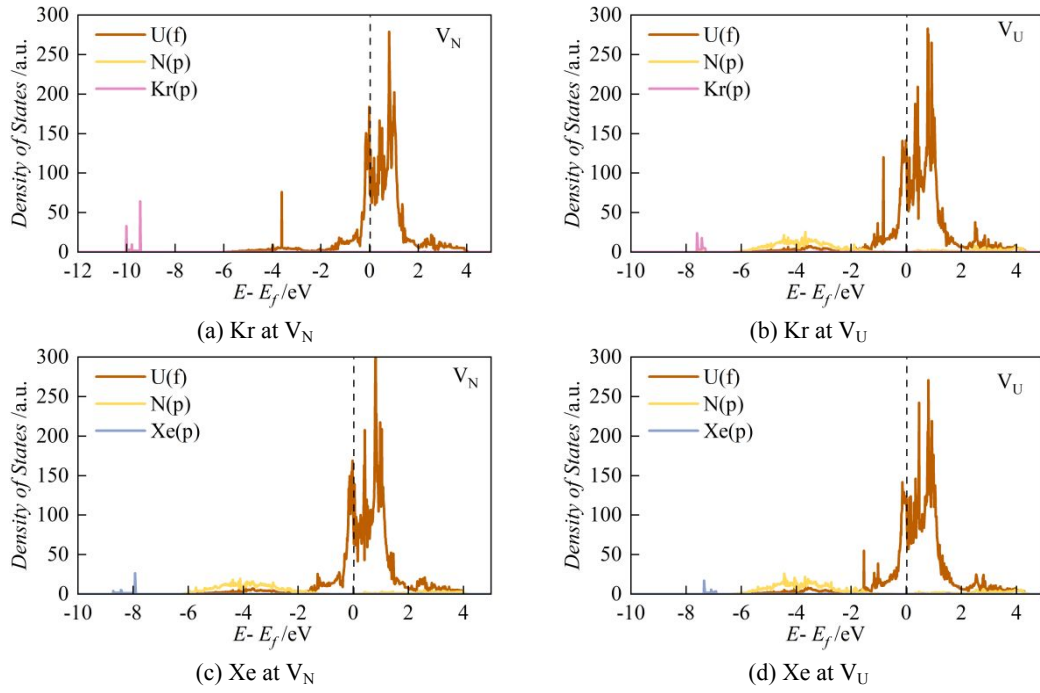


Figure S4. Density of states of the Kr and Xe incorporated UN supercell.

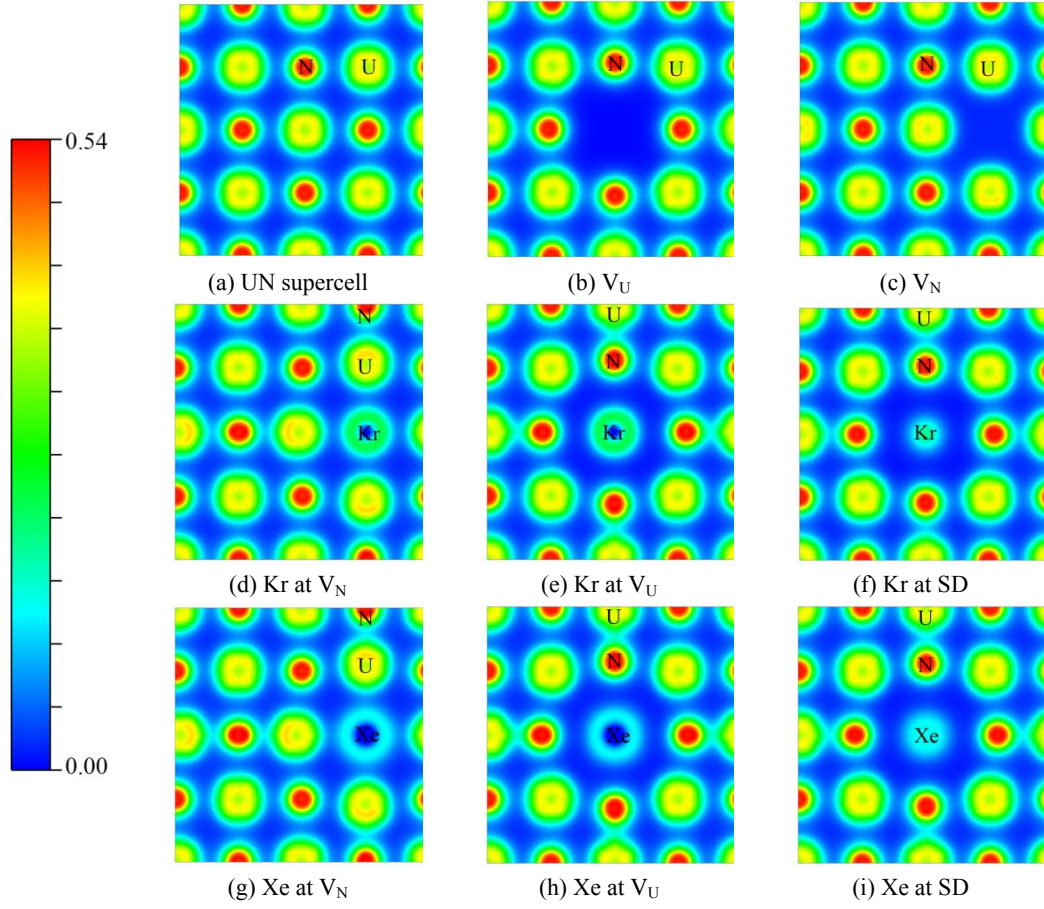


Figure S5. Charge density distribution (a.u.) of (001) surface for (a) U_N perfect supercell, (b) V_U and (c) V_N defect supercell, (d)-(f) Kr, and (g)-(i) Xe incorporated in AFM UN at different vacancy sites.

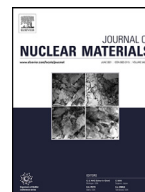
References

- (1) Klipfel, M.; Van Uffelen, P. Ab Initio Modelling of Volatile Fission Products in Uranium Mononitride. *J. Nucl. Mater.* **2012**, *422*, 137-142.
- (2) Bocharov, D.; Gryaznov, D.; Zhukovskii, Y. F.; Kotomin, E. A. DFT Calculations of Point Defects on UN(001) Surface. *Surf. Sci.* **2011**, *605*, 396-400.
- (3) Lan, J.-H.; Zhao, Z.-C.; Wu, Q.; Zhao, Y.-L.; Chai, Z.-F.; Shi, W.-Q. First-Principles DFT+U Modeling of Defect Behaviors in Anti-ferromagnetic Uranium Mononitride. *J. Appl. Phys.* **2013**, *114*, 223516.
- (4) Kotomin, E. A.; Grimes, R. W.; Mastrikov, Y.; Ashley, N. J. Atomic Scale DFT Simulations of Point Defects in Uranium Nitride. *J. Phys.: Condens. Matter* **2007**, *19*, 106208.

-Blank page-

4 Diffusion of Krypton and Xenon in Uranium Mononitride

This chapter is the author published article (Lin Yang and Nikolas Kaltsoyannis, Diffusion of Krypton and Xenon in Uranium Mononitride; a Density Functional Theory Study *J. Nucl. Mater.* 2022, 566, 153803, <https://doi.org/10.1016/j.jnucmat.2022.153803>), which has 10 pages in total. All work in this chapter was completed by myself under the supervision of Prof. Nikolas Kaltsoyannis.



Diffusion of krypton and xenon in uranium mononitride; a Density Functional Theory Study

Lin Yang, Nikolas Kaltsoyannis*

Department of Chemistry, School of Natural Sciences, The University of Manchester, Oxford Road, Manchester M13 9PL, England

ARTICLE INFO

Article history:

Received 12 January 2022

Revised 7 April 2022

Accepted 16 May 2022

Available online 18 May 2022

Keywords:

Uranium mononitride

Noble gas

Self-diffusion

Solute diffusion

Density Functional Theory

ABSTRACT

Uranium mononitride is a strong candidate for an advanced nuclear fuel. In this work we use density functional theory to model the diffusivity of matrix U atoms, as well as the noble gas (Ng) fission products Kr and Xe, at the atomic scale under three stoichiometric conditions (U-rich, stoichiometric, N-rich). U self-diffusion is found to be dependent on stoichiometry, being largest under N-rich conditions. The U formation entropy significantly affects the U self-diffusion coefficient, indicating that it is necessary to consider the vibrational properties of the system to accurately describe diffusion properties in UN. The calculated Kr and Xe diffusion coefficients from the U vacancy (V_U)-assisted mechanism are much larger than by interstitial mechanisms under the three stoichiometric conditions studied. The two mechanisms show opposite stoichiometric dependence, with the former increasing from U-rich to N-rich conditions and the latter decreasing. Kr moves significantly more quickly than Xe via the interstitial mechanism due to the larger atomic radius of the latter, while the effect of atomic size on the V_U -assisted mechanism is negligible, indicating similar diffusivity of Kr and Xe in UN. The good agreement with experiment of our calculated Xe monovacancy-assisted diffusion coefficient indicates that the monovacancy-assisted mechanism governs the Ng diffusion in UN, and supports the accuracy of our theoretical model.

© 2022 Elsevier B.V. All rights reserved.

1. Introduction

Nitride fuels such as UN are considered as ideal candidates for Generation IV nuclear reactors, especially lead-cooled fast reactors, due to their high metal density and melting temperature, excellent thermal conductivity, and good compatibility with lead coolant [1–3]. UN is also proposed as a potential replacement for UO_2 in light water reactors [4]. For the safe and efficient use of nitride fuels, it is important to have a comprehensive understanding of their properties, including the generation and migration of fission products in the fuel matrix.

During irradiation of uranium, the fission of uranium generates a large number of products, 15% of which are the noble gases (Ng) Xe and Kr in UO_2 [5]. These Ng atoms have low solubility in the fuel matrix, and may migrate in the fuel, form bubbles inside and on the boundary of the grains or escape to the fuel-clad gap, leading to fuel swelling and reduction in the thermal conductivity of the fuel rods [6]. In the fission gas evolution process, the first step is single atom diffusion in the grain to the intragranular bubbles or the grain boundaries. This bulk diffusion step is the slowest one, thus setting the timescale for fission gas release [7]. This

step has been experimentally well established for UO_2 by Turnbull et al. [8–10], who reported that intrinsic, radiation-enhanced, and athermal diffusion mechanisms govern the high temperature ($T > 1650$ K), intermediate temperature (1381 K $< T < 1650$ K), and low temperature ($T < 1381$ K) ranges, respectively. Using density functional theory (DFT) and empirical potential methods, the intrinsic and radiation-enhanced diffusion of Kr and Xe in non-stoichiometric UO_2 have been simulated, and the results obtained are well-matched with experiments [11–14], indicating the strong performance of these theoretical methods in predicting Ng diffusion properties.

By contrast to UO_2 , understanding of fission gas release in nitride fuels is rudimentary. Post-reactor studies using (U,Pu)N mixed fuel found relative yields of 18.6% and 19.4% of Kr and Xe, respectively, in the fuel-clad gap [15]. Tanaka et al. found that approximately 80% of fission gases were retained in the intragranular region of (U,Pu)N at burn-up of 4.3% FIMA in fast reactor JOYO [16]. Two published experimental studies give the Arrhenius diffusion laws for Xe in UN [17, 18], but there are no studies for Kr. The Arrhenius relationships from these two experiments are significantly different, and the stoichiometry of the UN samples used in the experiments is unclear. There are a few modeling studies of Ng behavior in UN, which mainly focus on their incorporation [19–22]. Our previous work studied the incorporation of Kr and Xe

* Corresponding author.

E-mail address: nikolas.kaltsoyannis@manchester.ac.uk (N. Kaltsoyannis).

in UN under different stoichiometric conditions, and a comprehensive comparison with other works was made [23]. Kocevski et al. compared the performance of various functionals and approaches in describing UN bulk properties and defect formation energies, concluding that the GGA approach is preferred over GGA+*U* [24]. For migration data, Zhang et al. calculated the Xe migration energy barriers of several pathways by DFT+*U*/CI-NEB methods and found that Xe is trapped in U vacancies (V_U) and is unable to move without the assistance of other U vacancies [21]. Kocevski et al. developed a new potential for the U-N-Xe system and calculated activation energies for Xe diffusion, finding that the V_U -assisted mechanism has the lowest activation energy [25]. Only two computed diffusion coefficient data are found, one by Starikov et al. using empirical potentials [26], and another one by Claisse et al. using the self-consistent mean field (SCMF) method [27]. Claisse et al. found Kr and Xe to have similar diffusivity, but their calculated Ng diffusion coefficient with equilibrium V_U concentration is significantly lower than the experiments. Starikov et al. studied only Xe, with the results in good agreement with the experiments and much larger than that reported by Claisse *et al.* Thus, more experiments and theoretical works are needed to construct a good fission gas release model in UN.

Based on the above considerations, in this work we systematically study the diffusion of Kr and Xe in UN using atomic scale calculations at the DFT level. Our previous work identified that GGA functionals are the most appropriate form of DFT to study UN and justified the use of ferromagnetic UN [23], which is also supported by Kocevski et al. [24]. Thus, all the calculations here are conducted in the DFT/PBE framework. The U self-diffusion coefficient is firstly calculated, and the contribution of defect formation entropy is studied. V_U -assisted Ng diffusion is then investigated by the five-frequency model, and the effect of non-stoichiometry is studied. Then, Ng diffusion by the interstitial mechanism is simulated. Finally, the total Ng diffusivity is compared with experiments to demonstrate the accuracy of our theoretical model, which we believe will contribute to understanding fission gas release in UN.

2. Computational and methodological details

2.1. Density functional theory calculations

All the DFT calculations in this work were conducted using the Vienna *ab initio* simulation package (VASP) version 6.1.2 [28–30]. The cutoff energy was set to 520 eV, as established by our previous work on UN [23]. The Methfessel-Paxton method was utilized to describe the orbital partial occupancy, with a smearing width of 0.2 eV. The Perdew-Burke-Ernzerhof (PBE) functional [31] was used to optimize geometries and calculate the entropy, which we have shown to perform well in describing the UN electronic structure [23]. The energies of the obtained structures were subsequently calculated using the vdW-DF functional (in which revPBE is used for the exchange part), a non-local correlation functional proposed by Dion *et al.* [32], to better account for the dispersion interactions.

The lattice parameter (4.868 Å) obtained from our previous calculation was used to construct the supercell [23]. Two types of supercell were used. The uranium vacancy self-diffusion was studied using a $2 \times 2 \times 2$ supercell (64 atoms). However, this size is not sufficient to study the vacancy-assisted Kr and Xe migration. Therefore, the supercell was expanded in the *c* direction, and $2 \times 2 \times 3$ (96 atoms) was used. To assess the effect of supercell expansion, we calculated the migration barrier of a U vacancy in the two supercells, obtaining values of 3.25 eV and 3.21 eV in $2 \times 2 \times 2$ and $2 \times 2 \times 3$, respectively, demonstrating the negligible impact of the supercell size.

A $3 \times 3 \times 3$ *k*-point mesh was used for the $2 \times 2 \times 2$ supercell while a $3 \times 3 \times 2$ mesh was used for the $2 \times 2 \times 3$ supercell. To avoid the

volume change induced by interaction between the defect and its periodic images [33], the volume and shape of the supercell were fixed and only the atomic positions allowed to relax during the geometry optimization. All the structures were optimized with the force convergence limit of 0.01 eV/Å.

The saddle-point structures and migration barriers were determined using the climbing image nudged elastic band (CI-NEB) method as implemented in the VTST package [34, 35] with the force convergence limit of 0.05 eV/Å. For the interstitial mechanism, 3 intermediate images were used due to the pronounced displacement of the matrix atoms. For the vacancy-assisted mechanism, convergence tests were conducted of images along the migration pathway required for CI-NEB calculation. The Kr elementary migration barriers (E_1 , see later) were 2.984 eV and 2.983 eV using 1 image and 3 images, respectively, indicating that a single image is sufficiently accurate, consistent with the literature [36]. Thus, 1 intermediate image was used for elementary migration barriers of the vacancy-assisted mechanism.

Vibrational defect entropies were calculated following the approach proposed by Mishin *et al.*, which is based on the normal mode vibrational frequencies [37]. In the harmonic approximation, the vibrational entropy of a crystalline solid is given by:

$$S = -k_B \sum_{n=1}^{3N-3} \ln \left(\frac{h\nu_n}{k_B T} \right) + (3N-3)k_B \quad (1)$$

in which N is the number of atoms in the system, and ν_n is the frequency of the n^{th} normal mode. Three zero frequency modes attributed to the translational invariance are neglected. In *ab initio* calculation, the normal mode frequencies can be calculated by diagonalizing the dynamical force matrix of the system. The PHONOPY software [38] was utilized for the frequency calculation using the finite differences method.

2.2. Diffusion coefficient calculations

2.2.1. U self-diffusion

The vacancy mechanism is accepted as the dominant mechanism for matrix and substitutional solute atom diffusion in metals. Considering the lower solution energy of Kr and Xe in U vacancy (V_U) than in N vacancy (V_U) [23], only V_U is considered as the assisting site in this work. Although Schottky defects (SD) are the most favorable site under U-rich conditions, V_U is the most favorable under N-rich and near-stoichiometric conditions. We here focus only on V_U , leaving diffusion via SD to a future study.

The self-diffusion coefficient of U by vacancy mechanism can be expressed as [39]:

$$D = \frac{1}{6} d^2 f_0 Z \omega_0 C_{V_U} \quad (2)$$

where d , f_0 , and Z are the jump distance of the nearest U atom to the vacancy, the correlation factor for self-diffusion, and the number of neighboring lattice sites around the U vacancy to jump to, respectively. Considering the FCC cubic structure of the U sublattice in UN, these variables are equal to $\frac{\sqrt{2}}{2}a$ (where a is the lattice parameter), 0.7815 [39–41], and 12, respectively. ω_0 is the vacancy jump rate, which can be expressed as following according to the method suggested by Vineyard based on statistical thermodynamics [42]:

$$\omega_0 = \nu_0 \exp \left(-\frac{E_v^m}{k_B T} \right) \quad (3)$$

in which k_B and T are the Boltzmann constant and temperature (K). The migration barrier E_v^m can be calculated by the CI-NEB method as introduced above. ν_0 is the attempt frequency, which

can be calculated by Eq. (4) as proposed by harmonic transition state theory [42]:

$$\nu_0 = \prod_{i=1}^{3N-3} \nu_i^{\text{IS}} / \prod_{i=1}^{3N-4} \nu_i^{\text{TS}} \quad (4)$$

The vibrational frequencies of the initial and transition states can be computed from the Hessian matrices. Due to the very high cost of full Hessian matrix construction, we approximated the full matrices by partial matrices including only the motion of the migrating atoms. Previous work shows that this approach captures the essence of the physics of self- and solute diffusion [43–45]. The calculations were conducted in VASP using the finite differences method with atom displacements of ± 0.015 Å.

C_{V_U} is the concentration of U vacancies, and we use the thermal equilibrium concentration in this work. C_{V_U} can be written as:

$$C_{V_U} = \exp\left(-\frac{G_{V_U}^f}{k_B T}\right) \quad (5)$$

in which $G_{V_U}^f$ is the Gibbs energy of U vacancy formation and can be calculated by:

$$G_{V_U}^f = E_{V_U}^f - TS_{V_U}^f \quad (6)$$

where $E_{V_U}^f$ and $S_{V_U}^f$ are the V_U formation energy and entropy, respectively. The calculation of formation entropy is similar to that of formation energy:

$$S_{V_U}^f = S_{\text{defect}} - S_{\text{perfect}} + S_u \quad (7)$$

where S_{defect} and S_{perfect} are the entropy of the UN supercell with and without U vacancies. S_u is the partial entropy of U atoms, which is estimated from U bulk. Combining Eqs. (2)–(7), the self-diffusion coefficient can be written as:

$$D = a^2 \nu_0 f_0 \exp\left(\frac{S_v^f}{k_B}\right) \exp\left(-\frac{E_v^f + E_v^m}{k_B T}\right) \quad (8)$$

By comparing Eq. (8) with the Arrhenius relation $D = D_0 \exp(-\frac{E_a}{k_B T})$, we can see that the self-diffusion coefficient is determined by two key variables: one is the frequency-related exponential prefactor $D_0 = a^2 \nu_0 f_0 \exp(\frac{S_v^f}{k_B})$, and the other is the activation energy $E_a = E_v^f + E_v^m$.

2.2.2. Kr and Xe diffusion through the monovacancy-assisted mechanism

Solute diffusion is more complicated than self-diffusion. In this work, only Ng diffusion in the uranium sublattice is considered. The probability to find a vacancy near the Ng atoms can be written as:

$$p = C_{V_U} \exp\left(\frac{E_B}{k_B T}\right) \quad (9)$$

in which E_B is the binding energy of Ng atom and V_U . As stated above, the thermal equilibrium C_{V_U} is used, which can be calculated using Eq. (5). Then like the self-diffusion coefficient, D of the vacancy-assisted mechanism can be expressed as:

$$D = a^2 \omega_2 f_2 p = a^2 \omega_2 f_2 \exp\left(\frac{S_v^f}{k_B}\right) \exp\left(-\frac{E_v^f + E_R - E_B}{k_B T}\right) \quad (10)$$

in which E_R is the reconfiguration energy, i.e. the Kr or Xe solution energy difference between that at the V_U site and the lowest energy site. ω_2 is the exchange rate of V_U -Ng pairs as shown below. f_2 is the correlation factor between two vacancy-solute exchanges, which reflects the dependence of two subsequent jumps of a solute atom. For FCC structure, this can be treated by the ‘five-frequency model’ proposed by Lidiard [46, 47], which assumes the

interaction and exchange limit between the solute and the nearest-neighbor sites. Five elementary exchange rates are involved in the five-frequency model, which are shown in Fig. 1 and represent:

ω_0 , exchange rate of V_U -U in the UN supercell without Kr or Xe;

ω_1 , exchange rate between the vacancy and the nearest uranium atoms around the Kr or Xe;

ω_2 , exchange rate of V_U -Ng pair;

ω_3 , dissociation rate of the V_U -Ng pair;

ω_4 , association rate of the V_U -Ng pair.

The rate of each elementary mechanism can be calculated by Eq. (3) with ν_0 and E_v^m being replaced by the attempt frequency (ν_i) and migration barrier (E_i) of each mechanism. ν_i is calculated by Eq. (4). It is worth noting that the difference in the energy barriers of V_U -Ng pair dissociation and association is the V_U -Ng pair binding energy E_B . A positive value represents binding of the V_U -Ng pair, and the larger the value, the stronger the interaction. Then f_2 can be calculated by the method proposed by Manning [48]:

$$f_2 = \frac{\omega_1 + 7F_3\omega_3/2}{\omega_2 + \omega_1 + 7F_3\omega_3/2} \quad (11)$$

where F_3 is the escape probability, representing the probability that the vacancy will not return to a neighbor site around the solute after a dissociation ω_3 jump. It has the numerical expression:

$$7F_3 = 7 - \frac{10\alpha^4 + 180.5\alpha^3 + 927\alpha^2 + 1341\alpha}{2\alpha^4 + 40.2\alpha^3 + 254\alpha^2 + 597\alpha + 436} \quad (12)$$

in which $\alpha = \omega_4/\omega_0$.

2.2.3. Kr and Xe diffusion through the interstitial mechanism

For the interstitial mechanism, the diffusion coefficient can be expressed as:

$$D = \frac{1}{6} d_{\text{int}}^2 \omega_{\text{int}} f_{\text{int}} \quad (13)$$

in which d_{int} is the jump distance of the solute atom from one interstitial site to another, and is equal to $\frac{1}{2}a$ in UN. f_{int} is the correlation factor for the interstitial mechanism, which is equal to 1 if the interstitial solute concentration is low enough. The interstitial jump rate ω_{int} has a similar form to Eq. (3) with ν_0 and E_v^m being replaced by the attempt frequency ν_{int} and migration barrier E_{int}^m , with ν_{int} being calculated by Eq. (4). Then the interstitial diffusion coefficient at low solute concentration can be written as:

$$D = \frac{1}{24} a^2 \nu_{\text{int}} \exp\left(-\frac{E_{\text{int}} + E_R}{k_B T}\right) \quad (14)$$

3. Results

3.1. Uranium self-diffusion by the vacancy mechanism

As introduced in Section 2.2, the U self-diffusion coefficient by the vacancy mechanism is determined by the activation energy and prefactor, with the former being the sum of vacancy formation energy and migration energy. The calculated energy terms from the PBE and vdW-DF functionals are listed in Table 1. As reported in the literature [23, 24], the uranium vacancy formation energy was found to vary under different stoichiometric conditions and depends on the uranium chemical potential μ_U . The range of μ_U calculated by the vdW-DF functional is 1.28 eV, close to the 0.83 eV and 1.53 eV obtained by PW91 [23] and PBE+U [24], but still much smaller than the 7.59 eV for UO_2 [12]. This is consistent with the reported narrow stoichiometric range of UN [49], which indicates the UN can maintain a slight non-stoichiometry which can be expressed as $\text{UN}_{1\pm x}$ with the $x = 0.11$.

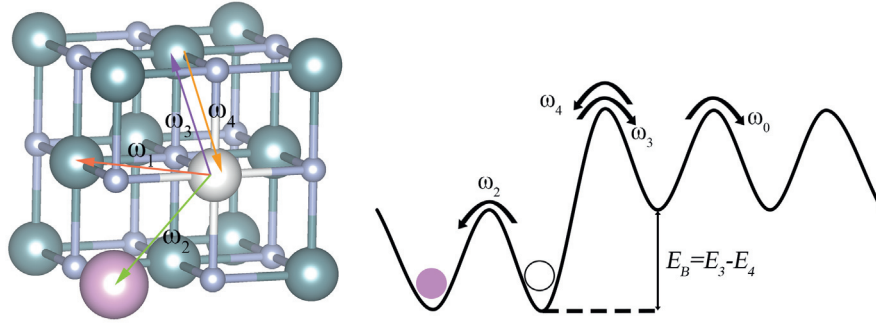


Fig. 1. Schematic of the five-frequency model. The teal, gray, purple, and white balls represent uranium, nitrogen, krypton, and uranium vacancy sites, respectively. (For interpretation of the references to colour in this figure legend, the reader is referred to the web version of this article.)

Table 1

Calculated vacancy formation energy (E_v^f), migration energy (E_v^m), and activation energy (E_a), all in eV, calculated by vdW-DF and PBE functionals (in parentheses) for the uranium self-diffusion under U-rich (UN_{1-x}), near-stoichiometric (UN), and N-rich (UN_{1+x}) conditions.

	E_v^f	E_v^m	E_a
UN_{1-x}	2.97 (3.46)	3.24 (3.21)	6.21 (6.67)
UN	2.33 (3.05)	3.24 (3.21)	5.57 (6.26)
UN_{1+x}	1.69 (2.63)	3.24 (3.21)	4.93 (5.84)

The PBE-calculated E_v^f are very close to the values of 3.43 eV, 3.01 eV, and 2.60 eV from U-rich (UN_{1-x}) to N-rich (UN_{1+x}) conditions reported in our previous work [23] using the PW91 functional, as well as the 3.66 eV and 2.09 eV under U-rich and N-rich conditions reported by Kocovski et al. using PBE+U [24]. From the vdW-DF functional, the calculated E_v^f are smaller, with the difference from the GGA values increasing from U-rich to N-rich condition. The calculated V_U migration barrier from vdW-DF is slightly larger than the value obtained by PBE, and within the range 3.10–3.52 eV reported in other work using DFT or empirical potential methods [25, 27]. Due to the stoichiometry-dependence of E_v^f , the activation energy varies between the three stoichiometric conditions, decreasing from U-rich to N-rich, the trend also reported for self-diffusion in UO_2 [50].

It can be seen from Eq. (8) that the prefactor depends on two parameters, the attempt frequency ν_0 and the defect formation entropy S_v^f , both of which are determined by the vibrational properties of the supercell. ν_0 is calculated to be $9.86 \times 10^{12} \text{ s}^{-1}$, which is within the range of self-diffusion attempt frequencies in FCC metals and U-based fuels [36, 51–53]. The formation entropy is explicitly calculated using Eqs. (1) and (7) and is shown in Fig. 2. We can see that S_v^f is around 5–6 k_B at 500–2000 K, consistent with the 6 k_B estimated by Starikov et al. [26]. A mid-range value of 5.5 k_B was adopted. To minimize computational cost, other work usually replaces the vacancy formation Gibbs free energy by the formation enthalpy, neglecting the entropy [51, 54–56], which can generate reasonable results when the vacancy formation entropy is negligible. However, our results suggest such an approximation is unsuitable for UN, in which the V_U formation entropy is significant.

Using the above activation energy and prefactor, the U self-diffusion coefficients under three stoichiometric conditions are calculated and shown in Fig. 3. To study the effect of entropy on the diffusion coefficient, the results using $S_v^f = 0$ are also shown. To estimate the accuracy of our modeling, we compare our results with experiment. Two experimental datasets were found [57, 58], but they are contradictory. Although a pronounced dependence on N_2 pressure ($p(N_2)$) was reported by both works, Exp [1] [57] found

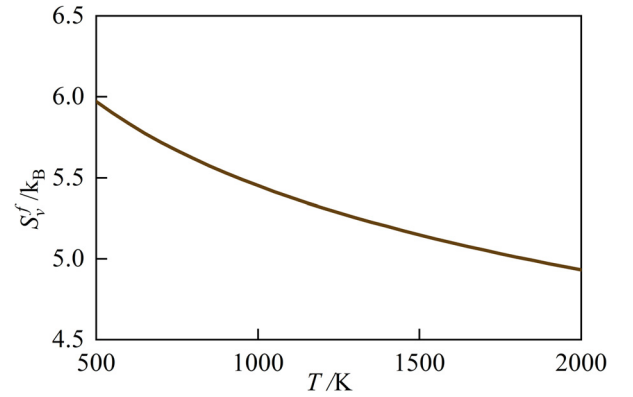


Fig. 2. DFT/PBE calculated uranium vacancy formation entropy in UN as a function of temperature.

that D_U is independent of temperature while Exp [2] [58] found the opposite. Furthermore, the diffusion coefficient from Exp [2] is about 100 times lower than that from Exp [1] (Fig. 3). Another simulation result reported by Starikov et al. using empirical interatomic potentials [26] is also plotted for comparison (labelled Cal).

It can be seen from Fig. 3(a) that the V_U diffusivity shows high stoichiometric dependence, with the largest value under the N-rich condition. This is as expected given the lowest activation energy under N-rich condition (Table 1). Our calculated values agree with both experiments at the high-temperature range better than the Cal data do. As shown in Fig. 3(b), the result for the N-rich condition matches Exp [1] best, which is consistent with the experimental condition in which hyperstoichiometric UN (UN_{1+x}) was used. Neglecting defect formation entropy significantly underestimates the diffusion coefficient, further indicating the importance of the vibrational properties of the system. The result for the U-rich condition agrees well with Exp [2], indicating that the contradiction between the two experiments might be due to the use of different non-stoichiometric UN samples. It is worth emphasizing that the experimental U diffusion coefficient may arise from multiple mechanisms, such as U vacancy, U interstitial, and U antisite, while our calculations considered only the U vacancy mechanism. Starikov et al. considered all the above contributions, while the U self-diffusion coefficient was overestimated [26]. The excellent agreement between our results and experiment indicates that the V_U mechanism is the dominant one for U self-diffusion in UN.

Fig. 3(a) shows that the slope of Exp [1] is very flat, indicating near temperature independence. According to Eq. (8), the slope of $\ln(D)$ depends on the activation energy, which is 0.69 eV, 5.01, and 3.38 eV for Exp [1], Exp [2], and Cal, respectively. Our calculated value (Table 1) is in the same order of magnitude as the Cal,

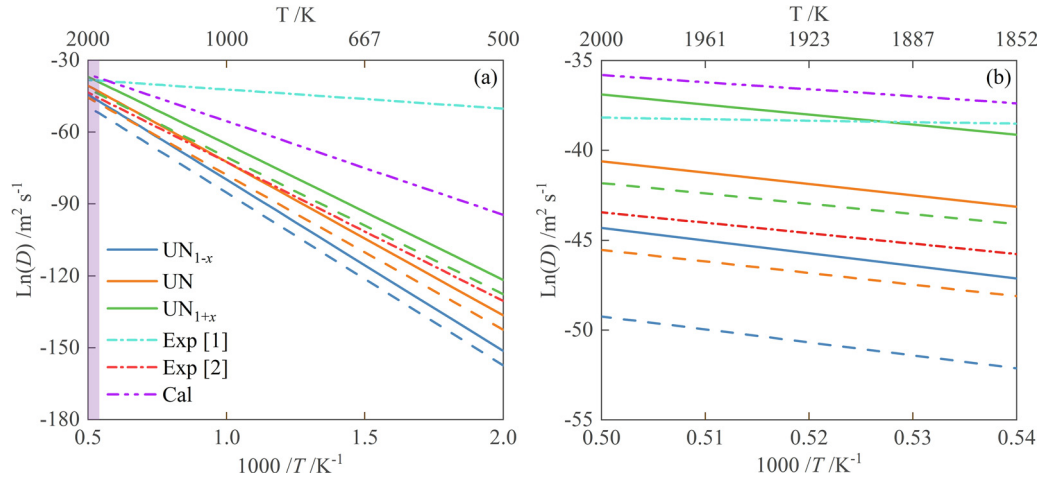


Fig. 3. (a) Calculated uranium self-diffusion coefficient in UN as a function of temperature under three stoichiometric conditions. The results with and without *ab initio* vacancy formation entropy are plotted in solid and dashed line, respectively. Exp [1] [57] and Exp [2] [58] were at N₂ pressure of 0.5 atm, and 1 atm, respectively. Exp [1] was conducted over the temperature range 1873–2133 K (purple area in (a)). The Cal line is the simulation results reported by Starikov et al. at N₂ pressure of 0.5 atm [26]. Diffusion coefficients at 1850–2000 K are zoomed in (b). (For interpretation of the references to colour in this figure legend, the reader is referred to the web version of this article.)

Table 2

Energy barrier (E_i / eV) and attempt frequency (ν_i / s⁻¹) for each elementary mechanism involved in the V_U-assisted Kr or Xe diffusion obtained from the vdW-DF and PBE functionals (in parentheses). The binding energy (E_B) of V_U-Ng (Ng = Kr or Xe) pairs is also listed.

	Kr	Xe		Kr	Xe
E_0	3.24 (3.21)	3.24 (3.21)	ν_0	9.86×10^{12}	9.86×10^{12}
E_1	3.28 (2.98)	3.29 (3.00)	ν_1	3.17×10^{12}	3.23×10^{12}
E_2	0.78 (0.72)	1.16 (1.12)	ν_2	2.76×10^{12}	2.03×10^{12}
E_3	3.91 (3.98)	3.99 (4.06)	ν_3	2.76×10^{13}	2.57×10^{13}
E_4	2.96 (2.82)	3.09 (2.95)	ν_4	1.56×10^{13}	1.39×10^{13}
E_B	0.95 (1.16)	0.90 (1.11)			

and very close to Exp [2], but much higher than Exp [1]. We suggest that 0.69 eV is suspect not only because it is out of step with other UN data, but also because it is significantly lower than the experimental range of 2.6–7.8 eV for U self-diffusion in UO₂ [59], as well as the experimental range of 2.6–5.3 eV for Co and Fe self-diffusion [36, 60]. We would welcome further experiments on this subject.

Overall, the very good agreement between our calculated U self-diffusion coefficient and experiment at high temperature indicates the accuracy of our modeling.

3.2. Vacancy-assisted diffusion of Ng (Ng = Kr, Xe)

As introduced in Section 2.2, the diffusion coefficient of the vacancy-assisted mechanism depends on the rate of each elementary jump, which themselves are decided by the elementary migration barrier and attempt frequency. The calculated energy barrier and attempt frequency are listed in Table 2, with the former being close to the results reported by Kocevski et al. [25], Claisse et al. [27], and Zhang et al. [21]. The similar E_i obtained from the PBE and vdW-DF functionals indicate that dispersion effects are negligible.

The individual contributions from the five elementary jumps are not equally important in determining solute diffusivity. As shown in Fig. 1, the ω_2 jump, *i.e.* the vacancy-solute exchange, directly contributes to solute migration. Its energy barrier is significantly lower than the others (Table 2), indicating the higher mobility of Ng in UN than the U matrix atom. E_0 and E_1 are close to each other, which correspond to the energy barriers of V_U-U ex-

change with and without the solute atoms. This reflects the limited effect of Kr and Xe on the V_U-U exchange energy barrier, which is different from in UO₂ [12]. However, ν_1 is much lower than ν_0 , indicating the significant effect of solute atom on the vibrational properties of the system. Moreover, the positive binding energy indicates that it is always favorable for a uranium vacancy to be close to the Kr and Xe atom in its trap site, which has a positive effect on Ng diffusion by the V_U-assisted mechanism. The E_b of 0.95 eV and 0.90 eV for Xe- and Kr-V_U are close to the 0.90 eV and 0.74 eV reported by Claisse et al. using the PBE+*U* method [27], while Kocevski et al. obtained negative Xe-V_U binding (−0.465 eV) using empirical potentials, which they attributed to the simplification of atomic interactions [25].

Comparison of E_i for Kr and Xe reveals that they are similar (except for E_2), and have the same trend of $E_2 \ll E_4 < E_0 \approx E_1 \ll E_3$. The energy barrier for Xe-V_U exchange is much higher than that of Kr-V_U exchange due to the larger atomic radius of the former. The effect of solute size on matrix U atoms is very limited.

The rates of each elementary mechanism were calculated using the above energy barriers and attempt frequencies. Fig. 4 shows that the rates for both Kr and Xe follow the same order: $\omega_2 \gg \omega_4 > \omega_0 \approx \omega_1 \gg \omega_3$, which is the same as that obtained from the energy barriers although the attempt frequencies lie in a wide range of 2.03×10^{12} to 1.56×10^{13} s⁻¹. Significant difference between Kr and Xe is found only in ω_2 , further demonstrating the effect of solute atomic size on the V_U-solute exchange jump. According to the ω_i order, the correlation factor (Eq. (11)) can be approximated as $f_2 = \omega_1/\omega_2$. Applying this simplified f_2 to Eq. (10), the V_U-assisted Kr and Xe diffusion coefficient is:

$$D = a^2 \nu_1 \exp\left(\frac{S_v^f}{k_B T}\right) \exp\left(-\frac{E_1 + E_v^f + E_R - E_B}{k_B T}\right) \quad (15)$$

As with U self-diffusion, the solute diffusion coefficient through the V_U-assisted mechanism depends on two key parameters: the prefactor $D_0 = a^2 \nu_1 \exp(\frac{S_v^f}{k_B T})$ and activation energy $E_a = E_1 + E_v^f + E_R - E_B$. We summarize in Table 3 the data needed to calculate the activation energy. Due to the stoichiometry dependence of the V_U formation and Ng reconfiguration energy, the activation energy varies under the three stoichiometric conditions considered. Due to the decreasing formation energy of U vacancies from U-rich to N-rich conditions, the activation energies for both Kr and Xe decrease from UN_{1-x} to UN_{1+x}, similar to the trend reported for UO₂ and

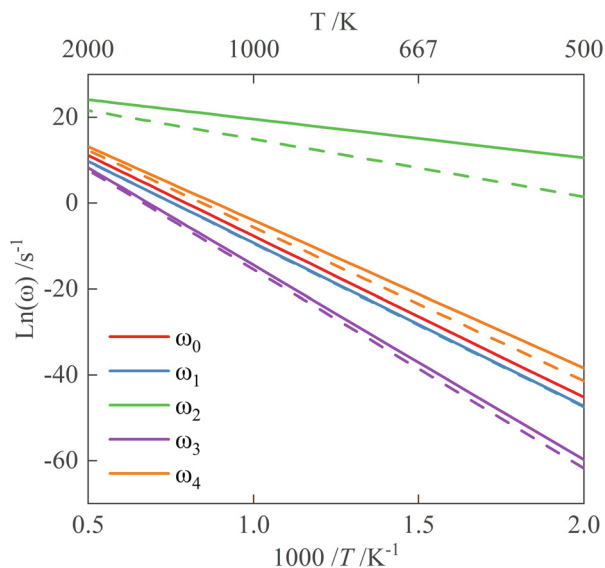


Fig. 4. Rates of each elementary mechanism for Kr (solid line) and Xe (dashed line) diffusion in UN by the V_U -assisted mechanism, as a function of temperature.

Table 3

Energy terms (eV) needed to calculate the activation energy of the vacancy-assisted Kr and Xe diffusion coefficient under different stoichiometric conditions, obtained with the vdW-DF functional.

	Stoichiometry	Kr	Xe
E_B		0.95	0.90
E_1		3.28	3.29
E_v^f	UN _{1-x}	2.97	2.97
	UN	2.33	2.33
	UN _{1+x}	1.69	1.69
	UN _{1-x}	0.32	0.40
E_R	UN	0.00	0.00
	UN _{1+x}	0.00	0.00
	UN _{1-x}	5.62	5.75
E_a	UN	4.66	4.71
	UN _{1+x}	4.02	4.07

U_3Si_2 [11, 12, 52]. The activation energies of Xe are slightly larger than those of Kr, but the differences are very small, indicating the limited effect of atomic size on vacancy-assisted Ng diffusion. The positive reconfiguration energies of 0.32 eV and 0.40 eV calculated by the vdW-DF functional under U-rich conditions for Kr and Xe indicate that V_U is not the most stable trap site for Ng in these circumstances. According to our previous work [23], the Schottky defect is the most stable trap site for Kr and Xe in UN_{1-x}, with reconfiguration energies (0.26 eV and 0.38 eV) close to the PW91 functional.

The diffusion coefficients for the vacancy-assisted mechanism calculated by Eq. (15) are shown in Fig. 5. It can be seen that the diffusivity of Kr and Xe is governed by both non-stoichiometry and temperature, with the latter being the intrinsic characteristic of thermal-induced diffusion. Considering the non-stoichiometry, both Kr and Xe have the largest diffusion coefficient under the N-rich condition due to the lowest activation energy in UN_{1+x}. The diffusion coefficient decreases from N-rich to U-rich conditions, the same trend as activation energy. By comparing the diffusivities of Kr and Xe, we can see the diffusion coefficient of Kr is slightly larger than that of Xe. Similar to U self-diffusion, including the V_U formation entropy brings the calculated Kr and Xe diffusion coefficients significantly closer to the experimental data (the experimen-

Table 4

Energy terms (eV) needed to calculate the activation energy of the Kr and Xe interstitial diffusion mechanism under different stoichiometric conditions. The values are obtained using the vdW-DF functional.

	Non-stoichiometry	Kr	Xe
E_{int}		0.29	0.27
E_R	UN _{1-x}	7.32	8.97
	UN	7.63	9.22
	UN _{1+x}	8.27	9.86
E_a	UN _{1-x}	7.61	9.24
	UN	7.92	9.49
	UN _{1+x}	8.56	10.13

tal results are plotted in Fig. 7), further illustrating the importance of the vibrational properties of the system on solute diffusion.

3.3. Interstitial diffusion of Ng (Ng = Kr, Xe)

The calculated activation energy ($E_a = E_{int} + E_R$) of the interstitial mechanism is given in Table 4. The migration barriers (E_{int}) of Kr and Xe are close to one another, with the values being significantly lower than the V_U -Ng exchange energy barrier (E_2) in the monovacancy-assisted mechanism (Table 3). This indicates only weak interaction between interstitial Kr and Xe and the matrix atoms, which is consistent with the low Bader charge on the interstitial Ng [21, 23]. The calculated value of 0.27 eV for Xe is much smaller than the 1.5 eV reported by Zhang et al. [21], possibly due to the different theoretical approach used in their work (PBE + U), while our result is close to the 0.307 eV of Xe-U dumbbell interstitial migration energy reported by Kocovski et al. using empirical potentials [25].

Due to the large solution energy of Kr and Xe at the interstitial trap site, the reconfiguration energies are significant, leading to the pronounced activation energies. Opposite to the activation energy of the vacancy-assisted mechanism, E_a of the interstitial mechanism increases from U-rich to N-rich conditions, consistent with the trend of Kr in UO_2 [12]. The values for Xe are much higher than that for Kr, different from the vacancy-assisted mechanism, indicating the significant effect of atomic size on the interstitial mechanism. The calculated 9.49 eV for Xe interstitial diffusion is close to the 8.685 eV reported by Kocovski et al. using empirical potentials for Xe-U dumbbell interstitials, with the difference being attributed to the different interstitial configuration and theoretical method [25].

The attempt frequencies are calculated to be $8.75 \times 10^{12} s^{-1}$ and $1.16 \times 10^{12} s^{-1}$ for Kr and Xe diffusion, respectively. Based on the above energies and frequencies, the interstitial diffusion coefficients are calculated by Eq. (14). As shown in Fig. 6, the diffusion coefficients of the interstitial mechanism are much lower than those of the vacancy-assisted mechanism (Fig. 5) under the three stoichiometric conditions, indicating that the vacancy-assisted mechanism is the dominant one for Kr and Xe diffusion in UN. This is different from what Vathonne et al. found in UO_2 under very U-rich conditions, where the interstitial mechanism is the most favorable [12]. Under near-stoichiometric and O-rich conditions, the diffusivity via interstitials is 10–20 orders of magnitude lower than that by vacancy, which is similar to our results. Another difference between interstitial and vacancy-assisted mechanisms lies in the stoichiometric dependence, with the diffusion coefficient of the former decreasing from U-rich to N-rich conditions, while the latter is opposite.

Comparison of the diffusivity of Kr and Xe shows that Kr moves much more quickly than Xe under the three stoichiometric condi-

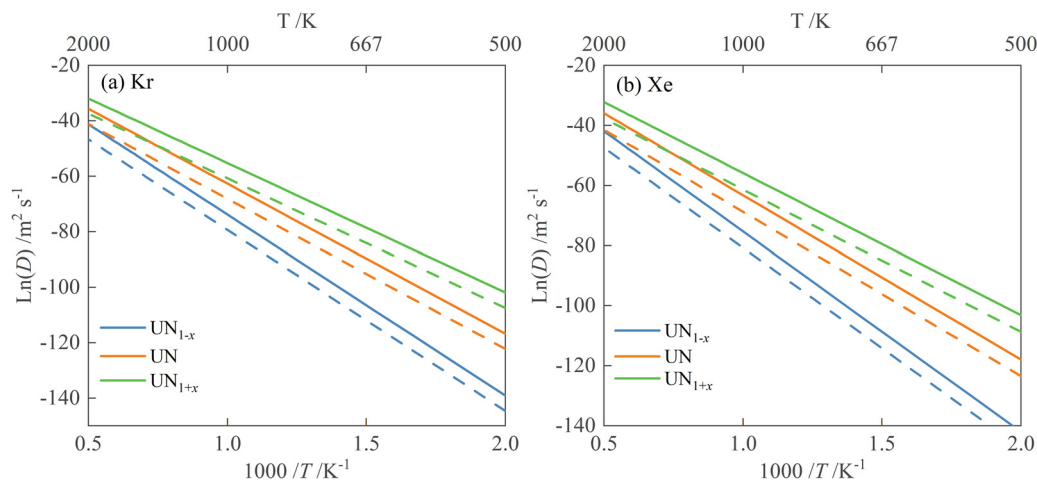


Fig. 5. Diffusion coefficient as a function of temperature for the V_U -assisted mechanism of (a) Kr and (b) Xe in UN under three stoichiometric conditions. The results with and without *ab initio* vacancy formation entropy are plotted in solid and dashed line, respectively.

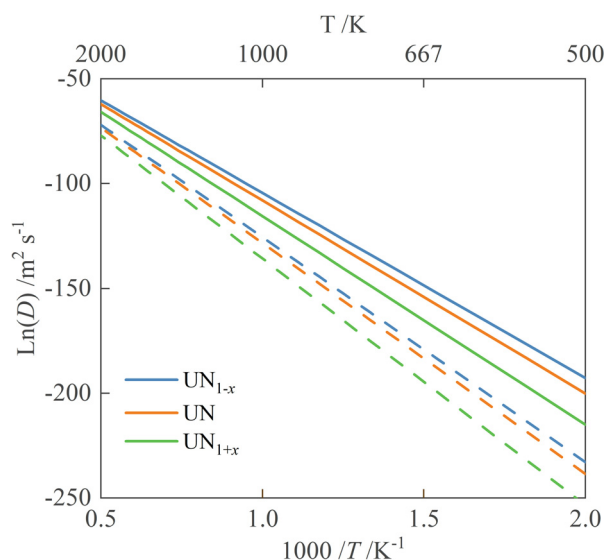


Fig. 6. Diffusion coefficient as a function of temperature for the interstitial mechanism for Kr (solid line) and Xe (dashed line) in UN, under three stoichiometric conditions.

tions studied, which can be attributed to the smaller reconfiguration energy induced by the smaller atomic size of Kr.

4. Discussion

Comparison between our simulated results and the two available Xe experimental datasets [17, 18] over the temperature range of the latter is made in Fig. 7. Although the experimental Xe diffusion coefficient will have a variety of contributing mechanisms, given the present dominance of the V_U -assisted mechanism, we use only that process in the construction of our data. As shown in Eq. (9) and (10), the diffusion coefficient is proportional to the vacancy concentration. The thermal equilibrium C_{V_U} under near-stoichiometric conditions lies in the range 10^{-4} to 10^{-7} , which increases with increasing temperature (Eq. (5)). To study the effect of C_{V_U} , the diffusion coefficients for higher C_{V_U} of 10^{-3} and 10^{-2} are also plotted. For comparison, we plot the simulated Xe diffusion coefficient in UN reported by Starikov et al. (Cal [1]) [26] and Claisse et al. (Cal [2]) [27] using the empirical potential and the self-consistent mean field method, respectively. Our sim-

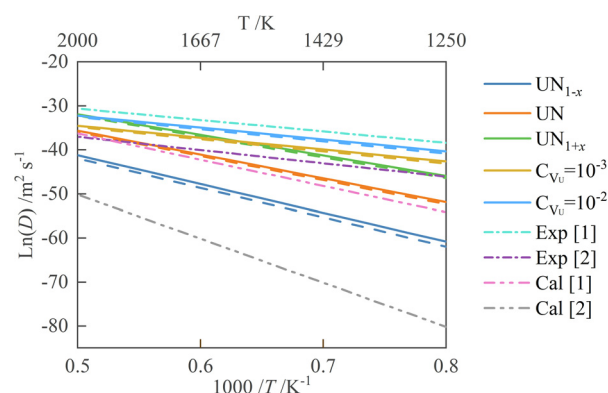


Fig. 7. Calculated diffusion coefficient of Kr (solid line) and Xe (dashed line) in UN as a function of temperature for thermal equilibrium U vacancy concentration under three stoichiometric conditions. The diffusion coefficients for various U vacancy concentrations (C_{V_U}) under near-stoichiometric conditions are plotted to illustrate the effect of vacancy concentration. The experimental temperature ranges for Exp [1] [17] and Exp [2] [18] are 1573–2673 K and 1273–1873 K, respectively. Diffusion coefficient equations were not reported for Cal [1] [26] and Cal [2] [27], thus the lines were fitted from the reported data. Cal [1], Cal [2] and experimental data refer to Xe diffusion only.

ulated results agree well with experiment, again indicating that the monovacancy-assisted mechanism is the dominant one for Ng diffusion in UN. Both the Kr and Xe diffusivities are dependent on stoichiometry, but to a smaller extent than in UO_2 [11, 12], consistent with the narrower nonstoichiometric range of UN [49]. The diffusion coefficient increases as the vacancy concentration increases.

The diffusivity relations corresponding to Fig. 7 are summarized in Table 5. The calculated activation energies for thermal equilibrium C_{V_U} are larger than those from experiments, leading to the steeper slopes of the calculated lines in Fig. 7, although our results are close to the 5.12 eV reported by Starikov et al. [26] for near-stoichiometric UN. The activation energies for higher C_{V_U} are close to the experiments. As shown in Eq. (8), the activation energy for equilibrium C_{V_U} depends on the vacancy formation energy, reconfiguration energy, migration energy barrier and vacancy-solute binding energy. For fixed C_{V_U} , the E_b^i term, which is the key parameter for calculating the vacancy concentration, is omitted. Thus, the significant overestimation of E_a for equilibrium C_{V_U} could be attributed to the overestimation of vacancy formation energy. The inability of DFT to accurately describe vacancies in metals has been

Table 5

Diffusion coefficient relations of Kr and Xe in UN under the three stoichiometric conditions corresponding to Fig. 7. The units of D , k_B , and T are $\text{m}^2 \text{s}^{-1}$, eV K^{-1} , and K , respectively.

	Kr	Xe	Vacancy concentration in our simulation, temperature range for Exp, or method for Cal
UN _{1-x}	$D = 2 \times 10^{-4} \exp(-\frac{5.62}{k_B T})$	$D = 2 \times 10^{-4} \exp(-\frac{5.75}{k_B T})$	Thermal equilibrium C_{V_U}
UN	$D = 2 \times 10^{-4} \exp(-\frac{4.66}{k_B T})$	$D = 2 \times 10^{-4} \exp(-\frac{4.71}{k_B T})$	Thermal equilibrium C_{V_U}
UN _{1+x}	$D = 2 \times 10^{-4} \exp(-\frac{4.02}{k_B T})$	$D = 2 \times 10^{-4} \exp(-\frac{4.07}{k_B T})$	Thermal equilibrium C_{V_U}
UN	$D = 8 \times 10^{-10} \exp(-\frac{2.33}{k_B T})$	$D = 8 \times 10^{-10} \exp(-\frac{2.38}{k_B T})$	$C_{V_U} = 10^{-3}$
UN	$D = 8 \times 10^{-9} \exp(-\frac{2.33}{k_B T})$	$D = 8 \times 10^{-9} \exp(-\frac{2.33}{k_B T})$	$C_{V_U} = 10^{-2}$
Cal [1]		$D = 1.4 \times 10^{-3} \exp(-\frac{5.12}{k_B T})$	Empirical potentials [26]
Cal [2]		$D = 8.67 \times 10^{-1} \exp(-\frac{8.62}{k_B T})$	Self-consistent mean field method [27]
Exp [1]		$D = 2.05 \times 10^{-8} \exp(-\frac{2.60}{k_B T})$	1573–2673 K [17]
Exp [2]		$D = 3 \times 10^{-10} \exp(-\frac{2.60}{k_B T})$	1273–1873 K [18]

well studied [61, 62]. Vacancies are created by the removal of an atom from the bulk, resulting in a small internal surface in the metal [63]. Inaccurate description of the electronic states at these surfaces leads to discrepancies between calculated and experimental vacancy formation energy in metals, e.g. 1.71 eV (calculated) [64] vs 1.34 eV (experiment) [65] for V_{Co} in FCC Co. It is also worth noting that the experimental activation energy was indirectly determined by measuring the Xe release fraction and fitting the diffusion coefficient, so arguably the difference between experiment and simulation is not unexpected.

Table 5 also shows that our calculated prefactor for thermal equilibrium C_{V_U} is several orders of magnitude higher than the experimental values, though close to Cal [1]. As stated in Section 2.2, our attempt frequency calculations are limited to the moving atoms only and the harmonic approximation is used for phonon calculation. Ho et al. found that although the attempt frequencies for Al vacancy diffusion obtained from the moving atom-only approach agree well with the literature, a well-converged value is obtained when 12 atoms are included, differing by a factor of about 1.6 from the value obtained from the moving atom only [44]. Glensk et al. reported the significance of anharmonic contribution to Al and Cu vacancy formation entropy [66]. Thus, these approximations do introduce uncertainties into the results. The significantly different prefactors from the two experiments indicate the difficulty of accurately describing the vibrational properties of the system. Large discrepancy between calculated and experimental prefactors has also been reported for Kr and Xe diffusion in UO_2 [11, 12] for equilibrium vacancy concentration.

Compensation of simulated activation energy and prefactor results in the good agreement between calculated and experimental diffusion coefficients over the experimental temperature range, with better agreement for near-stoichiometric and N-rich conditions. And the diffusion coefficients for higher C_{V_U} fit the experiments better. This is most likely because the samples used in the experiments are irradiated, for which the vacancy concentration might be 1–2 orders of magnitude higher than the equilibrium vacancy concentration.

Our near-stoichiometric result agrees well with Cal [1], which also simulates near-stoichiometric UN. However, Cal [2] gives significantly lower values than other studies [27], which is unexpected considering the generally good performance of the SCMF method, which considers vacancies beyond the first nearest neighbor in describing the solute diffusion. This might be because this study employed the vacancy formation energy reported by Lan et al. [67] in calculating the thermal equilibrium vacancy concentration; these are much higher than the values reported in other works. As a consequence, significantly underestimated C_{V_U} and diffusion coefficient are obtained.

Our calculated diffusivities for Kr and Xe are similar, indicating the small influence of solute atomic size. Due to the absence of experimental work on Kr diffusion in UN, comparison with exper-

iment cannot be made, but the similar diffusivity of Kr and Xe in UO_2 qualitatively supports our finding [68, 69]. It is also consistent with the similar yields of Kr (18.6%) and Xe (19.4%) in the fuel-clad gap for (Pu, U)N [15].

5. Conclusions

In this contribution, we have reported the results of modeling studies of the diffusion behavior of the fission gases Kr and Xe in UN. We began by studying the U self-diffusion via the U monovacancy mechanism, finding that this is affected by UN non-stoichiometry and temperature. The calculated activation energies are 6.21 eV, 5.57 eV and 4.93 eV under U-rich, near stoichiometric, and N-rich conditions, respectively. The calculated vacancy formation entropy of 5–6 k_B demonstrates that the explicit calculation of the entropy is required to accurately study the self-diffusion. Under N-rich conditions, U has the largest diffusion coefficient due to the lowest activation energy. The excellent agreement between our calculated U self-diffusion coefficient and experiment validates the accuracy of our theoretical model, and indicates that the monovacancy mechanism is the dominant one for U self-diffusion.

Using the five-frequency model, we studied Kr and Xe diffusivity in UN by the monovacancy-assisted mechanism. We calculated the energy barrier of each elementary jump in the five-frequency model and found that the values are close for Kr and Xe except for that of the $V_U\text{-Ng}$ exchange jump, which directly contributes to the Ng migration. This indicates the significant effect of solute atomic size on $V_U\text{-Ng}$ exchange, while the effect on matrix atom movement is negligible. The rates of each elementary jump have been calculated, decreasing in the order $\omega_2 \gg \omega_4 > \omega_0 \approx \omega_1 \gg \omega_3$ for both Kr and Xe. The activation energy for Kr and Xe is dependent upon the non-stoichiometry, which decreases from U-rich to N-rich conditions. The values for Xe are slightly larger than that for Kr, indicating a minor atomic size effect. The diffusion coefficient for Kr and Xe is governed by temperature and non-stoichiometry, increasing from U-rich to N-rich conditions, with the values for Xe being slightly lower than for Kr.

We then studied Kr and Xe diffusivity in UN via the interstitial mechanism. The calculated activation energies are significantly larger than by the monovacancy-assisted mechanism, while the diffusion coefficients are much lower, indicating that the interstitial mechanism is not the dominant one for Ng diffusion in UN. Opposite to the monovacancy-assisted mechanism, the diffusion coefficient from the interstitial mechanism increases from N-rich to U-rich conditions, and the values for Kr are much larger than for Xe, indicating the pronounced effect of solute atomic size.

Finally, we compared our simulated results with experimental data for Xe diffusion and studied the effect of vacancy concentration. The reasonable agreement between our calculated monovacancy-assisted diffusion coefficient with experiment - similar to or better than existing theoretical and empirical models - indicates that the monovacancy-assisted mechanism governs Xe dif-

fusion in UN. The diffusion coefficient increases with increasing vacancy concentration. We believe our work provides a good theoretical basis to predict the diffusivity of Ng in UN grains, and that it will contribute to fission gas release models in UN.

Declaration of Competing Interest

The authors declare that they have no known competing financial interests or personal relationships that could have appeared to influence the work reported in this paper.

CRediT authorship contribution statement

Lin Yang: Conceptualization, Investigation, Methodology, Formal analysis, Software, Writing – original draft, Writing – review & editing. **Nikolas Kaltsoyannis:** Supervision, Resources, Funding acquisition, Project administration, Writing – review & editing.

Acknowledgements

We are grateful to the China Scholarship Council and The University of Manchester for a PhD studentship for LY. We are also grateful to The University of Manchester for its Computational Shared Facility (CSF3 and HPC pool) and associated support services.

References

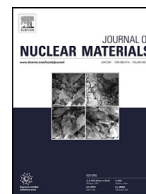
- [1] V.M. Troyanov, A.F. Grachev, L.M. Zabudko, M.V. Skupov, Prospects for using nitride fuel in fast reactors with a closed nuclear fuel cycle, *At. Energ.* 117 (2) (2014) 85–91.
- [2] T.R. Allen, D.C. Crawford, Lead-cooled fast reactor systems and the fuels and materials challenges, *Sci. Technol. Nucl. Installations* (2007) (2007) 1–11.
- [3] D. Petti, D. Crawford, N. Chauvin, Fuels for advanced nuclear energy systems, *MRS Bull.* 34 (1) (2009) 40–45.
- [4] J.K. Watkins, A. Gonzales, A.R. Wagner, E.S. Sooby, B.J. Jaques, Challenges and opportunities to alloyed and composite fuel architectures to mitigate high uranium density fuel oxidation: uranium mononitride, *J. Nucl. Mater.* 553 (2021) 153048.
- [5] J. Rest, M.W.D. Cooper, J. Spino, J.A. Turnbull, P. Van Uffelen, C.T. Walker, Fission gas release from UO_2 nuclear fuel: a review, *J. Nucl. Mater.* 513 (2019) 310–345.
- [6] M. Tonks, D. Andersson, R. Devanathan, R. Dubourg, A. El-Azab, M. Freyss, F. Iglesias, K. Kulacsy, G. Pastore, S.R. Phillpot, Unit mechanisms of fission gas release: current understanding and future needs, *J. Nucl. Mater.* 504 (2018) 300–317.
- [7] D. Andersson, Density functional theory calculations applied to nuclear fuels, in: W. Andreoni, S. Yip (Eds.), *Handbook of Materials Modeling: Applications: Current and Emerging Materials*, Springer International Publishing, Cham, 2020, pp. 2121–2140.
- [8] J. Turnbull, C. Friskney, J. Findlay, F. Johnson, A. Walter, The diffusion coefficients of gaseous and volatile species during the irradiation of uranium dioxide, *J. Nucl. Mater.* 107 (2–3) (1982) 168–184.
- [9] J. Turnbull, The effect of grain size on the swelling and gas release properties of UO_2 during irradiation, *J. Nucl. Mater.* 50 (1) (1974) 62–68.
- [10] J. Turnbull, C. Friskney, The relation between microstructure and the release of unstable fission products during high temperature irradiation of uranium dioxide, *J. Nucl. Mater.* 71 (2) (1978) 238–248.
- [11] D.A. Andersson, P. Garcia, X.Y. Liu, G. Pastore, M. Tonks, P. Millett, B. Dorado, D.R. Gaston, D. Andrs, R.L. Williamson, R.C. Martineau, B.P. Uberuaga, C.R. Stanek, Atomistic modeling of intrinsic and radiation-enhanced fission gas (Xe) diffusion in UO_2 : implications for nuclear fuel performance modeling, *J. Nucl. Mater.* 451 (1–3) (2014) 225–242.
- [12] E. Vathonne, D.A. Andersson, M. Freyss, R. Perriot, M.W. Cooper, C.R. Stanek, M. Bertolus, Determination of krypton diffusion coefficients in uranium dioxide using atomic scale calculations, *Inorg. Chem.* 56 (1) (2017) 125–137.
- [13] C. Matthews, R. Perriot, M.W.D. Cooper, C.R. Stanek, D.A. Andersson, Cluster dynamics simulation of xenon diffusion during irradiation in UO_2 , *J. Nucl. Mater.* 540 (2020).
- [14] R. Perriot, C. Matthews, M.W. Cooper, B.P. Uberuaga, C.R. Stanek, D.A. Andersson, Atomistic modeling of out-of-pile xenon diffusion by vacancy clusters in UO_2 , *J. Nucl. Mater.* 520 (2019) 96–109.
- [15] B. Rogozkin, N. Stepennova, Y.E. Fedorov, M. Shishkov, F. Kryukov, S. Kuzmin, O. Nikitin, A. Belyaeva, L. Zabudko, Results of $\text{U}_{0.55}\text{Pu}_{0.45}\text{N}$ and $\text{U}_{0.4}\text{Pu}_{0.6}\text{N}$ mixed mononitride fuel tests in a bor-60 reactor to burnup 12% ha, *At. Energ.* 110 (6) (2011) 412.
- [16] K. Tanaka, K. Maeda, K. Katsuyama, M. Inoue, T. Iwai, Y. Arai, Fission gas release and swelling in uranium–plutonium mixed nitride fuels, *J. Nucl. Mater.* 327 (2–3) (2004) 77–87.
- [17] N. Oi, Xe-133 diffusion in UN single crystals, *Zeitschrift für Naturforschung A* 21 (6) (1966) 863–864.
- [18] J.B. Melchan, J.E. Gates, In-pile fission-gas release from uranium carbide and uranium nitride, Battelle Memorial Inst. 1964.
- [19] D. Bocharov, D. Gryaznov, Y.F. Zhukovskii, E.A. Kotomin, DFT calculations of point defects on UN(001) surface, *Surf. Sci.* 605 (3–4) (2011) 396–400.
- [20] M. Klipfel, P. Van Uffelen, Ab initio modelling of volatile fission products in uranium mononitride, *J. Nucl. Mater.* 422 (1–3) (2012) 137–142.
- [21] Y.-J. Zhang, J.-H. Lan, C.-Z. Wang, Q.-Y. Wu, T. Bo, Z.-F. Chai, W.-Q. Shi, Theoretical investigation on incorporation and diffusion properties of Xe in Uranium Mononitride, *J. Phys. Chem. C* 119 (11) (2015) 5783–5789.
- [22] A. Claisse, M. Klipfel, N. Lindbom, M. Freyss, P. Olsson, GGA+U study of uranium mononitride: a comparison of the U-ramping and occupation matrix schemes and incorporation energies of fission products, *J. Nucl. Mater.* 478 (2016) 119–124.
- [23] L. Yang, N. Kaltsoyannis, Incorporation of Kr and Xe in Uranium Mononitride: a Density Functional Theory Study, *J. Phys. Chem. C* 125 (48) (2021) 26999–27008.
- [24] V. Kocovski, D.A. Rehn, M.W. Cooper, D.A. Andersson, First-principles investigation of uranium mononitride (UN): effect of magnetic ordering, spin-orbit interactions and exchange correlation functional, *J. Nucl. Mater.* 559 (2022) 153401.
- [25] V. Kocovski, M.W. Cooper, A.J. Claisse, D.A. Andersson, Development and application of a uranium mononitride (UN) potential: thermomechanical properties and Xe diffusion, *J. Nucl. Mater.* 562 (2022) 153553.
- [26] S. Starikov, A. Kuksin, D. Smirnova, A. Dolgodvorov, V. Ozrin, Multiscale modeling of uranium mononitride: point defects diffusion, self-diffusion, phase composition, *Defect Diffusion Forum* 375 (2017) 101–113.
- [27] A. Claisse, T. Schuler, D.A. Lopes, P. Olsson, Transport properties in dilute UN(X) solid solutions (X=Xe,Kr), *Phys. Rev. B* 94 (17) (2016).
- [28] G. Kresse, J. Hafner, Ab initio molecular dynamics for liquid metals, *Phys. Rev. B* 47 (1) (1993) 558.
- [29] G. Kresse, J. Furthmüller, Efficiency of ab-initio total energy calculations for metals and semiconductors using a plane-wave basis set, *Comput. Mater. Sci.* 6 (1) (1996) 15–50.
- [30] G. Kresse, J. Furthmüller, Efficient iterative schemes for ab initio total-energy calculations using a plane-wave basis set, *Phys. Rev. B* 54 (16) (1996) 11169.
- [31] J.P. Perdew, K. Burke, M. Ernzerhof, Generalized gradient approximation made simple, *Phys. Rev. Lett.* 77 (18) (1996) 3865.
- [32] M. Dion, H. Rydberg, E. Schröder, D.C. Langreth, B.I. Lundqvist, Van der Waals density functional for general geometries, *Phys. Rev. Lett.* 92 (24) (2004) 246401.
- [33] G.-Y. Huang, N. Juslin, B.-D. Wirth, First-principles study of vacancy, interstitial, noble gas atom interstitial and vacancy clusters in bcc-W, *Comput. Mater. Sci.* 123 (2016) 121–130.
- [34] G. Henkelman, H. Jónsson, Improved tangent estimate in the nudged elastic band method for finding minimum energy paths and saddle points, *J. Chem. Phys.* 113 (22) (2000) 9978–9985.
- [35] G. Henkelman, B.P. Uberuaga, H. Jónsson, A climbing image nudged elastic band method for finding saddle points and minimum energy paths, *J. Chem. Phys.* 113 (22) (2000) 9901–9904.
- [36] S.S. Naghavi, V.I. Hegde, C. Wolverton, Diffusion coefficients of transition metals in fcc cobalt, *Acta Mater.* 132 (2017) 467–478.
- [37] Y. Mishin, M.R. Sorensen, A.F. Voter, Calculation of point-defect entropy in metals, *Philos. Mag.* A 81 (11) (2001) 2591–2612.
- [38] A. Togo, I. Tanaka, First principles phonon calculations in materials science, *Scripta Mater.* 108 (2015) 1–5.
- [39] H. Mehrer, *Diffusion in solids: fundamentals, methods, materials*, Diffusion-Controlled Processes, Springer Science & Business Media, 2007.
- [40] K. Compaan, Y. Haven, Correlation factors for diffusion in solids, *Trans. Faraday Soc.* 52 (1956) 786–801.
- [41] G. Montet, Integral methods in the calculation of correlation factors in diffusion, *Phys. Rev. B* 7 (2) (1973) 650.
- [42] G.H. Vineyard, Frequency factors and isotope effects in solid state rate processes, *J. Phys. Chem. Solids* 3 (1–2) (1957) 121–127.
- [43] N. Zou, H.-J. Lu, X.-G. Lu, Impurity diffusion coefficients in BCC Nb from first-principles calculations, *J. Alloys Compd.* 803 (2019) 684–688.
- [44] G. Ho, M.T. Ong, K.J. Caspersen, E.A. Carter, Energetics and kinetics of vacancy diffusion and aggregation in shocked aluminium via orbital-free density functional theory, *Phys. Chem. Chem. Phys.* 9 (36) (2007) 4951–4966.
- [45] X. Tang, R. Salehin, G.B. Thompson, C.R. Weinberger, Statistical study of vacancy diffusion in TiC and TaC, *Phys. Rev. Materials* 4 (9) (2020) 093602.
- [46] A. Lidiard, CXXXIII. Impurity diffusion in crystals (mainly ionic crystals with the sodium chloride structure), *The London, Edinburgh, and Dublin Philosophical Magazine and J. Sci.* 46 (382) (1955) 1218–1237.
- [47] A. Lidiard, The influence of solutes on self-diffusion in metals, *Philos. Mag.* 5 (59) (1960) 1171–1180.
- [48] J.R. Manning, Correlation factors for impurity diffusion. bcc, diamond, and fcc structures, *Phys. Rev.* 136 (6A) (1964) A1758.
- [49] T. Ogawa, Thermodynamic properties of $(\text{U}, \text{Pu})\text{N}_{1-x}$ with a sublattice formalism—Equilibrium involving the nonstoichiometric nitrides, *J. Nucl. Mater.* 201 (1993) 284–292.
- [50] D.A. Andersson, B.P. Uberuaga, P.V. Nerikar, C. Unal, C.R. Stanek, U and Xe transport in UO_{2+x} : density functional theory calculations, *Phys. Rev. B* 84 (5) (2011).

- [51] S. Schuwalow, J. Rogal, R. Drautz, Vacancy mobility and interaction with transition metal solutes in Ni, *J. Phys. Condens. Matter* 26 (48) (2014) 485014.
- [52] D.A. Andersson, X.Y. Liu, B. Beeler, S.C. Middleburgh, A. Claisse, C.R. Stanek, Density functional theory calculations of self- and Xe diffusion in U_3Si_2 , *J. Nucl. Mater.* 515 (2019) 312–325.
- [53] H. Liu, D.R. Costa, D.A. Lopes, A. Claisse, L. Messina, P. Olsson, Compatibility of UN with refractory metals (V, Nb, Ta, Cr, Mo and W): an ab initio approach to interface reactions and diffusion behavior, *J. Nucl. Mater.* 560 (2022) 153482.
- [54] J.G. McHugh, K. Jolley, P. Mouratidis, Ab-initio calculations of fission product diffusion on graphene, *J. Nucl. Mater.* 533 (2020) 152123.
- [55] K. Pötting, W. Schmickler, T. Jacob, Self-Diffusion on Au (100): a density functional theory study, *ChemPhysChem* 11 (7) (2010) 1395–1404.
- [56] B. Dorado, J. Durinck, P. Garcia, M. Freyss, M. Bertolus, An atomistic approach to self-diffusion in uranium dioxide, *J. Nucl. Mater.* 400 (2) (2010) 103–106.
- [57] S. Hayes, J. Thomas, K. Peddicord, Material property correlations for uranium mononitride: III. Transport properties, *J. Nucl. Mater.* 171 (2–3) (1990) 289–299.
- [58] H. Matzke, Atomic mechanisms of mass transport in ceramic nuclear fuel materials, *J. Chem. Soc., Faraday Trans.* 86 (8) (1990) 1243–1256.
- [59] H. Matzke, Atomic transport properties in UO_2 and mixed oxides (U, Pu) O_2 , *J. Chem. Soc. Faraday Trans.* 2 83 (7) (1987) 1121–1142.
- [60] F. Buffington, K.-i. Hirano, M. Cohen, Self diffusion in iron, *Acta Metall* 9 (5) (1961) 434–439.
- [61] K. Carling, G. Wahnström, T.R. Mattsson, A.E. Mattsson, N. Sandberg, G. Grimvall, Vacancies in metals: from first-principles calculations to experimental data, *Phys. Rev. Lett.* 85 (18) (2000) 3862.
- [62] C. Freysoldt, B. Grabowski, T. Hickel, J. Neugebauer, G. Kresse, A. Janotti, C.G. Van de Walle, First-principles calculations for point defects in solids, *Rev Mod Phys* 86 (1) (2014) 253.
- [63] W. Kohn, A.E. Mattsson, Edge electron gas, *Phys. Rev. Lett.* 81 (16) (1998) 3487.
- [64] M.R. LaBrosse, L. Chen, J.K. Johnson, First principles study of vacancy and tungsten diffusion in fcc cobalt, *Modell. Simul. Mater. Sci. Eng.* 18 (1) (2009) 015008.
- [65] H. Matter, J. Winter, W. Triftshäuser, Phase transformations and vacancy formation energies of transition metals by positron annihilation, *Applied physics* 20 (2) (1979) 135–140.
- [66] A. Glensk, B. Grabowski, T. Hickel, J. Neugebauer, Breakdown of the Arrhenius law in describing vacancy formation energies: the importance of local anharmonicity revealed by ab initio thermodynamics, *Phys. Rev. X* 4 (1) (2014) 011018.
- [67] J.-H. Lan, Z.-C. Zhao, Q. Wu, Y.-L. Zhao, Z.-F. Chai, W.-Q. Shi, First-principles DFT+ *U* modeling of defect behaviors in anti-ferromagnetic uranium mononitride, *J. Appl. Phys.* 114 (22) (2013) 223516.
- [68] W. Miekeley, F. Felix, Effect of stoichiometry on diffusion of xenon in UO_2 , *J. Nucl. Mater.* 42 (3) (1972) 297–306.
- [69] A. Auskern, The diffusion of krypton-85 from Uranium Dioxide Powder, Office of Technical Services, Department of Commerce, 1960.

-Blank page-

5 Incorporation and Migration of Xenon in Uranium-plutonium Mixed Nitride

This chapter is the author published article (Lin Yang and Nikolas Kaltsoyannis, Incorporation and migration of xenon in uranium-plutonium mixed nitride; A density functional theory study, *J. Nucl. Mater.* 2023, 577, 154330, <https://doi.org/10.1016/j.jnucmat.2023.154330>), which has 18 pages in total. All work in this chapter was completed by myself under the supervision of Prof. Nikolas Kaltsoyannis.



Nuclear fuels and materials

Incorporation and migration of xenon in uranium-plutonium mixed nitride; A density functional theory study

Lin Yang, Nikolas Kaltsoyannis*

Department of Chemistry, School of Natural Sciences, The University of Manchester, Oxford Road, Manchester M13 9PL



ARTICLE INFO

Article history:

Received 17 October 2022

Revised 21 December 2022

Accepted 8 February 2023

Keywords:

Uranium-plutonium mixed nitride

Nuclear fuel

Actinide vacancy

Noble gas incorporation and migration

Density functional theory

ABSTRACT

Actinide nitride materials are promising candidates for advanced nuclear fuels. In this work, we investigate the bulk properties of the mixed nitrides $U_{0.75}Pu_{0.25}N$ and $U_{0.5}Pu_{0.5}N$, and study the incorporation and migration behaviour of the fission gas Xe. The disordered $U_{0.75}Pu_{0.25}N$ and $U_{0.5}Pu_{0.5}N$ structures are constructed using the special quasi-random structure method. Their lattice parameters are closer to the experimentally determined values than the corresponding ordered structures. The density of states show that Pu f states are located at lower energy than U f, consistent with the trend of increasing f orbital stability across the actinide series. The actinide vacancy formation energy (E_f) in disordered and ordered $U_{0.5}Pu_{0.5}N$ is highly dependent on the chemical environment around the vacancy: it increases as the number of U atoms in the first nearest-neighbour shell ($N_U(1NN)$) increases, but decreases as the number of U atoms in the second nearest-neighbour shell ($N_U(2NN)$) increases. The Xe incorporation energy (E_i) is found to be independent of vacancy species, depending only on the chemical environment of the vacancy. As does E_f , E_i increases with increasing $N_U(1NN)$, while decreases with increasing $N_U(2NN)$, because the smaller the $N_U(1NN)$ and the larger the $N_U(2NN)$, the larger the vacancy steric space. The E_i of Xe and Kr are calculated to be within the ranges 4.47–6.01 eV and 3.30–4.64 eV, respectively. The Xe migration energy barrier in ordered $U_{0.5}Pu_{0.5}N$ allows us to set the energy range for Xe diffusion in disordered $U_{0.5}Pu_{0.5}N$ as 0.50–1.75 eV. A lower range of 0.30–1.25 eV is found for Kr diffusion.

© 2023 The Author(s). Published by Elsevier B.V.

This is an open access article under the CC BY license (<http://creativecommons.org/licenses/by/4.0/>)

1. Introduction

Compared with the widely used uranium dioxide nuclear fuel, metal nitride fuels have higher metal density and thermal conductivity, which makes them good candidates for future Generation IV fast reactors, especially metal-cooled fast reactors, due to their good compatibility with metal coolants. Some research reactors have been constructed to study the serviceability of mixed nitride fuels, e.g. the BOR-60 reactor with fuel of composition $U_{0.55}Pu_{0.45}N$ and $U_{0.4}Pu_{0.6}N$, and the JOYO reactor with $U_{0.8}Pu_{0.2}N$ fuel [1–3]. To support reactor design, simulation codes are used to evaluate fuel performance and assess risk [4,5]. These codes are developed by fitting experimental data in which the fuel microstructure parameters are not included. As a result, significant discrepancies have been obtained between the simulated and experimental fission gas (mainly the noble gas (Ng) Xe) release rates [4]. Fission gas atoms have low solubility in fuel matrices, and their trapping and release may lead to fuel swelling and degeneration of thermal conductivity.

Thus, a comprehensive understanding of the micro properties of mixed nitride fuels, such as defect structure and fission gas incorporation and diffusion, is necessary for the development of accurate fission gas release models. Considering the difficulties in the experimental study of Pu and its compounds, atomistic simulation is a powerful tool to obtain these properties.

By contrast to mononitride fuels, work on mixed nitride fuels is extremely limited. Kurosaki *et al.* studied $U_{0.8}Pu_{0.2}N$ by molecular dynamics, and found that the physicochemical properties of the mixed nitrides are intermediate between those of UN and PuN [6]. Zhang *et al.* studied the electronic and mechanical properties of $U_{0.5}Pu_{0.5}N$ by the GGA+U method [7]. To save calculation resources, they simplified the $U_{0.5}Pu_{0.5}N$ model into UN and PuN layers orderly stacked in a 1:1 ratio, although in reality, similar to mixed oxide fuels, (U, Pu)N is a solid solution with U and Pu being randomly distributed in the actinide sublattice. To accurately study the mechanical and thermodynamic properties of mixed nitrides, the construction of fully disordered (U, Pu)N structures is necessary. Several methods are used in the literature to model the chemical disorder of different elements in size-limited systems [8–10]. Amongst them, the special quasi-random structure (SQS) method, based on the Monte Carlo search scheme, is commonly

* Corresponding author.

E-mail address: nikolas.kaltsoyannis@manchester.ac.uk (N. Kaltsoyannis).

used for small supercells [11,12], and has been proven to perform well for disordered mixed oxides, e.g. (Pu, U)O₂, (Pu, Th)O₂, and (U, Th)O₂ [13,14]. To the best of our knowledge, disordered (U, Pu)N has not been studied at the atomistic level before.

For actinide oxides, density functional theory (DFT) calculations using conventional generalized gradient approximation (GGA) functionals usually overestimate the delocalization of 5f electrons and incorrectly predict these oxides as metallic, which is typically corrected by applying a Hubbard U term to the actinide 5f states [15]. By contrast, for UN, in which all the 5f electrons are delocalized, conventional GGA functionals well reproduce the experimental electronic spectrum [16–18], and including the U correction generates imaginary phonon modes [19]. However, PuN is located at the delocalized-localized 5f boundary in the actinide series [20–23], and the dual nature of the Pu 5f states makes it hard to well reproduce the PuN electronic properties. Different ground states have been suggested by different theoretical works, e.g. a f^3 ground state electronic configuration was suggested by Petit *et al.* using the SIC-LSD method [20], while Li *et al.* found a $f^{4.8}$ ground state by dynamic mean field theory [23]. Although the Hubbard U -corrected DFT method was used in some previous literature to study PuN, conventional GGA functionals correctly predict PuN as metallic, and the obtained lattice parameter is close to the experiments [22,24–26]. Moreover, the DFT+ U formalism was found to increase the number of metastable states, and ground state control methods are necessary [27]. Therefore, conventional GGA is used to study (U, Pu)N in this work, on the basis that it performs well for both UN and PuN.

Based on the above considerations, we here study the microstructure properties of U_xPu_{1-x}N, as well as the incorporation and migration of Xe in it. Considering that the Pu content of the (U, Pu)N fuel studied experimentally ranges from 0.2 to 0.6, we here focus on U_{0.75}Pu_{0.25}N and U_{0.5}Pu_{0.5}N. We first investigate the geometric, electronic, and thermodynamic properties of disordered U_{0.75}Pu_{0.25}N and U_{0.5}Pu_{0.5}N, and compare the results with those of the corresponding ordered structures. Then, defect formation energies in U_{0.5}Pu_{0.5}N are calculated to establish their relationship with the defect chemical environment. Finally, the incorporation and migration of Xe are simulated. Comparative calculations of Kr in ordered U_{0.5}Pu_{0.5}N are also conducted to give an energy range for Kr incorporation and migration in disordered U_{0.5}Pu_{0.5}N. We believe our work will contribute to the understanding of the microstructure properties of uranium-plutonium mixed nitride fuels, and fission gas behaviour within them.

2. Computational and methodological details

Modelling U_{0.75}Pu_{0.25}N and U_{0.5}Pu_{0.5}N. (U, Pu)N is a solid solution with U and Pu randomly distributed on the cationic sublattice, with a rock-salt structure similar to that of UN. The Special Quasi-random Structure (SQS) method was used to construct disordered U_{0.75}Pu_{0.25}N and U_{0.5}Pu_{0.5}N, employing the “mcsqs” module in the Alloy Theoretic Automated Toolkit (ATAT) [11,12]. A very large supercell is necessary to model the fully random-distributed solid solution, which will lead to high computational cost. To balance efficiency and accuracy, we therefore tested two supercell sizes, 2×2×2 and 3×3×3. The details of the SQS modelling are given in the supplementary information (Figure S1 and S2). For comparison, ordered U_{0.75}Pu_{0.25}N and U_{0.5}Pu_{0.5}N were also constructed by replacing 1 and 2 U atoms with Pu atoms in bulk UN, as shown in Figure S3. The ordered U_{0.5}Pu_{0.5}N structure is the same as that used by Zhang *et al.* [7]. A 2×2×2 supercell was constructed for ordered U_{0.5}Pu_{0.5}N to study the defect formation energy, and a 2×2×3 supercell was used for the Ng (Ng = Xe, Kr) migration study, as tested in our previous work on UN [28].

DFT calculations. All the structure optimization and energy calculations in this work were conducted using DFT within the Vienna *Ab initio* Simulation Package (VASP) 6.1.2 [29–31]. The cutoff energy was set to 520 eV, as tested in our previous work [18]. The Perdew-Burke-Ernzerhof (PBE) functional [32] was used for geometry optimization with the force convergence limit of 0.01 eV/Å. The energy of the obtained structures was calculated by the vdW-DF functional to better account for the dispersion interactions [33], with the energy convergence limit of 10^{−5} eV. The Monkhorst-Pack sampling method with a 10×10×10 k mesh was used for the ordered bulk, and 3×3×3 and 3×3×2 k meshes were used for 2×2×2 and 2×2×3 supercells, respectively. To determine saddle point structures and migration energy barriers, the climbing image nudged elastic band (CI-NEB) method, as implemented in the VTST package, was used [34,35]. 3 intermediate images were used with the force convergence limit of 0.05 eV/Å.

The chemical potentials of Pu and U were calculated from α -U and α -Pu bulk, while those of N and Ng were calculated from an N₂ molecule and isolated Ng atom by putting N₂ or Ng into a 20×20×20 Å³ cell and fully relaxing. The convergence criteria and functional used are as above.

Defect formation energies and Ng incorporation Energies. Previous studies have suggested that Ng has the lowest solution energy at the uranium vacancy (V_U) site in UN, and the V_U-assisted mechanism is the dominant one for fission gas atom diffusion in UN [18,28,36]. Thus, the current work focuses on the cationic actinide vacancy (V_{An}) defect (V_{Pu} and V_U) and V_{An}-assisted Ng migration. The vacancy formation energies are calculated from:

$$E_f = E_{\text{defect}} - E_{\text{perfect}} + \mu_{\text{An}} \quad (1)$$

in which E_{defect} and E_{perfect} are the total energies of the defect and perfect supercell, respectively. μ_{U} is the chemical potential of the actinide atom (U or Pu) removed to create the vacancy. Bathellier *et al.* studied the effect of chemical disorder on E_f of bound Schottky defects (BSDs) in (Pu, U)O₂ [37]. They found that choosing a U-based or Pu-based BSD is equally valid, since the difference between the E_f of two BSD types is a shift in the reference energy. The same E_f range is obtained by using U-based or Pu-based BSD. Therefore, we here choose to focus on the E_f of V_U to study the effect of chemical disorder, with the results for E_f (V_{Pu}) shown in the supplementary information.

As the periodic model is implemented in the supercell approach, the inclusion of defects and incorporated Ng atoms can induce spurious interactions between periodic images [38]. Elastic field correction terms can help to correct for such interactions in the calculation of defect formation energy and Ng incorporation energy, but our previous work suggests that this energy term is negligible for the 2×2×2 UN supercell [18]. Thus, we do not employ elastic field corrections in the current work.

Similar to the defect formation energy, the incorporation energies of Ng in the defect (U, Pu)N supercell are calculated from:

$$E_i = E_{\text{Ng} \in \text{defect}} - E_{\text{defect}} - \mu_{\text{Ng}} \quad (2)$$

where $E_{\text{Ng} \in \text{defect}}$ is the (U, Pu)N supercell containing an Ng atom at the vacancy site, and μ_{Ng} is the chemical potential of an isolated Ng atom.

3. Results and discussion

3.1. U_xPu_{1-x}N bulk properties

Structural Properties. We first compared our calculated U_{0.75}Pu_{0.25}N and U_{0.5}Pu_{0.5}N lattice parameters a and bond length d with experiment, and the data are plotted in Fig. 1. As introduced in the supplementary information, the optimized a and d of

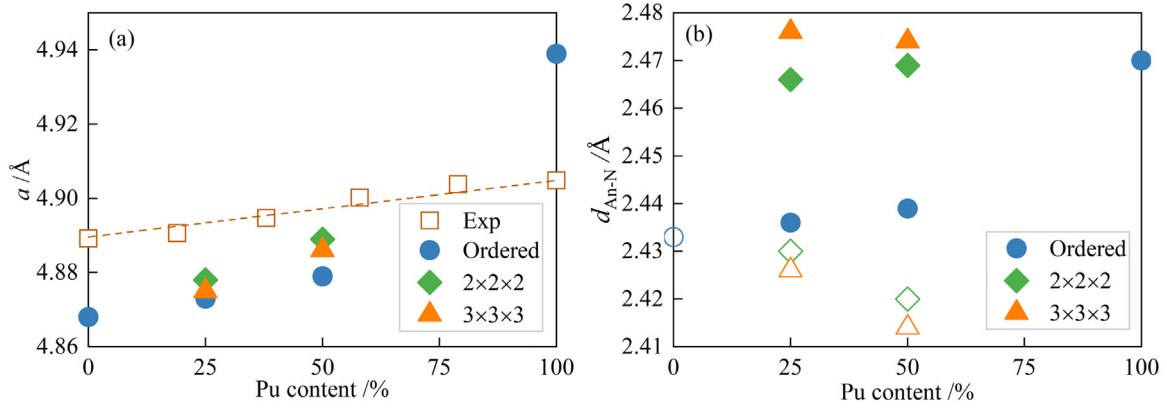


Fig. 1. (a) Lattice parameter of $U_xPu_{1-x}N$ against Pu content. The experimental values are from Reference [39]. (b) Calculated U-N (hollow) and Pu-N (solid) bond lengths of $U_xPu_{1-x}N$ against the Pu content. The dashed line in (a) is the expected lattice parameter derived from Vegard's law.

the disordered $U_{0.75}Pu_{0.25}N$ and $U_{0.5}Pu_{0.5}N$ in Fig. 1 are the average values of the three selected SQS supercells, with the values of each SQS supercell being listed in Table S1. The a and d of the ordered $U_{0.75}Pu_{0.25}N$ and $U_{0.5}Pu_{0.5}N$ are obtained by optimizing the (U, Pu)N bulk, and the dashed line in Fig. 1(a) is the expected lattice parameter of (U, Pu)N derived from the experimental a of UN and PuN based on Vegard's law [39,40].

The experimental a of (U, Pu)N does not strictly obey Vegard's law [39], with the a of $U_{0.81}Pu_{0.19}N$ and $U_{0.62}Pu_{0.38}N$ being slightly lower than the values expected from Vegard, while the a of $U_{0.42}Pu_{0.58}N$ and $U_{0.21}Pu_{0.79}N$ are larger (Fig. 1(a)). This indicates that (U, Pu)N are not ideal mixtures. The calculated a of $U_{0.75}Pu_{0.25}N$ and $U_{0.5}Pu_{0.5}N$ also deviate from Vegard's law, consistent with experiment. Compared with the lattice parameter of the ordered structures, the deviation of the disordered structures is smaller and the values are closer to the experimental values. The a of the $2 \times 2 \times 2$ and $3 \times 3 \times 3$ disordered supercells are quite close for both $U_{0.75}Pu_{0.25}N$ and $U_{0.5}Pu_{0.5}N$, with differences of 0.07% and 0.05%, respectively, indicating that the $2 \times 2 \times 2$ supercell is sufficient to represent disordered (U, Pu)N. Moreover, Table S1 shows that the lattice parameters of the selected SQS supercells are similar. While there are no previous simulations of disordered (U, Pu)N with which to compare our results, our calculated a for ordered $U_{0.5}Pu_{0.5}N$ is smaller than the 4.917 Å reported by Zhang *et al.* [7]. The difference could be attributed to the different method they used (PBE+ U), which is consistent with the fact that the Hubbard correction tends to overestimate the lattice parameter of UN (4.900 vs 4.889 vs 4.868 Å, by PBE+ U , experiment and PBE, respectively) [7,39].

The U-N and Pu-N distances in the ordered structures are nearly the same due to symmetry, and increase slightly as the Pu content increases. In the disordered supercells, however, the U-N and Pu-N distances are quite different, with the latter being 1.5% to 2.5% larger than the former in each structure. This is consistent with the larger experimental lattice parameter of PuN than UN (Fig. 1(a)), which indicates that the Pu-N and U-N bonds in disordered (U, Pu)N tend to perform as in the pure mononitride. This leads to the sizeable displacement towards U of the N atoms from their ideal sites (Figure S4). With increasing Pu content, the average U-N distance decreases, while the Pu-N distance remains nearly constant, being similar to the Pu-N bond length in PuN. The values obtained from the $2 \times 2 \times 2$ and $3 \times 3 \times 3$ supercells are close to each other, with differences of 0.18% and 0.41% for $d_{\text{U-N}}$ and $d_{\text{Pu-N}}$ in $U_{0.75}Pu_{0.25}N$, and 0.26% and 0.17% for $d_{\text{U-N}}$ and $d_{\text{Pu-N}}$ in $U_{0.5}Pu_{0.5}N$. This further indicates that the $2 \times 2 \times 2$ supercell is sufficient to study disordered $U_{0.75}Pu_{0.25}N$ and $U_{0.5}Pu_{0.5}N$. As with the lattice parameter, the bond lengths of the selected SQS super-

Table 1
Calculated Bader charge ($q/|e|$) of disordered and ordered $U_{0.75}Pu_{0.25}N$ and $U_{0.5}Pu_{0.5}N$. The charges of U and Pu in UN and PuN are calculated to be 1.60 and 1.46, respectively.

	Disordered structure		Ordered structure	
	q_{Pu}	q_{U}	q_{Pu}	q_{U}
$U_{0.75}Pu_{0.25}N$	1.56	1.82	1.37	1.62
$U_{0.5}Pu_{0.5}N$	1.39	1.65	1.40	1.65

cells with the same composition are close. Therefore, the $2 \times 2 \times 2$ supercells with the best cluster correlations (details in the supplementary information) are used to study the electronic and thermodynamic properties of $U_{0.75}Pu_{0.25}N$ and $U_{0.5}Pu_{0.5}N$ in the following sections, with the relaxed structures being shown in Fig. 2.

Electronic properties. The Bader atomic charges q of Pu and U in disordered and ordered $U_{0.75}Pu_{0.25}N$ and $U_{0.5}Pu_{0.5}N$ are given in Table 1; q_{U} in the mixed nitrides are larger than in UN, especially in the disordered structures, indicating that the U-N bond is more ionic in the mixed nitrides. By contrast, q_{Pu} are smaller than in the PuN (except for disordered $U_{0.75}Pu_{0.25}N$), which is consistent with the findings of Zhang *et al.* that the Pu-N bond is less ionic in ternary actinide nitrides than in the binary PuN [7]. Moreover, in the mixed nitrides, the Bader charge of U is larger than that of Pu, indicating that more electrons transfer between U-N than Pu-N. In the disordered structure, the charges of both U and Pu decrease as the Pu content increases, but stays nearly constant in the ordered structure.

To further study the electronic properties of $U_{0.75}Pu_{0.25}N$ and $U_{0.5}Pu_{0.5}N$, the density of states (DOS) were calculated, and are plotted in Fig. 3 and Figure S5. Both $U_{0.75}Pu_{0.25}N$ and $U_{0.5}Pu_{0.5}N$ are metallic with the main contributions to the DOS around the Fermi level being from the An f orbitals. Pu f states are located at lower energy than U f, consistent with the trend of increasing f orbital stability across the actinide series [17,41]. Experimental valence band photoelectron spectra of PuN show that there are three peaks of Pu f states within 1 eV [42]. For UN, a strong peak near the Fermi level is found experimentally [16]. These features were well reproduced by the PBE functional, while the addition of a Hubbard U correction predicts lower peak locations due to the overestimation of the localization of An 5f states [17,18]. Fig. 3 shows that these peak features are retained in the mixed nitrides. In other words, the DOS of the mixed nitrides are the superposition of those of UN and PuN. The N p states are located between -6 and -2 eV, with clear hybridization between N p and An f and d. The latter hybridization lies at a lower energy than the former, indicating that both the An d and f orbitals contribute

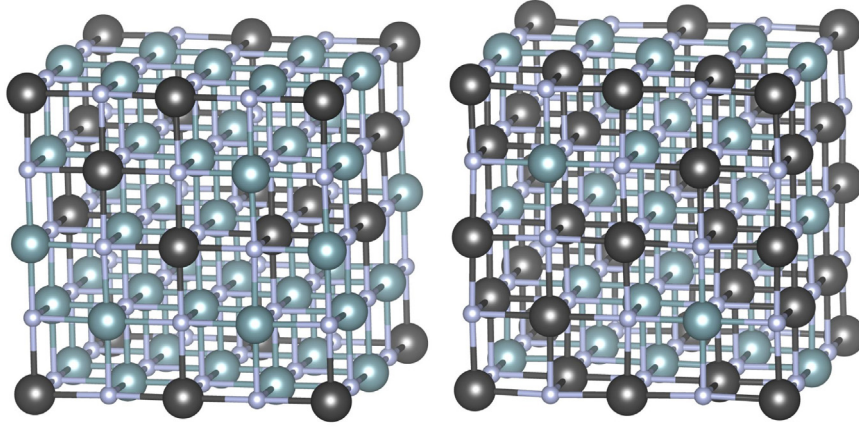


Fig. 2. Optimized disordered $\text{U}_{0.75}\text{Pu}_{0.25}\text{N}$ (left) and $\text{U}_{0.5}\text{Pu}_{0.5}\text{N}$ (right) supercells generated by the SQS method. Black, teal, and grey balls represent plutonium, uranium and nitrogen, respectively.

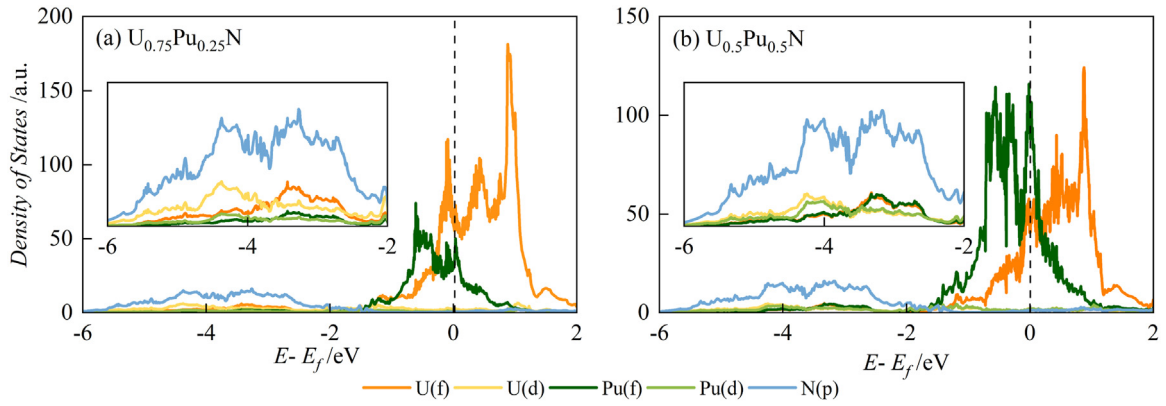


Fig. 3. Density of states of disordered $\text{U}_{0.75}\text{Pu}_{0.25}\text{N}$ (a) and $\text{U}_{0.5}\text{Pu}_{0.5}\text{N}$ (b).

to the An-N bond. Moreover, the peak positions of $\text{U}_{0.75}\text{Pu}_{0.25}\text{N}$ and $\text{U}_{0.5}\text{Pu}_{0.5}\text{N}$ are quite similar, suggesting little effect of the Pu content on the peak location in the DOS, although the difference in peak intensity can be attributed to the Pu concentration. This is different from the mixed oxides, in which the UO_2 band gap significantly narrows in $(\text{U}, \text{Pu})\text{O}_2$ [43]. The DOS of the ordered $\text{U}_{0.75}\text{Pu}_{0.25}\text{N}$ and $\text{U}_{0.5}\text{Pu}_{0.5}\text{N}$ (Figure S5) are generally similar to those of the corresponding disordered $(\text{U}, \text{Pu})\text{N}$, and also show hybridization between An d/f and N p states. Note that the Pu f states slightly overlap with U f below the Fermi level, indicating interaction between the An atoms in ordered $(\text{U}, \text{Pu})\text{N}$.

Energetic properties. To study the thermodynamic stability of $\text{U}_{0.75}\text{Pu}_{0.25}\text{N}$ and $\text{U}_{0.5}\text{Pu}_{0.5}\text{N}$, we have calculated their formation enthalpy and mixing enthalpy using the total energy results from electronic structure calculations:

$$\Delta H_f = E_{\text{U}_x\text{Pu}_{1-x}\text{N}} - x\mu_{\text{U}} - (1-x)\mu_{\text{Pu}} - \mu_{\text{N}} \quad (3)$$

$$\Delta H_{\text{mix}} = E_{\text{U}_x\text{Pu}_{1-x}\text{N}} - xE_{\text{UN}} - (1-x)E_{\text{PuN}} \quad (4)$$

in which $E_{\text{U}_x\text{Pu}_{1-x}\text{N}}$, E_{UN} and E_{PuN} are the total energies of $\text{U}_x\text{Pu}_{1-x}\text{N}$, UN and PuN, respectively, and μ_{U} , μ_{Pu} and μ_{N} are the calculated chemical potentials of U, Pu, and N. We also calculated the formation enthalpy of UN and PuN (Table 2), for comparison with experiments and previous theoretical work. As shown in Table 2, compared with the experimental results, the absolute values of the formation enthalpies are significantly underestimated by the PBE functional. On inclusion of dispersion (vdW-DF), the calculated ΔH_f of UN and PuN agree well with experiment and other computational work, indicating that van der Waals interactions are impor-

Table 2

Calculated formation enthalpy (ΔH_f) of UN and PuN using the PBE and vdW-DF functionals. Experimental and previous simulated results are listed for comparison.

	ΔH_f /eV			
	Exp [44,46]	APW+lo/PBE [47]	PBE	vdW-DF
UN	-3.01 ± 0.02	-3.02	-2.60	-2.93
PuN	-3.10 ± 0.03	-3.23	-2.74	-3.08

Table 3

Formation enthalpy (ΔH_f) and mixing enthalpy (ΔH_{mix}) of disordered and ordered $\text{U}_x\text{Pu}_{1-x}\text{N}$ using the vdW-DF functional.

	ΔH_f /eV		ΔH_{mix} /eV	
	disordered	ordered	disordered	ordered
$\text{U}_{0.75}\text{Pu}_{0.25}\text{N}$	-2.84	-2.86	0.12	0.10
$\text{U}_{0.5}\text{Pu}_{0.5}\text{N}$	-2.91	-2.88	0.10	0.13

tant in describing nitrides. By contrast to AnO_2 [44,45], the absolute value of the formation enthalpy of PuN is slightly larger than that of UN, indicating that the former is more energetically stable.

The formation enthalpies of the mixed nitrides can be found in Table 3; the values for disordered and ordered $\text{U}_{0.75}\text{Pu}_{0.25}\text{N}$ and $\text{U}_{0.5}\text{Pu}_{0.5}\text{N}$ are all negative, with the absolute values slightly increasing as the Pu content increases. This is consistent with the above finding that PuN has more negative ΔH_f than UN. The formation enthalpies of the disordered and ordered structures are close for $\text{U}_{0.75}\text{Pu}_{0.25}\text{N}$, but that for disordered $\text{U}_{0.5}\text{Pu}_{0.5}\text{N}$ is more

negative than for the ordered structure, indicating that the former is more energetically stable. The mixing enthalpies are positive for both $U_{0.75}Pu_{0.25}N$ and $U_{0.5}Pu_{0.5}N$, indicating that demixing is a possibility for the mixed nitrides. The non-zero values indicate (U, Pu)N are not ideal solid solutions, consistent with the lattice parameter data discussed earlier.

In summary, the uranium-plutonium mixed nitrides are not ideal solid solutions, and the $2 \times 2 \times 2$ supercell is sufficient to study the geometric properties of disordered $U_{0.75}Pu_{0.25}N$ and $U_{0.5}Pu_{0.5}N$. The DOS near the Fermi level of the mixed nitrides are the superposition of the f states of UN and PuN, and the peak positions are nearly independent of the Pu content. The formation enthalpy of $U_xPu_{1-x}N$ becomes more negative as the Pu content increases, indicating that $U_{0.5}Pu_{0.5}N$ is slightly more stable than $U_{0.75}Pu_{0.25}N$. Furthermore, ordered $U_{0.5}Pu_{0.5}N$ can be considered as consisting of UN and PuN layers stacked in a 1:1 ratio, and hence Xe incorporation and migration data within an ordered $U_{0.5}Pu_{0.5}N$ UN layer can be compared with our previous UN work to investigate the effect of mixing in Pu. Thus, we focus primarily on $U_{0.5}Pu_{0.5}N$ in the following defect and Ng migration studies.

3.2. Actinide vacancies in $U_{0.5}Pu_{0.5}N$

During the normal operation of a nuclear reactor, defects in the fuel matrix will be produced by the neutrons emitted and by fission product cascade, or by high temperature, with the former and the latter being called irradiation-induced defects and thermal defects, respectively [48]. These defects are critical for fission gas diffusion because they may serve as the accommodation site for fission gas atoms and assist fission gas migration. Previous studies have suggested that Ng has the lowest solution energy at the uranium vacancy (V_U) site in UN, as well as in UC which has a similar structure to UN [36,49]. Thus, we here focus mainly on actinide vacancies (V_{An}) in $U_{0.5}Pu_{0.5}N$, with some supporting results for $U_{0.75}Pu_{0.25}N$ also shown. As noted above, (U, Pu)N are not ideal solid solutions, and may have local ordering. We here assume that short-range ordering effects due to non-ideality can be neglected, as indeed did the recent study of (Pu, U)O₂ [37].

Zhao *et al.* found variable vacancy formation energy in the solid solution alloys, dependent on chemical environment [50]. This is also expected here for mixed nitrides considering the random distribution of the An sublattice. Therefore, we classify the vacancy according to the number of uranium atoms in the first and second nearest-neighbour shells ($N_U(1NN)$ and $N_U(2NN)$, respectively), and denote it as (a, b), where a and b are $N_U(1NN)$ and $N_U(2NN)$, respectively. For example, the structure of (8, 2) V_{Pu} is shown in Figure S6. The V_{An} formation energies in $U_{0.5}Pu_{0.5}N$ were calculated using Eq. (1), with the results shown in Fig. 4. Some V_{An} formation energies in $U_{0.75}Pu_{0.25}N$ were also calculated, and are given in Table S2.

Fig. 4 shows that E_f of V_U increases as $N_U(1NN)$ increases, but decreases as $N_U(2NN)$ increases, a trend also true for $U_{0.75}Pu_{0.25}N$ (Table S2). E_f of V_U in ordered $U_{0.5}Pu_{0.5}N$ is much smaller than that in the disordered structure. This is as expected considering that the chemical environment of V_U in ordered $U_{0.5}Pu_{0.5}N$ is (4, 6). The V_U formation energy in pure UN is calculated to be 2.97 eV (dotted line in Fig. 4) [28], which is larger than that of some V_U in disordered $U_{0.5}Pu_{0.5}N$. This indicates that the mixing in of Pu creates some low energy cost U vacancy sites. E_f of V_{Pu} shows the same trend as that of V_U (Figure S7).

3.3. Incorporation of Xe in $U_{0.5}Pu_{0.5}N$

In the previous section we found that defect formation energies are dependent on the chemical environment around the vacancy. To study the effect of chemical environment on Xe incor-

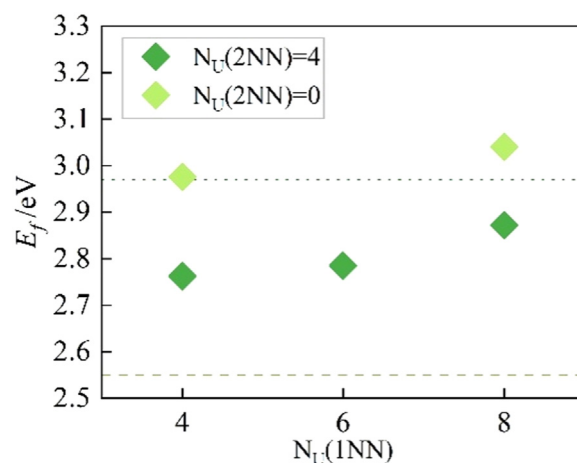


Fig. 4. U vacancy formation energy against the number of U atoms in the first nearest-neighbour shell ($N_U(1NN)$) and second nearest-neighbour shell ($N_U(2NN)$) in disordered $U_{0.5}Pu_{0.5}N$. The green dashed and dotted lines are the U vacancy formation energies in ordered $U_{0.5}Pu_{0.5}N$ and UN. The UN data are taken from Ref [28].

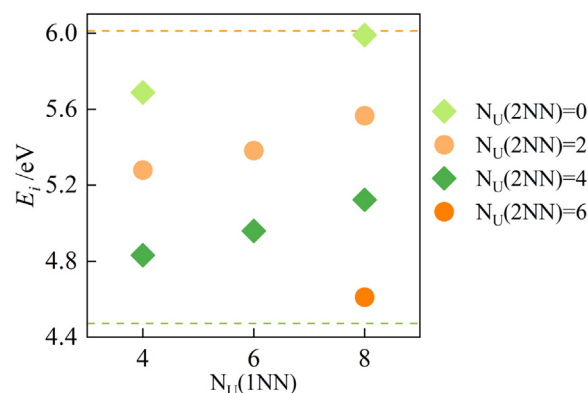


Fig. 5. Calculated Xe incorporation energy (E_i) at V_U (green) and V_{Pu} (orange) sites in disordered $U_{0.5}Pu_{0.5}N$ against the number of U atoms in the first nearest-neighbour shell ($N_U(1NN)$) and second nearest-neighbour shell ($N_U(2NN)$) around the Xe in disordered $U_{0.5}Pu_{0.5}N$. The green and orange dashed lines represent the E_i of Xe at V_U and V_{Pu} sites in ordered $U_{0.5}Pu_{0.5}N$.

poration, we calculated the incorporation energy of Xe in disordered $U_{0.5}Pu_{0.5}N$. The chemical environment around the Xe is as defined above. Fig. 5 shows that the E_i of Xe increases with increasing $N_U(1NN)$, but decreases with increasing $N_U(2NN)$, which is the same trend as that of E_f . Due to limited supercell size, there are no V_U and V_{Pu} vacancies that are in the same chemical environment, but it can be seen from the points in the $N_U(1NN) = 8$ column that E_i increases uniformly as $N_U(2NN)$ decreases regardless of the vacancy species, indicating the negligible effect of vacancy species on Xe incorporation. The E_i of Xe at the V_U and V_{Pu} sites in ordered $U_{0.5}Pu_{0.5}N$ are calculated to be 4.47 eV and 6.01 eV, respectively, shown as the green and orange dashed lines in Fig. 5. The E_i of Xe at the (8, 0) V_U site (5.98 eV) in disordered $U_{0.5}Pu_{0.5}N$ is close to the 6.01 eV of Xe at the V_{Pu} site in ordered $U_{0.5}Pu_{0.5}N$, the chemical environment of which is also (8, 0). This further illustrates that the Xe incorporation energy is independent of the vacancy species, but highly dependent on the vacancy chemical environment. Bader analysis (Table S3) shows that the charge of Xe at the vacancy sites is low and similar at different sites, indicating weak interaction between the matrix atoms and the solute Xe atom, also shown by the charge density distribution (Figure S8).

The dependence of Xe incorporation energy on the chemical environment can be attributed to the vacancy steric space. The de-

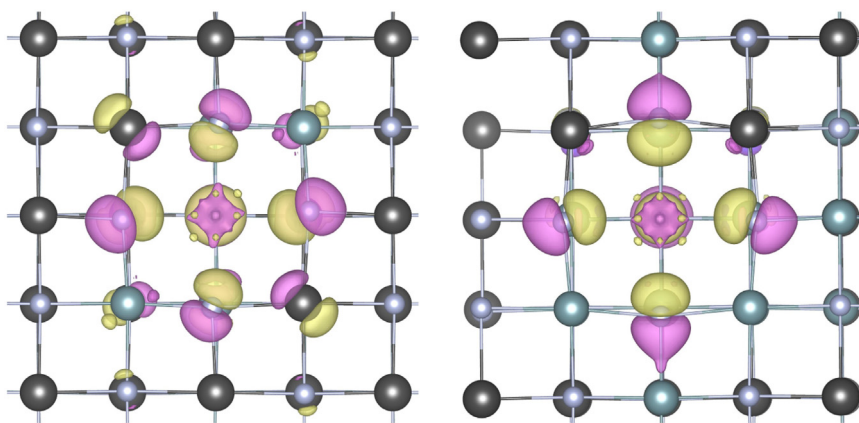


Fig. 6. Charge density difference of (8, 2) and (8, 6) V_{Pu} in disordered $U_{0.5}Pu_{0.5}N$. The purple and yellow represent positive and negative charge density, respectively.

pendence on $N_U(1NN)$ is because the cationic size of U is slightly larger than that of Pu. Thus, the smaller $N_U(1NN)$, the larger the vacancy space. To study the dependence of E_i on $N_U(2NN)$, the charge density differences of the (8, 2) and (8, 6) V_{Pu} supercells were calculated. Fig. 6 shows that compared with the perfect supercell, the charge density between the N and the vacancy site in the defect supercells decreases, while the density around the N increases in the direction away from the vacancy. Meanwhile, the neighbouring N atoms move away from the vacancy towards the 2NN actinide atoms. As noted in Section 3.1, charge transfer between U and N is more significant than that between Pu and N. Thus, the displacements of the N atom bonded to the U(2NN) are larger than those of the N atoms bonded to the Pu(2NN), which are calculated to be 0.21 Å and 0.14 Å for the N atoms bonded to the U(2NN) and Pu(2NN), respectively, in $U_{0.5}Pu_{0.5}N$ with (6, 2) V_U . As a result, the larger the $N_U(2NN)$, the larger the vacancy space, and the lower the Xe incorporation energy.

In previous work, we found that the incorporation behaviour of Kr in UN is similar to that of Xe [18]. Thus, the trend in the effect of the chemical environment is expected to be the same for Kr as for Xe. The E_i of Kr at the V_U and V_{Pu} sites in ordered $U_{0.5}Pu_{0.5}N$ are calculated to be 3.30 eV and 4.64 eV, respectively, which are smaller than for Xe due to the smaller atomic size. The E_i of Kr in disordered $U_{0.5}Pu_{0.5}N$ are expected to be within this range.

3.4. Migration of Xe in $U_{0.5}Pu_{0.5}N$

The energy barriers for Xe migration in $U_{0.5}Pu_{0.5}N$ are presented in this section. We here mainly consider the direct exchange of Xe atoms with nearest neighbour vacancies, considering that the vacancy-assisted mechanism governs fission gas diffusion in UN [28,36]. As we found above that the Xe incorporation energy is highly dependent on the chemical environment of the vacancy, but independent of the vacancy species, it is therefore expected that the vacancy chemical environment will also affect the migration energy. To probe this, we calculated the Xe migration energy barrier (E_m) along two possible pathways that can be identified in our disordered $U_{0.5}Pu_{0.5}N$ model, with the results being listed in Table 4. The initial and final states are represented by the vacancy chemical environment as defined above. The forward (E_m^f) or reverse (E_m^r) migration energy is the energy difference between the transition state (TS) and the initial (IS) or the final state (FS).

Table 4 shows that E_m^f and E_m^r are different for the same pathway, which is also found for Ni-based solid solution alloys [50]. This can be attributed to the chemical disorder of the mixed nitride. Wolverton *et al.* found that the incorporation of the solute atoms generates strain on the neighbouring matrix atoms [51], and

Table 4

Migration energy barrier (E_m) for Xe diffusion in $U_{0.5}Pu_{0.5}N$ at the (a, b) vacancy site, in which a and b are the number of U atoms in the first and second nearest-neighbour shells around the vacancy.

	E_m /eV	
	E_m^f	E_m^r
(4, 2) \rightarrow (4, 0)	1.15	0.73
(4, 4) \rightarrow (4, 0)	1.33	0.64

a vacancy at the nearest-neighbouring position around the solute helps to relieve the strain by relaxing the solute atom towards that vacancy. Naghavi *et al.* also reported displacement of the solute atom towards the other vacancy in FCC cobalt [52]. In UN, the displacement of Xe in the IS and FS are the same considering the equivalent structures of the IS and FS, and the TS is located at the mid point of the two vacancies. The total energy of the system increases smoothly from the IS to the TS, and then decreases to the FS, giving the same energy barrier (1.16 eV) forwards or backwards along the migration pathway [28]. However, in disordered $U_{0.5}Pu_{0.5}N$, the IS and FS structures are nonequivalent, which leads to different degrees of displacement of Xe towards the TS. We here take the (4, 2) \rightarrow (4, 0) pathway as an example; Fig. 7 shows that the Xe atom in the IS and FS deviates from the lattice sites, more obviously in the FS. This is because the steric space of the (4, 0) vacancy is smaller than that of the (4, 2), so Xe displaces more to relieve the strain. In other words, the smaller the vacancy space, the larger the displacement of Xe towards another vacancy. In the transition state (TS), Xe is located between two vacancies and is surrounded by four Pu atoms (Figure S9). N atoms move away from Xe to create enough space for Xe to pass through. The (4, 4) \rightarrow (4, 0) pathway has a similar TS configuration, in which Xe is also surrounded by 4 Pu atoms. By comparing the E_m^f of the two pathways we can see that with the same FS, the larger the IS vacancy space, the higher the energy barrier, while for the pathway with the same IS, the larger the FS vacancy space, the smaller the energy barrier.

Due to the complicated situation of the disordered supercell, it is impractical to calculate all migration pathways. We found above that the Xe incorporation energy at the V_{Pu} and V_U sites in ordered $U_{0.5}Pu_{0.5}N$ set the upper and lower limits for Xe incorporation in $U_{0.5}Pu_{0.5}N$, because the (8, 0) V_{Pu} and (4, 6) V_U have the smallest and largest vacancy steric space. Thus, it is expected that the E_m

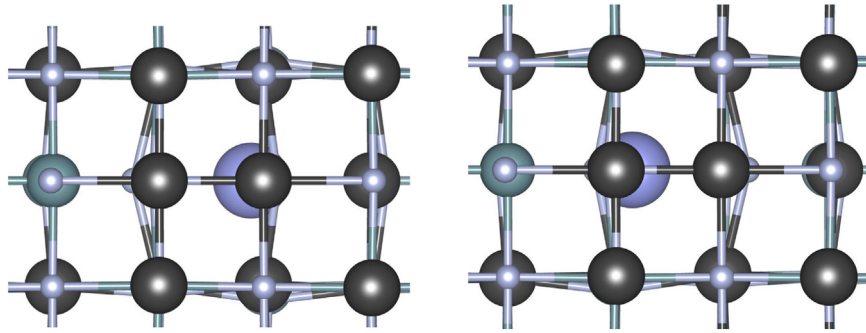


Fig. 7. Initial state (left) and final state (right) structures of Xe migration along the (4, 2) → (4, 0) pathway.

Table 5

Migration energy barriers (E_m) for Xe in $U_{0.5}Pu_{0.5}N$ along four processes. The initial and final state vacancy site is defined as (a, b), in which a and b are the number of U atoms in the first and second nearest-neighbour shells around the vacancy.

	E_m /eV
(i) (4,6) → (4, 6)	1.40
(ii) (4, 6) → (8, 0)	1.75
(iii) (8, 0) → (4, 6)	0.50
(iv) (8, 0) → (8,0)	1.01

in ordered $U_{0.5}Pu_{0.5}N$ could also set the range for Xe diffusion in disordered $U_{0.5}Pu_{0.5}N$.

As shown in Figure S3, the UN and PuN layers are stacked in a 1:1 ratio in ordered $U_{0.5}Pu_{0.5}N$, similar to the L1₀-ordered TiAl alloy. Ikeda *et al.* experimentally studied the monovacancy-assisted impurity (Ni and In) diffusion in TiAl and theoretically proposed a solute diffusion model, which can be used in our work [53]. Based on their model, vacancy-assisted Xe diffusion could happen by four processes: (i) within the UN layer; (ii) from the UN layer to the PuN layer; (iii) from the PuN layer to UN layer; (iv) within the PuN layer. We simulated the migration of Xe by these processes, and the calculated energy barriers are listed in Table 5.

We can see that Xe has the highest and lowest migration barriers by processes (ii) and (iii), with E_m of 1.75 eV and 0.50 eV, respectively. This suggests that the E_m range of Xe in disordered $U_{0.5}Pu_{0.5}N$ is 0.5–1.75 eV. As expected, the E_m of the two representative Xe pathways in disordered $U_{0.5}Pu_{0.5}N$ (Table 4) are within this range. The comparison between processes (i) and (iii), as well as (ii) and (iv), illustrates our finding that with the same FS, the larger the IS vacancy space, the higher the energy barrier. Furthermore, the comparison between processes (i) and (ii), as well as (iii) and (iv), shows that with the same IS, the larger the FS vacancy space, the lower the energy barrier. The migration energies of Kr by these four processes (Table S4) have the same trend as that of Xe, with the energy range of 0.30–1.25 eV. It is not unexpected to find the lower energy barrier for Kr considering the smaller atomic size of Kr compared with that of Xe, which is consistent with the trend in UN [28].

As reported in our previous work, the migration energy barrier of Ng in UN is 1.16 eV and 0.78 eV for Xe and Kr, respectively [28], which are smaller than the E_m of Xe and Kr within the UN layer (process (i)) in $U_{0.5}Pu_{0.5}N$. This shows that the mixing of PuN into UN inhibits the migration of fission gas atoms within the UN sublattice. However, with the help of a Pu vacancy site, the energy barriers are lower than that in UN (process (iii)).

Finally, we note that our Xe incorporation and migration energy ranges, and chemical environment dependence, are based on some representative structures, as DFT is too expensive to conduct an exhaustive study. A similar situation holds true for the defect

formation energies studied in Section 3.2. Future work, most likely using empirical potentials as employed by Bathellier *et al.* for (U, Pu)O₂ [37], should be able to interrogate a more complete set of structures.

4. Conclusions

In this contribution, we have investigated the bulk properties of $U_{0.75}Pu_{0.25}N$ and $U_{0.5}Pu_{0.5}N$, and studied the migration behaviour of fission gas atom Xe, in $U_{0.5}Pu_{0.5}N$. We began by modelling disordered $U_{0.75}Pu_{0.25}N$ and $U_{0.5}Pu_{0.5}N$ structures using the Special Quasi-random Structure method with $2 \times 2 \times 2$ and $3 \times 3 \times 3$ supercells. The similar lattice parameter and bond length obtained from the two supercells suggest that the $2 \times 2 \times 2$ is sufficient to study disordered mixed nitrides. The density of states (DOS) indicates that both $U_{0.75}Pu_{0.25}N$ and $U_{0.5}Pu_{0.5}N$ are metallic with the main contributions to the DOS around the Fermi level being from the An f orbital. Pu f states are located at lower energy than U f, consistent with the trend of increasing f orbital stability across the actinide series. The formation enthalpies of $U_{0.75}Pu_{0.25}N$ and $U_{0.5}Pu_{0.5}N$ are −2.84 eV and −2.91 eV, respectively, indicating that the latter is more stable. The non-zero mixing enthalpies indicate that (U, Pu)N are not ideal solid solutions.

We then simulated the actinide vacancy in disordered and ordered $U_{0.5}Pu_{0.5}N$ and studied the effect of the chemical environment. We found that the defect formation energies of V_{Pu} and V_U increase as the number of U atoms in the first nearest-neighbour shell ($N_U(1NN)$) increases, but decrease as the number of U atoms in the second nearest-neighbour shell ($N_U(2NN)$) increases.

Then, we studied the incorporation of Xe at the actinide vacancy in disordered and ordered $U_{0.5}Pu_{0.5}N$. The incorporation energy of Xe in disordered $U_{0.5}Pu_{0.5}N$ is found to be independent of vacancy species, depending only on the chemical environment of the vacancy. The incorporation energy increases with increasing $N_U(1NN)$, but decreases with increasing $N_U(2NN)$, as does E_f . This is because the smaller the $N_U(1NN)$ and the larger the $N_U(2NN)$, the larger the vacancy steric space. The incorporation energy of Xe at V_U and V_{Pu} sites in ordered $U_{0.5}Pu_{0.5}N$ are 4.47 eV and 6.01 eV, respectively, which are the lower and upper limits for the E_i in disordered $U_{0.5}Pu_{0.5}N$. This is as expected considering the steric space of V_U and V_{Pu} in ordered $U_{0.5}Pu_{0.5}N$ are the largest and smallest compared with that in the disordered $U_{0.5}Pu_{0.5}N$. Comparative calculations for Kr show that its incorporation energy range is 3.30–4.64 eV.

Finally, we simulated the migration of Xe in disordered $U_{0.5}Pu_{0.5}N$ along two representative pathways. The calculated energy barriers show that with the same final state (FS), the larger the initial state (IS) vacancy space, the higher the energy barrier. While for the pathway with the same IS, the larger the FS vacancy space, the smaller the energy barrier. The migration energy barrier in ordered $U_{0.5}Pu_{0.5}N$ is expected to set the energy range for

Xe diffusion in disordered $U_{0.5}Pu_{0.5}N$ considering that V_{Pu} and V_U in ordered $U_{0.5}Pu_{0.5}N$ have the smallest and largest vacancy steric space; the range is 0.50–1.75 eV. The energy range for Kr is 0.30–1.25 eV, which is lower than Xe due to the smaller atomic size of Kr. Comparison with E_m of 1.16 eV and 0.78 eV for Xe and Kr in UN indicates that the mixing of PuN into UN creates some low-barrier diffusion pathways.

Declaration of Competing Interest

The authors declare that they have no known competing financial interests or personal relationships that could have appeared to influence the work reported in this paper.

CRediT authorship contribution statement

Lin Yang: Conceptualization, Investigation, Methodology, Formal analysis, Funding acquisition, Software, Writing – original draft, Writing – review & editing. **Nikolas Kaltsoyannis:** Supervision, Resources, Funding acquisition, Project administration, Writing – review & editing.

Data availability

Data will be made available on request.

Acknowledgements

We are grateful to the China Scholarship Council and The University of Manchester for a PhD studentship for LY. We are also grateful to The University of Manchester for its Computational Shared Facility (CSF3, CSF4 and HPC pool) and associated support services.

Supplementary materials

Supplementary material associated with this article can be found, in the online version, at [doi:10.1016/j.jnucmat.2023.154330](https://doi.org/10.1016/j.jnucmat.2023.154330).

References

- [1] A. Grachev, L. Zabud'ko, A. Glushenkov, Y.A. Ivanov, G. Kireev, M. Skupov, I. Gil'mutdinov, P. Grin, E. Zvir, F. Kryukov, Investigations of mixed uranium–plutonium nitride fuel in project breakthrough, *Atomic Energy* 122 (3) (2017) 185–199.
- [2] B. Rogozkin, N. Stepenova, Y.E. Fedorov, M. Shishkov, F. Kryukov, S. Kuzmin, O. Nikitin, A. Belyaeva, L. Zabudko, Results of $U_{0.55}Pu_{0.45}N$ and $U_{0.4}Pu_{0.6}$ mixed mononitride fuel tests in a BOR-60 reactor to burnup 12% ha, *Atomic Energy* 110 (6) (2011) 412–429.
- [3] K. Tanaka, K. Maeda, K. Katsuyama, M. Inoue, T. Iwai, Y. Arai, Fission gas release and swelling in uranium–plutonium mixed nitride fuels, *J. Nucl. Mater.* 327 (2–3) (2004) 77–87.
- [4] D. Veprev, A. Boldyrev, S.Y. Chernov, Validation of the BERKUT fuel rod module against mixed nitride fuel experimental data, *Ann. Nucl. Energy* 135 (2020) 106963.
- [5] L.A. Bolshov, V.F. Strizhov, N.A. Mosunova, Codes of new generation for safety justification of power units with a closed nuclear fuel cycle developed for the “PRORYV” project, *Nucl. Energy Technol.* 6 (2020) 203.
- [6] K. Sato, L. Bergqvist, J. Kudrnovský, P.H. Dederichs, O. Eriksson, I. Turek, B. Sanyal, G. Bouzerar, H. Katayama-Yoshida, V. Dinh, First-principles theory of dilute magnetic semiconductors, *Rev. Mod. Phys.* 82 (2) (2010) 1633.
- [7] A. Seko, K. Yuge, F. Oba, A. Kuwabara, I. Tanaka, Prediction of ground-state structures and order-disorder phase transitions in II–III spinel oxides: a combined cluster-expansion method and first-principles study, *Phys. Rev. B* 73 (18) (2006) 184117.
- [8] J. von Pezold, A. Dick, M. Friák, J. Neugebauer, Generation and performance of special quasirandom structures for studying the elastic properties of random alloys: application to Al–Ti, *Phys. Rev. B* 81 (9) (2010) 094203.
- [9] A. Zunger, S.-H. Wei, L. Ferreira, J.E. Bernard, Special quasirandom structures, *Phys. Rev. Lett.* 65 (3) (1990) 353.
- [10] A. Van de Walle, P. Tiwary, M. De Jong, D. Olmsted, M. Asta, A. Dick, D. Shin, Y. Wang, L.-Q. Chen, Z.-K. Liu, Efficient stochastic generation of special quasirandom structures, *CALPHAD: Comput. Coupl. Phase Diagram. Thermochem.* 42 (2013) 13–18.
- [11] P. Ghosh, A. Arya, Structural, thermodynamic, electronic and elastic properties of $Th_{1-x}U_xO_2$ and $Th_{1-x}Pu_xO_2$ mixed oxides, *Phys. Chem. Chem. Phys.* 22 (11) (2020) 6406–6417.
- [12] M.S. Talla Noutack, G. Geneste, G. Jomard, M. Freyss, Investigation of the bulk and point defect properties in uranium–plutonium mixed oxides (U, Pu) O_2 using DFT+ U: effect of a low americium content, *J. Appl. Phys.* 131 (22) (2022) 225106.
- [13] S. Dudarev, D.N. Manh, A. Sutton, Effect of Mott–Hubbard correlations on the electronic structure and structural stability of uranium dioxide, *Philos. Mag. B* 75 (5) (1997) 613–628.
- [14] S.-i. Fujimori, T. Ohkouchi, T. Okane, Y. Saitoh, A. Fujimori, H. Yamagami, Y. Haga, E. Yamamoto, Y. Onuki, Itinerant nature of U 5f states in uranium mononitride revealed by angle-resolved photoelectron spectroscopy, *Phys. Rev. B* 86 (23) (2012).
- [15] X.-D. Wen, R.L. Martin, G.E. Scuseria, S.P. Rudin, E.R. Batista, A Screened hybrid DFT study of actinide oxides, nitrides, and carbides, *J. Phys. Chem. C* 117 (25) (2013) 13122–13128.
- [16] L. Yang, N. Kaltsoyannis, Incorporation of Kr and Xe in uranium mononitride: a density functional theory study, *J. Phys. Chem. C* 125 (48) (2021) 26999–27008.
- [17] V. Kocovski, D.A. Rehn, M.W. Cooper, D.A. Andersson, First-principles investigation of uranium mononitride (UN): effect of magnetic ordering, spin-orbit interactions and exchange correlation functional, *J. Nucl. Mater.* 559 (2022) 153401.
- [18] L. Petit, A. Svane, Z. Szotek, W.M. Temmerman, G.M. Stocks, Ground-state electronic structure of actinide monocarbides and mononitrides, *Phys. Rev. B* 80 (4) (2009) 045124.
- [19] L. Petit, A. Svane, W. Temmerman, Z. Szotek, Electronic structure of Pu monochalcogenides and mononitrides, *Eur. Phys. J. B-Condensed Matter Complex Syst.* 25 (2) (2002) 139–146.
- [20] R. Atta-Fynn, A.K. Ray, Density functional study of the actinide nitrides, *Phys. Rev. B* 76 (11) (2007) 115101.
- [21] R.-s. Li, N.-h. Tong, J.-t. Wang, D.-q. Xin, S.-q. Huang, A first principle calculation on electronic properties of plutonium mononitride: insights from dynamical mean field theory, *J. Nucl. Mater.* 511 (2018) 277–283.
- [22] R. Yang, B. Tang, T. Gao, A hybrid density functional study on PuN, *Acta Physica Polonica A* 133 (1) (2018) 32–38.
- [23] A. Boeuf, R. Caciuffo, J. Fournier, L. Manes, J. Rebizant, E. Roudaut, F. Rustichelli, ^{239}PuN powder neutron diffraction study, *Solid State Commun.* 52 (4) (1984) 451–453.
- [24] P. Söderlind, E.E. Moore, C.J. Wu, Thermodynamics modeling for actinide monocarbides and mononitrides from first principles, *Appl. Sci.* 12 (2) (2022) 728.
- [25] J.-L. Chen, N. Kaltsoyannis, DFT+ U study of uranium dioxide and plutonium dioxide with occupation matrix control, *J. Phys. Chem. C* 126 (27) (2022) 11426–11435.
- [26] L. Yang, N. Kaltsoyannis, Diffusion of krypton and xenon in uranium mononitride: a density functional theory study, *J. Nucl. Mater.* 566 (2022) 153803.
- [27] G. Kresse, J. Hafner, Ab initio molecular dynamics for liquid metals, *Phys. Rev. B* 47 (1) (1993) 558.
- [28] G. Kresse, J. Furthmüller, Efficiency of ab-initio total energy calculations for metals and semiconductors using a plane-wave basis set, *Comput. Mater. Sci.* 6 (1) (1996) 15–50.
- [29] G. Kresse, J. Furthmüller, Efficient iterative schemes for ab initio total-energy calculations using a plane-wave basis set, *Phys. Rev. B* 54 (16) (1996) 11169.
- [30] J.P. Perdew, K. Burke, M. Ernzerhof, Generalized gradient approximation made simple, *Phys. Rev. Lett.* 77 (18) (1996) 3865.
- [31] M. Dion, H. Rydberg, E. Schröder, D.C. Langreth, B.I. Lundqvist, Van der Waals density functional for general geometries, *Phys. Rev. Lett.* 92 (24) (2004) 246401.
- [32] G. Henkelman, H. Jónsson, Improved tangent estimate in the nudged elastic band method for finding minimum energy paths and saddle points, *J. Chem. Phys.* 113 (22) (2000) 9978–9985.
- [33] G. Henkelman, B.P. Uberuaga, H. Jónsson, A climbing image nudged elastic band method for finding saddle points and minimum energy paths, *J. Chem. Phys.* 113 (22) (2000) 9901–9904.
- [34] A. Claisse, T. Schuler, D.A. Lopes, P. Olsson, Transport properties in dilute UN(X) solid solutions (X=Xe,Kr), *Phys. Rev. B* 94 (17) (2016) 174302.
- [35] D. Bathellier, L. Messina, M. Freyss, M. Bertolus, T. Schuler, M. Nastar, P. Olsson, E. Bourasseau, Effect of cationic chemical disorder on defect formation energies in uranium–plutonium mixed oxides, *J. Appl. Phys.* 132 (17) (2022) 175103.
- [36] P.A. Burr, M.W.D. Cooper, Importance of elastic finite-size effects: neutral defects in ionic compounds, *Phys. Rev. B* 96 (9) (2017) 094107.
- [37] V. Tennery, E. Bomar, Lattice Parameters of (U, Pu) N Solid Solutions, *J. Am. Ceramic Soc.* 54 (5) (1971) 247–249.
- [38] A.R. Denton, N.W. Ashcroft, Vegard's law, *Phys. Rev. A* 43 (6) (1991) 3161.
- [39] J.-L. Chen, N. Kaltsoyannis, Hybrid functional/embedded cluster study of uranium and actinide (actinide= Np, Pu, Am or Cm) mixed dioxides bulk and {110} surfaces, *J. Nucl. Mater.* 560 (2022) 153490.

- [42] L. Havela, F. Wastin, J. Rebizant, T. Gouder, Photoelectron spectroscopy study of PuN, *Phys. Rev. B* 68 (8) (2003) 085101.
- [43] I.C. Njifon, M. Bertolus, R. Hayn, M. Freyss, Electronic structure investigation of the bulk properties of uranium-plutonium mixed oxides (U, Pu)O₂, *Inorg Chem.* 57 (17) (2018) 10974–10983.
- [44] G.K. Johnson, E.H. Van Deventer, O.L. Kruger, W.N. Hubbard, The enthalpies of formation of plutonium dioxide and plutonium mononitride, *J. Chem. Thermodyn.* 1 (1) (1969) 89–98.
- [45] G. Johnson, W. Steele, The standard enthalpy of formation of uranium dioxide by fluorine bomb calorimetry, *J. Chem. Thermodyn.* 13 (8) (1981) 717–723.
- [46] G.K. Johnson, E. Cordfunke, The enthalpies of formation of uranium mononitride and α - and β -uranium sesquinitride by fluorine bomb calorimetry, *J. Chem. Thermodyn.* 13 (3) (1981) 273–282.
- [47] D. Sedmidubský, R. Konings, P. Novak, Calculation of enthalpies of formation of actinide nitrides, *J. Nucl. Mater.* 344 (1–3) (2005) 40–44.
- [48] V.V. Rondinella, T. Wiss, The high burn-up structure in nuclear fuel, *Mater. Today* 13 (12) (2010) 24–32.
- [49] G.-Y. Huang, G. Pastore, B.D. Wirth, First-principles study of intrinsic point defects and Xe impurities in uranium monocarbide, *J. Appl. Phys.* 128 (14) (2020) 145102.
- [50] S. Zhao, G.M. Stocks, Y. Zhang, Defect energetics of concentrated solid-solution alloys from ab initio calculations: $\text{Ni}_{0.5}\text{Co}_{0.5}$, $\text{Ni}_{0.5}\text{Fe}_{0.5}$, $\text{Ni}_{0.8}\text{Fe}_{0.2}$ and $\text{Ni}_{0.8}\text{Cr}_{0.2}$, *Phys. Chem. Chem. Phys.* 18 (34) (2016) 24043–24056.
- [51] C. Wolverton, Solute–vacancy binding in aluminum, *Acta Mater.* 55 (17) (2007) 5867–5872.
- [52] S.S. Naghavi, V.I. Hegde, C. Wolverton, Diffusion coefficients of transition metals in fcc cobalt, *Acta Mater.* 132 (2017) 467–478.
- [53] T. Ikeda, H. Kadowaki, H. Nakajima, Diffusion of ⁴⁴Ti and ⁶³Ni in TiAl single crystal, *Acta Mater.* 49 (17) (2001) 3475–3485.

**Incorporation and migration of xenon in uranium-plutonium mixed nitride; a Density
Functional Theory Study**

Lin Yang and Nikolas Kaltsoyannis*

Department of Chemistry, School of Natural Sciences, The University of Manchester, Oxford
Road, Manchester M13 9PL

Supplementary Information

Modeling the disordered $U_{0.75}Pu_{0.25}N$ and $U_{0.5}Pu_{0.5}N$. Mixed (U, Pu)N is a solid solution that has the same face-centred cubic (FCC) structure as that of UN and PuN. Pu and U atoms are randomly distributed in the actinide sublattice with the N sublattice being the same as that in the mononitrides. We modeled the disordered $U_{0.75}Pu_{0.25}N$ and $U_{0.5}Pu_{0.5}N$ by the SQS method using the *mcsqs* module implemented in the Alloy Theoretic Automated Toolkit (ATAT) [1, 2]. This method is based on Monte Carlo simulation to minimize an objective function that seeks to match the maximum number of cluster correlation functions. We considered pair, triplet, and quadruple correlation with the cut-off of the fifth, second, and nearest-neighbour sites, respectively. Two different supercell sizes, $2 \times 2 \times 2$ and $3 \times 3 \times 3$, were used. The search for the perfect SQS structure was considered to have stopped when no new structures were generated within 24 hours. The total energies of the generated structures were calculated using the settings given in the main text, and shown in Figure S1 and S2. The cluster correlations of the generated SQS supercells are also shown in Figure S1 and S2.

The relative cluster correlations Π_{ab} represents the correlation of a -vertex cluster with the cut-off of b (e.g., Π_{22} represents the pair correlation between an atom and its second nearest-neighbour atoms) related to the corresponding perfectly random alloy. Thus, the more zeros are in the Π_{ab} , the closer the generated SQS is to an ideally random distribution. The ideal SQS is reached if all Π_{ab} values are zero. Due to the large cluster and cut-off that we considered, the ideal SQS is only found for $2 \times 2 \times 2$ $U_{0.5}Pu_{0.5}N$. But the best SQS does not represent the lowest-energy structure. It can be found from Figure S1 that for $2 \times 2 \times 2$ $U_{0.5}Pu_{0.5}N$, the SQS-4 has the lowest total energy, i.e., the most thermodynamically stable, although the degree of random distribution is worse than that of SQS-17. This is also true for other systems.

The standard deviations of the total energies are quite small, 0.02 eV and 0.03 eV for $2 \times 2 \times 2$ $U_{0.75}Pu_{0.25}N$ and $U_{0.5}Pu_{0.5}N$, and 0.09 eV and 0.05 eV for $3 \times 3 \times 3$ $U_{0.75}Pu_{0.25}N$ and $U_{0.5}Pu_{0.5}N$, respectively. This suggests the thermodynamic stabilities of the generated SQS supercells are close.

To study the geometric properties of disordered $U_{0.75}Pu_{0.25}N$ and $U_{0.5}Pu_{0.5}N$, we selected three structures for each $U_xPu_{1-x}N$: one has the best relative cluster correlations, one has the lowest total energy, and one by combining the total energy and cluster correlations. The optimized lattice parameter and bond distance of the selected structures are shown in Table S1. The average value of three structures is used in the main text.

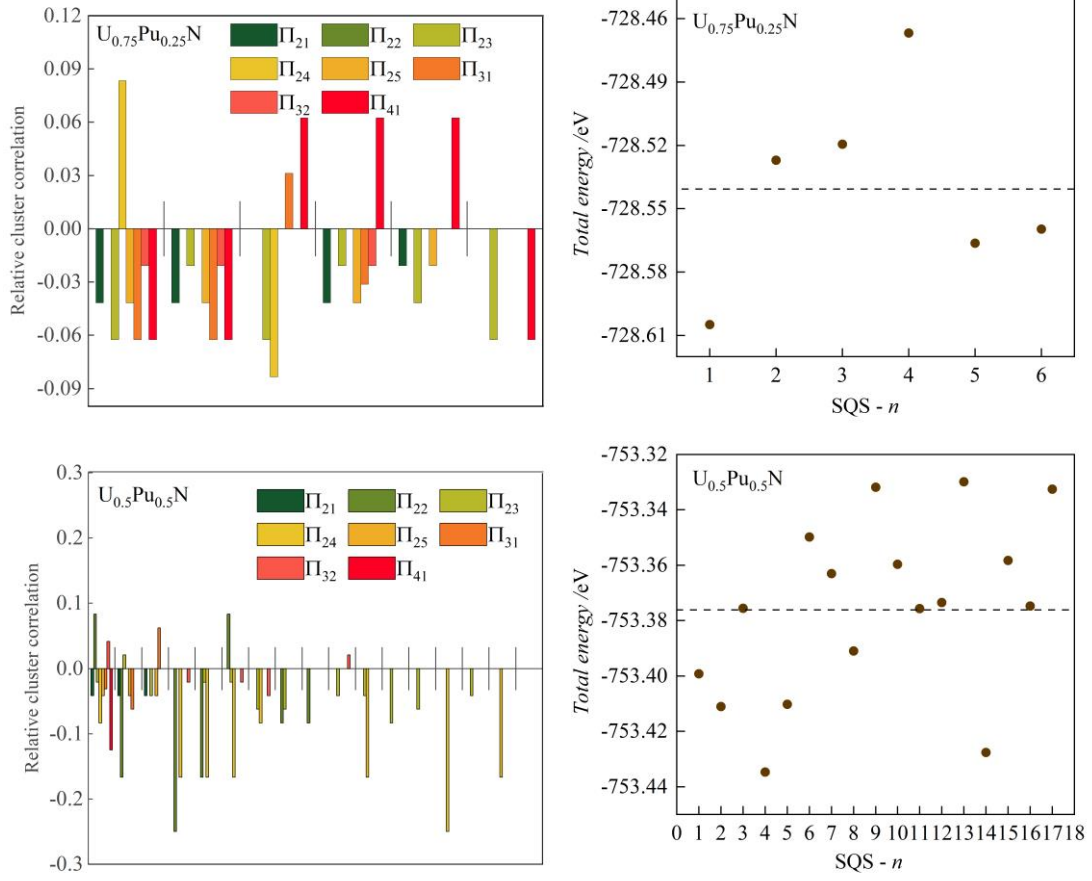


Figure S1. Relative cluster correlations (Π_{ab}) (left) and total energies (right) of the generated $2 \times 2 \times 2$ $\text{U}_{0.75}\text{Pu}_{0.25}\text{N}$ and $\text{U}_{0.5}\text{Pu}_{0.5}\text{N}$ SQS supercells. The dashed lines in the right figures represent the average total energy. SQS- n represents the n^{th} generated SQS supercells.

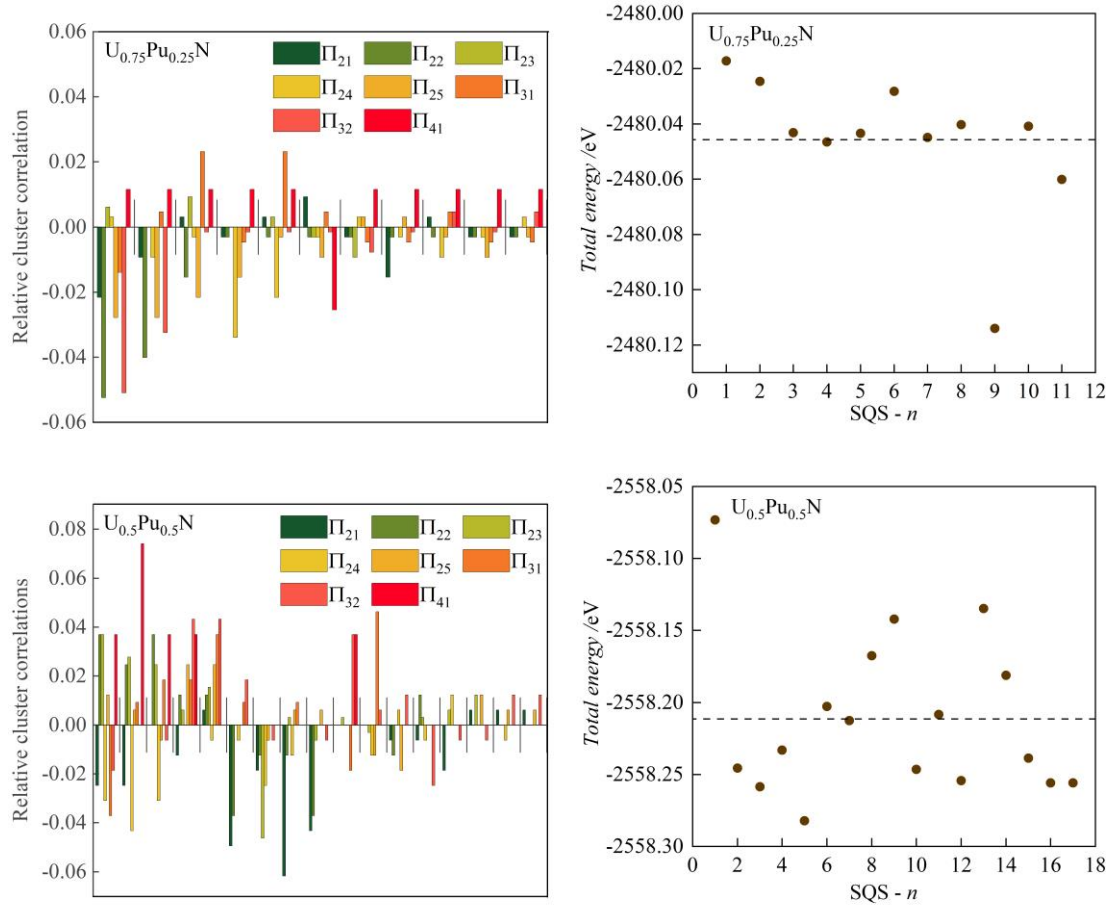


Figure S2. Relative cluster correlations (Π_{ab}) (left) and total energies (right) of the generated $3 \times 3 \times 3$ $U_{0.75}Pu_{0.25}N$ and $U_{0.5}Pu_{0.5}N$ SQS supercells. The dashed lines in the right figures represent the average total energy. SQS- n represents the n^{th} generated SQS supercells.

Table S1. Calculated lattice parameter (a), U-N bond distance ($d_{\text{U-N}}$), and Pu-N bond distance ($d_{\text{Pu-N}}$) in selected $\text{U}_{0.75}\text{Pu}_{0.25}\text{N}$ and $\text{U}_{0.5}\text{Pu}_{0.5}\text{N}$ supercells.

	Supercell size	SQS structure	a / Å	$d_{\text{U-N}}$ / Å	$d_{\text{Pu-N}}$ / Å
$\text{U}_{0.75}\text{Pu}_{0.25}\text{N}$	$2 \times 2 \times 2$	SQS-1	4.878	2.431	2.466
		SQS -5	4.878	2.430	2.466
		SQS -6	4.878	2.430	2.466
	$3 \times 3 \times 3$	SQS -9	4.874	2.425	2.476
		SQS -10	4.876	2.426	2.476
		SQS -11	4.874	2.425	2.475
$\text{U}_{0.5}\text{Pu}_{0.5}\text{N}$	$2 \times 2 \times 2$	SQS -4	4.889	2.417	2.473
		SQS -14	4.888	2.422	2.467
		SQS -17	4.889	2.422	2.468
	$3 \times 3 \times 3$	SQS -5	4.886	2.414	2.474
		SQS -10	4.886	2.415	2.473
		SQS -17	4.886	2.414	2.474

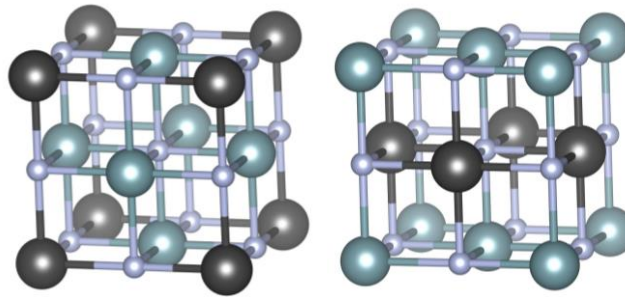


Figure S3. Ordered $\text{U}_{0.75}\text{Pu}_{0.25}\text{N}$ (left) and $\text{U}_{0.5}\text{Pu}_{0.5}\text{N}$ (right) bulk. Black, teal, and grey balls represent plutonium, uranium, and nitrogen, respectively.

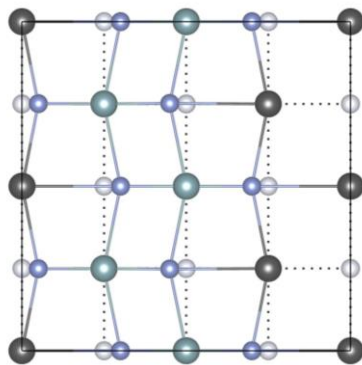


Figure S4. Schematic of N displacements in $\text{U}_{0.5}\text{Pu}_{0.5}\text{N}$. Grey, teal, and black balls represent the N, U, and Pu, respectively. The white ball represents the ideal site for N. The degree of displacement has been exaggerated to show the direction of N displacement.

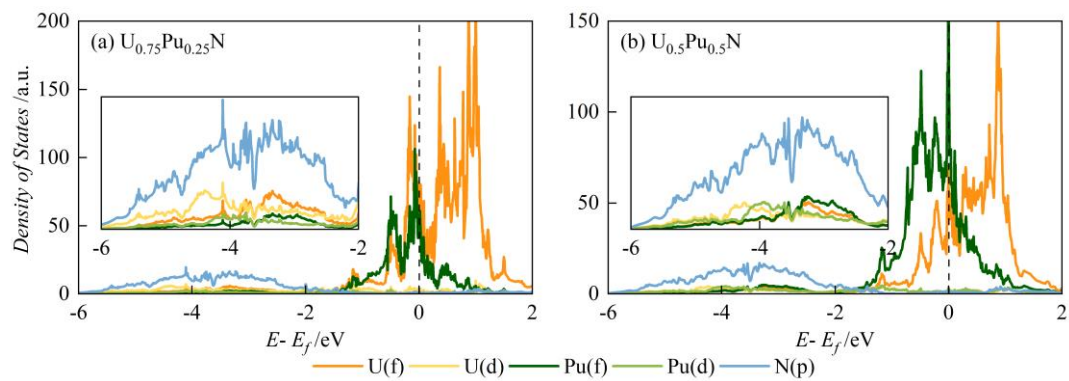


Figure S5. Density of states of ordered $\text{U}_{0.75}\text{Pu}_{0.25}\text{N}$ and $\text{U}_{0.5}\text{Pu}_{0.5}\text{N}$.

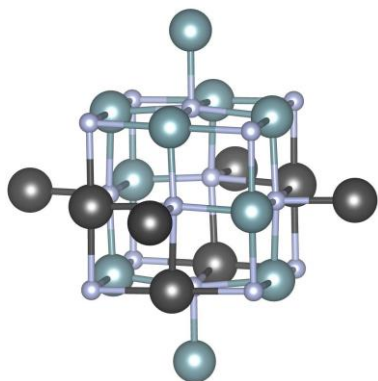


Figure S6. $(8, 2) V_{\text{pu}}$ in disordered $\text{U}_{0.5}\text{Pu}_{0.5}\text{N}$. Black, teal, and grey ball represent plutonium, uranium, and nitrogen, respectively.

Table S2. Calculated U and Pu vacancy formation energies in disordered $U_{0.75}Pu_{0.25}N$ against the chemical environment (a, b), where a and b are the number of U atoms in the first nearest-neighbour shell ($N_U(1NN)$) and second nearest-neighbour shell ($N_U(2NN)$) around the vacancy.

V_U		V_{Pu}	
(a, b)	E_f /eV	(a, b)	E_f /eV
(6,4)	2.92	(8,6)	3.19
(8,6)	2.91	(9,6)	3.26
(9,6)	2.93		

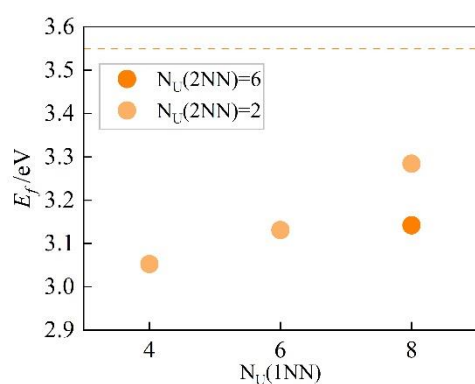


Figure S7. Pu vacancy formation energy against the number of U atoms in the first nearest-neighbour shell ($N_U(1NN)$) and second nearest-neighbour shell ($N_U(2NN)$) in disordered $U_{0.5}Pu_{0.5}N$. The dashed line is the Pu vacancy formation energies in ordered $U_{0.5}Pu_{0.5}N$.

Table S3. Bader charge of Xe at uranium or plutonium vacancy sites in disordered $U_{0.5}Pu_{0.5}N$ against the number of U atoms in the first nearest-neighbour shell ($N_U(1NN)$) and second nearest-neighbour shell ($N_U(2NN)$).

$N_U(2NN) \backslash N_U(1NN)$	$N_U(1NN)$			
		4	6	8
6				-0.02
4		0.04	0.01	0.01
2		0.04	0.04	0.05
0		0.06		0.07

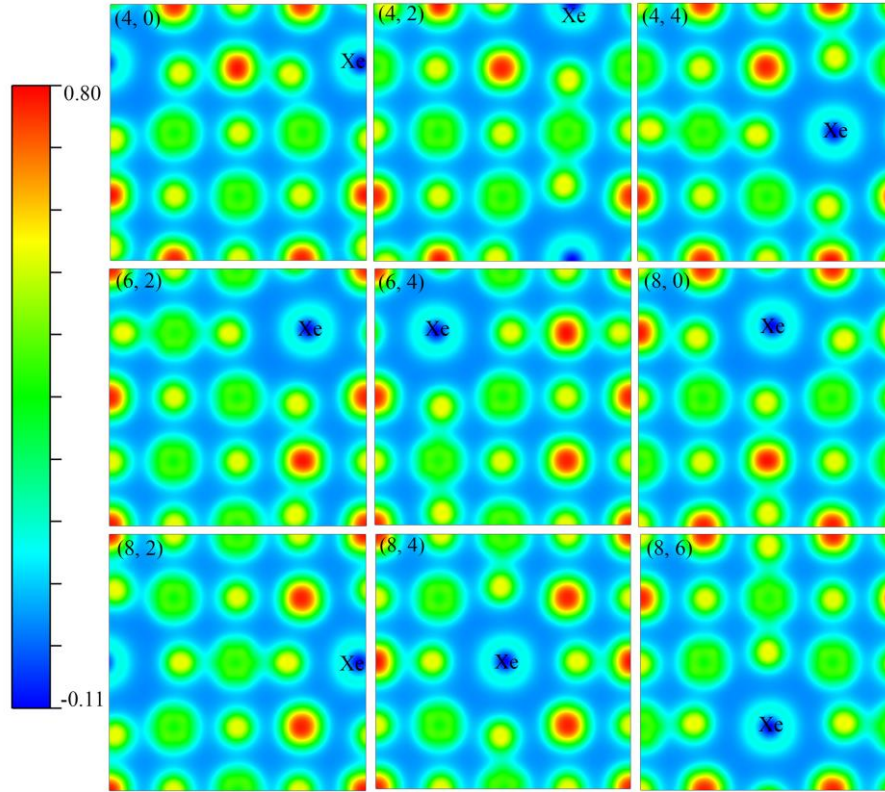


Figure S8. Charge density distribution (a.u.) of the (001) surface for Xe at different vacancy sites in disordered $\text{U}_{0.5}\text{Pu}_{0.5}\text{N}$. The chemical environment around the Xe is defined as (a, b) , where a and b are the number of U atoms in the first nearest-neighbour shell ($\text{N}_{\text{U}}(1\text{NN})$) and second nearest-neighbour shell ($\text{N}_{\text{U}}(2\text{NN})$) around the vacancy.

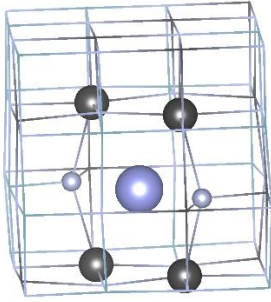


Figure S9. Transition state structure of Xe migration along the $(4, 2) \rightarrow (4, 0)$ pathway.

Table S4. Migration energy barriers (E_m) for Kr in the $\text{U}_{0.5}\text{Pu}_{0.5}\text{N}$ along four processes. The initial and final state vacancy site is defined as (a, b) , in which a and b are the number of U atoms in the first nearest-neighbour shell ($\text{N}_{\text{U}}(1\text{NN})$) and second nearest-neighbour shell ($\text{N}_{\text{U}}(2\text{NN})$).

	E_m /eV
(i) $(4, 6) \rightarrow (4, 6)$	0.90
(ii) $(4, 6) \rightarrow (8, 0)$	1.25
(iii) $(8, 0) \rightarrow (4, 6)$	0.30
(iv) $(8, 0) \rightarrow (8, 0)$	0.71

References

- [1] A. Zunger, S.-H. Wei, L. Ferreira, J.E. Bernard, Special quasirandom structures, *Physical Review Letters* 65(3) (1990) 353.
- [2] A. Van de Walle, P. Tiwary, M. De Jong, D. Olmsted, M. Asta, A. Dick, D. Shin, Y. Wang, L.-Q. Chen, Z.-K. Liu, Efficient stochastic generation of special quasirandom structures, *CALPHAD: Computer Coupling of Phase Diagrams and Thermochemistry* 42 (2013) 13-18.

-Blank page-

6 High Coordination Number Actinide-Noble Gas Complexes

This chapter is the author published article (Lin Yang, Sophie Cooper and Nikolas Kaltsoyannis, High Coordination Number Actinide-Noble Gas Complexes; a Computational Study, *Phys. Chem. Chem. Phys.* 2021, 23 4167. DOI: [10.1039/d0cp06175a](https://doi.org/10.1039/d0cp06175a)), which has 32 pages in total. I am responsible for conceptualization, investigation, methodology, formal analysis, software, and writing, under the supervision of Prof. Nikolas Kaltsoyannis. S. Cooper has performed MP2 calculation and the corresponding analysis.



Cite this: *Phys. Chem. Chem. Phys.*,
2021, **23**, 4167

High coordination number actinide-noble gas complexes; a computational study†

Lin Yang,  Sophie Cooper  and Nikolas Kaltsoyannis  *

The geometries, electronic structures and bonding of early actinide-noble gas complexes are studied computationally by density functional and wavefunction theory methods, and by *ab initio* molecular dynamics. AcHe_{18}^{3+} is confirmed as being an 18-coordinate system, with all of the He atoms accommodated in the primary coordination shell, and this record coordination number is reported for the first time for Th^{4+} and Th^{3+} . For Pa and U in their group valences of 5 and 6 respectively, the largest number of coordinated He atoms is 17. For AnHe_{17}^{q+} ($\text{An} = \text{Ac}$, $q = 3$; $\text{An} = \text{Th}$, $q = 4$; $\text{An} = \text{Pa}$, $q = 5$; $\text{An} = \text{U}$, $q = 6$), the average An–He binding energy increases significantly across the series, and correlates linearly with the extent of $\text{He} \rightarrow \text{An}^{q+}$ charge transfer. The interatomic exchange–correlation term V_{xc} obtained from the interacting quantum atoms approach correlates linearly with the An–He quantum theory of atoms-in-molecules delocalization index, both indicating that covalency increases from AcHe_{17}^{3+} to UHe_{17}^{6+} . The correlation energy in AnHe_{16}^{3+} obtained from MP2 calculations decreases in the order $\text{Pa} > \text{Th} > \text{U} > \text{Ac}$, the same trend found in V_{xc} . The most stable complexes of Ac^{3+} with the heavier noble gases Ar–Xe are 12 coordinate, best described as Ng_{12} cages encapsulating an Ac^{3+} ion. There is enhanced $\text{Ng} \rightarrow \text{Ac}^{3+}$ charge transfer as the Ng gets heavier, and Ac–Ng covalency increases.

Received 28th November 2020,
Accepted 2nd February 2021

DOI: 10.1039/d0cp06175a

rsc.li/pccp

1. Introduction

The noble gas (Ng) elements, with their completely filled principal quantum shells, were considered unreactive for a long time. However, the 1962 report of the first stable Ng compound, $\text{Xe}^+[\text{PtF}_6]^-$ disproved that view,¹ and a new field of chemistry was opened. After that, many scientists devoted themselves to noble gas chemistry, and various new Ng compounds were reported from both experimental and theoretical studies.^{2–5} Among them, actinide–Ng complexes, $\text{CUO}(\text{Ar})_{4-n}(\text{Ng})_n$ ($\text{Ng} = \text{Kr–Xe}$, $n = 1–4$), were first reported by Andrews *et al.* in 2002.⁶ During the synthesis of CUO by laser ablation of U and CO in Ng matrices, it was found that the vibrational spectrum of CUO in an Ar matrix was different from that in a Ne matrix, with the spectral shift from Ne to Ar being much larger than the normal “matrix shift”. Combined with density functional theory (DFT) calculations, Andrews *et al.* assigned the spectrum in Ar to triplet CUO, but to singlet CUO in Ne. Such matrix-induced ground-state reversal suggested direct Ar–U bonding, and U–Ng bonds were also found in Kr and Xe. The interaction between U and Ng was attributed to the donation of Ng lone pair electrons into vacant

orbitals of U, suggesting that positively charged actinide compounds such as UO_2^{2+} would have stronger interaction with Ng elements, and the U–Ng complexes $[\text{UO}_2(\text{Ne})_6]^+$, $[\text{UO}_2(\text{Ng})_5]^+$ ($\text{Ng} = \text{Ar–Xe}$) and $\text{UO}_2(\text{Ng})_4$ ($\text{Ng} = \text{Ne, Ar}$) were indeed subsequently reported.^{7,8} The larger average U–Ng binding energy in $[\text{UO}_2(\text{Ng})_5]^+$ vs. $\text{UO}_2(\text{Ng})_4$ and $\text{CUO}(\text{Ng})_4$ (e.g. 23.6 kJ mol^{−1}, 14.6 kJ mol^{−1} and 16.2 kJ mol^{−1} respectively for $\text{Ng} = \text{Ar}$) supports the influence of charge on U–Ng interaction strength, also found in AuXe_n^{q+} .^{2,9}

Actinide–Ng (especially He) complexes are candidate molecules for achieving high coordination numbers. Coordination number (CN), originally defined as the total number of neighboring atoms directly bonded to the central atom in a molecule or ion, is a fundamental concept in coordination chemistry, and the experimental and theoretical search for compounds with high CN has a long history.^{10–13} Hermann *et al.* predicted the existence of PbHe_{15}^{2+} with a CN of 15 by DFT calculation,¹⁴ and that even higher CN systems may be achievable in charged actinide–He interactions. Motivated by this work, our group¹⁵ theoretically studied actinide ions coordinated by He atoms and reported 17-coordinated AcHe_{17}^{3+} , PaHe_{17}^{4+} and ThHe_{17}^{4+} complexes, a step forward as for several years the highest known CN was 16.^{11–13} UHe_n^{q+} ($q = 2–6$) and PaHe_n^{5+} were also studied, but no stable structures were found with $n > 15$. However, a year later, AcHe_{18}^{3+} was reported by Ozama *et al.*, using coupled cluster theory and path integral molecular dynamics (PIMD).¹⁶ According to their work, 18 He atoms can be accommodated in the first

Department of Chemistry, School of Natural Sciences, The University of Manchester, Oxford Road, Manchester M13 9PL, UK.

E-mail: nikolas.kaltsoyannis@manchester.ac.uk

† Electronic supplementary information (ESI) available. See DOI: 10.1039/d0cp06175a



coordination shell, in a highly symmetrical D_{4d} structure, the increase in CN from our work potentially being due to omission of basis set superposition error (BSSE) in our CCSD(T) calculations. Although CN higher than 18 has recently been reported for $M(H_2)_{12}^{n+}$ ($M = \text{Ac, Th, Pa, U, La, } n = 3, 4$)¹⁷ and $\text{An}(\text{BH})_{24}$ ($\text{An} = \text{Th-Cm}$),¹⁸ genuine CNs of 24 are debatable given the strong H-H interaction in $M(H_2)_{12}^{n+}$ and lack of direct evidence for true 24 M-B bonds in $\text{An}(\text{BH})_{24}$. High coordination number is also observed in metal cluster-based compounds. $M(\text{EH})_{12}$ ($M = \text{Cr, Mo, W; E = Zn, Cd, Hg}$)¹⁹ possess 12 M-ER bond paths which are characterized as 6 three-centre two-electron bonds by quantum theory of atoms-in-molecules (QTAIM) and MO analysis. Weak peripheral E-E bonding is also observed with lower bond order than the M-E bonds. By contrast, $[\text{Pt}@\text{Pb}_{12}]^{2-}$,^{20,21} which has similar geometry, is stabilized by strong interactions in the Pb icosahedron.

In this contribution, we study AnHe_n^{q+} ($\text{An} = \text{Ac-U}$) using wavefunction theory, DFT and *ab initio* molecular dynamics (AIMD) calculations, and probe the nature of the An-He interaction. The latter is investigated *via* the QTAIM, interacting quantum atoms (IQA) and natural population analysis (NPA) methods. We also extend the helium work to the heavier Ng elements neon, argon, krypton, and xenon, systemically investigating the nature of the An^{q+} -Ng interaction, including the influence of Ng polarizability.

2. Computational details

All the geometrical structures, binding energies and thermodynamic stabilities of AnNg_n^{q+} complexes were studied by dispersion-corrected density functional theory methods (DFT-D3),²² as implemented in TURBOMOLE 7.3.²³ Effective core potentials (ECPs) with 60 core electrons were used for the actinide elements along with the def-TZVPP valence basis sets,²⁴⁻²⁶ and the aug-cc-pV5Z basis set²⁷ was used for He. Stuttgart RLC basis sets and ECPs with 2, 10, 28, and 46 core electrons respectively were used for Ne, Ar, Kr, and Xe.^{28,29} To ensure valid comparisons with the He results, both the aug-cc-pV5Z and Stuttgart RLC ECP basis sets were used for benchmark AcNe_n^{3+} calculations (Table S1, ESI†). The average Ac^{3+} -Ne distance and distance range obtained, as well as the binding energies, are close, suggesting that comparisons may indeed be justifiably made between the He and heavier Ng results, despite the difference in Ng basis sets employed. Harmonic vibrational frequency analysis³⁰ was conducted for all optimized structures to ensure that they are true minimum structures.

To benchmark the density functional selection, CCSD(T)³¹ calculations were conducted in MOLPRO 2019³² using the 60 electron ECP along with associated ECP60MWB_SEG valence basis set for An (Ac, U)²⁴⁻²⁶ and aug-cc-pV5Z basis set for He.²⁷ HF³³ and MP2³⁴ calculations were performed in Gaussian 16³⁵ with the same basis sets as used for the CCSD(T) calculations. BSSE corrections were evaluated by the counterpoise correction method.³⁶

QTAIM and IQA³⁷ calculations were conducted using the AIMAll software.³⁸ The input files for the IQA calculations were

generated from DFT calculations based on the B3LYP-D3 density functional³⁹ because the BHLYP-D3 density functional (which is used for our other production DFT calculations) is not currently supported for IQA analysis in AIMAll. The details for the IQA calculations were as reported in our previous work.⁴⁰ Natural population analysis (NPA) was carried out using NBO 7.0⁴¹ to obtain the natural charges and electron configurations of the AnNg_n^{q+} complexes.

To study the thermodynamic stability of the optimized AnNg_n^{q+} structures, AIMD calculations were performed in TURBOMOLE, using the Nosé-Hoover thermostat.⁴² The time step was set to 1.21 fs and the total simulation time to 1.25 ps for Ac^{3+} -Ng compounds. For the Th^{4+} -He complexes, longer simulation times were used, 2.47 ps and 3.71 ps for temperatures of 3 K and 10 K respectively. The simulations for AcHe_{18}^{3+} and ThHe_{18}^{4+} were conducted twice, yielding similar results. Hence, simulations for the Ac^{3+} -Ng complexes were conducted only once.

3. Results and discussion

3.1. Potential energy curves for An^{3+} -He

As stated in the Introduction, Ozama *et al.* reported that BSSE has a significant influence on the Ac^{3+} -He potential energy curve at the ECP60MWB/CCSD(T) level.¹⁶ To verify this, we began by studying BSSE, calculating the potential energy curve for the Ac^{3+} -He interaction with CCSD(T), with and without BSSE correction. Both contracted and uncontracted valence basis sets were used for Ac. As shown in Fig. 1(a), the effect of BSSE depends on whether the Ac basis set is contracted or uncontracted. The contracted basis set without BSSE gives the deepest potential well of 35.13 kJ mol⁻¹, close to the 34.98 kJ mol⁻¹ and 35.0 kJ mol⁻¹ calculated by Ozama *et al.* and by us, respectively. However, the potential well without BSSE but using the uncontracted basis set is much shallower, 22.68 kJ mol⁻¹ at 2.61 Å. BSSE correction leads to a shallowing of the potential energy curve, to 21.93 kJ mol⁻¹ and 22.18 kJ mol⁻¹ for contracted and uncontracted basis set respectively, close to the value of 21.94 kJ mol⁻¹ predicted by Ozama *et al.* This suggests that BSSE correction has a marked influence on CCSD(T) calculations using contracted basis sets, but that the impact on uncontracted basis set calculations is slight. BSSE at the DFT level was also studied, using the PBE-D3 functional as a representative example (Fig. S1, ESI†). The results suggest that the effect is very small, with potential well depths of 27.40 kJ mol⁻¹ and 27.46 kJ mol⁻¹ with and without BSSE correction, respectively. On the basis of these results, we (i) use BSSE-corrected contracted basis set CCSD(T) data as a benchmark to determine the most appropriate density functional (contracted basis sets are used for DFT calculations in the TURBOMOLE software) and (ii) neglect BSSE corrections in our DFT calculations.

Ac^{3+} -He potential energy curves were calculated by various density functionals; the results from PBE-D3 and BHLYP-D3 are shown in Fig. 1(b) with the other data being plotted in Fig. S2 (ESI†). All functionals match reasonably well with BSSE-corrected CCSD(T), with hybrid functionals performing slightly better than GGA. Among the hybrids, the BHLYP curve is the best match for



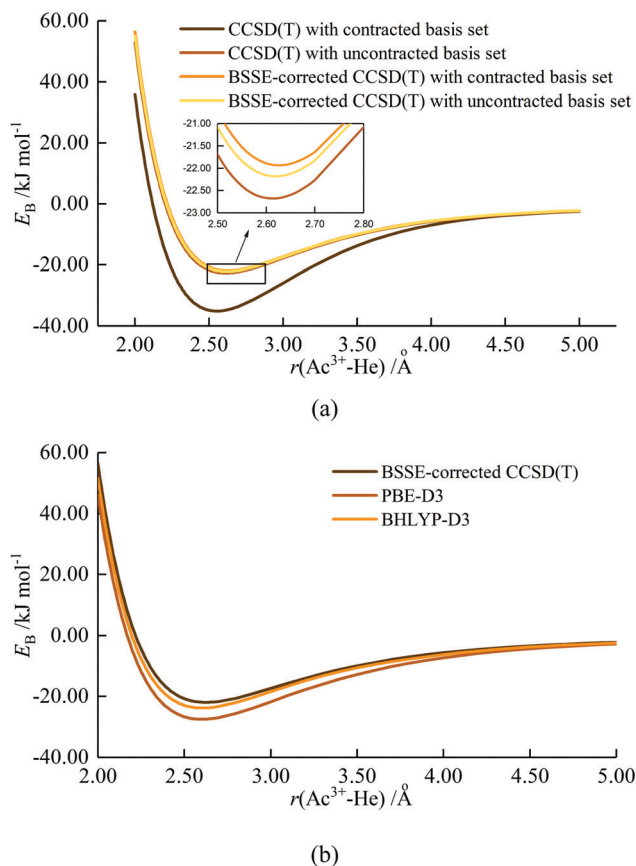


Fig. 1 Potential energy curves of $\text{Ac}^{3+}\text{-He}$ by (a) CCSD(T) calculation and (b) DFT calculation using PBE-D3 and B3LYP-D3 density functionals.^{39,43}

the coupled cluster results, and hence B3LYP-D3 is used for geometry optimization and binding energy calculations of AnNg_n^{q+} . The only exception is UHe_n^{3+} , for which B3LYP-D3 gave a poor description of the UHe_{18}^{3+} average binding energy (Fig. S3, ESI[†]) and $\text{U}^{3+}\text{-He}$ potential energy curve (Fig. S4, ESI[†]). Fig. S4 (ESI[†]) shows that the binding energies obtained from B3LYP-D3 are very large, leading to an extremely deep potential well which does not converge to 0 at large $\text{U}^{3+}\text{-He}$ distance. Further examination indicates that the total energy of U^{3+} obtained by B3LYP-D3 is appreciably less negative than from the other methods employed (Table S2, ESI[†]), and also less negative than obtained from the same calculation performed in Gaussian 16, suggesting that TURBOMOLE does not converge to the correct ground state of U^{3+} with B3LYP. Given this observation and, as the curve from B3LYP-D3 matches better with that of CCSD(T), it is used for the study of $\text{U}^{3+}\text{-He}$ complexes.

3.2. $\text{An}^{q+}\text{-He}$ complexes

3.2.1 $\text{Ac}^{3+}\text{-He}$ complexes. Using the B3LYP-D3 functional, we were able to locate a AcHe_{18}^{3+} true minimum structure. This is an increase in CN of one from our previous work, which employed the HFS functional,¹⁵ and located only AcHe_{17}^{3+} . The data in the previous section indicate that this difference arises from the omission of BSSE in our previous benchmarking CCSD(T) calculations, which generated an $\text{Ac}^{3+}\text{-He}$ well which

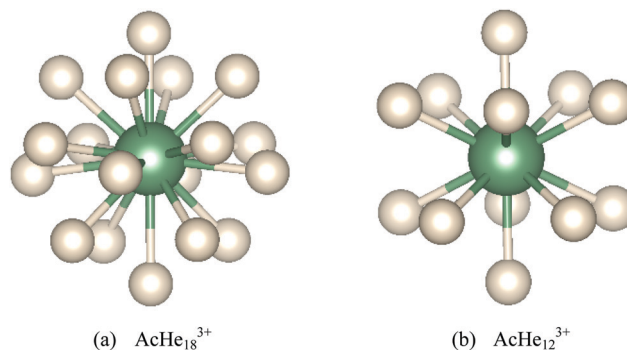


Fig. 2 Optimized geometries of AcHe_{18}^{3+} and AcHe_{12}^{3+} .

was too deep, and hence led to our using the HFS approach. The optimized structure of AcHe_{18}^{3+} is shown in Fig. 2(a); it is close to a distorted tetrakis cuboctahedron and has D_{4d} symmetry, as reported by Ozama *et al.*¹⁶ Efforts to coordinate 19 and 20 He atoms in the primary shell all failed.

The stability of AcHe_{18}^{3+} was studied by AIMD at 10 K, starting from the initial geometry shown in Fig. 2(a). The results are shown in Fig. 3; the lowest energy structure over the course of the simulation is the starting structure. Furthermore, the root mean square deviations of the He atoms from the initial structure are less than 0.15 \AA , also indicating the stability of the AcHe_{18}^{3+} structure, with only slight relaxation of the He atoms in the first coordination shell.

Geometrical parameters of $\text{Ac}^{3+}\text{-He}$ complexes from $n = 1$ to 18 are listed in Table 1. The average $\text{Ac}^{3+}\text{-He}$ distance increases by only 0.109 \AA from $n = 1$ to 17, with the bond distance range maximising at 0.039 \AA for the 16-coordinate system. However, the bond distance range jumps to 0.108 \AA at $n = 18$, with the average bond distance being 0.027 \AA longer than that at $n = 17$, suggesting a crowded distribution of He atoms in AcHe_{18}^{3+} . However, the range of 0.108 \AA is still small enough to assign all 18 He atoms to the primary coordination shell. That we find bond critical points (BCPs) between Ac^{3+} and all 18 He atoms also supports this conclusion. Note also the very small bond length range for $n = 12$ (Fig. 2(b)), 0.001 \AA , rising to 0.026 \AA at $n = 13$, due to disruption of the stable AcHe_{12}^{3+} icosahedral structure. The average Ac-He distance of AcHe_{17}^{3+} is 2.719 \AA ,

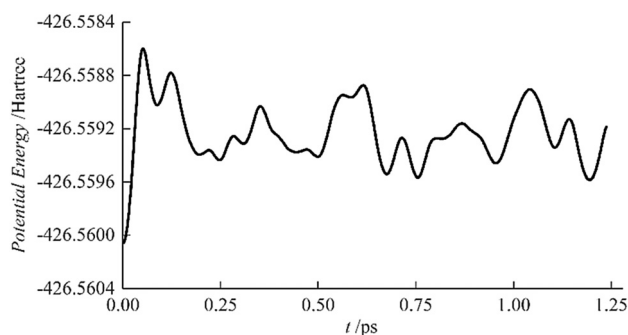
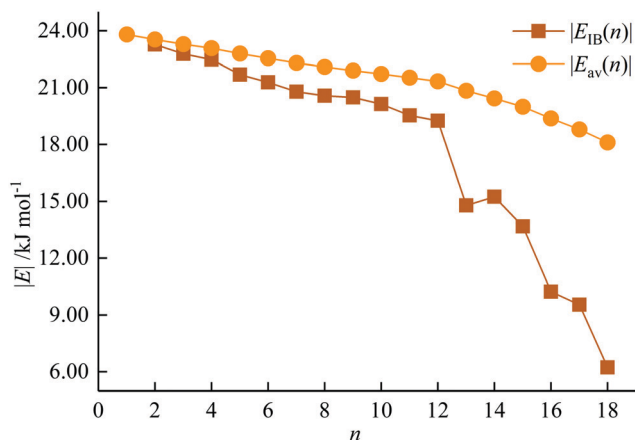


Fig. 3 Evolution of AcHe_{18}^{3+} potential energy with time at 10 K.



Table 1 Average Ac^{3+} -He distance (r_{av}) and distance range (Δr) in AcHe_n^{3+} ($n = 1-18$)

n	$r_{\text{av}}/\text{\AA}$	$\Delta r/\text{\AA}$	n	$r_{\text{av}}/\text{\AA}$	$\Delta r/\text{\AA}$
1	2.610	—	10	2.638	0.016
2	2.606	0.001	11	2.642	0.013
3	2.611	0.005	12	2.644	0.001
4	2.613	0.006	13	2.660	0.026
5	2.620	0.011	14	2.671	0.018
6	2.628	0.012	15	2.683	0.037
7	2.631	0.013	16	2.701	0.039
8	2.635	0.005	17	2.719	0.037
9	2.638	0.011	18	2.746	0.108

**Fig. 4** Incremental $|E_{\text{IB}}(n)|$ and average $|E_{\text{av}}(n)|$ binding energies of AcHe_n^{3+} ($n = 1-18$).

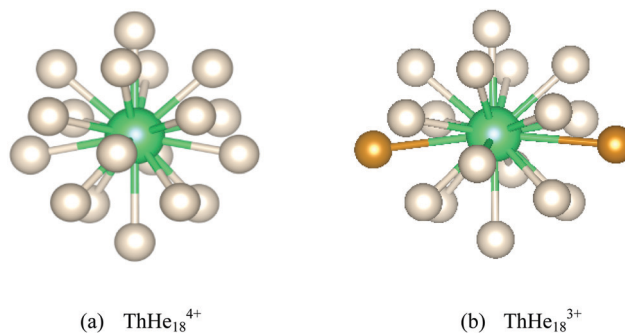
larger than the 2.671 Å that we reported before,¹⁵ consistent with the smaller revised Ac^{3+} -He well depth.

The incremental $|E_{\text{IB}}(n)|$ and average $|E_{\text{av}}(n)|$ binding energies of AcHe_n^{3+} ($n = 1-18$) are plotted in Fig. 4. $|E_{\text{IB}}(n)|$ is defined as the difference between the total energy of AcHe_n^{3+} and the sum of the total energy of AcHe_{n-1}^{3+} and He, and represents the energy gain for each He atom attachment. $E_{\text{av}}(n)$ is calculated by equation

$$E_{\text{av}}(n) = (E(n) - E(\text{Ac}^{3+}) - n \times E(\text{He}))/n$$

in which $E(n)$, $E(\text{Ac}^{3+})$ and $E(\text{He})$ are the total energy of AcHe_n^{3+} , Ac^{3+} , and He. As shown in Fig. 4, $|E_{\text{av}}(n)|$ decreases from $n=1$ to 18, which is as expected considering more He atoms are attached to the Ac^{3+} centre. $|E_{\text{IB}}(n)|$ is similar to our PBE results in ref. 15, while smaller than the HFS result. It decreases steadily from $n = 1$ to 12, and then suddenly drops at $n = 13$ before slightly increasing at 14. The energy change from $n = 12$ to 13 is consistent with the trend in Ac^{3+} -He distance range, and the increase at $n = 14$ is due to the establishment of a new stable structure as reported by Hermann and us.^{14,15} It is worth noting that the $|E_{\text{IB}}(n)|$ at $n = 18$ is only 6.24 kJ mol⁻¹ which, together with the large Ac-He distance range of AcHe_{18}^{3+} , explains the failure to coordinate more than 18 He atoms.

3.2.2 Th^{q+}-He ($q = 3, 4$) complexes. The search for the highest CN of charged actinide-Ng complexes was extended to other

**Fig. 5** Optimized (a) ThHe_{18}^{4+} and (b) ThHe_{18}^{3+} geometries. The furthest two He atoms in the latter are highlighted in orange in (b).**Table 2** Geometrical parameters and average binding energies of AnHe_n^{q+} in their highest CN structure

	$r_{\text{av}}/\text{\AA}$	$\Delta r/\text{\AA}$	$ E_{\text{av}} /\text{kJ mol}^{-1}$
ThHe_{18}^{4+}	2.541	0.151	42.001
ThHe_{18}^{3+}	2.729	0.538	19.452
PaHe_{17}^{5+}	2.360	0.053	90.604
PaHe_{16}^{3+}	2.623	0.213	22.257
UHe_{17}^{6+}	2.296	0.082	179.917
UHe_{16}^{3+}	2.623	0.083	22.908

early actinide elements from Th to U. Both their group valence and trivalent oxidation states were considered. The 18-coordinated structure was also located for ThHe_{18}^{q+} ($q = 3, 4$) with the geometries shown in Fig. 5 and Table 2. The geometry and symmetry of ThHe_{18}^{4+} are similar to AcHe_{18}^{3+} with a smaller Th-He distance (2.541 Å), while the average Th^{4+} -He binding energy is 42.001 kJ mol⁻¹, more than twice that of Ac^{3+} -He, likely due to the increased charge on Th^{4+} vs. Ac^{3+} .

To study the thermodynamic stability of ThHe_{18}^{4+} , AIMD calculations were conducted at 3 K and 10 K. As shown in Fig. 6, ThHe_{18}^{4+} remains as the minimum potential energy structure at 3 K. However, as the temperature is increased to 10 K, the minimum potential energy structure changes to ThHe_{17}^{4+} , with the 18th He atom located in the second shell, *i.e.* the system is better represented as ThHe_{17+1}^{4+} . The Th-He distance range in the ThHe_{17}^{4+} part is quite small (0.040 Å), and the distance difference between the two shells is 1.213 Å. Compared with AcHe_{18}^{3+} , the primary coordination shell of ThHe_{18}^{4+} is more crowded, which leads to a reduction in the CN at higher temperature.

Although a stable ThHe_{18}^{3+} structure was obtained, the range of Th^{3+} -He distances is quite large (2.645–3.183 Å). As shown in Fig. 5(b), there are two He atoms, highlighted in orange, with an average Th^{3+} -He distance of 3.178 Å, farther out than the other 16 He atoms (average Th^{3+} -He distance = 2.673 Å), making the CN 18 description debatable. However, QTAIM analysis shows BCPs between Th^{3+} and all 18 He atoms (Fig. 7). The presence of a BCP can be considered as the indicator of a chemical bond. The average electron density at the BCPs between Th^{3+} and the two more distant He atoms is only 0.005 a.u., while the value is 0.013–0.015 a.u. between Th^{3+}



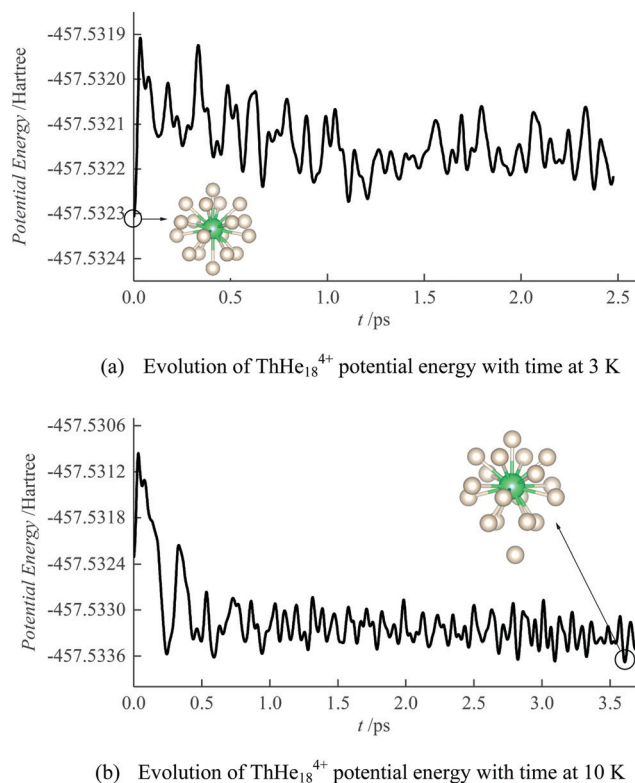


Fig. 6 Evolution of ThHe_{18}^{4+} potential energy by AIMD at (a) 3 K and (b) 10 K. The initial structures are as shown in Fig. 5(a).

and the other 16 He atoms. Therefore, we conclude that ThHe_{18}^{3+} is genuinely 18-coordinated, although two of the bonds are extremely weak. Note that the average Th^{3+} -He binding energy ($19.452 \text{ kJ mol}^{-1}$) is slightly larger than the $18.098 \text{ kJ mol}^{-1}$ of Ac^{3+} -He, but significantly less than that of Th^{4+} -He.

To further understand the actinide-Ng interaction within these highly coordinated complexes, QTAIM and NPA analysis for ThHe_{18}^{q+} ($q = 3, 4$) were conducted, and the results are

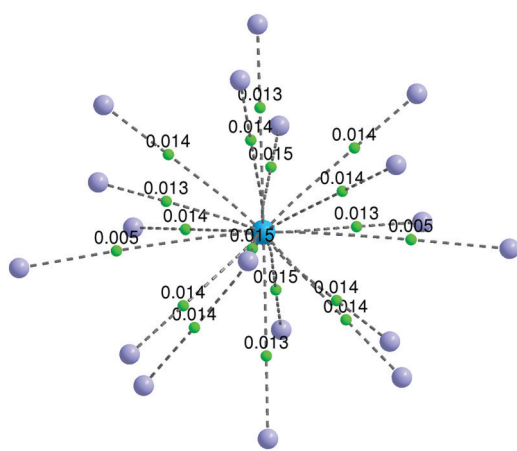


Fig. 7 Bond paths (dashed lines) and bond critical points (green dots) of ThHe_{18}^{3+} . The electron densities (a.u.) at the BCPs are displayed. He = purple spheres, Th = blue sphere.

presented in Table 3. The data for AcHe_{18}^{3+} are also given. Different from orbital-based analysis, QTAIM is based on the topology of the electron density.⁴⁴ BCP properties such as the electron density (ρ_{BCP}), Laplacian of the electron density ($\nabla^2 \rho_{\text{BCP}}$), the ratio of kinetic and potential energy densities ($-G_{\text{BCP}}/V_{\text{BCP}}$), and the energy density (H_{BCP}) are all useful descriptors of chemical bonds. A general rule is that $\rho_{\text{BCP}} > 0.2 \text{ a.u.}$ and $H_{\text{BCP}} < 0$ are features of covalent interaction, while $\rho_{\text{BCP}} < 0.1 \text{ a.u.}$ represents closed-shell interactions (ionic bonding, hydrogen bonding, van der Waals bonding).⁴⁵ However, for chemical bonds involving actinides, ρ_{BCP} is rarely larger than 0.2 and usually less than 0.1 a.u. $\nabla^2 \rho_{\text{BCP}}$ describes whether the electron density is concentrated ($\nabla^2 \rho_{\text{BCP}} < 0$) or depleted ($\nabla^2 \rho_{\text{BCP}} > 0$) at the BCP. For highly polarized bonds, positive $\nabla^2 \rho_{\text{BCP}}$ is possible. For BCPs with positive $\nabla^2 \rho_{\text{BCP}}$, $-G_{\text{BCP}}/V_{\text{BCP}}$ between 0.5 and 1 is a feature of covalent character, while $-G_{\text{BCP}}/V_{\text{BCP}} > 1$ is considered to indicate non-covalent interaction.⁴⁰ Moreover, the delocalization indices (δ), which represent the number of electrons shared between two atomic basis, is a widely used measure of bond order, and also a good indicator of covalence.

The QTAIM atomic charges in Table 3 indicate that the overall $q+$ charge partially redistributes between An and He due to electron transfer from the He atoms to the An centres. That said, the An QTAIM charges are close to the formal oxidation state in all cases, and the He charges are small. These charges indicate closed-shell bonding in Th^{q+} -He and Ac^{3+} -He; this has been previously characterized as a charge-induced dipole interaction.¹⁵ The BCP data and small δ values further confirm this. Although the An/He charges calculated by NPA are not as disparate as those from the QTAIM, they are also suggestive of ionic bonding. Charge transfer, as well as ρ_{BCP} and δ , for ThHe_{18}^{4+} are larger than for ThHe_{18}^{3+} and AcHe_{18}^{3+} (which are similar to one another) consistent with the average An $^{q+}$ -He binding energy being mainly determined by the charge on the metal centre, as noted above.

3.2.3 An $^{q+}$ -He (An = Pa, $q = 3, 5$; An = U, $q = 3, 6$) complexes.

The highest CN obtained for Pa^{5+} -He and U^{6+} -He complexes is 17, and 16 for Pa^{3+} -He and U^{3+} -He complexes. It is not unexpected to find lower CN of Pa^{q+} and U^{q+} than Th^{q+} and Ac^{3+} , given the smaller ionic radii of the former and the increased An $^{q+}$ -He distance range from Ac^{3+} to Th^{q+} . The CNs of 17 and 16 reported here are higher than the 15 suggested in our previous work for Pa^{5+} -He and U^{q+} -He ($q = 2-6$),¹⁵ as well as in other reported actinide complexes.^{46,47}

18-Coordinated structures were also located for PaHe_{18}^{3+} and UHe_{18}^{3+} , but were found to have imaginary frequencies. To obtain true minima, the PaHe_{18}^{3+} and UHe_{18}^{3+} structures were distorted along the largest imaginary mode and re-optimized, resulting in lower energy AnHe_{16}^{3+} (An = Pa, U) structures with the remaining two He atoms located in the second shell. The geometries of these complexes are given in Fig. 8 and Table 2. PaHe_{17}^{5+} and UHe_{17}^{6+} have similar symmetry and geometry to one another, with the average An $^{q+}$ -He distances being 2.360 \AA and 2.296 \AA , respectively. The average Pa^{5+} -He and U^{6+} -He binding energies are much larger than that of Th^{4+} -He, which



Table 3 QTAIM metrics (a.u.) and NPA charges for optimized AcHe_{18}^{3+} and ThHe_{18}^{q+} ($q = 3, 4$)

	Atomic charge				BCP properties				
	QTAIM		NPA						
	q_{An}	q_{He}	q_{An}	q_{He}	ρ_{BCP}	$\nabla^2 \rho_{\text{BCP}}$	$-(G_{\text{BCP}}/V_{\text{BCP}})$	H_{BCP}	δ
AcHe_{18}^{3+}	2.843	0.009	2.211	0.048	0.012	0.055	1.278	0.002	0.048
ThHe_{18}^{3+}	2.827	0.010	1.766	0.069	0.013	0.061	1.247	0.002	0.053
ThHe_{18}^{4+}	3.613	0.021	2.226	0.099	0.020	0.083	1.154	0.002	0.077

we attribute in part to the reduced steric effect induced by the reduction in CN, but primarily to the increased metal charge of Pa^{5+} and U^{6+} , as found in the comparison of ThHe_{18}^{4+} and AcHe_{18}^{3+} . For PaHe_{16}^{3+} and UHe_{16}^{3+} , the average An^{3+} –He distances are the same with the distance range of the latter being smaller. The average binding energy of UHe_{16}^{3+} is slightly larger than that of PaHe_{16}^{3+} , but this increase is small compared with that from PaHe_{17}^{5+} to UHe_{17}^{6+} , as found for ThHe_{18}^{q+} complexes as noted above. This further indicates the significant influence of metal charge on An^{q+} –He interaction.

3.2.4 The nature of the An^{q+} –He interaction. In order to study the dependence of the nature of the An^{q+} –He interaction on An and oxidation state, QTAIM, IQA, and NPA analyses were conducted on AnHe_{17}^{q+} and AnHe_{16}^{3+} (An = Ac–U), selected as they form families of closed-shell and trivalent AnHe_n^{q+} complexes, respectively.

AnHe_{17}^{q+} . As shown in Table 4, the average An–He distance in AnHe_{17}^{q+} decreases significantly from Ac to U, while the average binding energy increases substantially. The atomic

charges on the actinide ions deviate from their formal oxidation states, suggesting that part of the overall positive charge is acquired by the He atoms. This charge transfer increases across the series from Ac to U, with the partial charge on Ac(III) close to its formal oxidation state but increasingly less so from Th(IV) to U(VI). The average binding energy correlates linearly with this charge transfer ($R^2 = 0.999$). We noted above that the Th^{q+} –He ($q = 3, 4$) and Ac^{3+} –He interaction is primarily charge-induced dipole, with little charge transfer and small delocalization indices. This description is also suitable for the Pa–He interaction in PaHe_{17}^{5+} , given the small ρ_{BCP} value, positive H_{BCP} , and $-G_{\text{BCP}}/V_{\text{BCP}}$ greater than 1. However, considering the charge loss of 1.73 for U(VI) and small negative H_{BCP} , this description is arguably less appropriate for U–He, which shows more Lewis acid–base interaction characteristics. $-G_{\text{BCP}}/V_{\text{BCP}}$ between 0.5 and 1.0 further evidences this. Furthermore, ρ_{BCP} and δ rise from Ac to U, suggesting increasing covalency.

The exchange–correlation energy (V_{xc}) between An and He, obtained from IQA analysis, is also listed in Table 4. IQA is a real-space energy partitioning method based on topology theory, with good performance in quantifying chemical bonding, which has only recently begun to be employed in the 5f series.^{40,48} According to the IQA approach, the interatomic energy (V_{int}) can be decomposed into electrostatic (V_{elec}) and exchange–correlation terms (V_{xc}).³⁷ The former is composed of the nuclear–nuclear repulsive energy, electron–electron coulombic repulsion energy, and the electron–nuclear attraction energy. V_{xc} is a good descriptor of the covalent contribution to the interatomic energy, and it can be seen from Table 4 that V_{xc} becomes more negative as the series is crossed. Considering that the more negative V_{xc} , the higher the degree of covalency, IQA gives the same trend as the other QTAIM metrics, *i.e.* that covalency increases from Ac to U in this closed-shell family. As shown in Fig. 9(a), V_{xc} shows excellent correlation with δ ($R^2 = 0.991$), which is a more widely used indicator of covalency. This further suggests that the IQA method can be a useful tool in the study of covalency in the 5f series.

To further analyze the electronic structures of these complexes, the natural charges and natural electron configurations were explored using NPA, and are listed in Table 5, together with the Wiberg bond indices (WBIs). The trend in the NPA charges of He in AnHe_{17}^{q+} is the same as that obtained from QTAIM but with more charge being acquired by He, similar to the behaviour noted above, indicating less closed-shell interaction compared with QTAIM. Like V_{xc} , WBI is very strongly correlated with δ ($R^2 = 0.985$). Given the charge transfer, it is unsurprising that the natural electron configurations show

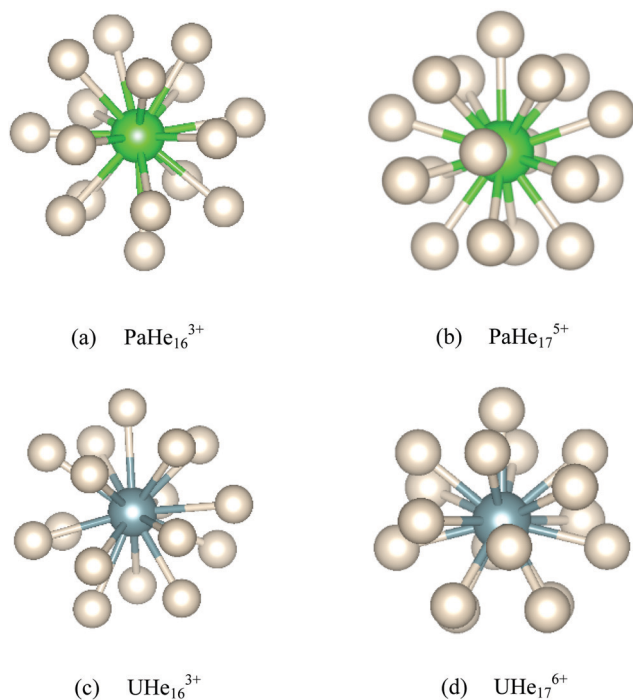
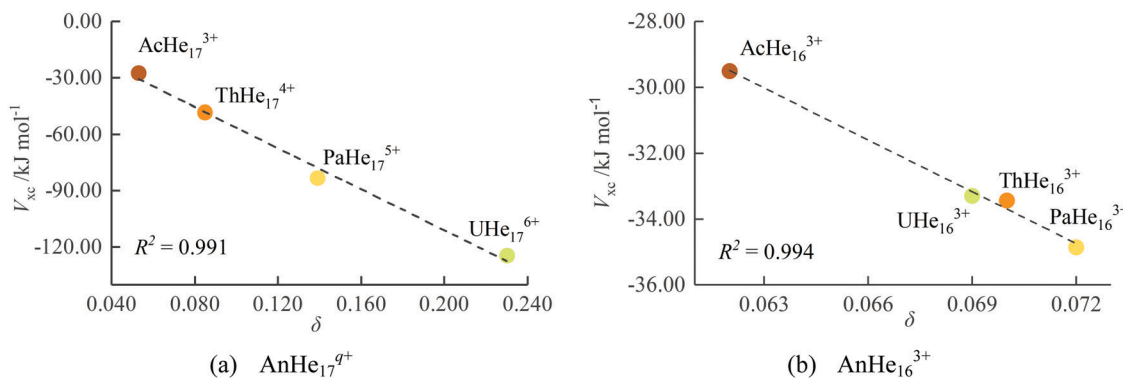
**Fig. 8** Optimized AnHe_n^{q+} (An = Pa, $q = 3, 5$; An = U, $q = 3, 6$) configurations.

Table 4 Average An^{q+}–He distance, An^{q+}–He binding energies, QTAIM (a.u.) and IQA metrics for the optimized AnHe_n^{q+} complexes

	$r_{av}/\text{\AA}$	$E_{av}/\text{kJ mol}^{-1}$	q_{An}	q_{He}	ρ_{BCP}	$\nabla^2\rho_{BCP}$	$\frac{G_{BCP}}{V_{BCP}}$	H_{BCP}	δ	$V_{xc}/\text{kJ mol}^{-1}$
AcHe ₁₇ ³⁺	2.719	−18.796	2.802	0.009	0.013	0.058	1.263	0.002	0.053	−27.543
ThHe ₁₇ ⁴⁺	2.511	−44.121	3.604	0.023	0.022	0.090	1.138	0.002	0.085	−48.296
PaHe ₁₇ ⁵⁺	2.360	−90.604	4.144	0.050	0.033	0.118	1.023	0.001	0.139	−83.375
UHe ₁₇ ⁶⁺	2.296	−179.917	4.259	0.102	0.040	0.123	0.958	−0.001	0.230	−124.580
AcHe ₁₆ ³⁺	2.701	−19.374	2.802	0.012	0.014	0.059	1.247	0.002	0.062	−29.507
ThHe ₁₆ ³⁺	2.650	−21.270	2.779	0.014	0.015	0.067	1.213	0.002	0.070	−33.444
PaHe ₁₆ ³⁺	2.623	−22.257	2.761	0.015	0.016	0.071	1.198	0.003	0.072	−34.859
UHe ₁₆ ³⁺	2.623	−22.908	2.754	0.015	0.015	0.069	1.198	0.002	0.069	−33.302

**Fig. 9** The correlation between V_{xc} and δ for AnHe_n^{q+}.

significant deviation from the formal oxidation states, in which the valence orbitals are expected to be empty. The occupancies of all valence orbitals increase from AcHe₁₇³⁺ to UHe₁₇⁶⁺, although the details differ. For AcHe₁₇³⁺, the electrons mainly occupy the 6d orbitals, with the 5f occupancy being 0.08. Although the 6d populations are also larger than 5f for ThHe₁₇⁴⁺ and PaHe₁₇⁵⁺, the 5f increases significantly and, for UHe₁₇⁶⁺, the occupation of 5f exceeds that of 6d. The increasing occupation of the 5f orbitals in part reflects their stabilization across the actinide series, as reported in previous theoretical work.^{49,50}

Table 5 Wiberg bond index (WBI) of An^{q+}–He, natural charge, and natural electronic configuration of An^{q+} in AnHe₁₇^{q+} and AnHe₁₆³⁺. For the electronic configurations, the values listed are those above the formal populations (shown in parentheses). As the 7p populations are negligible, they are not shown. Note that there are 0.22, 0.29, and 0.15 metal Rydberg electrons in ThHe₁₆³⁺, PaHe₁₆³⁺ and UHe₁₆³⁺ respectively

	WBI	q_{An}	$q_{He(av)}$	Natural electronic configuration		
				7s	5f	6d
AcHe ₁₇ ³⁺	0.054	2.251	0.044	(0) 0.18	(0) 0.08	(0) 0.48
ThHe ₁₇ ⁴⁺	0.119	2.338	0.098	(0) 0.29	(0) 0.44	(0) 0.92
PaHe ₁₇ ⁵⁺	0.187	2.292	0.159	(0) 0.36	(0) 1.02	(0) 1.31
UHe ₁₇ ⁶⁺	0.286	1.789	0.248	(0) 0.37	(0) 2.23	(0) 1.58
AcHe ₁₆ ³⁺	0.053	2.304	0.044	(0) 0.17	(0) 0.17	(0) 0.45
ThHe ₁₆ ³⁺	0.138	1.827	0.073	(0) 0.21	(1) 0.10	(0) 0.65
PaHe ₁₆ ³⁺	0.151	1.714	0.080	(0) 0.22	(2) 0.11	(0) 0.67
UHe ₁₆ ³⁺	0.136	1.846	0.072	(0) 0.21	(3) 0.12	(0) 0.67

AnHe₁₆³⁺. As discussed in Section 3.1, the B3LYP-D3 functional failed to convincingly describe U³⁺-based complexes, and hence we employed B3LYP-D3 for calculations on UHe₁₆³⁺. To systematically study trivalent An–He, QTAIM and NBO analyses for AnHe₁₆³⁺ (An = Ac–U) were all conducted from single-point calculations using B3LYP-D3, and the results are collected in Table 4. The average An–He distance shortens across the early actinide series, following the An trivalent radius contraction; that $r(\text{Pa–He})$ and $r(\text{U–He})$ are the same as one another is likely due to the very similar ionic radii of Pa³⁺ (1.04 Å) and U³⁺ (1.03 Å). The average binding energy increases slightly from AcHe₁₆³⁺ to UHe₁₆³⁺, and the values for the Th, Pa and U systems are significantly smaller than in the corresponding AnHe₁₇^{q+}. Moreover, the energy difference between AnHe₁₆³⁺ and the corresponding closed-shell AnHe₁₇^{q+} rises from Ac to U, further illustrating the strong influence of metal charge on the An^{q+}–He interaction.

Turning to the QTAIM metrics, the small values of ρ_{BCP} and δ , and the positive $\nabla^2\rho_{BCP}$ and H_{BCP} , all indicate charge-induced dipole interaction for all AnHe₁₆³⁺ complexes. The charge difference between metal and He decreases slightly from Ac to U, although this change is small compared with the closed-shell AnHe₁₇^{q+} complexes. The BCP electron densities are very similar for all four complexes, with that for Ac–He being slightly smaller, similar to the charge transfer trend. $-G_{BCP}/V_{BCP}$ also suggests that the Ac system is the most ionic, as does δ , from which the covalency trend is Pa > Th > U > Ac. V_{xc} indicates the same trend and once again shows excellent



correlation with δ ($R^2 = 0.994$, Fig. 9(b)). Notably, the difference in δ and V_{xc} between the trivalent AnHe_{16}^{3+} and group valent AnHe_{17}^{q+} complexes increase very significantly from Ac to U, suggesting significantly greater covalency in the higher oxidation state systems. To place the QTAIM metrics for the An–He complexes in context, the values of ρ_{BCP} , δ , and V_{xc} as a function of the shortening and elongation of the An–He bond length are studied for An^{3+} –He diatomic systems (Fig. S5, ESI†).

The natural charge and WBI data (Table 5) show the same trend as the QTAIM and IQA metrics, and once again the correlation of WBI with δ is very strong ($R^2 = 0.978$). As discussed above, the enhanced charge transfer predicted by NPA suggests less of a closed-shell interaction nature. The natural electronic configuration data show that the largest enhancement in all valence orbitals is in the 6d, indicating that the An 6d orbital is the principal acceptor of He electron density in AnHe_{16}^{3+} .

In order to study the effect of correlation on the An^{3+} –He bonding, HF and MP2 calculations were performed at the DFT optimized geometries, and the results are plotted in Fig. S6 (ESI†). Although the average binding energies are smaller at the HF level than the DFT, the trend as function of actinide is similar, with a slight increase from Ac to U. At the MP2 level, the binding energies are extremely close to the DFT values for Th to U, but that for AcHe_{16}^{3+} is rather larger than from DFT. As with the CCSD(T) data presented in Section 3.1, correction for BSSE significantly reduces the depth of the potential energy curve of Ac^{3+} –He at the MP2 level, bringing it close to the DFT value and resulting in a trend similar to that from DFT and HF. BSSE has less of an effect on the MP2 data for the later members of our target series. The correlation energy, obtained as the difference between the MP2 and HF results, is largest for Pa (8.62 kJ mol^{-1}) and smallest for Ac (5.52 kJ mol^{-1}) with an overall trend of $\text{Pa} > \text{Th} > \text{U} > \text{Ac}$. This is the same trend as V_{xc} , further demonstrating the reliability of the IQA method. The strengthening of the An^{3+} –He bond with the inclusion of MP2-level correlation is reminiscent of the increase in the closed-shell metallophilic interaction in $[\text{Cl-M-PH}_3]_2$ ($\text{M} = \text{Cu, Ag, Au, Rg}$) from HF to MP2.⁵¹

3.2.5 Ac^{3+} –Ng (Ng = Ne–Xe) complexes. To investigate the influence of noble gas species on the structure and bonding of AcNg_n^{q+} complexes, we extended our work to the heavier noble gas elements Ne–Xe. DFT search for the highest CN of AcNg_n^{3+} (Ng = Ne–Xe) complexes resulted in an n of 15, 10, 10, and 8 for Ng = Ne, Ar, Kr, and Xe, respectively, with the structures shown

in Fig. 10. The highest CN reduces down the Ng group, which is not unexpected considering the increasing atomic radii of the Ng elements. The highest CNs of Ac^{3+} –Ar and Ac^{3+} –Kr are both 10, with similar structure, and the average metal–ligand distance of the latter (3.383 \AA) is larger than the former (3.173 \AA). AIMD calculations were performed to confirm the thermodynamic stability of these structures (Fig. S7, ESI†), and all of them remain as the potential energy minimum during the whole relaxation time at 10 K.

During the AIMD relaxations, an interesting effect was discovered. It is logical that, for a compound consisting of n Ng atoms and an An ion, if n is larger than the highest CN, the system will have the highest-coordinated geometry with the remaining Ng atoms accommodated in the second shell. If n is less than the highest CN, an n -coordinated structure is expected. But this is not true for AcAr_{12}^{3+} (Ng = Ar–Xe). The optimized structures of AcAr_n^{3+} ($n = 10$ –12, 14) are shown in Fig. 11. It can be seen that for $n = 10, 11$ and 14, 10-coordinated structures with the remaining Ar atoms in the second shell are obtained after AIMD relaxation at $T = 10 \text{ K}$. For $n = 12$, however, the minimum potential energy structure is the icosahedral 12-coordinated one, which is stable even at $T = 100 \text{ K}$ (as shown in Fig. S8, ESI†). The 10-coordinated structure with 2 more Ar atoms in the second shell was also obtained, but its energy is $11.64 \text{ kJ mol}^{-1}$ higher than that of AcAr_{12}^{3+} . This 12-coordinated structure is also located for Kr and Xe.

To further study these AcNg_{12}^{3+} structures, QTAIM analysis was conducted, with the results being presented in Table 6. QTAIM analysis of the actinide-free Ng_{12} clusters were also conducted (Table 6). BCPs are found between Ac^{3+} and Ng atoms (Ng = He–Xe) in all AcNg_{12}^{3+} , confirming direct Ac^{3+} –Ng bonding. For the Ng_{12} clusters, BCPs are present between neighbouring Ng atoms in all systems (Ng = He–Xe). In AcHe_{12}^{3+} and AcNe_{12}^{3+} , the Ng–Ng BCPs disappear, suggesting that the stability of these two complexes is mainly due to the interaction between Ac and Ng. However, for AcNg_{12}^{3+} (Ng = Ar–Xe), BCPs are retained between neighbouring Ng atoms, indicating that Ng–Ng interactions also contribute to the stability of these structures. As shown in Table 6, the electron densities at these Ng–Ng BCPs (Ar–Xe) are uniform down the group, even though the average Ng–Ng distance increases from 3.44 \AA for Ar to 4.09 \AA for Xe. The delocalization indices also increase from Ar to Xe, indicating enhanced interaction between Ng and Ng. Moreover, the Ng–Ng BCP data in AcNg_{12}^{3+} (Ng = Ar–Xe) are slightly larger than that in the bare Ng_{12} . It seems that the 12 Ng atoms in AcNg_{12}^{3+}

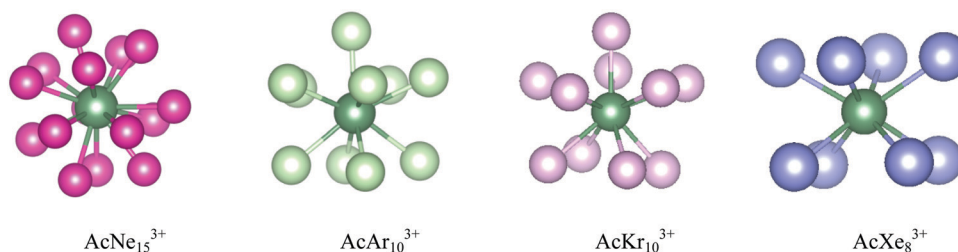


Fig. 10 Optimized highest CN structures of Ac^{3+} –Ng.



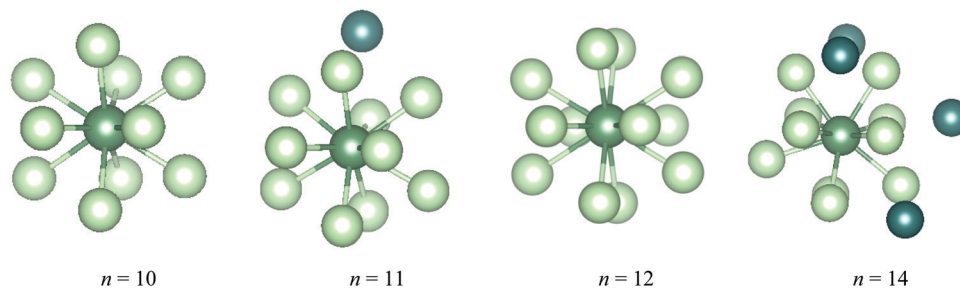


Fig. 11 The lowest potential energy structures of AcAr_n^{3+} determined by AIMD at $T = 10$ K. The Ar atoms in the second shell are highlighted in dark green.

Table 6 Structural, energetic, and QTAIM parameters (a.u.) for Ac–Ng and Ng–Ng BCPs in AcNg_{12}^{3+} complexes. The QTAIM parameters for Ng–Ng BCPs in bare Ng_{12} are listed in parentheses

	$r_{\text{av}}/\text{\AA}$	$ E_{\text{av}} /\text{kJ mol}^{-1}$	q_{Ac}	$q_{\text{Ng}}(\text{av})$	Ac–Ng			Ng–Ng		
					ρ_{BCP}	$\nabla^2\rho_{\text{BCP}}$	δ	ρ_{BCP}	$\nabla^2\rho_{\text{BCP}}$	δ
AcHe_{12}^{3+}	2.644	21.338	2.848	0.013	0.016	0.069	0.072	— (0.002)	— (0.009)	— (0.007)
AcNe_{12}^{3+}	2.779	33.445	2.800	0.017	0.019	0.092	0.092	— (0.003)	— (0.021)	— (0.015)
AcAr_{12}^{3+}	3.272	66.859	2.550	0.038	0.015	0.047	0.118	0.007 (0.006)	0.026 (0.025)	0.052 (0.048)
AcKr_{12}^{3+}	3.521	78.037	2.478	0.043	0.012	0.033	0.120(7)	0.007 (0.006)	0.023 (0.022)	0.067 (0.061)
AcXe_{12}^{3+}	3.887	88.278	2.403	0.050	0.009	0.019	0.121(3)	0.006 (0.006)	0.017 (0.016)	0.084 (0.075)

(Ng = Ar–Xe) form a cage, trapping Ac^{3+} within and enhancing the binding strength of Ng_{12} in return. This phenomenon is also found in ThNg_{12}^{4+} (geometrical and QTAIM parameters are listed in Table S3, ESI†). In summary, we suggest that the highest CN for AcNg_n^{3+} (Ng = Ar–Xe) is 12 considering the BCPs found between Ac^{3+} and all Ng atoms, although not all AcNg_n^{3+} structures are stable from $n = 1$ to 12 (e.g. AcAr_{11}^{3+} , AcKr_{11}^{3+} , AcXe_n^{3+} , $n = 9$ –11). The bonding situation in these complexes are similar to the $\text{M}(\text{EH})_{12}^{19}$ which possess strong radial M–EH bonding and weak peripheral E–E bonding.

The partial positive charge found on the Ng increases down the group (Table 6), with a corresponding decrease in q_{Ac} , reflecting the increasing polarizability of the heavier Ng elements, and hence greater transfer of electrons from $\text{Ng} \rightarrow \text{Ac}$. The small values of ρ_{BCP} and δ , as well as the positive $\nabla^2\rho_{\text{BCP}}$, indicate the closed-shell nature of the Ac^{3+} –Ng interaction. It is interesting to note that the Ac^{3+} –Ng ρ_{BCP} data increase from He to Ne before reducing in the heavier members of group 18. This is inconsistent with the metal–Ng interaction trend reported in previous theoretical work, which finds the largest BCP data at metal–Xe,⁵² but the difference in behaviour likely arises from the direct Ng–Ng interaction in AcNg_{12}^{3+} (Ng = Ar–Xe). The delocalization indices rise from He to Xe, although the change from Ar to Xe is quite small compared to the increase in binding energies, also due to the Ng–Ng interaction.

The effect of outer coordination on the properties of AcNg_{12}^{3+} are also studied. AIMD simulation of an Ac^{3+} – Ar_{42} cluster clearly shows separate first, second and outer Ar atom shells (Fig. S9, ESI†) with the former two containing 12 and 20 Ar atoms, respectively. The structure of Ac^{3+} –Ar with two Ar shells is shown in Fig. S10 (ESI†). It can be seen that the second

shell Ar has the same symmetry as that of the first shell. This structure is also located for Ne and Kr. The structural and QTAIM parameters for these compounds are shown in Table S4 (ESI†). Comparison with Table 6 shows that the average Ac–Ng bond distance decreases slightly as the second shell is included. Moreover, the cluster size has no effect on the trend in Ac–Ng and first shell Ng–Ng BCP properties. It is worth noting there are very weak bonds between the Ng atoms in the second shell even though the distances are large (e.g. ca. 4 Å for Ar).

4. Conclusions

In this contribution, we have studied the geometric and electronic structures and bonding of a range of complexes involving early actinide ions and the noble gases. We began by identifying the most appropriate form of DFT to study these systems, benchmarking the An^{3+} –He interaction energy curves against BSSE-corrected coupled cluster data, and concluding that dispersion-corrected B3LYP is a good choice for $\text{An} = \text{Ac}$ –Pa and for U(vi), with B3LYP–D3 being better for U(III). Using this approach, we verified that 18 He atoms can be accommodated in the primary coordination shell of Ac^{3+} , and checked the stability of this system by AIMD. The very low incremental binding energy for the 18th He supports our conclusion that a coordination number of 18 is the maximum. We also report new 18-coordinate Th^{4+} –He and Th^{3+} –He complexes. The former is stable at 3 K by AIMD, but increasing the temperature to 10 K leads to one He migrating into the second coordination shell. In ThHe_{18}^{3+} , two of the He are ca. 0.5 Å further from the metal than



the other 16, but QTAIM analysis supports the CN = 18 description. Further QTAIM and NPA of the 18 coordinated systems indicates closed shell bonding, supporting previous conclusions of charge-induced dipole interactions.

For Pa^{5+} -He and U^{6+} -He complexes, the highest CN is 17, whereas for Pa^{3+} and U^{3+} it is 16. As expected, the average An-He binding energies in the 17 coordinate group valent species is significantly larger than in all four An(III) systems, and there is greater transfer of charge from He \rightarrow An $^{q+}$ in the more highly charged complexes. The average An-He binding energy correlates linearly with this charge transfer. The interatomic exchange-correlation energy V_{xc} determined by the IQA approach correlates linearly with the more widely used QTAIM delocalization index covalency metric, both indicating that An-He covalency increases from AcHe_{17}^{3+} to UHe_{17}^{6+} . NPA of these 17 CN systems shows that the He \rightarrow An $^{q+}$ charge transfer is primarily into metal 6d orbitals for Ac, Th and Pa, but mainly into 5f for U.

QTAIM analysis of the bonding in AnHe_{16}^{3+} suggests charge-induced interactions in all cases. HF and MP2 calculations on these systems indicate that the trend in correlation energy is $\text{Pa} > \text{Th} > \text{U} > \text{Ac}$; the same trend is seen in V_{xc} .

Finally, we studied complexes of Ac^{3+} with the heavier noble gases. DFT searches show that the maximum coordination number decreases down the group, being 15, 10, 10 and 8 for Ne, Ar, Kr and Xe respectively. These complexes are confirmed as being stable at 10 K by AIMD. However, further AIMD analysis suggest that the highest coordination number for the Ar, Kr and Xe systems is actually 12 as the 12 Ac^{3+} -Ng bond paths are confirmed by QTAIM. Comparison of the bonding in AcNg_{12}^{3+} (Ng = He-Xe) using QTAIM shows enhanced Ng \rightarrow Ac^{3+} charge transfer as the Ng gets heavier, and the Ac-Ng delocalization index increases.

Conflicts of interest

There are no conflicts to declare.

Acknowledgements

We are grateful to the China Scholarship Council and The University of Manchester for a PhD studentship for LY. We are also grateful to The University of Manchester for a PhD studentship to SC, and to its Computational Shared Facility and associated support services.

References

- N. Bartlett, *Proc. Chem. Soc.*, 1962, 218.
- L. Belpassi, I. Infante, F. Tarantelli and L. Visscher, *J. Am. Chem. Soc.*, 2008, **130**, 1048–1060.
- K. O. Christe, *Angew. Chem., Int. Ed.*, 2001, **40**, 1419–1421.
- V. I. Feldman, F. F. Sukhov, A. Y. Orlov and I. V. Tyulpina, *J. Am. Chem. Soc.*, 2003, **125**, 4698–4699.
- J. P. Wagner, D. C. McDonald, 2nd and M. A. Duncan, *Angew. Chem., Int. Ed.*, 2018, **57**, 5081–5085.
- B. Liang, L. Andrews, J. Li and B. E. Bursten, *J. Am. Chem. Soc.*, 2002, **124**, 9016–9017.
- I. Infante, L. Andrews, X. Wang and L. Gagliardi, *Chem. – Eur. J.*, 2010, **16**, 12804–12807.
- X. Wang, L. Andrews, J. Li and B. E. Bursten, *Angew. Chem., Int. Ed.*, 2004, **43**, 2554–2557.
- S. Seidel and K. Seppelt, *Science*, 2000, **290**, 117–118.
- T. R. Galeev, C. Romanescu, W. L. Li, L. S. Wang and A. I. Boldyrev, *Angew. Chem., Int. Ed.*, 2012, **51**, 2101–2105.
- D. Pollak, R. Goddard and K. R. Porschke, *J. Am. Chem. Soc.*, 2016, **138**, 9444–9451.
- X. Gu, G. H. Chen, M. Ji, Y. X. Yao and X. G. Gong, *Nanoscale*, 2012, **4**, 2567–2570.
- I. A. Popov, T. Jian, G. V. Lopez, A. I. Boldyrev and L. S. Wang, *Nat. Commun.*, 2015, **6**, 8654.
- A. Hermann, M. Lein and P. Schwerdtfeger, *Angew. Chem., Int. Ed.*, 2007, **46**, 2444–2447.
- N. Kaltsoyannis, *Angew. Chem., Int. Ed.*, 2017, **56**, 7066–7069.
- E. Ozama, S. Adachi, T. Takayanagi and M. Shiga, *Chemistry*, 2018, **24**, 12716–12721.
- M. Joshi and T. K. Ghanty, *Chem. Commun.*, 2019, **55**, 7788–7791.
- S. X. Hu, P. Zhang, W. Zou and P. Zhang, *Nanoscale*, 2020, **12**, 15054–15065.
- M. von Hopffgarten and G. Frenking, *J. Phys. Chem. A*, 2011, **115**, 12758–12768.
- E. N. Esenturk, J. Fetting, Y. F. Lam and B. Eichhorn, *Angew. Chem., Int. Ed.*, 2004, **43**, 2132–2134.
- E. N. Esenturk, J. Fetting and B. Eichhorn, *J. Am. Chem. Soc.*, 2006, **128**, 9178–9186.
- S. Grimme, J. Antony, S. Ehrlich and H. Krieg, *J. Chem. Phys.*, 2010, **132**, 154104.
- R. Ahlrichs, M. Bär, M. Häser, H. Horn and C. Kölmel, *Chem. Phys. Lett.*, 1989, **162**, 165–169.
- W. Küchle, M. Dolg, H. Stoll and H. Preuss, *J. Chem. Phys.*, 1994, **100**, 7535–7542.
- X. Cao, M. Dolg and H. Stoll, *J. Chem. Phys.*, 2003, **118**, 487–496.
- X. Cao and M. Dolg, *THEOCHEM*, 2004, **673**, 203–209.
- C. Hättig, *Phys. Chem. Chem. Phys.*, 2005, **7**, 59–66.
- A. Nicklass, M. Dolg, H. Stoll and H. Preuss, *J. Chem. Phys.*, 1995, **102**, 8942–8952.
- B. P. Pritchard, D. Altarawy, B. Didier, T. D. Gibson and T. L. Windus, *J. Chem. Inf. Model.*, 2019, **59**, 4814–4820.
- P. Deglmann, F. Furche and R. Ahlrichs, *Chem. Phys. Lett.*, 2002, **362**, 511–518.
- M. J. Deegan and P. J. Knowles, *Chem. Phys. Lett.*, 1994, **227**, 321–326.
- H.-J. Werner, P. J. Knowles, G. Knizia, F. R. Manby, M. Schutz, P. Celani, W. Gyorffy, D. Kats, T. Korona, R. Lindh, A. Mitrushenkov, G. Rauhut, K. R. Shamasundar, T. B. Adler, R. D. Amos, S. J. Bennie, A. Bernhardsson, A. Berning, D. L. Cooper, M. J. O. Deegan, A. J. Dobbyn, F. Eckert, E. Goll, C. Hampel, A. Hesselmann, G. Hetzer, T. Hrenar,



- G. Jansen, C. Koppl, S. J. R. Lee, Y. Liu, A. W. Lloyd, Q. Ma, R. A. Mata, A. J. May, S. J. McNicholas, W. Meyer, T. F. Miller III, M. E. Mura, A. Nicklass, D. P. O'Neill, P. Palmieri, D. Peng, K. Pfluger, R. Pitzer, M. Reiher, T. Shiozaki, H. Stoll, A. J. Stone, R. Tarroni, T. Thorsteinsson, M. Wang and M. Welborn, *MOLPRO (Version 2019.2) a package of ab initio programs*, 2019.
- 33 C. C. J. Roothaan, *Rev. Mod. Phys.*, 1951, **23**, 69.
- 34 M. J. Frisch, M. Head-Gordon and J. A. Pople, *Chem. Phys. Lett.*, 1990, **166**, 275–280.
- 35 M. J. Frisch, G. W. Trucks, H. B. Schlegel, G. E. Scuseria, M. A. Robb, J. R. Cheeseman, G. Scalmani, V. Barone, G. A. Petersson, H. Nakatsuji, X. Li, M. Caricato, A. V. Marenich, J. Bloino, B. G. Janesko, R. Gomperts, B. Mennucci, H. P. Hratchian, J. V. Ortiz, A. F. Izmaylov, J. L. Sonnenberg, D. Williams-Young, F. Ding, F. Lipparini, F. Egidi, J. Goings, B. Peng, A. Petrone, T. Henderson, D. Ranasinghe, V. G. Zakrzewski, J. Gao, N. Rega, G. Zheng, W. Liang, M. Hada, M. Ehara, K. Toyota, R. Fukuda, J. Hasegawa, M. Ishida, T. Nakajima, Y. Honda, O. Kitao, H. Nakai, T. Vreven, K. Throssell, J. A. Montgomery Jr., J. E. Peralta, F. Ogliaro, M. J. Bearpark, J. J. Heyd, E. N. Brothers, K. N. Kudin, V. N. Staroverov, T. A. Keith, R. Kobayashi, J. Normand, K. Raghavachari, A. P. Rendell, J. C. Burant, S. S. Iyengar, J. Tomasi, M. Cossi, J. M. Millam, M. Klene, C. Adamo, R. Cammi, J. W. Ochterski, R. L. Martin, K. Morokuma, O. Farkas, J. B. Foresman and D. J. Fox, *Gaussian 16 (Version A.03)*, Gaussian, Inc., Wallingford, CT, 2016.
- 36 S. F. Boys and F. Bernardi, *Mol. Phys.*, 1970, **19**, 553–566.
- 37 M. A. Blanco, A. Martin Pendas and E. Francisco, *J. Chem. Theory Comput.*, 2005, **1**, 1096–1109.
- 38 T. A. Keith, *AIMAll (Version 19.10.12)*, TK Gristmill Software, Overland Park KS, USA, 2019.
- 39 A. D. Becke, *J. Chem. Phys.*, 1993, **98**, 1372–1377.
- 40 V. E. J. Berryman, J. J. Shephard, T. Ochial, A. N. Price, P. L. Arnold, S. Parsons and N. Kaltsoyannis, *Phys. Chem. Chem. Phys.*, 2020, **22**, 16804–16812.
- 41 E. D. Glendening, J. K. Badenhoop, A. E. Reed, J. E. Carpenter, J. A. Bohmann, C. M. Morales, P. Karafiloglou, C. R. Landis and F. Weihold, *NBO 7.0*, Theoretical Chemistry Institute, University of Wisconsin, Madison, WI, 2018.
- 42 W. G. Hoover, *Phys. Rev. A: At., Mol., Opt. Phys.*, 1985, **31**, 1695–1697.
- 43 J. P. Perdew, K. Burke and M. Ernzerhof, *Phys. Rev. Lett.*, 1996, **77**, 3865.
- 44 R. F. W. Bader, *Atoms in molecules: a quantum theory*, Clarendon Press, Oxford, New York, 1990.
- 45 C. F. Matta and R. J. Boyd, in *The Quantum Theory of Atoms in Molecules*, ed. C. F. Matta and R. J. Boyd, Wiley-VCH Verlag GmbH & Co. KGaA, Weinheim, 2007, vol. 1, pp. 1–34.
- 46 S. R. Daly, P. M. Piccoli, A. J. Schultz, T. K. Todorova, L. Gagliardi and G. S. Girolami, *Angew. Chem., Int. Ed.*, 2010, **49**, 3379–3381.
- 47 T. Arliguie, L. Belkhir, S. E. Bouaoud, P. Thuery, C. Villiers, A. Boucekkine and M. Ephritikhine, *Inorg. Chem.*, 2009, **48**, 221–230.
- 48 J. A. Platts and R. J. Baker, *Dalton Trans.*, 2020, **49**, 1077–1088.
- 49 M. J. Tassell and N. Kaltsoyannis, *Dalton Trans.*, 2010, **39**, 6719–6725.
- 50 I. Kirker and N. Kaltsoyannis, *Dalton Trans.*, 2011, **40**, 124–131.
- 51 E. O'Grady and N. Kaltsoyannis, *Phys. Chem. Chem. Phys.*, 2004, **6**, 680–687.
- 52 W. Zou, D. Nori-Shargh and J. E. Boggs, *J. Phys. Chem. A*, 2013, **117**, 207–212.



High Coordination Number Actinide-Noble Gas Complexes; a Computational Study

Lin Yang, Sophie Cooper and Nikolas Kaltsoyannis*

Department of Chemistry, School of Natural Sciences, The University of Manchester, Oxford
Road, Manchester M13 9PL

Supplementary Information

Table S1. Average Ac^{3+} -Ne distances (r_{av}), distance ranges (Δr), and average Ac^{3+} -Ne binding energies of AcNe_n^{3+} by BHLYP-D3 method with different basis sets

	Basis set	$r_{\text{av}} / \text{\AA}$	$\Delta r / \text{\AA}$	$ E_{\text{av}} / \text{kJ mol}^{-1}$
AcNe^{3+}	aug-cc-pV5Z	2.678	-	41.365
	Stuttgart RLC	2.685	-	40.439
AcNe_{16}^{3+}	aug-cc-pV5Z	2.932	0.215	28.457
	Stuttgart RLC	2.936	0.216	28.411

Table S2. Total energies of U^{3+} , He, and U^{3+} -He by various functionals at equilibrium U^{3+} -He distance. The unit of energy is Hartree. Total energy of U^{3+} by Gaussian 16/BHLYP is -475.2299.

	U^{3+}	He	U^{3+} -He
PBE	-475.3993	-2.8929	-478.3070
B3LYP	-475.3565	-2.9081	-478.2796
PBE0	-475.3745	-2.8951	-478.2834
BHLYP	-475.1612	-2.9057	-478.1472

Table S3. Structural, energetic, and QTAIM parameters for Th-Ng and Ng-Ng BCPs in ThNg₁₂⁴⁺ complexes. The QTAIM parameters for Ng-Ng BCPs in bare Ng₁₂ are listed in parentheses.

	$r_{av} / \text{\AA}$	$ E_{av} / \text{kJ mol}^{-1}$	q_{Ac}	$q_{Ng(av)}$	Ac-Ng			Ng-Ng		
					ρ_{BCP}	$\nabla^2 \rho_{BCP}$	δ	ρ_{BCP}	$\nabla^2 \rho_{BCP}$	δ
ThHe ₁₂ ⁴⁺	2.430	52.573	3.627	0.031	0.027	0.106	0.116	- (0.003)	- (0.016)	- (0.011)
ThNe ₁₂ ⁴⁺	2.582	78.072	3.510	0.041	0.032	0.136	0.147	- (0.006)	- (0.039)	- (0.024)
ThAr ₁₂ ⁴⁺	3.116	145.437	3.053	0.079	0.023	0.055	0.194	0.010 (0.008)	0.037 (0.036)	0.069 (0.063)
ThKr ₁₂ ⁴⁺	3.371	165.687	2.895	0.092	0.019	0.035	0.207	0.009 (0.008)	0.031 (0.029)	0.086 (0.077)
ThXe ₁₂ ⁴⁺	3.740	185.498	2.676	0.110	0.014	0.018	0.226	0.008 (0.007)	0.023 (0.022)	0.104 (0.093)

Table S4. Average Ac-Ng distance (r_{av}) and QTAIM parameters (au) for Ac-Ng and Ng-Ng BCPs in AcNg₁₂³⁺ complexes when including the second Ng shell. The average distance and BCP properties between Ac and second shell Ng atoms are listed in parentheses.

	$r_{av} / \text{\AA}$	Ac-Ng			Ng-Ng		
		ρ_{BCP}	$\nabla^2 \rho_{BCP}$	$\frac{G_{BCP}}{-V_{BCP}}$	ρ_{BCP}	$\nabla^2 \rho_{BCP}$	$\frac{G_{BCP}}{-V_{BCP}}$
AcNe ₁₂ ³⁺	2.760 (4.307)	0.021	0.094	1.170	- (0.003)	- (0.015)	- (1.684)
AcAr ₁₂ ³⁺	3.238 (5.569)	0.017	0.050	1.120	0.008 (0.002)	0.028 (0.008)	1.340 (1.576)
AcKr ₁₂ ³⁺	3.489 (6.002)	0.013	0.034	1.103	0.007 (0.002)	0.024 (0.007)	1.315 (1.678)

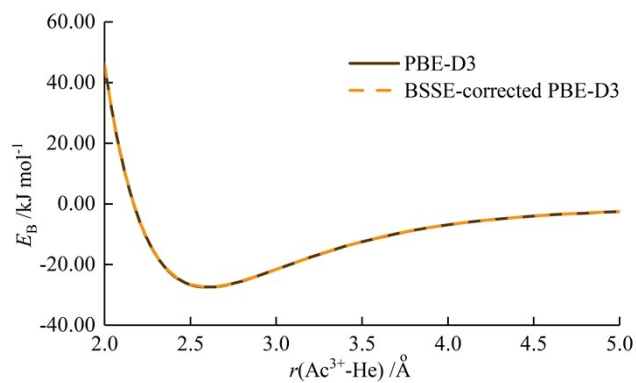


Figure S1. Potential energy curves of $\text{Ac}^{3+}\text{-He}$ by DFT calculation using PBE-D3 functionals with and without BSSE correction.

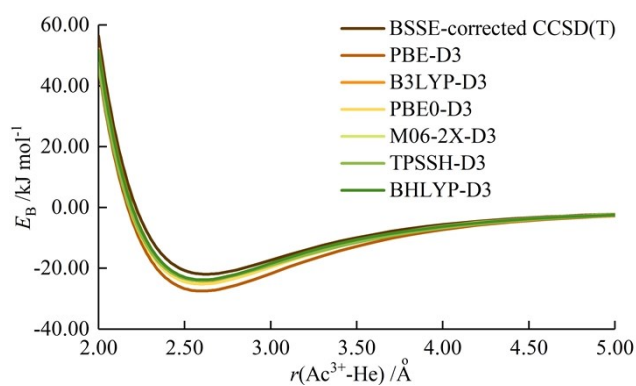


Figure S2. Potential energy curves of $\text{Ac}^{3+}\text{-He}$ by DFT calculation using various density functionals

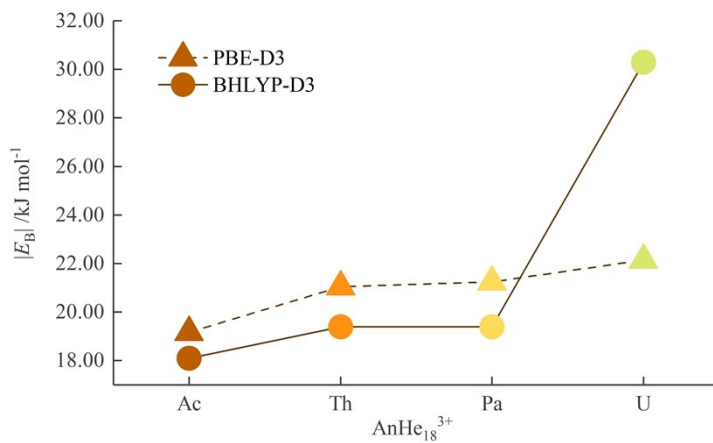


Figure S3. Average $\text{An}^{3+}\text{-He}$ binding energy of AnHe_{18}^{3+} complexes

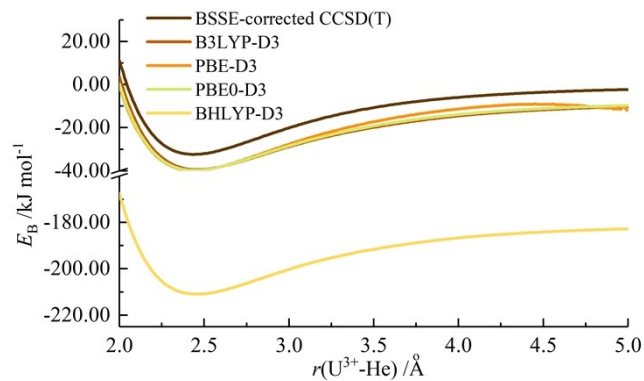


Figure S4. Potential energy curves for $\text{U}^{3+}\text{-He}$ using various functionals

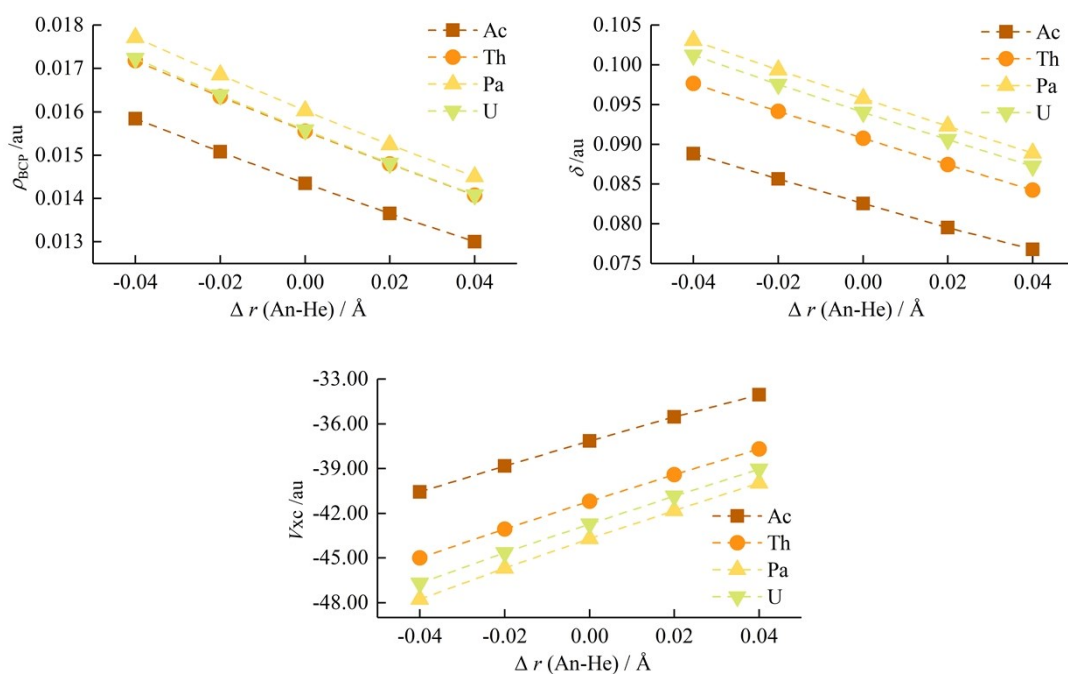


Figure S5. The electron density (ρ) at the An-He BCPs, delocalization index (δ) and IQA exchange-correlation energy (V_{xc}) for the An-He bond in diatomic $\text{An}^{3+}\text{-He}$ as a function of the shortening and elongation of An-He bond length from equilibrium ($\Delta r(\text{An-He})$). The equilibrium An-He distances in the AnHe_{16}^{3+} systems are used as references.

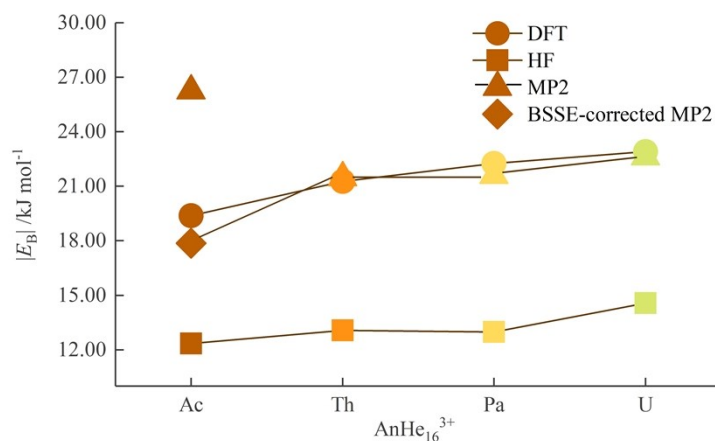


Figure S6. Average binding energies of AnHe_{16}^{3+} ($\text{An}=\text{Ac-U}$) obtained from DFT, HF, and MP2 calculation.

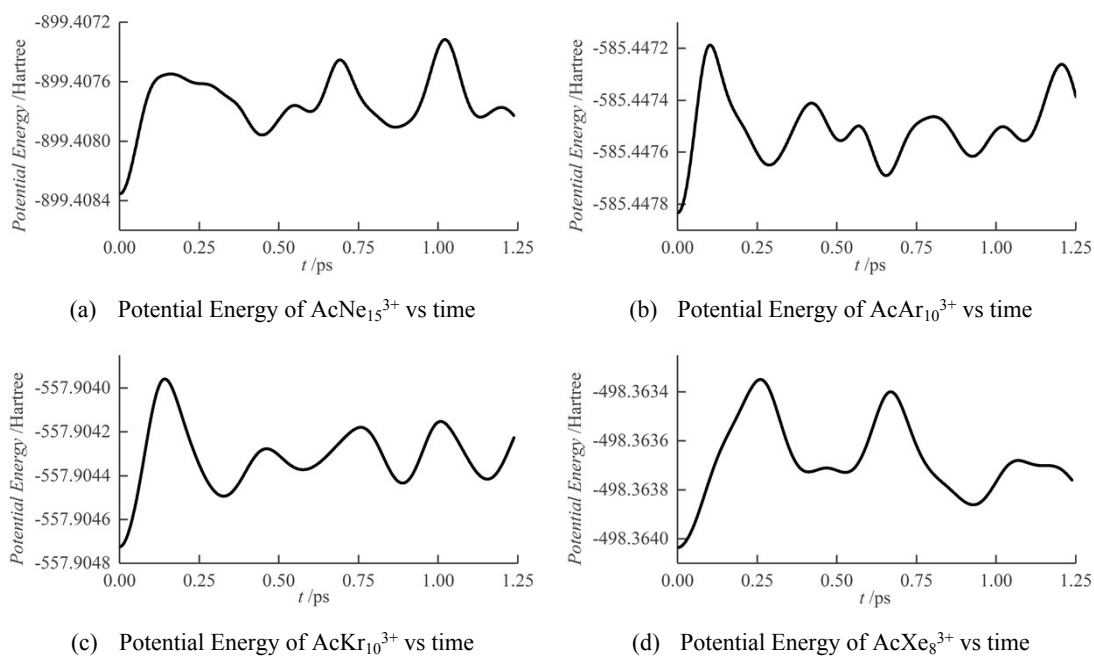


Figure S7. Evolution of AcNe_{15}^{3+} , AcAr_{10}^{3+} , AcKr_{10}^{3+} and AcXe_8^{3+} potential energy with time at 10 K. The initial structures are the ones shown in Figure 10, which remain as the potential energy minimum structure during the whole relaxation time.

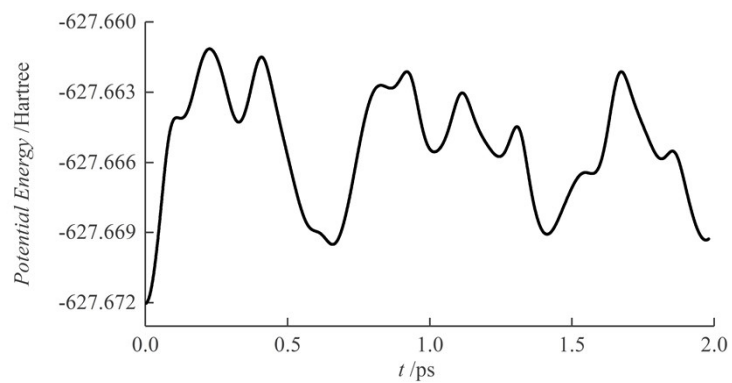


Figure S8. Evolution of AcAr_{12}^{3+} potential energy with time at 100 K. The initial structure is as in Figure 11.

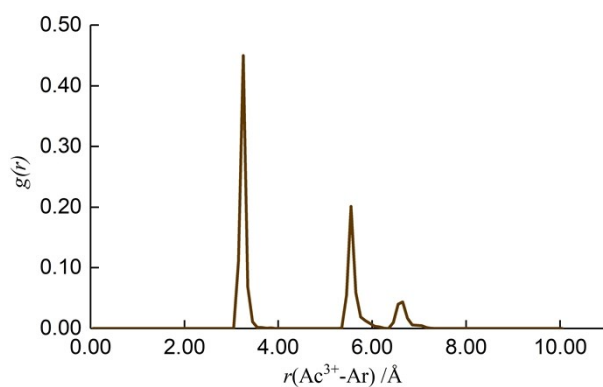


Figure S9. Ac^{3+} -Ar radial distribution function in Ac^{3+} - Ar_{42} obtained from AIMD calculation at 10 K. The time step is 1.21 fs and the total simulation time is 3.63 ps.

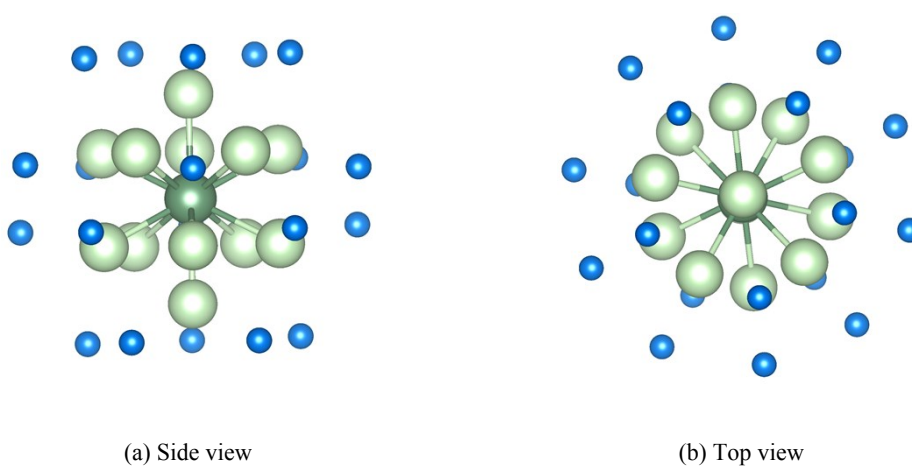


Figure S10. (a) side and (b) top views of optimized AcAr_{12}^{3+} with a second Ar shell. The green and blue balls are the Ar atoms in the first and second shell, respectively.

Cartesian Coordinates (Å) of the optimized $\text{AnNg}_n^{\text{q}+}$

Cartesian Coordinates (Å) of AcHe_n^{3+} ($n=1-18$)

$n = 1$

Ac	-0.0023290	-0.0000000	0.0000000
He	2.6023290	0.0000000	0.0000000

$n = 2$

Ac	0.0382391	0.2454927	-0.0880064
He	0.2808210	2.3239681	-1.6403215
He	-2.2702233	1.3678086	-0.5402914

$n = 3$

Ac	0.0409476	0.2438557	-0.0872425
He	0.2805622	2.3241608	-1.6404209
He	-2.2726730	1.3692529	-0.5409558
He	2.2378698	1.5989099	0.3166649

$n = 4$

Ac	0.0412087	0.2414614	-0.0863626
He	-0.2956683	2.3489158	1.4167260
He	0.2808454	2.3248755	-1.6405016
He	-2.2746778	1.3700397	-0.5415843
He	2.2393304	1.5998027	0.3164942

$n = 5$

Ac	0.0447718	0.2361947	-0.0854993
He	-0.2954896	2.3502015	1.4177138
He	0.2812081	2.3262624	-1.6414467
He	-2.2787845	1.3720559	-0.5424984
He	2.2393326	1.6003807	0.3165022
He	2.2131074	-1.2131229	0.2175539

$n = 6$

Ac	0.0423648	0.2292704	-0.0884083
He	-0.2961524	2.3568516	1.4222588
He	0.2812478	2.3292086	-1.6430198
He	-2.2813962	1.3738372	-0.5433457
He	2.2382895	1.5986912	0.3161002
He	2.2197923	-1.2158868	0.2187403
He	-0.3374344	-1.9626089	1.3172350

$n = 7$

Ac	0.0001836	0.1662686	-0.0821978
----	-----------	-----------	------------

He	-0.3257753	2.3683066	1.3022218
He	0.2541668	2.3457056	-1.5365573
He	-2.2242285	1.4955572	-0.5361210
He	2.2038480	1.5643514	0.2586475
He	2.2328454	-1.1846661	0.2768064
He	-0.2743286	-2.0461600	1.3167610
He	-2.1890790	-1.2348703	-0.5097760

$n = 8$

Ac	0.0023889	0.1618814	-0.0882796
He	-0.3277025	2.3764885	1.3031599
He	0.2544138	2.3477557	-1.5335135
He	-2.2254818	1.4959249	-0.5366654
He	2.2059382	1.5652380	0.2570001
He	2.2375628	-1.1850270	0.2793210
He	-0.2756846	-2.0524985	1.3169165
He	-2.1938025	-1.2352700	-0.5081545
He	0.3025107	-2.0263010	-1.5226995

$n = 9$

Ac	0.0032627	0.1618915	-0.0839424
He	-0.3291320	2.3801288	1.3005454
He	0.2553383	2.3540672	-1.5325875
He	-2.2285374	1.4976520	-0.5365297
He	2.2088465	1.5671807	0.2562882
He	2.2405448	-1.1868987	0.2784425
He	-0.2770263	-2.0563509	1.3145702
He	-2.1966664	-1.2369862	-0.5080639
He	0.3035130	-2.0324924	-1.5216379
He	0.9114768	0.1861787	2.3848439

$n = 10$

Ac	-0.0112610	0.1615869	-0.1020644
He	-0.2984238	2.4070008	1.2518255
He	0.2361037	2.4048464	-1.4797035
He	-2.2332301	1.5163122	-0.5465077
He	2.1859920	1.5746805	0.2916684
He	2.2166317	-1.1954907	0.3119205
He	-0.2407372	-2.0807032	1.2680693
He	-2.2014643	-1.2525256	-0.5223864
He	0.2873813	-2.0848201	-1.4644174
He	0.9506276	0.1834835	2.3435245
He	-1.7764724	0.1492180	1.8459846

$n = 11$

Ac	-0.0121343	0.1615844	-0.1093546
He	-0.2983404	2.4080075	1.2505757
He	0.2361411	2.4099242	-1.4788010
He	-2.2360685	1.5192315	-0.5458002
He	2.1868477	1.5755202	0.2930426
He	2.2174710	-1.1964321	0.3131736
He	-0.2400501	-2.0816527	1.2666476
He	-2.2042685	-1.2552968	-0.5215475
He	0.2877443	-2.0900115	-1.4632009
He	0.9544980	0.1832084	2.3491796
He	-1.7766928	0.1495057	1.8439986
He	-0.9579454	0.1335887	-2.5795415

$n = 12$

Ac	-0.0076487	0.1617199	-0.1149765
He	-0.2972288	2.4075779	1.2497841
He	0.2342020	2.4147383	-1.4772994
He	-2.2347518	1.5190476	-0.5475493
He	2.1878242	1.5772023	0.2968274
He	2.2180772	-1.1978053	0.3169811
He	-0.2382546	-2.0812177	1.2656173
He	-2.2031956	-1.2551638	-0.5229165
He	0.2854721	-2.0945548	-1.4618418
He	0.9553944	0.1828111	2.3475051
He	-1.7796014	0.1497451	1.8469783
He	-0.9630870	0.1330767	-2.5807380
He	1.7589467	0.1799774	-2.0817297

$n = 13$

Ac	0.1430889	0.0802236	-0.1099349
He	-0.1083749	2.4230444	1.1277185
He	-0.1123193	2.4096748	-1.3679471
He	-2.3990659	0.8162248	-0.1215836
He	2.0819640	1.9001960	-0.1075564
He	1.0331209	-2.0160128	1.2547938
He	-1.4727035	-1.6622105	1.1138167
He	-1.4726919	-1.6817400	-1.3031210
He	1.0345059	-1.9968040	-1.5069087
He	1.5983370	0.4760924	2.0750341
He	-1.0127440	0.4490843	2.2626800
He	-1.0025923	0.4092497	-2.4920765
He	1.6056238	0.4901321	-2.2882726
He	2.7156119	-0.5777924	-0.1096471

$n = 14$

Ac	-0.0001304	0.0412995	-0.1108330
He	0.0007925	2.3269766	1.2732721
He	-0.0015603	2.3200334	-1.5079306
He	-1.9658288	1.8569701	-0.1201861
He	1.9656756	1.8569183	-0.1214458
He	1.2044235	-1.9748077	1.1755683
He	-1.2071576	-1.9694062	1.1824574
He	-1.2052014	-1.9752151	-1.3940135
He	1.2069728	-1.9693690	-1.4015027
He	1.3562616	0.3635058	2.1549904
He	-1.3575843	0.3678229	2.1532874
He	-1.3567655	0.3537916	-2.3780666
He	1.3594131	0.3596447	-2.3750490
He	2.6324498	-0.4388027	-0.1035530
He	-2.6327329	-0.4387832	-0.1069665

$n = 15$

Ac	-0.0001567	0.0228384	0.0487785
He	0.0002138	2.1877550	1.5890202
He	-0.0013094	2.2615816	-1.4490518
He	-1.9040952	1.9146289	-0.1014281
He	1.9037470	1.9140764	-0.1039430
He	1.2830339	-2.0311052	1.1724658
He	-1.2843819	-2.0292901	1.1739505
He	-1.1721091	-1.9889449	-1.3070401
He	1.1712266	-1.9863997	-1.3106940
He	1.9363407	0.5064938	1.8572119
He	-1.9368282	0.5045326	1.8575917
He	-1.2807427	0.3024918	-2.2792402
He	1.2847597	0.3067519	-2.2768571
He	2.6339141	-0.4034734	-0.2742906
He	-2.6345849	-0.4013578	-0.2764451
He	0.0008191	-0.5293311	2.6816190

$n = 16$

Ac	-0.0000710	0.1863385	0.1165788
He	0.0006637	2.8855453	0.4999944
He	-0.0004864	1.6578461	2.3971746
He	-0.0002068	2.1719645	-1.7244554
He	-2.0228192	1.9124858	-0.2756364
He	2.0230095	1.9121147	-0.2768496
He	1.2897774	-1.9274026	1.1589433

He	-1.2898895	-1.9277329	1.1586820
He	-1.1332802	-1.8990901	-1.2121794
He	1.1334295	-1.8988687	-1.2118810
He	2.0248620	0.5064316	1.8563042
He	-2.0247705	0.5056592	1.8560319
He	-1.2707729	0.2420227	-2.2501737
He	1.2705802	0.2417365	-2.2500682
He	2.6235168	-0.3755776	-0.2664213
He	-2.6237859	-0.3752392	-0.2667455
He	-0.0001413	-0.6618888	2.6892008

$n = 17$

Ac	0.0000107	0.0308856	0.1565480
He	0.0005040	2.6592700	0.8006187
He	0.0003953	-2.6546656	0.7089590
He	-0.0003566	1.2430349	2.6186469
He	-0.0000211	2.0915685	-1.6448259
He	-1.9030192	1.9130352	-0.3691315
He	1.9032501	1.9125788	-0.3696690
He	1.9051031	-1.5252328	1.3268214
He	-1.9048150	-1.5257342	1.3258914
He	-1.1931852	-1.9755522	-1.2128824
He	1.1927797	-1.9753516	-1.2134734
He	2.0768475	0.8026000	1.7081145
He	-2.0770117	0.8018824	1.7079725
He	-1.1868764	0.1464384	-2.2746605
He	1.1869317	0.1466514	-2.2746034
He	2.6443696	-0.2664080	-0.4610180
He	-2.6445110	-0.2659112	-0.4611351
He	-0.0003851	-1.0574103	2.6352856

$n = 18$

Ac	0.0000118	0.0000090	-0.0000451
He	-0.0000029	2.8009788	-0.0014354
He	-0.0000047	-2.8263926	0.0003837
He	-0.0000111	1.8200657	2.0328342
He	-0.0000040	1.8187695	-2.0337611
He	-2.0327915	1.8191737	-0.0002060
He	2.0327995	1.8191796	-0.0002063
He	1.4292665	-1.8162637	1.4312339
He	-1.4292618	-1.8162570	1.4312305
He	-1.4299741	-1.8167675	-1.4304128
He	1.4299768	-1.8167725	-1.4304178
He	1.9085923	0.5120517	1.9097714

He	-1.9085887	0.5120496	1.9097655
He	-1.9086173	0.5115316	-1.9096302
He	1.9086180	0.5115279	-1.9096319
He	2.7043184	-0.5104605	0.0001254
He	-2.7043077	-0.5104579	0.0001273
He	-0.0000088	-0.5102862	2.7077333
He	-0.0000107	-0.5116793	-2.7074586

Cartesian Coordinates (Å) of ThHe₁₈^{q+} (q=3, 4)

ThHe₁₈³⁺

Th	0.0003130	0.0200369	0.0147806
He	0.0280231	2.6782793	-0.4339479
He	-0.0281616	-2.6153862	0.5855044
He	-0.1127778	2.0345873	1.7477625
He	0.1476722	1.3113897	-2.2932266
He	-1.9950524	1.7308297	-0.4388175
He	2.0369528	1.6994387	-0.3508238
He	1.6448820	-1.4085998	1.5658043
He	-1.7055973	-1.4281033	1.4745790
He	-1.6664130	-1.9033270	-0.8417927
He	1.6557887	-1.9422023	-0.7303804
He	1.8400205	0.8601829	1.7572442
He	-1.9994090	0.8011723	1.6328566
He	-1.7695385	0.0941036	-1.9909280
He	1.9517721	0.0065871	-1.8428762
He	3.1614649	-0.3244829	0.1575708
He	-3.1549132	-0.3009135	-0.0792697
He	-0.0683923	-0.2623922	2.6439607
He	0.0538323	-1.3080232	-2.2843361

ThHe₁₈⁴⁺

Th	-0.0000321	0.0037873	-0.0000048
He	0.0000031	2.6593151	-0.0007429
He	0.0000005	-2.6843630	0.0004364
He	-0.0000037	1.6874199	1.8648168
He	-0.0000018	1.6864772	-1.8657890
He	-1.8649678	1.6869803	-0.0003230
He	1.8649806	1.6870001	-0.0003248
He	1.3103783	-1.6849335	1.3115522
He	-1.3103729	-1.6849199	1.3115431
He	-1.3105970	-1.6854031	-1.3107873
He	1.3106002	-1.6854109	-1.3107928
He	1.7742940	0.4678604	1.7739492
He	-1.7742917	0.4678560	1.7739322

He	-1.7743640	0.4670802	-1.7740620
He	1.7743657	0.4670814	-1.7740789
He	2.5108167	-0.4671788	0.0002087
He	-2.5107998	-0.4671720	0.0002102
He	-0.0000046	-0.4651265	2.5118551
He	-0.0000036	-0.4663500	-2.5115984

Cartesian Coordinates (Å) of AnHe₁₇^{q+} (An=Th, $q=4$; An=Pa, $q=5$; An=U, $q=6$)

ThHe₁₇⁴⁺

Th	-0.0154794	0.1311564	-0.0005670
He	-0.0333124	2.6591750	0.0164723
He	-0.3233917	1.6989723	1.9278647
He	0.2734643	1.7297360	-1.9064689
He	-1.9485532	1.6988488	0.2796589
He	1.8954301	1.7286899	-0.2591395
He	1.0433601	-1.8987448	1.0433311
He	-1.1245661	-1.8318462	1.0950030
He	-1.0453777	-1.9012589	-1.0698692
He	1.1194268	-1.8033962	-1.1215208
He	1.6711782	0.8693882	1.7204546
He	-1.8277624	0.1270908	1.7854177
He	-1.7106098	0.8745167	-1.7114102
He	1.7956087	0.1735717	-1.7894206
He	2.4171055	-0.4587444	0.1901123
He	-2.4398873	-0.4895016	-0.2043820
He	0.1519504	-0.4912967	2.4266468
He	-0.1772593	-0.4607093	-2.4340123

PaHe₁₇⁵⁺

Pa	-0.0074424	-0.0454443	0.0111894
He	0.1232187	-2.4153917	-0.0118233
He	-0.1414568	1.7660083	1.5053967
He	-0.1051486	1.7957722	-1.4487106
He	-1.5305990	1.7705814	0.0108044
He	1.2570564	1.9662193	0.0479676
He	1.1355174	-1.4798012	1.4849261
He	-1.0147340	-1.5995311	1.4618838
He	-0.9788289	-1.5686490	-1.4959360
He	1.1719374	-1.4491876	-1.4626352
He	1.6846711	0.6117932	1.5055033
He	-1.7876657	0.3975223	1.4890587
He	-1.7513313	0.4285439	-1.5014012
He	1.7203044	0.6429599	-1.4262425
He	2.2907215	-0.6521837	0.0335150

He	-2.2186680	-0.8916022	-0.0252327
He	-0.0221310	-0.0714171	2.4145647
He	0.0371787	-0.0223766	-2.3921913

UHe₁₇⁶⁺

U	0.0039430	-0.0058398	-0.0028691
He	0.0011812	2.3154442	0.0107271
He	-0.2956298	1.4236771	1.7506397
He	0.2850061	1.4405704	-1.7431702
He	-1.7524203	1.4260362	0.2507761
He	1.7539298	1.4371554	-0.2547634
He	0.9640934	-1.8749027	0.9642279
He	-1.0153288	-1.7852324	0.9997214
He	-0.9351695	-1.8843933	-0.9765670
He	1.0406823	-1.7706934	-1.0133626
He	1.5429009	0.7028398	1.5740994
He	-1.6912947	-0.0106288	1.6496408
He	-1.5443095	0.6985247	-1.5795239
He	1.6923929	0.0132864	-1.6637931
He	2.2131858	-0.5453781	0.1911358
He	-2.1989725	-0.5660834	-0.2063068
He	0.1552028	-0.5598733	2.2066553
He	-0.1487358	-0.5509225	-2.2138991

Cartesian Coordinates (Å) of AnHe₁₆³⁺ (An=Th-U)

ThHe₁₆³⁺

Th	0.0254051	-0.0218638	0.0094330
He	-0.1782360	1.6599194	2.0372880
He	0.2042833	-1.7852892	1.9451895
He	-1.6129509	-0.1972652	2.0470910
He	1.6483173	0.1061865	2.0625969
He	1.3497690	-1.0809653	-1.9756790
He	-1.0315535	-1.4407961	-1.9506450
He	-1.0197891	0.8949010	-2.2030757
He	1.3261926	1.2885340	-1.8777635
He	2.0670120	-1.7253645	0.4146971
He	-1.7110178	-1.9742758	0.5055312
He	-1.9693025	1.6689305	0.5078277
He	1.5933490	2.0607323	0.5935217
He	2.6937808	0.2941151	-0.2623216
He	-2.5444818	-0.1881468	-0.6303654
He	0.2318726	-2.6595264	-0.4440350
He	-0.2436681	2.5431359	-0.6597915

PaHe₁₆³⁺

Pa	0.0378538	0.0146467	0.0079519
He	-0.0256383	1.3839512	2.2573920
He	0.1368500	-1.7758256	1.8685232
He	-1.6659741	-0.2061589	1.9537183
He	1.7069567	-0.0524821	2.0157497
He	1.3219633	-1.0482914	-1.9417568
He	-1.0096935	-1.5293322	-1.8341614
He	-0.9012300	0.6558891	-2.3335907
He	1.3609366	1.2867232	-1.8373129
He	2.0671424	-1.6815394	0.3265547
He	-1.7315334	-1.8925104	0.4093556
He	-1.7072277	1.8340478	0.7457816
He	1.2742569	2.2185377	0.5481769
He	2.6257696	0.4501780	-0.1218766
He	-2.4689862	0.0879888	-0.5858193
He	0.2426847	-2.7296095	-0.3696993
He	-0.4351486	2.4267487	-0.9894875

UHe₁₆³⁺

U	-0.0112333	0.0103284	0.0062710
He	1.6232539	1.8771590	0.9014782
He	-1.4310616	0.3312864	2.2108052
He	-0.6633128	2.2381632	1.1148273
He	0.8061922	0.3776776	2.4860927
He	-0.6290860	-2.4810004	-0.6164208
He	-1.8552952	-0.7467697	-1.6113509
He	0.7147035	-1.3594940	-2.1297462
He	1.6017716	-2.0789566	-0.1002521
He	-1.9056838	-1.5615925	0.9836798
He	-1.4213408	1.9613028	-1.0692050
He	0.8857837	2.1740575	-1.2076147
He	2.4351159	-0.2826525	0.9670723
He	0.2802868	-1.7937375	1.8121570
He	-0.2262120	0.6474258	-2.5574981
He	-2.5905674	0.5179066	0.2074266
He	2.1860654	0.2458516	-1.3032303

Cartesian Coordinates (Å) of Acn_{gn}³⁺ (ng=ne-Xe)

Acne₁₅³⁺

Ac	0.0649089	0.0374574	-0.0842097
ne	-0.7301278	2.3808119	1.5004672
ne	-0.2941238	2.3970812	-1.5590759
ne	-2.4540755	1.5129865	-0.1705287

ne	1.6001231	2.4558837	0.4254928
ne	1.5890502	-1.7620539	1.6627125
ne	-0.8151548	-2.4290434	1.1894670
ne	-0.6758719	-2.3538666	-1.4566864
ne	1.9594319	-1.8652829	-0.9806477
ne	1.0340101	0.6682458	2.5117670
ne	-1.5858081	-0.0590368	2.2040448
ne	-1.7458412	0.1592806	-2.3081171
ne	2.1182923	1.1501184	-1.7935565
ne	2.8988724	0.1769591	0.5271491
ne	-2.6250572	-1.0840760	-0.1079119
ne	0.6398915	-0.5977066	-2.9156596

AcAr₁₀³⁺

Ac	-0.3567782	0.7265734	-0.2300788
Ar	-0.5772107	3.5234594	1.3052302
Ar	-0.3854128	2.1160940	-3.0604747
Ar	-3.0111041	2.3904742	-0.8202945
Ar	2.0763068	2.7343745	-0.7034171
Ar	2.5104530	-0.6485413	-0.6297476
Ar	-0.1893949	-2.1482962	1.0277506
Ar	-2.9904791	-1.0247935	-0.7495303
Ar	-0.1631655	-1.3232921	-2.6547252
Ar	1.3773972	0.7955615	2.3861020
Ar	-2.2092375	0.5558364	2.2981995

AcKr₁₀³⁺

Ac	-0.0004260	0.0232246	-0.0506911
Kr	-0.2416594	3.0302771	1.5774009
Kr	-0.0277725	1.4908501	-3.0446000
Kr	-2.8415353	1.7956987	-0.6702414
Kr	2.6037483	2.1658224	-0.5413135
Kr	3.0858528	-1.4466482	-0.4970818
Kr	0.1760212	-3.0247055	1.2550756
Kr	-2.8384850	-1.8494789	-0.6301640
Kr	0.2060649	-2.1790022	-2.6192606
Kr	1.8485724	0.1064053	2.7030297
Kr	-1.9679374	-0.1529032	2.6154212

AcXe₈³⁺

Ac	-0.0001944	0.0004863	0.0003323
Xe	-0.2006829	3.3142520	1.0918181
Xe	0.8797183	1.9738265	-2.7414508
Xe	-3.0764723	1.0938363	-1.2427562

Xe	3.1388785	-1.1303005	-1.0391934
Xe	0.1324823	-3.2807289	1.1931258
Xe	-0.7227900	-2.0475573	-2.7328110
Xe	2.0805535	0.2256210	2.7958932
Xe	-2.2312394	-0.1464035	2.6833455

AcAr₁₂³⁺

Ac	-0.0064321	0.1613828	-0.1126065
Ar	-0.3569055	2.9493779	1.5683140
Ar	0.2761831	2.9423875	-1.8170246
Ar	-2.7651033	1.8465367	-0.6342013
Ar	2.7116720	1.9203437	0.3924955
Ar	2.7523255	-1.5238930	0.4086246
Ar	-0.2891103	-2.6194634	1.5923734
Ar	-2.7245511	-1.5977689	-0.6176913
Ar	0.3439262	-2.6270428	-1.7930608
Ar	1.1755828	0.1899758	2.9434158
Ar	-2.2100788	0.1450782	2.3070474
Ar	-1.1882409	0.1325036	-3.1686210
Ar	2.1968810	0.1777352	-2.5324220

AcKr₁₂³⁺

Ac	-0.0064609	0.1613050	-0.1126145
Kr	-0.3826153	3.1589140	1.6936062
Kr	0.2963391	3.1517449	-1.9443858
Kr	-2.9725790	1.9724941	-0.6733540
Kr	2.9154266	2.0507721	0.4309139
Kr	2.9597370	-1.6495599	0.4472938
Kr	-0.3093927	-2.8281639	1.7202355
Kr	-2.9282337	-1.7284680	-0.6560840
Kr	0.3696194	-2.8368753	-1.9179210
Kr	1.2634013	0.1918925	3.1753014
Kr	-2.3749951	0.1437606	2.4899818
Kr	-1.2759134	0.1304088	-3.4006078
Kr	2.3618155	0.1789283	-2.7157221

AcXe₁₂³⁺

Ac	-0.0063746	0.1612593	-0.1125097
Xe	-0.4210592	3.4620122	1.8753730
Xe	0.3274809	3.4530775	-2.1298069
Xe	-3.2720626	2.1551167	-0.7297988
Xe	3.2106775	2.2418562	0.4863145
Xe	3.2590979	-1.8324598	0.5047673
Xe	-0.3403766	-3.1304085	1.9045021

Xe	-3.2236764	-1.9192436	-0.7114511
Xe	0.4081659	-3.1393375	-2.1006408
Xe	1.3922992	0.1952062	3.5080264
Xe	-2.6123648	0.1419400	2.7522930
Xe	-1.4052203	0.1274805	-3.7330450
Xe	2.5995621	0.1806539	-2.9773807

Cartesian Coordinates (Å) of the potetial energy minimum structure of AcAr_n^{3+} by AIMD

AcAr_{10}^{3+}

Ac	-0.341723	0.724974	-0.228494
Ar	-0.573627	3.531934	1.320062
Ar	-0.405558	2.102679	-3.047847
Ar	-3.007184	2.397427	-0.842387
Ar	2.079925	2.732924	-0.712099
Ar	2.516414	-0.645057	-0.638566
Ar	-0.186009	-2.157332	1.031794
Ar	-2.998035	-1.028356	-0.735354
Ar	-0.155496	-1.306967	-2.653594
Ar	1.372507	0.786558	2.391087
Ar	-2.219839	0.558666	2.284410

AcAr_{11}^{3+}

Ac	0.130921	-0.274761	-0.058243
Ar	-0.019834	2.442194	1.620510
Ar	0.348832	3.947579	-1.545343
Ar	-2.245538	1.614507	-0.959315
Ar	2.654103	1.521801	-0.399833
Ar	2.944645	-1.861379	-0.067842
Ar	-0.066866	-3.140085	1.194310
Ar	-2.552767	-1.763997	-0.889436
Ar	0.463312	-2.548805	-2.293389
Ar	1.562438	-0.443207	2.741835
Ar	-2.002680	-0.320781	2.255836
Ar	0.458741	0.777742	-3.031223

AcAr_{14}^{3+}

Ac	-0.379845	-0.113810	-0.141952
Ar	0.310617	3.233884	2.976142
Ar	0.318553	3.462513	-2.945343
Ar	-1.765577	2.717495	0.022367
Ar	1.692561	2.220635	-0.029788
Ar	1.829447	-3.793907	2.927315
Ar	-1.186119	-2.684237	1.510482

Ar	-1.288349	-2.500567	-2.046038
Ar	1.709723	-2.508248	-0.376321
Ar	1.537511	-0.312975	2.330371
Ar	-1.796525	0.502967	2.674790
Ar	-1.918681	0.795271	-2.825804
Ar	1.434847	-0.000023	-2.719706
Ar	4.207572	-0.135650	-0.248764
Ar	-3.531940	-0.566206	-0.098750

Cartesian Coordinates (Å) of the structure of $\text{Ac}^{3+}\text{-Ng}_{32}$

$\text{Ac}^{3+}\text{-Ne}_{32}$

Ac	-0.2557642	-0.0021300	-0.0329163
Ne	-0.5587989	2.4423933	1.2109196
Ne	0.1072413	2.2481639	-1.5910966
Ne	-2.5446496	1.4116516	-0.6442176
Ne	2.0276362	1.4707031	0.4508044
Ne	2.0205464	-1.4308226	0.5947508
Ne	-0.6078562	-2.2751687	1.4909097
Ne	-2.5461581	-1.4652977	-0.5151873
Ne	0.0347948	-2.4397809	-1.2981961
Ne	0.5736939	0.1409147	2.5966771
Ne	-2.2009524	0.1632670	1.9211082
Ne	-1.0798125	-0.1336120	-2.6639635
Ne	1.7171178	-0.1846285	-1.9559249
Ne	1.2801902	4.0384617	0.0407959
Ne	1.5769574	2.6317245	2.8445563
Ne	-1.7467442	3.9799563	-0.6637484
Ne	2.7650903	2.2964542	-2.0042965
Ne	-1.1711443	1.8477249	3.7648016
Ne	-2.1065118	2.3120114	-3.1393394
Ne	-3.2128448	2.6454968	1.6604578
Ne	0.7796577	1.2790707	-4.0194054
Ne	-3.7718832	-0.1156363	-2.5068390
Ne	4.0243624	-0.0324760	-0.5623095
Ne	3.2663247	0.1182222	2.4267481
Ne	-4.5225767	0.0234492	0.5627881
Ne	-1.2320700	-1.3482242	3.9414087
Ne	-2.1126821	-2.6102901	-2.9189513
Ne	-3.2592551	-2.3132736	1.9408914
Ne	0.6816771	-1.8182225	-3.8400590
Ne	1.5613575	-2.3093511	3.1014562
Ne	-1.8181337	-4.0401160	-0.1452003
Ne	2.6914635	-2.6831633	-1.7017224

Ne	1.2381888	-4.0092768	0.5478735
----	-----------	------------	-----------

Ac³⁺-Ar₃₂

Ac	-0.2869763	0.0034966	-0.0206506
Ar	-0.6848861	2.8416309	1.4318416
Ar	0.1343762	2.6249213	-1.8432795
Ar	-3.0250010	1.7059192	-0.7820436
Ar	2.4031841	1.7208497	0.5343885
Ar	2.4122436	-1.6791274	0.7353064
Ar	-0.6811930	-2.6339024	1.7715830
Ar	-3.0028658	-1.7213505	-0.5963264
Ar	0.1091246	-2.8368218	-1.4993672
Ar	0.7482411	0.1849346	3.0412916
Ar	-2.5760142	0.1331575	2.2227824
Ar	-1.2985175	-0.1674447	-3.0701423
Ar	2.0338151	-0.1677577	-2.2581531
Ar	1.8234909	5.1483608	-0.0491050
Ar	2.0586531	3.4730209	3.6118636
Ar	-2.2183979	5.1639672	-0.9733312
Ar	3.6626104	2.9229422	-2.5915375
Ar	-1.3680322	2.2886956	4.8939843
Ar	-2.5058031	3.0748522	-4.1388007
Ar	-4.1005689	3.3711427	2.3053111
Ar	1.1289502	1.5952150	-5.1304956
Ar	-4.9089071	-0.0953479	-3.2456084
Ar	5.2576482	-0.0114779	-0.6817396
Ar	4.3754911	0.0747965	3.0824206
Ar	-5.8517235	0.0467285	0.7502471
Ar	-1.3946356	-1.6656344	5.1315374
Ar	-2.5371818	-3.4503448	-3.7810384
Ar	-4.1244735	-3.0971456	2.5443368
Ar	1.0027096	-2.1869921	-4.9334258
Ar	2.0451623	-3.0377075	4.0143078
Ar	-2.2266267	-5.1884937	-0.2297617
Ar	3.4827764	-3.4691305	-2.1989730
Ar	1.7117896	-5.1277573	0.8461517

Ac³⁺-Kr₃₂

Ac	-0.2550842	-0.0047875	-0.0332154
Kr	-0.6597942	3.0721779	1.5611173
Kr	0.2014729	2.8396181	-1.9918405
Kr	-3.1242047	1.8044087	-0.8456495
Kr	2.6472456	1.8444258	0.5551451
Kr	2.6129393	-1.8134464	0.7798306

Kr	-0.7096990	-2.8513897	1.9249203
Kr	-3.1566542	-1.8543899	-0.6222835
Kr	0.1506242	-3.0819534	-1.6294704
Kr	0.8265478	0.1920485	3.2810461
Kr	-2.7350639	0.1679868	2.4123693
Kr	-1.3343449	-0.2014433	-3.3460415
Kr	2.2287480	-0.1784094	-2.4800493
Kr	1.8725234	5.6049991	0.1171367
Kr	2.3287038	3.6872510	3.9299939
Kr	-2.2930274	5.5753706	-0.8904920
Kr	3.9557948	3.2631845	-2.7867410
Kr	-1.5596967	2.4912376	5.2698989
Kr	-2.7802687	3.2135557	-4.4209815
Kr	-4.4082258	3.6442548	2.2962395
Kr	1.0903874	1.7907766	-5.5997145
Kr	-5.1925671	-0.1684782	-3.4446648
Kr	5.7004662	-0.1088426	-0.7849952
Kr	4.6871793	0.1624069	3.3697408
Kr	-6.2089738	0.0985033	0.7311184
Kr	-1.5970580	-1.8039328	5.5315703
Kr	-2.8405547	-3.6923921	-4.0003958
Kr	-4.4659367	-3.2706292	2.7225349
Kr	1.0490622	-2.5019919	-5.3357022
Kr	2.2718442	-3.2215473	4.3554621
Kr	-2.3854005	-5.6133676	-0.1854534
Kr	3.8948660	-3.6609196	-2.3581187
Kr	1.7866119	-5.5860900	0.8112592

-Blank page-

Part III

Conclusions

-Blank page-

7 Conclusions and Future Work

7.1 Conclusions.

In this thesis, we have used density functional theory (DFT) to study the bulk properties of actinide nitrides and the diffusion of noble gases (Ng, especially Kr and Xe) in them. The first thing we investigated (chapter 3) is the most appropriate density functional for nitrides because standard DFT functionals sometimes can yield incorrect predictions for actinide materials. For example, conventional GGA functionals usually incorrectly predict actinide dioxides as metallic due to the overestimation of the delocalization of actinide f states, which is typically corrected by the application of the Hubbard U term or avoided by using hybrid functionals. In chapter 3, we reported that the electronic structure of UN is well reproduced by conventional GGA functionals, while Hubbard U corrections, as well as hybrid functionals, overestimate the localization of U f states in UN. Chapter 5 also showed that the main features of Pu f and U f states in (U, Pu)N are well reproduced by the PBE functional. The addition of a Hubbard U correction predicts lower peak locations. Thus we conclude that conventional GGA functionals perform better than hybrid ones and the GGA + U approach when studying UN and (U, Pu)N, and thus conventional GGA functionals have been used throughout chapters 3-5.

We then explored intrinsic point defects and the incorporation of Ng atoms (Kr and Xe) in UN (chapter 3). We found that the defect formation energies of U and N vacancies and Ng solution energies are highly dependent on stoichiometry. The most stable defects are N vacancies under U-rich and near-stoichiometric conditions but U vacancies under N-rich conditions. The calculated solution energy of Kr and Xe shows that the preferred trap sites are Schottky defects and U vacancies under U-rich and N-rich conditions, respectively. Under near-stoichiometric conditions, Kr prefers a U vacancy but Xe has similar solution

energies at U vacancy and Schottky defects, with the latter being slightly more stable.

Considering that Ng atoms prefer U vacancy defects, we then studied Ng diffusion in UN by the U vacancy (V_U)-assisted mechanism (chapter 4). The interstitial mechanism is also investigated for comparison. The calculated diffusion coefficients of the V_U -assisted mechanism are 10-20 orders of magnitude larger than that of the interstitial mechanism. The good agreement with experiment indicates that the monovacancy-assisted mechanism governs Xe diffusion in UN and proves the accuracy of our theoretical model. The two mechanisms have the opposite stoichiometric dependence, with the V_U -assisted mechanism increasing from U-rich to N-rich conditions while the interstitial mechanism decreasing.

In chapter 5, we moved to the more complicated uranium-plutonium mixed nitride ((U, Pu)N). Considering the findings from the UN work, *i.e.*, Ng atoms prefer defects containing U vacancies and the V_U -assisted mechanism is the dominant one for Ng diffusion, we focused on the actinide vacancy (V_{An}) defects. We found that the V_{An} formation energy (E_f) and Xe incorporation energy (E_i) at V_{An} highly depend on the local chemical environment around the vacancy due to the chemical disorder of (U, Pu)N. Both E_f and E_i increase as the number of uranium atoms in the first nearest-neighbour shell around the vacancy increases, while decrease as the number of uranium atoms in the second nearest-neighbour shell increases. Compared with that in binary UN, the E_f of some V_U are lower, indicating the mixing in of Pu creates some low energy cost U vacancy sites. For the migration energy barrier (E_m), the values of some pathways that involve V_{Pu} are lower than those in UN, indicating the mixing in of Pu also creates some low energy cost migration pathways.

Overall, in chapter 3-5, we systemically calculated intrinsic defect formation energy, Ng incorporation energy, Ng migration barriers in nitride fuels UN and (U, Pu)N, as well as Ng diffusion coefficient in UN. We believe our work provides a good theoretical basis to predict the diffusivity of Ng in nitride fuel grains and to parameterize subsequent mesoscale simulations, and will contribute to fission gas release models in nitride fuels.

In Chapter 6, we turned to molecular systems to study the nature of An-Ng interactions. The group valent and trivalent early actinides (from Ac to U) are considered. We found the charged actinide and Ng interactions are mainly charge-induced dipole with little charge transfer. This closed-shell interaction nature is consistent with the DOS and charge density results in chapter 3 and 5, in which Ng states do not overlap with U/Pu states and the calculated Ng Bader charges are quite small. This proves the extremely weak interaction between solute Ng atoms with matrix actinide atoms in nitride fuels. Moreover, the highest coordination number of 18 has been reported for $\text{Th}^{4+}\text{-He}$ and $\text{Th}^{3+}\text{-He}$ complexes for the first time. Then by looking at the group valent AnHe_{17}^{q+} ($\text{An} = \text{Ac}$, $q = 3$; $\text{An} = \text{Th}$, $q = 4$; $\text{An} = \text{Pa}$, $q = 5$; $\text{An} = \text{U}$, $q = 6$), we established a method of analysing covalency by implementing QTAIM and IQA. We found the IQA interatomic exchange-correlation energy term (V_{XC}) correlates linearly with the QTAIM bond order metric (δ), both indicating the An-He covalency increases from AcHe_{17}^{3+} to UHe_{17}^{6+} . For the An-Ng bond nature across Ng series, QTAIM metrics of AcNg_{12}^{3+} ($\text{Ng} = \text{He} - \text{Xe}$) shows the covalency increases as Ng gets heavier.

7.2 Future work

As discussed in chapter 3, conventional GGA functionals reproduce the UN electronic spectrum better than the hybrid and meta-GGA functionals, as well as the GGA+ U method. However, they incorrectly predict FM UN as the ground state, which is contradictory to

the experimental AFM state. Although we choose the conventional GGA functionals from the perspective of electronic structure, it does not mean they are the best choice for nitride fuels. Developing a new density functional, which could perform well in both electronic structure and magnetic state, is highly desirable. Additionally, as spin orbit coupling has been neglected in this work, it would be interesting to assess the effect of SOC in future work.

Another way to progress this work is radiation-enhanced diffusion. As seen in chapter 4, Ng diffusion coefficients with thermal equilibrium vacancy concentration do not fit well with experiments, since the samples used in experiments are irradiated, for which the vacancy concentration would be higher than the equilibrium values. Under irradiation, vacancy concentration cannot be directly calculated by equation (2.68). Instead, it is determined by the fission rate, the availability of defect sinks, and the recombination rate of vacancies and interstitials. Rate theory would be helpful to study the radiation-enhanced diffusion. Moreover, in the current intrinsic diffusion model, we focus on the monovacancy-assisted mechanism of Ng diffusion, and the effect of defect clusters was not considered. As introduced in chapter 1, U_xO_y vacancy clusters play an important role in Xe intrinsic diffusion in UO_2 . It is reasonable to expect that defect clusters will affect Ng diffusion in nitrides. But a very large supercell is necessary to study this, which is too costly for the DFT method. Future work could use molecular dynamics with empirical potentials to study this.

Furthermore, in the mixed (U, Pu)N work, a $2 \times 2 \times 2$ supercell was used to model the (U, Pu)N solid solution in this work due to the computational cost of DFT method. This is too small to identify all the possible chemical environments. Future work, most likely using empirical potentials as employed by Bathellier *et al.* for (U, Pu)O₂, should be able to take

a further step to draw some more definitive conclusions on the range of defect formation energies and Ng incorporation energies in uranium-plutonium mixed nitride.